

DOTTORATO DI RICERCA IN SCIENZE CHIMICHE - XXV CICLO

Settore Concorsuale di afferenza: 03/B1 Fondamenti delle Scienze Chimiche e Sistemi Inorganici

Settore Scientifico disciplinare: CHIM/03 – Chimica Generale ed Inorganica

Conductive Polymer Composites

Presentata da:

Dott. Filippo Pierini

Relatore:

Prof. Norbero Roveri

Coordinatore Dottorato:

Prof.ssa Adriana Bigi

ABSTRACT

In recent years, nanotechnologies have led to the production of materials with new and sometimes unexpected qualities through the manipulation of nanoscale components.

This research aimed primarily to the study of the correlation between hierarchical structures of hybrid organic-inorganic materials such as conductive polymer composites (CPCs).

Using a bottom-up methodology, we could synthesize a wide range of inorganic nanometric materials with a high degree of homogeneity and purity, such as thiol capped metal nanoparticles, stoichiometric geomimetic chrysotile nanotubes and metal dioxide nanoparticles. It was also possible to produce inorganic systems formed from the interaction between the synthesized materials.

These synthesized materials and others like multiwalled carbon nanotubes and grapheme oxide were used to produce conductive polymer composites.

Electrospinning causes polymer fibers to become elongated using an electric field. This technique was used to produce fibers with a nanometric diameter of a polymer blend based on two different intrinsically conducting polymers (ICPs): polyaniline (PANI) and poly(3-hexylthiophene) (P3HT).

Using different materials as second phase in the initial electrospun polymer fibers caused significant changes to the material hierarchical structure, leading to the creation of CPCs with modified electrical properties. Further study of the properties of these new materials resulted in a better understanding of the electrical conductivity mechanisms in these electrospun materials.

DEDICATION

To my wife Kamila

ACKNOWLEDGMENTS

First and foremost I want to would like to express my gratitude to my advisor, Prof. Norberto Roveri. I felt honored to be his Ph.D. student. I am very grateful for all of his contributions in terms of time, ideas, and funding that made my Ph.D. experience a very productive one.

The members of LEBSC have positively contributed to my personal and professional life in Bologna.

I would like to thank Prof. Elisabetta Foresti for her valuable assistance in the realization of many experimental setups.

I would like to thank Prof. Giuseppe Falini for giving me advice on many occasions.

I would like to thank Dr. Guido Fracasso. We worked together on the inorganic nanomaterial synthesis.

For the development of polymer materials, Prof. Massimiliano Lanzi made significant contributions to the experiments.

I also would like to thank Dr. Isidoro Giorgio Lesci, Marco Lelli, Eros D'Amen and Marco Marchetti for inspiring discussions regarding these experiments.

I would like to thank Maria Molinas. It was always nice to discuss things with you, always smiling and encouraging also in the most stressful periods.

I would like to thank Adria Costanzi for her good work.

Finally, I would also like to thank my family for their help and support.

TABLE OF CONTENTS

	Page
ABSTRACTS	ii
DEDICATION	iii
ACKNOWLEDGMENTS	iv
LIST OF FIGURES	xii
CHAPTER I: INTRODUCTION	1
1.1 Chrysotile Nanotubes.....	1
References.....	4
1.2 Metal Nanoparticles.....	5
References.....	8
1.3 Graphene Oxide.....	10
References.....	11
1.4 Inorganic Nanostructured Materials.....	14
References.....	18
1.5 Conductive Polymers.....	19
References.....	27
1.6 Conductive Polymer Composite.....	29
References.....	35
1.7 Electrospinning technique.....	37
References.....	43
CHAPTER II: RESEARCH AIMS	45

CHAPTER III: INSTRUMENTS AND CHEMICAL REAGENTS	46
3.1 Hydrothermal reactor.....	46
3.2 Electrospinning.....	46
3.3 Scanning electron microscopy (SEM).....	47
3.4 Energy dispersive x-ray spectroscopy (EDS).....	49
3.5 Transmission electron microscopy (TEM).....	52
3.6 Atomic force microscopy (AFM).....	53
3.7 Fourier Transform Infrared Spectroscopy (FT-IR).....	56
3.8 X-ray diffraction (XRD).....	57
3.9 Thermogravimetric analysis (TGA)	59
3.10 Differential scanning calorimetry (DSC).....	60
3.11 Ultraviolet and visible spectroscopy (UV/Vis).....	62
3.12 Four-Point-Probe method of conductivity measurement.....	63
3.13 Chemical reagents and solvents.....	64
CHAPTER IV: EXPERIMENTAL	65
4.1 Synthesis of chrysotile nanotubes.....	65
4.2 Synthesis of nanoparticles.....	65
4.2.1 Synthesis of 1-butanethiol capped silver nanoparticles.....	65
4.2.2 Synthesis of 4-methylbenzenethiol capped silver nanoparticles.....	66
4.2.3 Synthesis of silver nanoparticles.....	67
4.2.4 Synthesis of 1-butanethiol capped copper nanoparticles.....	67
4.2.5 Synthesis of 4-methylbenzenethiol capped copper nanoparticles.....	67
4.2.6 Synthesis of copper nanoparticles.....	68
4.2.7 Synthesis of 4-methylbenzenethiol capped gold nanoparticles.....	68
4.2.8 Synthesis of 4-methylbenzenethiol capped gold-silver 1:4 nanoparticles.....	69

4.2.9 Synthesis of 4-methylbenzenethiol capped gold-silver 4:1 nanoparticles.....	70
4.2.10 Synthesis of 1-butanethiol capped silver-copper 1:1 nanoparticles.....	70
4.2.11 Synthesis of silver-copper 1:1 nanoparticles.....	71
4.2.12 Synthesis of anatase nanoparticles.....	71
4.2.13 Synthesis of copper (I) chloride nanoparticles.....	71
4.3 Preparation of inorganic nanostructured composites.....	72
4.4 Electrospun conductive polymer fibers.....	73
4.4.1 Electrospun polyaniline (PANI) fibers.....	73
4.4.1.1 Electrospun polyaniline (PANI) mat.....	73
4.4.1.2 Electrospun polyaniline (PANI) yarn.....	73
4.4.2 Electrospun poly(3-hexylthiophene) (P3HT) fibers.....	74
4.5 Electrospun conductive polymer composite fibers.....	74
4.5.1 Electrospun polyaniline (PANI) and 4-methylbenzenethiol capped silver nanoparticles fibers.....	75
4.5.2 Electrospun polyaniline (PANI) and 1-butanethiol capped copper nanoparticles fiber.....	75
4.5.3 Electrospun polyaniline (PANI) and copper nanoparticles fibers	75
4.5.4 Electrospun polyaniline (PANI) and 4-methylbenzenethiol capped gold nanoparticles fibers	75
4.5.5 Electrospun polyaniline (PANI) and 4-methylbenzenethiol capped gold-silver 1:4 nanoparticles fibers.....	76
4.5.6 Electrospun polyaniline (PANI) and 4-methylbenzenethiol capped gold-silver 4:1 nanoparticles fibers.....	76
4.5.7 Electrospun polyaniline (PANI) and 1-butanethiol capped silver-copper 1:1 nanoparticles fibers	76
4.5.8 Electrospun polyaniline (PANI) and silver-copper 1:1 nanoparticles fiber.....	77
4.5.9 Electrospun polyaniline (PANI) and anatase nanoparticles fibers.....	77
4.5.10 Electrospun polyaniline (PANI) and copper (I) chloride nanoparticles fibers.....	77

4.5.11 Electrospun polyaniline (PANI) and chrysotile nanotubes 1-butanethiol capped copper nanoparticles system fibers.....	77
4.5.12 Electrospun polyaniline (PANI) and chrysotile nanotubes 4-methylbenzenethiol capped copper nanoparticles system fibers.....	78
4.5.13 Electrospun polyaniline (PANI) and chrysotile nanotubes 4-methylbenzenethiol capped gold nanoparticles system fibers.....	78
4.5.14 Electrospun polyaniline (PANI) and chrysotile nanotubes 4-methylbenzenethiol capped gold-silver 1:4 nanoparticles system fibers.....	78
4.5.15 Electrospun polyaniline (PANI) and chrysotile nanotubes 4-methylbenzenethiol capped gold-silver 4:1 nanoparticles system fibers.....	79
4.5.16 Electrospun polyaniline (PANI) and chrysotile nanotubes 1-butanethiol capped silver nanoparticles system fibers.....	79
4.5.17 Electrospun polyaniline (PANI) and chrysotile nanotubes 4-methylbenzenethiol capped silver nanoparticles system fiber.....	79
4.5.18 Electrospun polyaniline (PANI) and multiwalled carbon nanotubes fibers.....	80
4.5.19 Electrospun polyaniline (PANI) and chrysotile nanotubes fibers.....	80
4.5.20 Electrospun of poly(3-hexylthiophene) (P3HT) and graphene oxide fibers.....	80
4.5.21 Electrospun of poly(3-hexylthiophene) (P3HT) and multiwalled carbon nanotubes fibers.....	81
4.5.22 Electrospun of poly(3-hexylthiophene) (P3HT) and chrysotile nanotubes fibers.....	81

CHAPTER V: RESULTS AND DISCUSSION.....83

5.1 Characterization of chrysotile nanotubes.....83

5.2 Characterization of nanoparticles.....86

5.2.1 Characterization of 1-butanethiol capped silver nanoparticles.....86

5.2.2 Characterization of 4-methylbenzenethiol capped silver nanoparticles.....88

5.2.3 Characterization of silver nanoparticles.....90

5.2.4 Characterization of 1-butanethiol capped copper nanoparticles.....90

5.2.5 Characterization of 4-methylbenzenethiol capped copper nanoparticles.....92

5.2.6	Characterization of copper nanoparticles.....	94
5.2.7	Characterization of 4-methylbenzenethiol capped gold nanoparticles.....	95
5.2.8	Characterization of 4-methylbenzenethiol capped gold-silver 1:4 nanoparticles.....	97
5.2.9	Characterization of 4-methylbenzenethiol capped gold-silver 4:1 nanoparticles....	99
5.2.10	Characterization of 1-butanethiol capped silver-copper 1:1 nanoparticles.....	101
5.2.11	Characterization of silver-copper 1:1 nanoparticles.....	103
5.2.12	Characterization of anatase nanoparticles.....	104
5.2.13	Characterization of copper (I) chloride nanoparticles.....	105
5.2.14	Characterization of multiwalled carbon nanotubes.....	106
5.2.15	Characterization of graphene oxide.....	108
5.2.16	Conclusion.....	111
5.3	Characterization of inorganic nanostructured composites.....	112
5.3.1	Characterization of chrysotile nanotubes and 1-butanethiol capped copper nanoparticles system.....	112
5.3.2	Characterization of chrysotile nanotubes and 4-methylbenzenethiol capped copper nanoparticles system.....	113
5.3.3	Characterization of chrysotile nanotubes and 4-methylbenzenethiol capped gold nanoparticles system.....	114
5.3.4	Characterization of chrysotile nanotubes and 4-methylbenzenethiol capped gold-silver 1:4 nanoparticles system.....	116
5.3.5	Characterization of chrysotile nanotubes and 4-methylbenzenethiol capped gold-silver 4:1 nanoparticles system.....	118
5.3.6	Characterization of chrysotile nanotubes and 1-butanethiol capped silver nanoparticles system.....	120
5.3.7	Characterization of chrysotile nanotubes and 4-methylbenzenethiol capped silver nanoparticles system.....	121
5.3.8	Conclusion.....	122
5.4	Characterization of electrospun conductive polymer fibers.....	123
5.4.1	Characterization of electrospun polyaniline (PANI) fibers.....	123

5.4.1.1	Characterization of electrospun polyaniline (PANI) mat.....	123
5.4.1.2	Characterization of electrospun polyaniline (PANI) yarn.....	127
5.4.2	Characterization of electrospun poly(3-hexylthiophene) (P3HT) fibers.....	129
5.4.3	Conclusion.....	132
5.5	Characterization of electrospun conductive polymer fibers.....	134
5.5.1	Characterization of electrospun polyaniline (PANI) and 4-methylbenzenethiol capped silver nanoparticles fibers.....	134
5.5.2	Characterization of electrospun polyaniline (PANI) and 1-butanethiol capped copper nanoparticles fibers.....	136
5.5.3	Characterization of electrospun polyaniline (PANI) and copper nanoparticles fiber.....	138
5.5.4	Characterization of electrospun polyaniline (PANI) and 4-methylbenzenethiol capped gold nanoparticles fibers.....	139
5.5.5	Characterization of electrospun polyaniline (PANI) and 4-methylbenzenethiol capped gold-silver 1:4 nanoparticles fibers.....	141
5.5.6	Characterization of electrospun polyaniline (PANI) and 4-methylbenzenethiol capped gold-silver 4:1 nanoparticles fibers.....	143
5.5.7	Characterization of electrospun polyaniline (PANI) and 1-butanethiol capped silver-copper 1:1 nanoparticles fibers.....	145
5.5.8	Characterization of electrospun polyaniline (PANI) and silver-copper 1:1 nanoparticles fibers.....	146
5.5.9	Characterization of electrospun polyaniline (PANI) and anatase nanoparticles fibers.....	147
5.5.10	Characterization of electrospun polyaniline (PANI) and copper (I) chloride nanoparticles fibers.....	147
5.5.11	Characterization of electrospun polyaniline (PANI) and chrysotile nanotubes 1- butanethiol capped copper nanoparticles system fibers.....	149
5.5.12	Characterization of electrospun polyaniline (PANI) and chrysotile nanotubes 4-methylbenzenethiol capped copper nanoparticles system fibers.....	150
5.5.13	Characterization of electrospun polyaniline (PANI) and chrysotile nanotubes 4-methylbenzenethiol capped gold nanoparticles system fibers.....	151

5.5.14	Characterization of electrospun polyaniline (PANI) and chrysotile nanotubes 4-methylbenzenethiol capped gold-silver 1:4 nanoparticles system fibers.....	152
5.5.15	Characterization of electrospun polyaniline (PANI) and chrysotile nanotubes 4-methylbenzenethiol capped gold:silver 4:1 nanoparticles system fibers.....	154
5.5.16	Characterization of electrospun polyaniline (PANI) and chrysotile nanotubes 1-butanethiol capped silver nanoparticles system fibers.....	156
5.5.17	Characterization of electrospun polyaniline (PANI) and chrysotile nanotubes 4-methylbenzenethiol capped silver nanoparticles system fibers.....	157
5.5.18	Characterization of electrospun polyaniline (PANI) and multiwalled carbon nanotubes fibers.....	158
5.5.19	Characterization of electrospun polyaniline (PANI) and chrysotile nanotubes fibers.....	161
5.5.20	Characterization of electrospun of poly(3-hexylthiophene) (P3HT) and graphene oxide.....	164
5.5.21	Characterization of electrospun of poly(3-hexylthiophene) (P3HT) and multiwalled carbon nanotubes fibers.....	169
5.5.22	Characterization of electrospun of poly(3-hexylthiophene) (P3HT) and chrysotile nanotubes fibers.....	173
5.5.23	Conclusion.....	178

CHAPTER VI: COMPREHENSIVE CONCLUSION AND FUTURE PROSPECTS..... 185

LIST OF FIGURES

Page

Figure 1.1: a prospective view of OT layers in the chrysotile structure.....	1
Figure 1.2: TEM micrograph of natural chrysotile crystals.....	2
Figure 1.3: TEM micrograph of stoichiometric synthetic chrysotile nanocrystals.....	3
Figure 1.4: effect of chrysotile fibers on lactate dehydrogenase (LDH).....	4
Figure 1.5: structure of a capped metal nanoparticle.....	5
Figure 1.6: thiol capped metal nanoparticles prepared by Brust synthesis.....	8
Figure 1.7: molecular structure of a graphene oxide monolayer.....	10
Figure 1.8: schematic classification of nanostructured material.....	14
Figure 1.9: dimensional classification for the nanostructured materials.....	17
Figure 1.10: conductivity of polymers.....	19
Figure 1.11: structure of the main ICPs.....	20
Figure 1.12: scheme showing the formation of a polaron.....	22
Figure 1.13: scheme showing the formation of two polarons(A)and the formation of a bipolaron(B).....	22
Figure 1.14: polyaniline and its three oxidation states.....	23
Figure 1.15: structure of camphorsulfonic acid (HCSA).....	24
Figure 1.16: structure of the doping process for the emeraldine base with an acid.....	25
Figure 1.17: poly(3-hexylthiophene) (P3HT).....	25
Figure 1.18: main application fields for conductive polymers.....	27
Figure 1.19: HRTEM image of multiwalled carbon nanotubes-polyaniline composite.....	30
Figure 1.20: schematic drawing of the structure in nanoparticles filled polymer composites.....	31

Figure 1.21: comparison between a hair and electrospun polymeric fibers.....	38
Figure 1.22: detailed scheme of Taylor’s cone.....	39
Figure 1.23: whipping movement of a polymeric fiber.....	39
Figure 1.24: electrospinning process scheme.....	39
Figure 1.25: SEM image of a texture of polymeric fibers.....	40
Figure 1.26: structural imperfections as beads in an electrospun polymer.....	41
Figure 1.27: SEM images of an electrospun polymer with a distance needle-collector of 12 cm and of 24 cm, with consequent disappearing of the blobs.....	42
Figure 1.28: application of electrospun polymeric fibers.....	43
Figure 3.1: Parr reactor.....	46
Figure 3.2: electrospinning apparatus.....	47
Figure 3.3: schematic model of a SEM.....	48
Figure 3.4: SEM Zeiss EVO 10 MA.....	49
Figure 3.5: schematic model of the interaction between the electron beam and the sample.....	50
Figure 3.6: model of the different areas of electron-specimen interaction.....	50
Figure 3.7: EDS spectrum.....	51
Figure 3.8: EDS Oxford Inca x-act Energy 250.....	51
Figure 3.9: schematic model of a TEM.....	52
Figure 3.10: Philips CM100 Transmission Electron Microscope.....	53
Figure 3.11: schematic model of an atomic force microscope’s components.....	54
Figure 3.12: schematic model for piezoelectric electrodes for X, Y, and Z.....	54
Figure 3.13: schematic model of data acquisition component: laser, cantilever, photodiode and the sample located on the piezoelectric scanner.....	55

Figure 3.14: SEM image of AFM cantilever.....	55
Figure 3.15: Nicolet 380 FT-IR spectrometer.....	56
Figure 3.16: Nicolet 380 ATR-FT-IR.....	57
Figure 3.17: schematic diagram for X-ray diffraction between adjacent planes.....	58
Figure 3.18: Philips 1050/81-PW1710 Powder Diffractometer.....	58
Figure 3.19: picture of a TA SDT Q600 instrument.....	59
Figure 3.20: model for the thermocouples to be located inside the furnace of a heat-flux DSC.....	60
Figure 3.21: DSC curve for polymer.....	61
Figure 3.22: DSC TA Instruments 2920.....	61
Figure 3.23: Varian Cary 300 Bio UV-Vis Bio Spectrophotometer.....	62
Figure 3.24: block diagram of a UV-Vis spectrophotometer.....	62
Figure 3.25: model for a four-point probe method of conductivity measurement.....	63
Figure 5.1: diffraction pattern of a synthetic chrysotile sample.....	83
Figure 5.2: ATR-FT-IR spectrum of a synthetic chrysotile sample.....	84
Figure 5.3: TEM image of synthetic chrysotile nanotubes.....	84
Figure 5.4: TEM image of a chrysotile nanotube.....	85
Figure 5.5: (A) AFM image of two synthetic chrysotile nanotubes (B) phase variation in two synthetic chrysotile nanotubes obtained by AFM.....	85
Figure 5.6: TGA (blue line) and DTA (green line) curves of a sample of synthetic chrysotile nanotubes.....	86
Figure 5.7: ATR-FT-IR spectrum of a sample of 1-butanethiol capped silver nanoparticles.....	87
Figure 5.8: UV-Vis spectrum of a 1-butanethiol capped silver nanoparticles.....	87
Figure 5.9: TEM image of 1-butanethiol capped silver nanoparticles.....	88

Figure 5.10: FT-IR spectrum of 4-methylbenzenethiol capped silver nanoparticles.....	88
Figure 5.11: UV-Vis spectrum of 4-methylbenzenethiol capped silver nanoparticles.....	89
Figure 5.12: TEM image of 4-methylbenzenethiol capped silver nanoparticles.....	89
Figure 5.13: TGA curve of 4-methylbenzenethiol capped silver nanoparticles.....	90
Figure 5.14: ATR-FT-IR spectrum of 1-butanethiol capped copper nanoparticles.....	91
Figure 5.15: UV-Vis spectrum of 1-butanethiol capped copper nanoparticles.....	91
Figure 5.16: TEM image of 1-butanethiol capped copper nanoparticles.....	92
Figure 5.17: FT-IR spectrum of a sample of 4-methylbenzenethiol capped copper nanoparticles...	93
Figure 5.18: UV-Vis spectrum of a sample of 4-methylbenzenethiol capped copper nanoparticles.	93
Figure 5.19: TEM image of 4-methylbenzenethiol capped copper nanoparticles.....	94
Figure 5.20: TGA of 4-methylbenzenethiol capped copper nanoparticles.....	95
Figure 5.21: ATR-FT-IR spectrum of 4-methylbenzenethiol capped gold nanoparticles.....	95
Figure 5.22: UV-Vis spectrum of 4-methylbenzenethiol capped gold nanoparticles.....	96
Figure 5.23: TEM image of 4-methylbenzenethiol capped gold nanoparticles.....	96
Figure 5.24: FT-IR spectrum of 4-methylbenzenethiol capped gold-silver 1:4 nanoparticles.....	97
Figure 5.25: UV-Vis spectrum of 4-methylbenzenethiol capped gold-silver 1:4 nanoparticles.....	98
Figure 5.26: TEM image of 4-methylbenzenethiol capped gold-silver 1:4 nanoparticles.....	98
Figure 5.27: TGA curve of 4-methylbenzenethiol capped gold-silver 1:4 nanoparticles.....	99
Figure 5.28:ATR-FT-IR spectrum of 4-methylbenzenethiol capped gold-silver 4:1 nanoparticles..	99
Figure 5.29: UV-Vis spectrum of 4-methylbenzenethiol capped gold-silver 4:1 nanoparticles.....	100
Figure 5.30: TEM image of 4-methylbenzenethiol capped gold-silver 4:1 nanoparticles.....	100
Figure 5.31: TGA curve of 4-methylbenzenethiol capped gold-silver 4:1 nanoparticles.....	101
Figure 5.32: ATR-FT-IR spectrum of 1-butanethiol capped silver-copper 1:1 nanoparticles.....	101

Figure 5.33: UV-Vis spectrum of 1-butanethiol capped silver-copper 1:1 nanoparticles.....	102
Figure 5.34: TEM micrograph of 1-butanethiol capped silver-copper 1:1 nanoparticles.....	102
Figure 5.35: TGA thermogram of 1-butanethiol capped silver-copper 1:1 nanoparticles.....	103
Figure 5.36: XRPD diffractogram of anatase nanoparticles.....	104
Figure 5.37: TEM image of anatase nanoparticles.....	104
Figure 5.38: XRPD diffractogram of a copper (I) chloride sample.....	105
Figure 5.39: TEM image of copper (I) chloride nanoparticles.....	105
Figure 5.40: ATR-FT-IR spectra of multiwalled carbon nanotubes.....	106
Figure 5.41: XRPD diffractogram of multiwalled carbon nanotubes.....	106
Figure 5.42: TEM micrograph of multiwalled carbon nanotubes.....	107
Figure 5.43: TGA thermogram of multiwalled carbon nanotubes.....	107
Figure 5.44: ATR-FT-IR spectra of graphene oxide.....	108
Figure 5.45: XRPD diffractogram pattern of graphene oxide.....	108
Figure 5.46: UV-Vis spectra of graphene oxide.....	109
Figure 5.47: TEM micrograph of graphene oxide.....	110
Figure 5.48: TGA curve of graphene oxide.....	110
Figure 5.49: TEM image of chrysotile nanotubes and 1-butanethiol capped copper nanoparticles system.....	112
Figure 5.50: TEM image of chrysotile nanotubes and 4-methylbenzenethiol capped copper nanoparticles system.....	113
Figure 5.51: FT-IR spectrum of chrysotile nanotubes and 4-methylbenzenethiol capped gold nanoparticles system.....	114

Figure 5.52: UV-Vis spectrum of a sample of chrysotile nanotubes and 4-methylbenzenethiol capped gold nanoparticles system.....	114
Figure 5.53: TEM image of chrysotile nanotubes and 4-methylbenzenethiol capped gold nanoparticles system.....	115
Figure 5.54: FT-IR spectrum of chrysotile nanotubes and 4-methylbenzenethiol capped gold-silver 1:4 nanoparticles system.....	116
Figure 5.55: UV-Vis spectrum of a sample of chrysotile nanotubes and 4-methylbenzenethiol capped gold-silver 1:4 nanoparticles system.....	116
Figure 5.56: TEM image of chrysotile nanotubes and 4-methylbenzenethiol capped gold-silver 1:4nanoparticles system.....	117
Figure 5.57: FT-IR spectrum of chrysotile nanotubes and 4-methylbenzenethiol capped gold-silver 4:1 nanoparticles system.....	118
Figure 5.58: UV-Vis spectrum of a sample of chrysotile nanotubes and 4-methylbenzenethiol capped gold-silver 4:1 nanoparticles system.....	119
Figure 5.59: TEM image of chrysotile nanotubes and 1-butanethiol capped silver nanoparticles system.....	120
Figure 5.60: FT-IR spectrum of chrysotile nanotubes and 4-methylbenzenethiol capped silver nanoparticles system.....	121
Figure 5.61: TEM image of chrysotile nanotubes and 4-methylbenzenethiol capped silver nanoparticles system.....	121
Figure 5.62: XRD diffractogram of polyaniline (PANI).....	123
Figure 5.63: XRD diffractogram of poly(ethylene oxide) (PEO).....	124
Figure 5.64: XRD diffractogram of camphorsulfonic acid (HCSA).....	124
Figure 5.65: XRD diffractogram of not electrospun polymeric blend.....	124
Figure 5.66: image of electrospun (PANI-HCSA-PEO) mat.....	125
Figure 5.67: SEM image of electrospun (PANI-HCSA-PEO) fibers.....	125

Figure 5.68: XRD diffractogram of electrospun (PANI-HCSA-PEO) fibers.....	126
Figure 5.69: DSC curve of electrospun (PANI-HCSA-PEO) fibers.....	127
Figure 5.70: SEM micrograph of electrospun polyaniline (PANI) yarn.....	127
Figure 5.71: SEM micrograph of electrospun polyaniline (PANI) yarn.....	128
Figure 5.72: SEM micrograph of electrospun polyaniline (PANI) yarn.....	128
Figure 5.73: XRD diffractogram of poly(3-hexylthiophene) (P3HT).....	129
Figure 5.74: XRD diffractogram of poly(ethylene oxide) PEO.....	129
Figure 5.75: image of electrospun (P3HT-PEO) mat.....	130
Figure 5.76: SEM image of electrospun (P3HT-PEO) fibers.....	130
Figure 5.77: SEM image of electrospun (P3HT -PEO) fiber.....	131
Figure 5.78: XRD diffractogram of electrospun (P3HT-PEO) fibers.....	131
Figure 5.79: DSC curve of electrospun (P3HT-PEO) fibers.....	132
Figure 5.80: TEM micrograph electrospun polyaniline (PANI) and 4-methylbenzenethiol capped silver nanoparticles fibers.....	134
Figure 5.81: SEM micrograph of electrospun polyaniline (PANI) and 4-methylbenzenethiol capped silver nanoparticles fibers.....	135
Figure 5.82: XRD diffractogram of electrospun polyaniline (PANI) and 4-methylbenzenethiol capped silver nanoparticles fibers.....	135
Figure 5.83: TEM micrograph electrospun polyaniline (PANI) and 1-butanethiol capped copper nanoparticles fibers.....	136
Figure 5.84: SEM micrograph of electrospun polyaniline (PANI) and 1-butanethiol capped copper nanoparticles fibers.....	137
Figure 5.85: TEM micrograph of electrospun polyaniline (PANI) and copper nanoparticles fibers.....	138
Figure 5.86: TEM micrograph of electrospun polyaniline (PANI) and 4-methylbenzenethiol capped gold nanoparticles fibers.....	139

Figure 5.87: SEM micrograph of electrospun polyaniline (PANI) and 4-methylbenzenethiol capped gold nanoparticles fibers.....	140
Figure 5.88: XRD diffractogram of electrospun polyaniline (PANI) and 4-methylbenzenethiol capped gold nanoparticles fibers.....	140
Figure 5.89: TEM micrograph of electrospun polyaniline (PANI) and 4-methylbenzenethiol capped gold-silver 1:4 nanoparticles fibers.....	141
Figure 5.90: SEM micrograph of electrospun polyaniline (PANI) and 4-methylbenzenethiol capped gold-silver 1:4 nanoparticles fibers.....	142
Figure 5.91: XRD diffractogram of electrospun polyaniline (PANI) and 4-methylbenzenethiol capped gold-silver 1:4 nanoparticles fibers.....	142
Figure 5.92: TEM micrograph of electrospun polyaniline (PANI) and 4-methylbenzenethiol capped gold-silver 4:1 nanoparticles fibers.....	143
Figure 5.93: SEM micrograph of electrospun polyaniline (PANI) and 4-methylbenzenethiol capped gold-silver 4:1 nanoparticles fibers.....	143
Figure 5.94: XRD diffractogram of electrospun polyaniline (PANI) and 4-methylbenzenethiol capped gold-silver 4:1 nanoparticles fibers.....	144
Figure 5.95: TEM micrograph electrospun polyaniline (PANI) and 1-butanethiol capped silver-copper 1:1 nanoparticles fibers.....	145
Figure 5.96: SEM micrograph of electrospun polyaniline (PANI) and 1-butanethiol capped silver-copper 1:1 nanoparticles fibers.....	145
Figure 5.97: TEM micrograph of electrospun polyaniline (PANI) silver-copper 1:1 nanoparticles fibers.....	146
Figure 5.98: TEM micrograph of electrospun polyaniline (PANI) anatase nanoparticles fibers.....	147
Figure 5.99: TEM micrograph of electrospun polyaniline (PANI) copper (I) chloride nanoparticles fibers.....	148

Figure 5.100: SEM micrograph of electrospun polyaniline (PANI) and chrysotile nanotubes 1-butanethiol capped copper nanoparticles system fibers.....	149
Figure 5.101: SEM micrograph of electrospun polyaniline (PANI) and chrysotile nanotubes 4-methylbenzenethiol capped copper nanoparticles system fibers.....	150
Figure 5.102: SEM micrograph of electrospun polyaniline (PANI) and chrysotile nanotubes 4-methylbenzenethiol capped gold nanoparticles system fibers.....	151
Figure 5.103: XRD diffractogram of electrospun polyaniline (PANI) and chrysotile nanotubes 4-methylbenzenethiol capped gold nanoparticles system fibers.....	152
Figure 5.104: SEM micrograph of electrospun polyaniline (PANI) and chrysotile nanotubes 4-methylbenzenethiol capped gold-silver 1:4 nanoparticles system fibers.....	153
Figure 5.105: XRD diffractogram of electrospun polyaniline (PANI) and chrysotile nanotubes 4-methylbenzenethiol capped gold-silver 1:4 nanoparticles system fibers.....	153
Figure 5.106: SEM micrograph of electrospun polyaniline (PANI) and chrysotile nanotubes 4-methylbenzenethiol capped gold-silver 4:1 nanoparticles system fibers.....	154
Figure 5.107: XRD diffractogram of electrospun polyaniline (PANI) and chrysotile nanotubes 4-methylbenzenethiol capped gold-silver 4:1 nanoparticles system fibers.....	155
Figure 5.108: SEM micrograph of electrospun polyaniline (PANI) and chrysotile nanotubes 1-butanethiol capped silver nanoparticles system fibers.....	156
Figure 5.109: SEM micrograph of electrospun polyaniline (PANI) and chrysotile nanotubes 4-methylbenzenethiol capped silver nanoparticles system fibers.....	157
Figure 5.110: XRD diffractogram of electrospun polyaniline (PANI) and chrysotile nanotubes 4-methylbenzenethiol capped silver nanoparticles system fibers.....	158
Figure 5.111: TEM image of electrospun polyaniline (PANI) and multiwalled carbon nanotubes fibers.....	159
Figure 5.112: SEM image of electrospun polyaniline (PANI) and multiwalled carbon nanotubes fibers.....	159

Figure 5.113: XRD diffractogram of electrospun polyaniline (PANI) and multiwalled carbon nanotubes fibers.....	160
Figure 5.114: DSC curve of electrospun polyaniline (PANI) and multiwalled carbon nanotubes fibers.....	161
Figure 5.115: TEM image of electrospun polyaniline (PANI) and chrysotile nanotubes fibers.....	162
Figure 5.116: TEM image of electrospun polyaniline (PANI) and chrysotile nanotubes fibers.....	162
Figure 5.117: SEM image of electrospun polyaniline (PANI) and chrysotile nanotubes fibers.....	163
Figure 5.118: XRD diffractogram of electrospun polyaniline (PANI) and chrysotile nanotubes fibers.....	163
Figure 5.119: DSC curve of electrospun polyaniline (PANI) and chrysotile nanotubes fibers.....	164
Figure 5.120: TEM image of electrospun poly(3-hexylthiophene) and graphene oxide fibers.....	165
Figure 5.121: TEM image of electrospun poly(3-hexylthiophene) and graphene oxide fibers.....	165
Figure 5.122: SEM image of electrospun poly(3-hexylthiophene) and graphene oxide fibers.....	166
Figure 5.123: SEM image of electrospun poly(3-hexylthiophene) and graphene oxide fibers.....	166
Figure 5.124: reconstruction of the presence of sulfur using mapping mode EDS analysis of electrospun of poly(3-hexylthiophene) and graphene oxide fibers.....	167
Figure 5.125: reconstruction of the presence of carbon using mapping mode EDS analysis of electrospun of poly(3-hexylthiophene) and graphene oxide fibers.....	167
Figure 5.126: XRD diffractogram of electrospun of poly(3-hexylthiophene) and graphene oxide fibers.....	168
Figure 5.127: DSC curve of electrospun of poly(3-hexylthiophene) and graphene oxide fibers.....	168
Figure 5.128: TEM image of electrospun poly(3-hexylthiophene) and multiwalled carbon nanotubes fibers.....	169
Figure 5.129: TEM image of electrospun poly(3-hexylthiophene) and multiwalled carbon nanotubes fibers.....	169
Figure 5.130: SEM image of electrospun poly(3-hexylthiophene) and multiwalled carbon nanotubes fibers.....	170

Figure 5.131: SEM image of electrospun poly(3-hexylthiophene) and multiwalled carbon nanotubes fibers.....	170
Figure 5.132: reconstruction of the presence of sulfur using mapping mode EDS analysis of electrospun of poly(3-hexylthiophene) and multiwalled carbon nanotubes fibers.....	171
Figure 5.133: reconstruction of the presence of carbon using mapping mode EDS analysis of electrospun of poly(3-hexylthiophene) and multiwalled carbon nanotubes fibers.....	171
Figure 5.134: XRD diffractogram of electrospun of poly(3-hexylthiophene) and multiwalled carbon nanotubes fibers.....	172
Figure 5.135: DSC curve of electrospun of poly(3-hexylthiophene) and multiwalled carbon nanotubes fibers.....	172
Figure 5.136: TEM image of electrospun poly(3-hexylthiophene) and chrysotile nanotubes fiber.....	173
Figure 5.137: TEM image of electrospun poly(3-hexylthiophene) and chrysotile nanotubes fibers.....	174
Figure 5.138: SEM image of electrospun poly(3-hexylthiophene) and chrysotile nanotubes fibers.....	174
Figure 5.139: SEM image of electrospun of poly(3-hexylthiophene) and chrysotile nanotubes fibers.....	175
Figure 5.140: reconstruction of the presence of carbon using mapping mode EDS analysis of electrospun of poly(3-hexylthiophene) and chrysotile nanotubes fibers.....	175
Figure 5.141: reconstruction of the presence of silicon using mapping mode EDS analysis of electrospun of poly(3-hexylthiophene) and chrysotile nanotubes fibers.....	175
Figure 5.142: XRD diffractogram of electrospun of poly(3-hexylthiophene) and chrysotile nanotubes fibers.....	176
Figure 5.143: DSC curve of electrospun of poly(3-hexylthiophene) and chrysotile nanotubes fibers.....	176

Figure 5.144: chart of surface conductivity values for electrospun polyaniline CPCs and zero-dimensional (0D) nanostructured materials.....	179
Figure 5.145: chart with values for surface conductivity of electrospun polyaniline CPCs and one-dimensional (1D) nanostructured materials.....	180
Figure 5.146: chart with values for surface conductivity of electrospun polyaniline and chrysotile nanotubes thiol capped metal nanoparticles system mats.....	181
Figure 5.147: chart with values for surface conductivity of electrospun mats based on undoped poly(3-hexylthiophene).....	183
Figure 5.148: chart with values for surface conductivity of electrospun mats based on doped poly(3-hexylthiophene).....	183

CHAPTER I: INTRODUCTION

1.1 Chrysotile Nanotubes

Asbestos is a set of minerals made of amphiboles (inosilicates) like amosite, crocidolite and of serpentines (phyllosilicates) like chrysotile and lizardite. Chrysotile is the only mineral crystallizing with a nanotubular structure, which is a characteristic making it very investigated in the nanotechnological field. Chrysotile, $Mg_3Si_2O_5(OH)_4$, shows a peculiar structure made of layers presenting a pseudo-hexagonal network of tetrahedrons (T) centred on the silica and linked together by octahedral (O) sheets of magnesium hydroxides (Fig. 1.1)

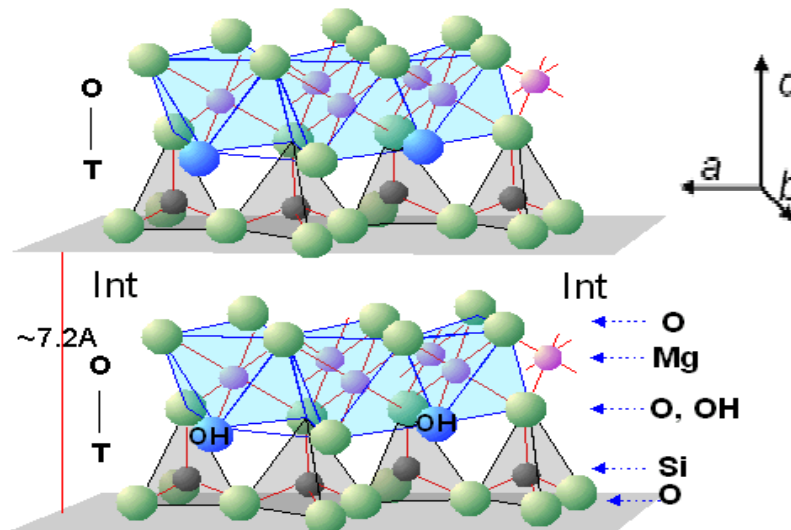


Figure 1.1: a prospective view of OT layers in the chrysotile structure

The OT layers may be concentric, rolled up along the x axis (clinochrysotile and orthochrysotile) or rolled up along the y axis (parachrysotile). The rolled layers consequently form a tubular structure, with an outside diameter of 22-27 nm and an inner central hollow with a diameter of about 7 nm. The tubular structure consequence of the rolled up layers is due to the dimensional phase-displacement which takes place along the *b* direction and caused by the lower dimension of the SiO_4 tetrahedron layers respect to the octahedral ones of $Mg(OH)_2$ [1].

You can hardly find just chrysotile in nature, since it usually forms together with its polymorphs like lizardite and antigorite [2]. Moreover, these fibers are commonly contaminated by metallic

traces, like iron, aluminum and nickel ones; replacing silica or magnesium, these metals may create several structural anomalies. These predispositions perfectly meet the presence of different crystalline morphologies in the natural chrysotile types: hollow cylinders, not-hollow cylinders, tube-in-tube fibers, fibers in cones, concentric spirals of cones-in-cones (CoCo), cylindrical (CyCy) and polygonal (PS) structures (Fig. 1.2).

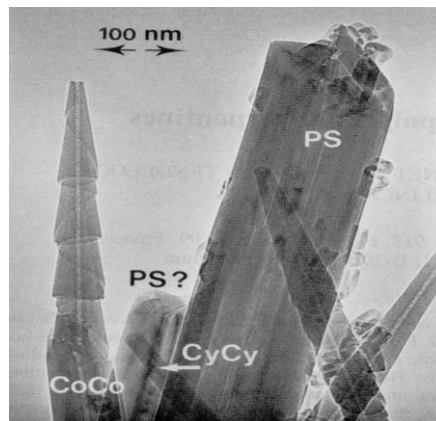


Figure 1.2: TEM micrograph of natural chrysotile crystals [3]

In nature chrysotile may be found as densely packed bundles of multiwalled hollow nanotubes. This is the right characteristic that makes it a very suitable mineral for the production of nanowires, by filling the central hollow tunnel with a proper material. Chrysotile nanotubes may act as host systems, where the separation between the large dimensioned channels is able to prevent the interaction between the molecules and the nano-materials hosted inside the nanotubes, therefore behaving as a barrier. Through high-pressure techniques [4] and metal-organic chemical vapor deposition (MOCVD) [5, 6], the chrysotile nanotubes have been filled with molten metals like Hg, Pb, Sn, with semi-metals, Bi, Te, Se and semiconductors like InSb, CdSe, GaAs, InP.

Besides, materials like CdSe and GaAs have been synthesized inside the channels of the mineral chrysotile nanotubes. The greatest problem concerning natural asbestos is its high toxicity. When present in the environment, its conformational peculiarity is exactly the reason for this unwelcome characteristic, that is the fibrous morphology and the metallic impurities. Some studies demonstrated the toxicity and carcinogenesis caused by the surface chemical characteristics of this material [7]. The outside area is in direct contact with the biological environment and at a high production of Reactive Oxygen Species (ROS) and other free radicals [8]. In the nanotechnological field, natural chrysotile is hardly used exactly for its high toxicity and its chemical and structural heterogeneities. Recently a hydro-thermal synthesis has been carried out in order to obtain new

pure inorganic chrysotile nanotubes to be used in developing nanotechnologies for highly potential applications. The problems explained above can therefore be by-passed through a synthesis controlling stoichiometry and morphology to obtain a geomimetic chrysotile. The first syntheses of this mineral took place in the 1920s and were based on hydrothermal reactions of H_2O , MgO and SiO_2 . In the 1950s and 1960s [9] these syntheses have been improved and today the most followed are those using SiO_2 , $\text{MgCl}_2 \cdot 6\text{H}_2\text{O}$, H_2O in a basic environment ($\text{pH} = 12.70$) at $300\text{ }^\circ\text{C}$ e 82 atm for 24 h.

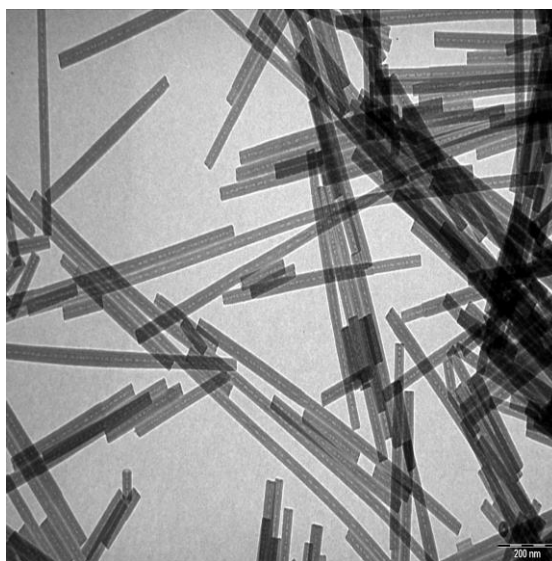


Figure 1.3: TEM micrograph of stoichiometric synthetic chrysotile nanocrystals

The synthesis described above allows to obtain nanotubes with variable length, with an outside diameter of about 21/22 nm and a central hollow with a diameter of 7 nm, without any structural deformations, polytypes or impurities (Fig. 1.3). Besides making it a very good material for nanotechnological aims, these characteristics makes it a non toxic material. In fact, studies carried out on the citotoxicity of synthetic [7] chrysotile allowed to understand that the absence of foreign ions (Fe, Ni Al, Ti, Co, Cr, Zn) is very important for the safe use of this mineral.

Therefore, the ability of the synthetic chrysotile to inhibit the action of the glucose-6-phosphate dehydrogenase enzyme in the pentose phosphate is far lower respect to the natural chrysotile. Synthetic stoichiometric chrysotile nanotubes have been suggested to be used as standard reference (control) for toxicological studies (Fig. 1.4).

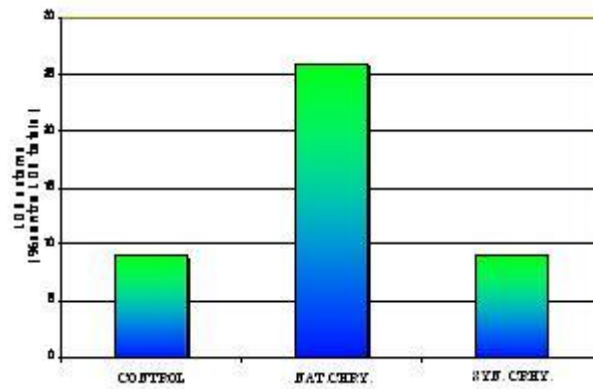


Figure 1.4: effect of chrysotile fibers on lactate dehydrogenase (LDH)

References

- [1] B.A. Cressey, E.J.W. Whittaker, and J.W. Eric, *Mineral. Mag.*, 57, 1993, 729.
- [2] D.R. Veblen, and P.R. Buseck, *Science*, 206 1979, 1398.
- [3] K. Yada, *Am. Mineral.*, 62, 1977, 958.
- [4] V.N. Bogomolov, *Usp. Fiz. Nauk.*, 124, 1978.
- [5] H.M. Yates, W.R. Flavell, M.E. Pemble, N.P. Johnson, S.G. Romanov, and C.M. Sotomayor-Torres, *J. Cryst. Growth*, 170, 1997, 62.
- [6] S.G. Romanov and C.M. Sotomayor Torres: *Nanoscale Science and Technology*, edited by N. Garia, M. Nieto-Vesperinas, and H. Rohrer (Kluwer Academic Publisher, Dordrecht, The Netherlands, 1997, 225.
- [7] E. Gazzano, E. Foresti, I. G. Lesci, M. Tomatis, C. Riganti, B. Fubini, N. Roveri, D. Ghigo, *Toxicology and Applied Pharmacology* 206, 2005, 356-364.
- [8] C. Riganti, E. Aldieri, L. Bergandi, I. Fenoglio, C. Costamagna, B. Fubini, A. Bosia, and D. Ghigo, *Free Radical Biol. Med.*, 32, 2002, 938.
- [9] D.M. Roy, and R. Roy, *Am. Mineral*, 39, 1954, 957.

1.2 Metal Nanoparticles

Metal nanoparticles are a whole of nanocrystals and colloids with a diameter ranging from 1 to 100 nm, made of materials like metals, semi-conductors and metallic oxides. They represent one of the most studied items in the recent years, thanks to their peculiar optical, electronic and catalytic properties. Metal nanoparticles arise great interest thanks to their simple methods for syntheses, their stability and the interesting properties observed. The basic characteristic of nanoparticles is the high ratio between the surface atoms composing the bulk. This allows nanoparticles to perform completely new chemical-physical, electronic and optical properties respect to the same macroscopic materials. The first problem met in the synthesis of metallic nanoparticles is due to their property in forming aggregates quickly, thus producing structures which are no longer nanometric. Besides, these tend to oxidation and to stay insoluble in mostly all solvents. In order to avoid these inconveniences, since the 80's the ability of some organic compounds (thiols, amines, isocyanates) to bond at the surface of the nanoparticles [10] has been exploited, by surrounding the conductive nucleus with a protective shell with different characteristics and creating in this way a new nanostructured material with new properties (Fig. 1.5).

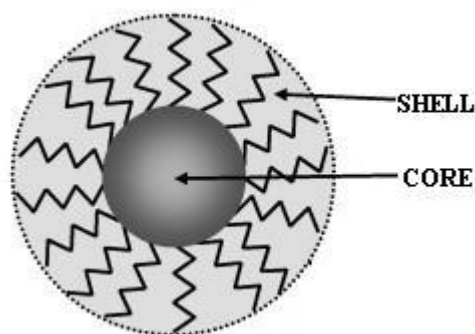


Figure 1.5: structure of a capped metal nanoparticle

The bottom-up approach utilizes the self-assembling and self-organizing properties of the molecular systems to produce nanoparticles surrounded by organic polymers to be used as building-blocks. These particles have half-way properties between bulk and single atoms. The insulating inorganic layer surrounding them acts as a tunnel barrier, while the inner conductive material is the potential hole where the charge carriers are trapped. This description leads us to include nanoparticles in the

quantum dot model. A quantum dot is a nanostructure formed by conductive or semi-conductive material, with a certain gap between the valence band and the conductive band, with the typical dimensions comparable to the De Broglie length wave. To be considered a quantum dot, this structure must be surrounded by another material with a bigger forbidden band gap (gap between the valence band and the conductive band). The resulting structure generates a well of potential able to trap the charge carriers into a small area. The new properties gained by the materials are clear on studying the structural, chemical, electronic and spectroscopic characteristics. A visible evidence is the presence of an absorption peak which is obtained by a spectroscopic analysis in UV-Vis, due to the surface plasmon resonance. The surface plasmon resonance (SPR) is an oscillation of the charge density which can occur at the interfacing of two means with different dielectric constants. An example is the use of a metal and a material with a very low electric conductivity and therefore used as an electric insulator. SPR is a phenomenon due to the motion resonance of the electrons after excitation, therefore strictly linked to the dimensions and shape of the nanoparticles. The main application of the quantum dots is to store energy and light source and they are therefore fundamental in the low cost production of innovative solar panels. Besides, the simple and cheap syntheses allow to use the nanoparticles as fillers in composite materials and in the catalysis field [11]. The research in chemistry aimed at the synthesis, characterization and application of metallic colloids in organic solvents [12, 13, 14, 15]. Organosol metals are interesting for the studies in the physical-chemical properties of metallic nanoparticles [16, 17] and their particular optics. The alternating use of organic and aqueous solvents is a promising solution against the formation of aggregates; in fact in these means the materials interact less thanks to the presence of hydrophobic ligands able to stabilize the systems. At first the organosols caught the attention of researches [18, 19, 20] for their applications as catalysts [21]. They can also be used to form self-assembling [22] monolayers and to build hybrid materials. These metallic particles clearly perform peculiar chemical-physical properties such as the surface plasmon resonance (SPR). The physical origin of this light absorption from metallic nanoparticles is the coherent oscillation of the electrons in the conductive band induced by the interaction with an electromagnetic field [23]. The SPR is actually due to the structural dimension; in fact it is not detectable in a single atom or in bulk material [24]. It is known that the metallic resonance frequency in nanoparticles depends on the dimensions, shape, material properties and environment [25, 26, 27]. Therefore the optical absorption spectrum can supply information on the electronic structure of small metallic particles. The synthesis of nanostructured materials with an active surface area motivated researches to synthesize metallic nanoparticles in organic solvents. Several methods to synthesize metallic

nanoparticles have been developed and classified in two ways: "top-down" [28] and "bottom-up" [29] processes. As for the synthesis methods, the researchers' activity focused on the study of special capping agents to stabilize the nanoparticles. The capping molecules generally contain functionalized groups like amines, alcohol, thiol and phosphines. Capping agents like amines and alcohols interact weakly [30] with the metallic surface of the nanoparticles and preserve their electronic properties. Thiols instead interact strongly with the metallic surface and produce a significant charge distribution [31].

The turning point in the synthesis of metallic organosols took place in 1944, thanks to Brust et al., who developed a simple biphasic procedure to synthesize metallic nanoparticles in organic solvents. This method allowed the easy synthesis of stable Au nanoparticles, scarcely tending to aggregation and with controlled dimensions smaller than 5 nm (Fig. 1.6). Besides, these nanoparticles can be isolated and repeatedly dispersed in the common organic solvents without performing irreversible decomposition and aggregation.

The synthesis technique developed by Brust is based on the transfer of a phase in a salt solution of the selected metal (for example HAuCl_4) followed by its reduction at the presence of thiols with long chains. The strong affinity of thiols with the metal eases the stability of the nanoparticles in an organic solvent. The particles are synthesized in a biphasic system to allow the development of the nucleating reaction and consequently the growth of the two solvents at the interfacing step. The choice of the reduction solvent depends both on the metal and the solvents used in the reaction [32]. During the first synthesis described by Brust AuCl_4^- was transferred from the aqueous solution to toluene by bromide tetraoctylammonium and reduced by NaBH_4 at the presence of dodecanthiol ($\text{C}_{12}\text{H}_{25}\text{SH}$). An instantaneous color change in the organic phase is visible immediately when adding the reducing agent. The interesting part of this protocol is that these metallic nanoparticles can be treated and characterized as a simple chemical compound. The dry product is soluble in non polar solvents as toluene, pentane and chloroform. Besides, the dimensions of the articles can be controlled by changing the thiol/metal ratio. High thiol/metal molar ratios produce smaller particles, same as the quick adding of the reducing agent and the reaction temperature control.

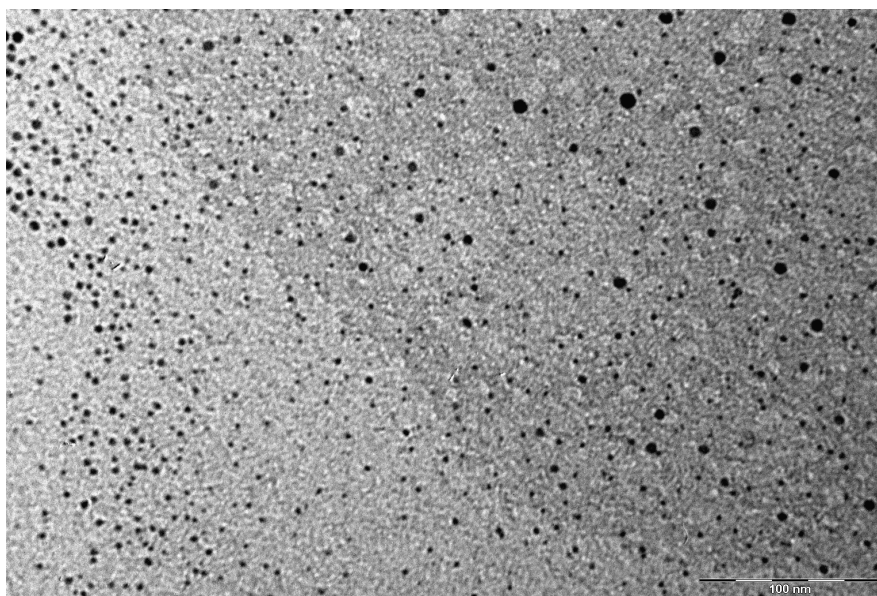


Figure 1.6: thiol capped metal nanoparticles prepared by Brust synthesis

As for the possible applications, there is a great interest in the behavior of the gold nanoparticles with surface modified with fluorophores for the development of biologic traces and optoelectronic devices [33]. The interest for these possibilities increased the spectroscopic investigations of these materials during the last years.

References

- [10] Young-Seok Shon, *Metal Nanoparticles Protected with Monolayer: Synthetic Methods*, Marcel Dekker, Inc.
- [11] Guohui Tian, Honggang Fu, Liqiang Jing, Chungui Tian, *Journal of Hazardous Materials*, 161, 2009, 1122-1130.
- [12] Y. Katayama, M. Sasaki, E. Ando *Journal of Non-Crystalline Solids*, 178, 1994, 227-232
- [13] M.Y. Han, C.H. Quek, *Langmuir* 20, 2004, 3431.
- [14] *Solid State Communications*, 128, 2003, 329-333.
- [15] M. Brust, J.M. Walker, D. Bethell, D.J. Schiffrin, R. Whyman, *Chem. Commun.* 1994, 801.
- [16] Chenjuan He, Bingsuo Zou, Zhenyu Wu, Yuxin Nie, *Optics Communications*, 281, 2008, 851-854.
- [17] K.S. Mayya, F. Caruso, *Langmuir*, 19, 2003, 6987.
- [18] H. Bonnemann, G. Braun, W. Brijoux, R. Brinkmann, A.S. Tilling, K. Seevogel, K.J. Siepen, *Organomet. Chem.*, 520, 1996, 143.
- [19] H. Bonnemann, G. Braun, W. Brijoux, R. Brinkmann, A.Schulze Tilling, K. Seevogel, K. Siepen, *Journal of Organometallic Chemistry*, 520, 1996, 143-162.
- [20] John S. Bradley, Ernestine Hill, Michael E. Leonowicz, Horst Witzke, *Journal of Molecular Catalysis*, 41, 1987, 59-74.
- [21] Y. Li, G. Luo, Y. Fan, Y. Chen, *Mater. Res. Bull.*, 39, 2004, 195.

- [22] Laongnuan Srisombat, Andrew C. Jamison, T. Randall Lee, *Colloids and Surfaces A: Physicochemical and Engineering Aspects*, 390, 2011, 1-19.
- [23] M.H. Tu, T. Sun, K.T.V. Grattan, *Sensors and Actuators B: Chemical*, 164, 2012, 43-53.
- [24] S. Link, M.A. El-Sayed, *J. Phys. Chem. B*, 103, 1999, 8410.
- [25] Masaru Mitsushio, Kensaku Watanabe, Yasuyuki Abe, Morihide Higo, *Sensors and Actuators A: Physical*, 163, 1, 2010, 1-8.
- [26] A. Henglein, Ber. Bunsen-Ges., *Phys. Chem.*, 99, 1995, 903.
- [27] S. Link, M.A. El-Sayed, *Int. Rev. Phys. Chem.*, 19, 2000, 409.
- [28] K. Yamazaki, H. Namatsu, *Microelectron. Eng.*, 85, 2004, 73.
- [29] C.H. Walker, J.V. St. John, P. Wisian-Neilson, *J. Am. Chem. Soc.*, 123, 2001, 3846.
- [30] E. Filippo, A. Serra, D. Manno, *Sensors and Actuators B: Chemical*, 138, 2009, 625-630
- [31] P. Zhang, T.K. Sham, *Phys. Rev. Lett.*, 90, 2003, 245502.
- [32] V.J. Cunnane, D.J. Schiffrin, C. Beltran, G. Geblewicz, T. Solomon, *J. Electroanal. Chem.*, 247, 1988, 103.
- [33] J.J. Hickman, D. Ofer, P.E. Laibnis, G.M. Whitesides, M.S. Wrighton, *Science*, 252, 1991, 688.

1.3 Graphene Oxide

Graphene is an atomic very thin and hybrid sp^2 carbon monolayer where the atoms are arranged in a honey comb pattern. The first studies concerning carbon graphene monolayers date back to 1960 [34, 35]. The studies have been occasional and aimless until 2004, when graphene was isolated for the first time simply following the Scotch Method [36, 37]. The subsequent findings about its unusual property [38, 39] arose a great interest among researchers in almost all scientific fields [40, 41]. Its characterization led to the discovery of its extraordinary mechanical [42], thermal [43], chemical [44, 45] and optical properties [46]. A branch of the research on graphene concerns chemically derived graphene (CDG) [47, 48]. CDG are a 2D shaped carbon with new additional chemical functionalities allowing very new performances thus maintaining some of the peculiar properties of the original material. An important feature of CDG is the ease in their synthesis, develop and application. There are simple methods to produce CDG efficiently, passing by the chemical synthesis of graphene oxide followed by its exfoliation into single graphene oxide (GO) sheets and their final reduction when required [47, 48]. CDG is a generic name for graphene oxide and other kinds deriving from fluorinated [49] or brominated [50] graphite can also be included in this class. The functional groups in graphene oxide perform a very good mechanical resistance [51, 52]. The hydroxyl group, epoxide and acidic groups are the most numerous groups functionalizing in the graphene oxide, as shown in Fig. 1.7.

The presence of functional groups entails a change in the electronic structure of graphene. Even if the relativistic charge-carrier transport and other effects of the condensed material observed for graphene are not present in GO, the availability, the ease of processing and the versatile properties make this material interesting in basic research and applications.

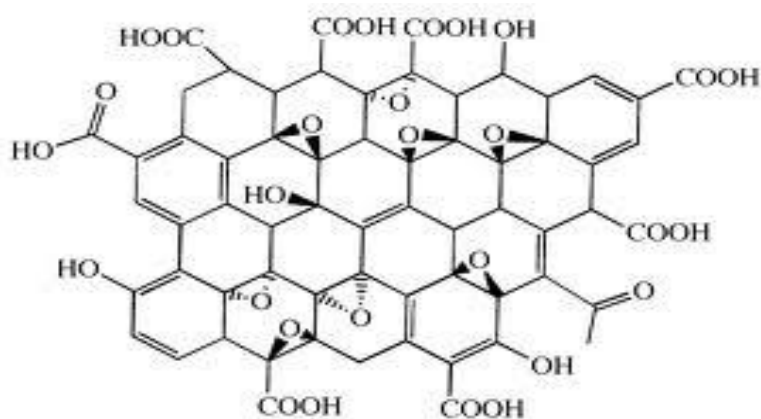


Figure 1.7: molecular structure of a graphene oxide monolayer

The production of GO is very attractive for many reasons: the large availability of the raw materials (graphite), the high productivity for exfoliation, the fact that the process is worked in liquid phase. All these features allow the easy deposition of a thin film and this chemical process simplifies the integration of GO in polymeric composites. Alternative production methods have recently been developed. The chemical approach aims at taking advantage of the new functionalities of GO, while not chemical approaches are based on the conservation of the properties of graphene. Thanks to the advantages offered by the easy production process and to the unique features, like mechanical and optical stability and optical properties, GO is attractive to obtain flexible and folding thin films useful in electronics and optoelectronics [53]. The unexpected optoelectronic properties of the thin GO films are promising to be used as conductors, chemical/biological sensors [54], thin-film transistors (TFTs), electrodes [53], ultracapacitors [55], field emitters [56], photovoltaics [57], photo-detectors [58], nano-electromechanical resonators [59], and nonvolatile memory devices [60]. In particular, recent studies underline how important the understanding of chemistry and of the atomic structure is to obtain the desired performances.

The graphene oxide has been used as filler in polymeric composites to produce materials for several applications [61]. Composites containing GO may be based on various polymers: Polystyrene (PS) [62], PMMA [63], polyvinyl alcohol (PVA) [64], polypropylene (PP) [65, 66], polyester [67], polyurethane [68, 69] and polycarbonate [70]. Heating [71] or ultrasound methods have been widely utilized to produce nanocomposites GO based, with the aim at making the resulting products electrically conductive [72]. Graphene oxide maintains its insulating chemical structure and must be reduced in a separate step to improve the conductivity [73]. Nanocomposites containing GO as filler showed considerable improvements in elasticity, tensile strength, electric conductivity and thermal stability. Besides, these improvements have often been observed also with low load of filler clearly due to the wide interfacial surface.

References

- [34] H. P. Boehm, A. Clauss, G. O. Fischer, U. Hofmann, *Z. Naturforsch. B: Anorg. Chem. Org. Chem. Biochem. Biophys. Bio.*, 17, 1962, 150.
- [35] J. W. May, *Surf. Sci.* 17, 1969, 267.
- [36] K. S. Novoselov, A. K. Geim, S. V. Morozov, D. Jiang, Y. Zhang, S. V. Dubonos, I. V. Grigorieva, A. A. Firsov, *Science*, 306, 2004, 666.

- [37] K. S. Novoselov, D. Jiang, F. Schedin, T. J. Booth, V. V. Khotkevich, S. V. Morozov, A. K. Geim, *Proc. Nat. Acad. Sci. U. S. A.*, 102, 2005, 10451.
- [38] K. S. Novoselov, A. K. Geim, S. V. Morozov, D. Jiang, M. I. Katsnelson, I. V. Grigorieva, S. V. Dubonos, A. A. Firsov, *Nature*, 438, 2005, 197.
- [39] Y. B. Zhang, Y. W. Tan, H. L. Stormer, P. Kim, *Nature*, 438, 2005, 201.
- [40] A. K. Geim, K. S. Novoselov, *Nat. Mater.*, 6, 2007, 183.
- [41] A. K. Geim, P. Kim, *Sci. Am.*, 298, 2008, 68.
- [42] Yilun Liu, Bo Xie, Zhong Zhang, Quanshui Zheng, Zhiping Xu, *Journal of the Mechanics and Physics of Solids*, 60, 2012, 591-605.
- [43] Khan M.F. Shahil, Alexander A. Balandin, *Solid State Communications*, 152, 2012, 1331-1340.
- [44] Sukju Hwang, Juhwan Lim, Hyung Goo Park, Whan Kyun Kim, Duck-Hwan Kim, In Sang Song, Jae Hun Kim, Seok Lee, Deok Ha Woo, Seong Chan Jun, *Current Applied Physics*, 12, 2012, 1017-1022.
- [45] D. C. Elias, R. R. Nair, T. M. G. Mohiuddin, S. V. Morozov, P. Blake, M. P. Halsall, A. C. Ferrari, D. W. Boukhvalov, M. I. Katsnelson, A. K. Geim, K. S. Novoselov, *Science*, 323, 2009, 610.
- [46] Kin Fai Mak, Long Ju, Feng Wang, Tony F. Heinz, *Solid State Communications*, 152, 2012, 1341-1349.
- [47] S. Stankovich, D. A. Dikin, R. D. Piner, K. A. Kohlhaas, A. Kleinhammes, Y. Jia, Y. Wu, S. T. Nguyen, R. S. Ruoff, *Carbon*, 45, 2007, 1558.
- [48] Jinkee Hong, Sang Wook Kang, *Colloids and Surfaces A: Physicochemical and Engineering Aspects*, 374, 2011, 54-57.
- [49] Zhaofeng Wang, Jinqing Wang, Zhangpeng Li, Peiwei Gong, Xiaohong Liu, Libin Zhang, Junfang Ren, Honggang Wang, Shengrong Yang, *Carbon*, 50, 2012, 5403-5410.
- [50] E. Widenkvist, D. W. Boukhvalov, S. Rubino, S. Akhtar, J. Lu, R. A. Quinlan, M. I. Katsnelson, K. Leifer, H. Grennberg, U. Jansson, *J. Phys. D: Appl. Phys.*, 42, 2009, 112003.
- [51] D. A. Dikin, S. Stankovich, E. J. Zimney, R. D. Piner, G. H. B. Dommett, G. Evmenenko, S. T. Nguyen, R. S. Ruoff, *Nature*, 448, 2007, 457.
- [52] J. T. Robinson, M. Zhalutdinov, J. W. Baldwin, E. S. Snow, Z. Wei, P. Sheehan, B. H. Houston, *Nano Lett.*, 8, 2008, 3441.
- [53] Jian-Ding Qiu, Jing Huang, Ru-Ping Liang, *Sensors and Actuators B: Chemical*, 160, 2011, 287-294.
- [54] X. Wang, L. Zhi, K. Mullen, *Nano Lett.*, 8, 2008, 323.
- [55] Guoqing Ning, Tianyou Li, Jun Yan, Chenggen Xu, Tong Wei, Zhuangjun Fan, *Carbon*, 2013, 241-248.
- [56] M. D. Stoller, S. Park, Y. Zhu, J. An, R. S. Ruoff, *Nano Lett.*, 8, 2008, 3498.
- [57] Qing-Dan Yang, Tsz-Wai Ng, Ming-Fai Lo, Ning-Bew Wong, Chun-Sing Lee, *Organic Electronics*, 13, 2012, 3220-3225.
- [58] Q. Liu, Z. Liu, X. Zhang, N. Zhang, L. Yang, S. Yin, Y. Chen, *Appl. Phys. Lett.* 92, 2008, 223-303.
- [59] X. Lv, Y. Huang, Z. Liu, J. Tian, Y. Wang, Y. Ma, J. Liang, S. Fu, X. Wan, Y. Chen, *Small* 5, 2009, 1682.
- [60] Yunhwan Park, Dipti Gupta, Changhee Lee, Yongtaek Hong, *Organic Electronics*, 13, 2012, 2887-2892.
- [61] B. Z. Jang, A. Zhamu, *J. Mater. Sci.*, 2008, 43, 5092.
- [62] Jintao Yang, Minjie Wu, Feng Chen, Zhengdong Fei, Mingqiang Zhong, *The Journal of Supercritical Fluids*, 56, 2011, 201-207.

- [63] Yi-Luen Li, Chen-Feng Kuan, Chia-Hsun Chen, Hsu-Chiang Kuan, Ming-Chuen Yip, Shao-Lung Chiu, Chin-Lung Chiang, *Materials Chemistry and Physics*, 134, 2012, 677-685.
- [64] J. J. Liang , Y. Huang , L. Zhang , Y. Wang , Y. F. Ma , T. Y. Guo , Y. S. Chen , *Adv. Funct. Mater.*, 19, 2009 , 2297.
- [65] Dongrui Wang, Xiaoman Zhang, Jun-Wei Zha, Jun Zhao, Zhi-Min Dang, Guo-Hua Hu ,*Polymer*, 54, 2013, 1916-1922.
- [66] K. Wakabayashi , C. Pierre , D. A. Dikin , R. S. Ruoff , T. Ramanathan , L. C. Brinson , J. M. Torkelson, *Macromolecules*, 41, 2008, 1905.
- [67] H. Kim , C. W. Macosko, *Macromolecules*, 41, 2008, 3317.
- [68] Yuqi Li, Diyuan Pan, Shoubin Chen, Qihua Wang, Guangqin Pan, Tingmei Wang, *Materials & Design*, 47, 2013, 850-856.
- [69] S. Ansari , E. P. Giannelis , *J. Pol. Sci., Part B Polym. Phys.*, 47, 2009, 888.
- [70] H. Kim , C. W. Macosko, *Polymer*, 50, 2009, 3797.
- [71] E. T. Thostenson , C. Y. Li , T. W. Chou , *Compos. Sci. Technol.*, 65, 2005, 491 .
- [72] M. J. McAllister , J.-L. Li , D. H. Adamson , H. C. Schniepp , A. A. Abdala , J. Liu , M. Herrera-Alonso , D. L. Milius , R. Car , R. K. Prud'homme , I. A. Aksay , *Chem. Mat.*, 19, 2007, 4396.
- [73] S. Park , R. S. Ruoff , *Nat. Nanotechnol.*, 4, 2009, 217.

1.4 Inorganic Nanostructured Materials

Nanostructured materials are divided into three main types according to their macroscopic number of dimensions (Fig. 1.8). Two-dimensional (2D) nanostructured materials are characterized by the two dimensions at the micro and macro scale. One-dimensional (1D) nanostructured materials are characterized by the presence of one dimension at the micro and macro scale. Zero-dimensional (0D) nanostructured materials are characterized by the absence of two dimensions at the micro and macro scale.

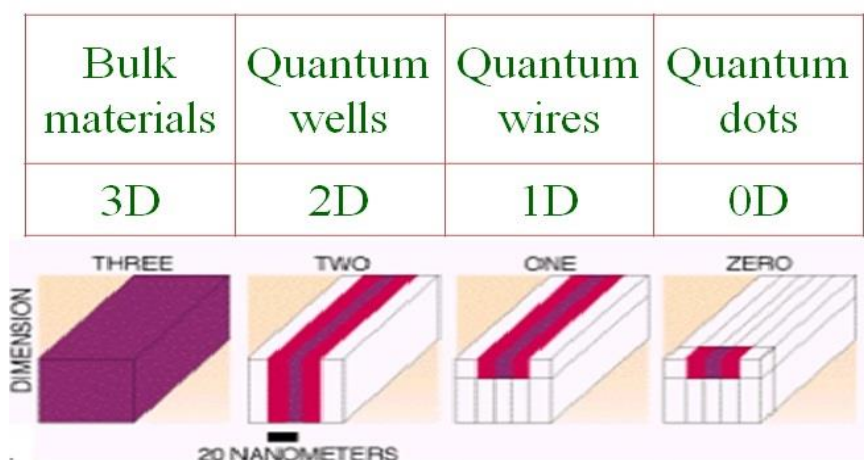


Figure 1.8: schematic classification of nanostructured material

One dimensional (1D) nanostructured inorganic materials (nanowires, nanorods or nanotubes) are structures arising great interest for many reasons. They are identified as possible basic structures for new sensors, devices for electronics and photonics.

The fascinating properties of these 1D inorganic nanostructure lie on their atomic structure and 1D morphology; in fact their length and diameter are nanometric dimensions. Based on these parameters, a variety of physical properties can be tailored, like electrical and electronic, piezoelectric and magnetic, catalytic. This potential relies on the subtle control of their physical properties such as their density of states and the transport of electrons and photons. Carbon nanotubes (CNT), nanotubes and nanowires of metallic oxides, metallic nanowires and also hybrids or structures of different composition are one dimensional (1D) nanostructured materials which have been studied.

One dimensional (1D) nanostructures have been called in many ways, like fibers or fibrils, nanowires and nanorods. In many cases nanotubules e nanocables are considered unidimensional

structures. Nanotubes are usually associated to materials able to host inside other materials at nanometric scale thanks to their morphology and, in particular, to their cavity [74]. A wide research has been carried out for carbon nanotubes, however inorganic nanotubes are performing new properties offering more advantages for applications.

Nanorods are usually considered shorter than fibers and nanowires but the definition is often arbitrary. Besides, monodimensional structures with diameters ranging from a few nanometers to many hundred microns have been called “whiskers” and fibers in the early literature, while nanowires and nanotubes with diameters not more than some hundred nanometers have been used prevalently in recent literature. Many basic knowledge and growth techniques about monodimensional nanostructures are based on the growth process of whiskers and fibers. Many techniques have developed in the synthesis and forming of monodimensional nanostructured materials; some techniques have been widely investigated while other techniques were considered less interesting. The bottom-up techniques many be generally classified as follows:

1) Spontaneous growth:

- Evaporation – condensation
- Vapor-Liquid-Solid (VLS) growth
- Stress-induced recrystallization

2) Template-based synthesis:

- Electroplating and electrophoretic deposition
- Colloid dispersion, melting or solution filling
- Conversion with chemical reaction
- Electrospinning

Spontaneous growth usually leads to the formation of single crystals along the preferential growth axis due to the crystal structure and the surface properties of the nanomaterial. Spontaneous growth is a process deriving from the Gibbs Energy reduction or chemical potential. The reduction of Gibbs Free Energy is commonly obtained by phase transformation or by chemical reaction. The formation of nanotubes and nanowires occurs along a certain fast orientation mainly in one direction and is of anisotropic nature. Nanowires of uniform dimensions can be obtained when the crystal growth proceeds along one direction, while no growth occurs for the remaining directions. In the

spontaneous growth methods, defects and impurities on the growth surfaces many considerably affect the morphology of the final products.

Template-based synthesis mainly produces polycrystals or even amorphous products. Template-based synthesis of nanostructured materials can be used in manufacturing of nanorods, nanowires, and nanotubules of polymers, metals, semiconductors and oxides [75]. Various templates have been used to obtain one dimensional nanostructures.

Template-based synthesis of nanostructured materials is a widely used method for the manufacture of nanorods, nanowires and nanotubules of polymers, metals, semiconductors and oxides [76]. Different templates with nanosized channels have been taken into consideration as models for the growth of nanostructures. The most commonly used templates are anodized alumina membranes [77] and radiation track-etched polymer membranes [78]. Other membranes have also been used as templates, such as nanochannel array glass [79], radiation track-etched mica [80] and mesoporous materials [81], porous silicon by electrochemical etching of silicon wafer [82] zeolites [83], carbon and inorganic nanotubes [84, 85]. Template materials must be compatible to the processing conditions. For example, the template must be an electric insulator when using the technique for electrochemical deposition. Template materials must be chemically and thermally inert during the synthesis and the processing steps; the solutions of the materials for deposition should be able to wet the inside wall of the template. Besides, the deposition should start from the lower end and go ahead from a side to the other in order to avoid discontinuity. Direct template filling is the easiest and most versatile preparation for nanotubes and nanowires. Usually a parent liquid or mixture or suspension is used to fill the pores. As for the filling step, the pore surface can be easily modified to become whether hydrophilic or hydrophobic by introducing a mono-layer of organic molecules. The control of the adherence between the template and the filler is very important in this method according to the results to be obtained. Researchers have studied the formation of various nanotubes simply filling the templates with colloidal dispersions [86, 87, 88]. In this method, a template is placed in a stable sol for a certain time. The capillary force leads the sol into the pores if the surface chemistry of the nanoparticles is appropriate and if the template pores have been correctly wetted by the sol. Once the pores are filled by the sol, the template properly filled up can be dried. Although the capillary force can grant the total filling of the colloidal dispersion into the template pores, the quantity of filler in to the pores can even be very little. After drying and eventual cooking part of the material may shrink, even if results have shown that mostly all the fillers only shrink slightly respect to the template pore dimensions. There are methods to increase the quantity of filler into the template pores. A possible mechanism of these may be the diffusion of the solvent through

the membrane, which takes to the enrichment of the solid along the inside surface of the template pores [89].

An important step for 1D nanostructures to be integrated into more organized structures (2D e 3D) is represented by the ability to let these nanostructures grow and organized in specific ways. The growth and alignment in a 3D array made of 1D nanostructures made it possible to fill the gap between the nano and macroworld, across microstructures: a crucial step for many applications in engineering. 1D nanostructures have different properties respect to nanoparticles since they have 2 dimensions, while the third dimension is generally a micro scale; for example, this is the reason why 1D structures can be more easily manipulated respect to 0D particles.

A correct distribution of 1D materials on big quantities of 2D or 3D (Fig. 1.9) materials may reduce to the minimum the manufacturing mistakes due to the outside solicitations of the devices, producing in this way flexible, foldable or soft matrices.

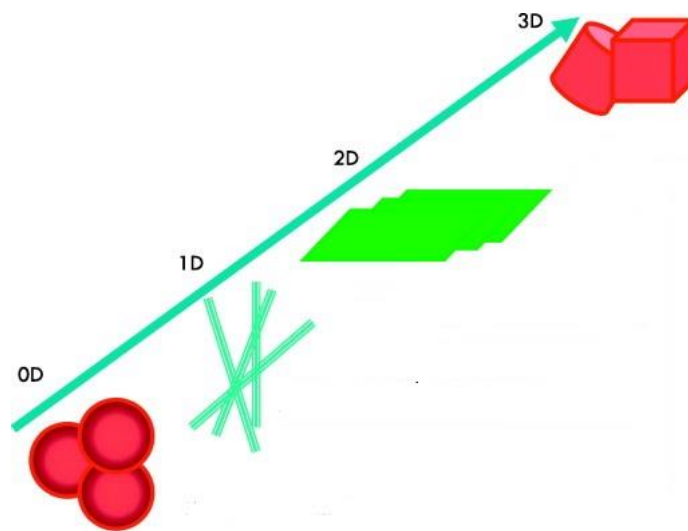


Figure 1.9: dimensional classification for the nanostructured materials

In the large family of nanomaterials, nanotubes and nanowires are therefore considered advanced materials. Their complexity together with their anisotropic nature require the elaboration of new approaches in order to include them in architectures and devices at the micro and macro scale. 0D and 1D nanostructures may be arranged in micro and macro nanostructured architectures and then aligned through bottom-up techniques and self-assembly growth. This may lead to a strong improvement for electric, optical and optoelectronic devices.

References

- [74] G.R. Patzke, F. Krumeich, and R. Nesper, *Angew. Chem. Int. Ed.* 41, 2002, 2446.
- [75] G.Z. Cao and D.W. Liu, *Adv. Coll. Inter. Sci.*, 136, 2008, 45.
- [76] Petar Djinović, Jurka Batista, Janez Levec, Albin Pintar, *Studies in Surface Science and Catalysis*, 175, 2010, 245-248.
- [77] R.C. Furneaux, W.R. Rigby, and A.P. Davidson, *Nature*, 337, 1989, 147.
- [78] S.K. Chakarvarti, *Radiation Measurements*, 44, 2009, 1085-1092.
- [79] R.J. Tonucci, B.L. Justus, A.J. Campillo, and C.E. Ford, *Science*, 258, 1992, 783.
- [80] Guozhong Cao, Dawei Liu, *Advances in Colloid and Interface Science*, 136, 2008, 45-64.
- [81] Shun-He Zhong, Chuan-Feng Li, Qing Li, Xiu-Fen Xiao, *Separation and Purification Technology*, 32, 2003, 17-22.
- [82] S. Fan, M.G. Chapline, N.R. Franklin, T.W. Tomblor, A.M. Cassell, and H. Dai, *Science*, 283, 1999, 512.
- [83] Huan Xu, Qiuming Gao, Hongliang Guo, Huanlei Wang, *Microporous and Mesoporous Materials*, 133, 2010, 106-114.
- [84] C. Guerret-Piecourt, Y. Le Bouar, A. Loiseau, and H. Pascard, *Nature*, 372, 1994, 761.
- [85] Mario Tagliavacchi, Rodolfo D. Sanchez, Horacio E. Troiani, Ernesto J. Calvo, *Solid State Communications*, 137 2006, 212-215.
- [86] B.B. Lakshmi, P.K. Dorhout, and C.R. Martin, *Chem. Mater.*, 9, 1997, 857.
- [87] Jianjun Liao, Shiwei Lin, Nengqian Pan, Danhong Li, Shipu Li, Jianbao Li, *Chemical Engineering Journal*, 211-212, 2012, 343-352.
- [88] B.B. Lakshmi, C.J. Patrissi, and C.R. Martin, *Chem. Mater.*, 9, 1997, 2544.
- [89] J.S. Reed, *Introduction to Principles of Ceramic Processing*, 1988.

1.5 Conductive Polymers

Polymers are macromolecules with high molecular weight made of a huge number of smaller molecules called monomers. They are linked by chains repeating the same kind of bond. The class of polymers include a very large number of molecules; their origins and characteristics are so different each other to be classified according to the following characteristics:

- origin: natural, synthetic
- degree of polymerization: oligomers, low polymers, medium polymers, high polymers
- number of monomers used: homopolymers, copolymers
- structure: linear, branched, reticulated, star-shaped
- physical status: crystalline, amorphous
- thermal behavior: thermo-plastic, thermo-hardening
- mechanism of polymerization: condensation, addition

Substances with very different chemical, mechanical and optical characteristics are included among polymers. One of the most exciting features for researches in the field of synthetic polymers is the production of conductive polymers, that is plastic materials able to conduct electric energy. Common synthetic polymers exhibit appreciable chemical-physical and mechanical properties, but are bad electrical conductors. Despite the idea that organic solids could be good electrical conductors had already been assumed, the turning point occurred in the 70s, when a series of polymers with good electrical conductivity was obtained (Fig. 1.10).

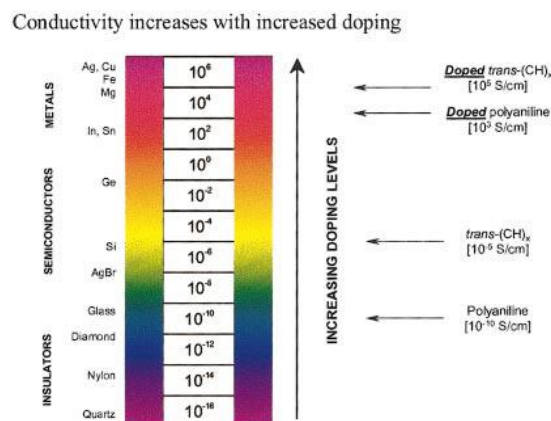


Figure 1.10: conductivity of polymers

H. Shirakawa et al discovered the conducting polymers in 1976. During the synthesis of polyacetylene, Shirakawa obtained a silvery shiny film performing a good electrical conductivity when doped [90].

The conductive polymers are divided into two classes: extrinsically conducting polymers (ECP) and intrinsically conducting polymers (ICPs). Normally ECP are not conductive, but they are able to become conductive if added with conducting materials (gold, silver, graphite...), in quantities even up to 50% [91]. ICPs are made of double bounds conjugated molecules; thanks to their structure they can be classified as semiconductors. These polymers are also called “synthetic metals” and are the most studied and most promising polymers thanks to their possibility of becoming highly conducting with low capping percentage.

The conducting polymers (ICPs) owe their intrinsic conductivity to the π electron system located along the main polymeric chain. So the synthetic polymers with double chains and double bonds like: polyacetylene (PA) [92], poly(para-phenylene) (PPP) [93], poly(para-phenylene)vinylene (PPV) [94], polyaniline (PANI) [95], polypyrrole (PPy) [96], polythiophene(PT) [97] and poly(3,4-ethylenedioxythiophene) (PEDOT) [98] (Fig. 1.11) are to be included in the ICP classification.

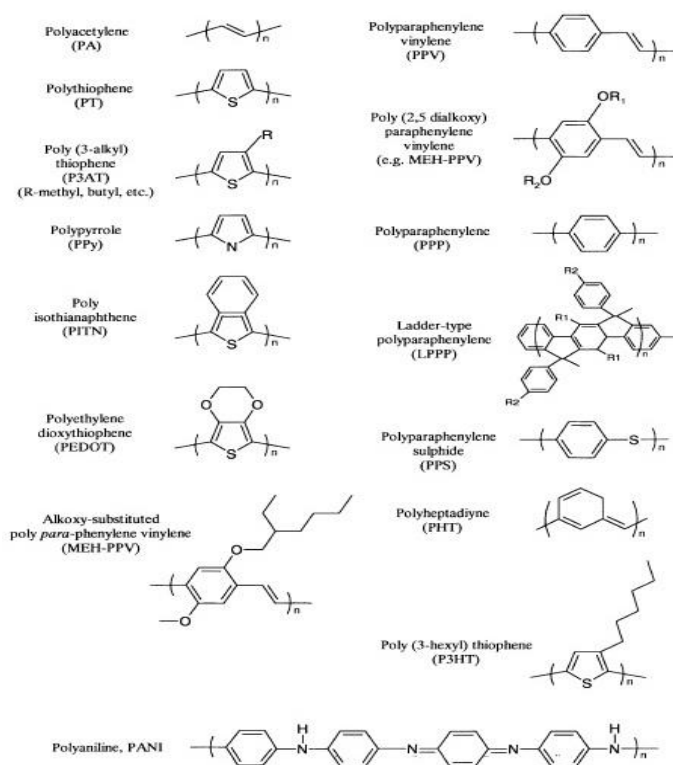


Figure 1.11: structure of the main ICPs

Like the inorganic materials, the electrical conductivity of these polymers has been explained by the electronic band structure. The electronic levels bearing a higher energy represent the valence band (VB) and the empty electronic levels bearing a lower energy represent the conduction band (CB). The energy band dividing them is called band-gap. The materials can be divided into conductors, semi-conductors and insulators according to the wideness of the band-gap.

The conductors have a valence band close to and even overlapped with the conduction band. This lets the electrons easily move from an energy level to another generating an electric current by potential differential or by adsorption of a certain photon (photoelectric effect).

In the semiconductors the conduction band is separate from the valence band by a small energetic gap, less than one electronvolt per electron mole. In these cases the band gap, also called prohibited band, can be reduced through capping making these materials more conductive.

The insulators have a strong energetic gap between the valence band and the conduction band, consisting of some electronvolts per electron mole. This high gap makes it impossible for electrons to flow and consequently no electric conductivity occurs. In polymers which are intrinsically conductive the conjugation of the double bonds is basic to allow the flow of electrons in particular conditions. The electrons of the double conjugated bonds can easily be removed or added to form a polymeric ionic species: doping. The oxidation/reduction of the polymeric chain is carried out by the charge acceptors/donators, which are able to make the polymer conductive or semi-conductive. Similar to the inorganic materials, the oxidative or reducing agents are called “dopants”.

The theory of the electronic band structure is based on three points:

- doping does not cause geometric relaxations or structural distortions of the material structure
- the generated positive charge is located over the entire polymeric chain
- the formation of a gap (not occupied level) at the top of the valence band gives the material a metallic property

Therefore, following this theory, it is assumed that a type p or n doping moves the electrons from the top of the valence band or adds them to the bottom of the conductive band, as for the inorganic semi-conductors' behavior. However, this model does not explain why the conductivity in the polymeric conductors (PPP,PPY,...) is due to the spin zero (bipolarons) charge carriers and not to the located electrons. Before applying this model to the conductivity of the conjugated polymers some considerations should be added. In the conducting polymers, locating the charge on a point of the chain and obtaining a local distortion of the reticule, respect to the locating of the charge, is

energetically more favorable [99]. This process produces the formation of localized electronic states in the band-gap (midgap state). Should an electron be removed along the chain, that is oxidation, we obtain the formation of a radical cation called polaron (Fig. 1.12).

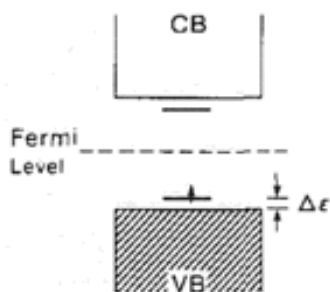


Figure 1.12: scheme showing the formation of a polaron

Fixed in one point, the polaron affects the polymeric chain only locally, modifying shortly the spatial distribution of the atoms. That is, a polaron is a radical ion bearing a spin $\frac{1}{2}$ with a single charge, associated to the reticule distortion at the presence of localized states in the band-gap. During the formation of the polaron, the valence band keeps full and the conducting band empty and no metallic characteristic appears, since the partially occupied level is located in the band-gap. On removing another electron from the chain, two situations may occur: the electron is removed from the polymeric chain producing a second polaronic state or the electron is removed from the same polaron forming a bipolaron. A bipolaron is a spin zero dication able to cause a strong distortion of the lattice. The formation of a bipolaron (Fig. 1.13B) is favoured respect to the formation of two polarons (Fig. 1.13A) since it is energetically convenient to have the interaction between two charges and the reticule respect to that of two charges of the same sign.

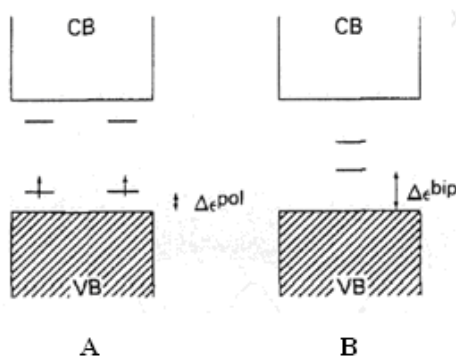


Figure 1.13: scheme showing the formation of two polarons(A) and the formation of a bipolaron(B)

As for inorganic semiconductors, the conducting polymers must be doped to conduct electricity. Unlike inorganic semiconductors, in polymeric conductors polarons and bipolarons, that are charged defects located along the polymeric chain, are those guaranteeing conductivity and not the electrons or the gaps located in the bands. It is therefore possible to say that you need the presence of a system conjugated with sp^2 hybrid atoms to make a polymer a conductive material, but this is not enough. To be able to conduct, the polymer needs the formation of polarons and bipolarons through doping. From the electronic band structure theory point of view, like the doping of inorganic materials, the formation of the polaron creates a new electronic state called midgap state, located at the centre of the prohibited band. At certain doping levels, the polarons interact each other, therefore at some levels in the prohibited band, and a formation of polaronic band may merge with the CB and VB making the polymer a good conductor. The charge carriage in the organic polymers occur through the moving of the charge carriers among localized states like the polaronic or bipolaronic ones. The transfer is regulated by the thermal activation, considering the hops of the charge carries, hopping, which can take place intra-chain or among different chains. The conductivity is mainly due to the charge transfers among different chains.

The doping process occurs simultaneously to the chain oxidation. The polyaniline form a part of the polymers intrinsically conductive and is different from those described up to now. The theory of conductivity for polyaniline (PANI) is the same, but the kind of doping changes. PANI may be doped through protonation, without any change in the number of electrons (oxidation/reduction) associated to the polymeric chain.

Polyaniline may assume different oxidation states: leucoemeraldine, emeraldine e pernigraniline (Fig. 1.14).

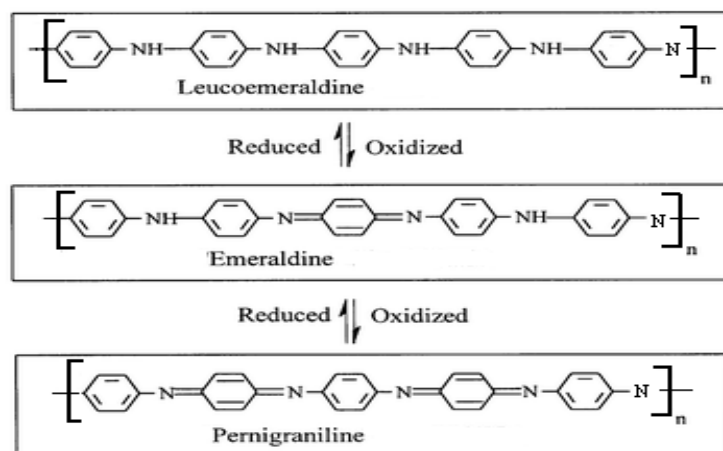


Figure 1.14: polyaniline and its three oxidation states

The leucoemeraldine is completely oxidized and formed by benzenic rings kept together by nitrogen atoms. The pernigraniline is the completely reduced form and is made of benzenic rings and quinone rings, alternated and bound by nitrogen atoms. The emeraldine is the partially oxidized form made of benzenic rings, alternated to chinoide-type rings, ratio 1:3, kept together by nitrogen atoms.

Polyaniline is part of the conductive polymers thanks to a conjugate π system. The conductive properties of the polymer, even when doped, varies considerably according to the oxidation status.

All kinds of PANI at the basic form are not electrical conductors, but this property can considerably changed by doping the polymer through protonization, in order to form a salt. No oxidation or reduction of the polymer occurs in this kind of doping. The electrical conductivity varies on changing the kind of doping used and its concentration related to PANI, eventually varying the quantity of conventional polymer with which the PANI [100] is mixed. The salt showing the best conductivity is the one in the partially oxidized form that is emeraldine. This salt can be obtained from oxidation and further protonization of the leucoemeraldine, or even better from the protonization of the basic emeraldine. For this kind of polymer, acids are therefore the doping agents. The mostly used acids are m-cresol and in particular camphorsulfonic acid (HCSA) (Fig. 1.15) [100].

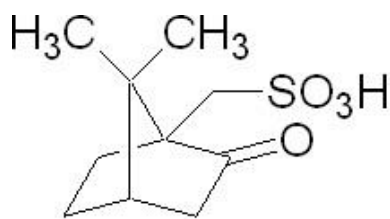


Figure 1.15: structure of camphorsulfonic acid (HCSA)

The protonization with HCSA of emeraldine (semi-conductor) leads to the formation of the emeraldine salt (conductor), where a positive charge and its respective counterion (Fig. 1.16) are always present in each repetitive unit.

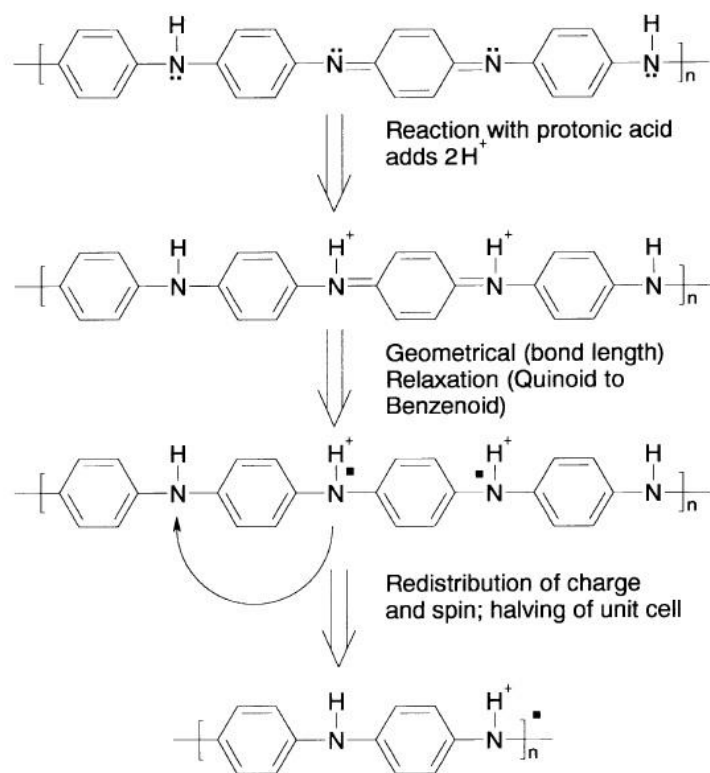


Figure 1.16: structure of the doping process for the emeraldine base with an acid

The doping with this acid allows a structural deformation leading to the separation of the spin without changing the number of electrons.

Currently, regioregular poly(3-hexylthiophene) (P3HT) is one of the conjugated polymers mostly studied thanks to its excellent electrical properties and easy processing. The regular arrangement of the hexyl-constitutents contributes to the high solubility of the polymer in organic solvents. The highest electrical mobility in the P3HT (Fig. 1.17), respect to other conjugated polymers, may be attributed to the presence of highly organized crystalline areas. The crystalline domains of regioregular P3HT are arranged in a lamellar regular structure where the thiophenic rings appear aligned [101].

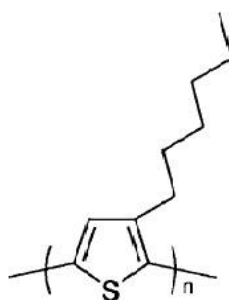


Figure 1.17: poly(3-hexylthiophene) (P3HT)

This strong arrangement in lamellar layers is promoted by strong interactions π - π inter-chains of the thiophenic rings. Comparing the charge carriers of P3HT at the presence of strong interactions inter-chains, it is noted that the conductivity is strongly influenced by the parallel or perpendicular orientation of the lamellar layers [101]. The presence of rigid areas strongly influences processes like electrospinning, where the presence of a “high viscosity” is fundamental.

Conductive polymers can be used for a lot of applications. To be useful a polymer must not only be a good conductor but also bear other characteristics like: workability, stability, not-toxicity and cheapness. When the conductive polymers were first synthesized, it was believed that some of their chemical-physical properties could limit their technological applications. The first ICP synthesized polymers were insoluble and not meltable and could not be operated like the other traditional thermoplastic polymers. The main part of these decomposed when exposed to air, diminishing their potential applications. When new synthetic processes were set, the applicative possibilities of conductive polymers multiplied. In order to obtain products which may be a trading success, the chemical-physical properties of conductive polymers must be perfectly suitable to each application. ICP bear properties placing them first to be alternative materials to those used in microelectronics at present. Their wide conducting interval, the easy chemical control, the lightness, operability and flexibility make these conductive polymers the protagonists of new electro-techniques. Among the various conducting polymeric species, the mostly utilized polymers in this field are polyaniline and polythiophene, in consideration of their peculiar structural characteristics.

During the last years many studies have been carried out in the lithographic field, the electric charge dissipation and in the production of conductive tracks on insulated matrices, where polyaniline and polythiophene were the protagonists. ICP can be used in the realization of the interconnections between various electronic components in an integrated circuit. Polyaniline is also applicable to protect metals from corrosion [102]. Another property of conductive polymers is to absorb low frequency electromagnetic radiations. For this reason they can be used as electromagnetic shields to eliminate the radioactive fallout off the calculators' terminals. In particular, the polyaniline is able to absorb microwaves very efficiently, putting it in evidence for this kind of application [103].

Many are the application fields for conductive polymers (Fig 1.18). In electronics the doped polymers are experimented in diodes [104], transistors [105], new sensors [106], conductive tracks for innovative printed circuits, substitution of joints for conventional semi-conductors. To conclude, these materials are interesting and being applied in the fields of transport and storage of energy

[105, 106] and information (printed circuit boards, microchips,), also as a consequence of the limited development of technology concerning silicon.

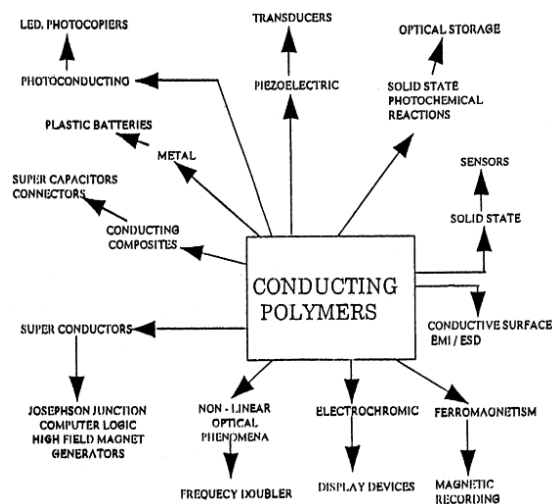


Figure 1.18: main application fields for conductive polymers

References

- [90] H. Shirakawa, E.J. Louis, A.G. MacDiarmid, C.K. Chiang, A.J. Heeger, *J. Chem. Soc. Chem. Commun.*, 1977, 578.
- [91] K. Jurewicz, S. Delpeux, V. Bertagna, F. Béguin, E. Frackowiak, *Chemical Physics Letters*, 347, 2001, 36-40.
- [92] M. Schwartz, R.J. Berry, D.S. Dudis, A.T. Yeates, *Journal of Molecular Structure: Theochem*, 859, 2008, 37-45.
- [93] Naoki Toshima, Susumu Hara, *Progress in Polymer Science*, 20, 1995, 155-183.
- [94] Jung-Il Jin, Chi-Kyun Park, Heung-Jung Kang, Sang-Hyun Yu, Jong-Chul Kim, Hong-Ku Shim
Synthetic Metals, 41 1991, 271-274.
- [95] Abdelaziz Rahy, Duck Joo Yang, *Materials Letters*, 62, 2008, 4311-4314.
- [96] H.C Kang, K.E Geckeler, *Polymer*, 41, 2000, 6931-6934.
- [97] Wu-Song Huang, *Polymer*, 35, 1994, 4057-4064.
- [98] P.-H. Aubert, L. Groenendaal, F. Louwet, L. Lutsen, D. Vanderzande, G. Zotti, *Synthetic Metals*, 126, 2002, 193-198.
- [99] S. Kivelson, A.J. Heeger *Synthetic Metals*, 17, 1987, 183-188.
- [100] Roch Chan Yu King, Frédérick Roussel, *Synthetic Metals*, 153 2005, 337-340.
- [101] H. Sirringhaus, P.J. Brown, R.H. Friend, M.M. Nielsen, K. Bechgaard, B.M.W. Langeveld-Voss, A.J.H. Spiering, R.A.J. Jansen, E.W. Meijer, P.T. Herwig, D.M. deLeeuw, *Nature*, 401, 1999, 685.
- [102] Elaine Armelin, Rosa Pla, Francisco Liesa, Xavier Ramis, José I. Iribarren, Carlos Alemán
Corrosion Science, 50, 2008, 721-728.
- [103] L. Olmedo, P. Hourquebie, F. Jousse, *Synthetic Metals*, 69, 1995, 205-208.

- [104] Hyun Jun Lee, Tae Hyun Park, Jin Hwan Choi, Eun Ho Song, Se Joong Shin, Hakkoo Kim, Kyung Cheol Choi, Young Wook Park, Byeong-Kwon Ju, *Organic Electronics*, 14, 2013, 416-422.
- [105] V. Saxena, B. D. Malhotra, *Current Applied Physics*, 2003, 293-305.
- [106] L.W. Shacklette, T.R. Jow, M. Maxfield, R. Hatami, *Synthetic Metals*, 28, 1989, 655-662.

1.6 Conductive Polymer Composite

In the last ten years nanotechnology has become a very active research field thanks its huge potentiality for many kinds of applications [107]. When the size of materials reduces to the nanometric scale some properties may improve radically or sometimes new unexpected characteristics may arise. There are four main kinds of nanostructures: 0D, 1D, 2D and 3D nanostructured materials. Among these, one-dimensional (1D) nanostructures have been deeply studied worldwide partially for their unique chemical and physical properties. Respect to the other three structures, the main characteristics of 1D nanostructures are their very small size and considerable elongation, which could allow the efficient transfer of electrical carriers along a controlled direction; therefore they are very suitable to produce systems at the nanoscale dimension and able to carry electrical charge. Recently conductive polymers have attracted a great interest for their advantages, like the readily tunable bandgaps, the important red-ox characteristics, the excellent flexibility and workability respect to the traditional inorganic nanotubes [108]. To improve and extend the properties of these inorganic nanomaterials one or more components are often incorporated to form nanocomposites for many applications in electronic field, for sensors, catalysis, energy, electromagnetic interferences and biomedicine. The intrinsically conductive polymers (ICP) are the most utilized to obtain this kind of nanocomposites. Among ICP, the more widespread are polyacetylene (PA), polyaniline (PANI), polypyrrole (PPy), polythiophene (PTh), poly(para-phenylene) (PPP), poly(phenylenevinylene) (PPV). These conjugated polymers may become electrical insulators, semi-conductors or conductors according to the doping level and kind of doping. Besides the formation of 1D nanostructured material, the addition of at least one secondary component in the conductive polymers to form a nanocomposite is another useful approach to improve or extend the functionalities of conductive polymers [109]. It is expected that the peculiar properties with synergetic effect of each component will be studied in the polymeric conductive nanocomposites. The improvement may include chemical, physical and biological properties. For example, it has been demonstrated that the addition of carbon nanotubes (CNT) to ICP may improve the electric properties [110]. Let's conclude with the discussion about manufacturing methods and the future research directions concerning 1D conducting polymer nanocomposites. As for the manufacture of 1D conducting polymer nanocomposites (CPC), there are two important points to examine: the manufacturing technique for 1D conducting polymer nanocomposites and the incorporating method at the second stage into the polymer.

CNT not only exhibit an excellent mechanical resistance, but also a good electrical conductivity together with excellent chemical stability. Most of all they exhibit a small size which makes them very promising for nanodevices. However, their poor workability limits their applications. Therefore many researchers are focusing on the chemical modification of CNTs with organic molecules or polymers, in order to improve their solubility. The use of carbon nanotubes in polymeric composites would be very efficient to improve and widen the properties of polymers or of CNT (Fig. 1.19).

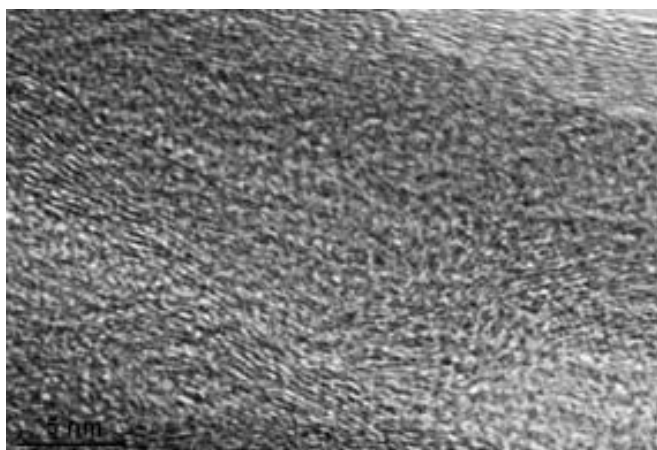


Figure 1.19: HRTEM image of multiwalled carbon nanotubes-polyaniline composite

In particular, conducting polymer nanocomposites with CNTs demonstrated to bear a better charge carriage [111]. The morphology and properties of the nanocomposites may be controlled in experimental conditions. Respect to not aligned CNTs, arrays of aligned nanotubes have demonstrated to be an excellent substratum for the electrospinning of conductive polymers, since these can grow on the surface of any single CNT, facilitating the manufacture of conductive nanocomposites [112]. Besides the production of thin layers of CPC through the use of CNT has been deeply studied to obtain 1D polymeric nanocomposite conductors [113]. The first example of a 1D CNT/PA nanocomposite has been the polymerization in situ of phenylacetylene at the presence of CNTs. Imaging by TEM showed that a certain quantity of carbon nanotubes has been wrapped in PA coils along the tubular surface latitudes. To improve the interactions between the conductive polymers and CNT, the introduction of covalent bonds between the conductive polymers and the CNT has been deeply investigated. Surfactants have also been used to improve the uniformity of the conductive polymeric coatings on carbon nanotubes. These agents are able to absorb and arrange in a regular display on the surface of the nanotubes at quite high concentrations. Cable-like structures [114] can also be obtained through the in situ polymerization at the presence

of surfactant molecules like sodium dodecyl sulphate (SDS). However, only by ultrasonic radiation it is possible to obtain very regular polymeric nanocoatings on the surface of CNT. Microscopic studies have demonstrated that films 20-50nm thick of PTH have been displayed uniformly on the surface of CNT. Besides the polymerization in solution, an emulsion polymerization has been used to prepare CNT.1D conductive polymeric nanocomposites bearing a uniform core-shell structure [115]. Methods with microemulsion to manufacture 1D CNT / PpY nanocomposites have been well investigated. The results of these researches have shown the formation of core-sheath shaped nanostructured agglomerates. The thickness of the polymeric layer on the MWNTs surface can be controlled by varying the content of MWNT. Conductive polymeric monomers can also be used as a fillers and then polymerized inside the carbon nanotubes to form 1D nanocomposites

Metallic nanoparticles 1D structured nanomaterials (Fig. 1.20) are most important for their electrical, optical, catalytic properties, which make these materials suitable for a wide range of applications, like in nanoelectronics and detection devices [116].

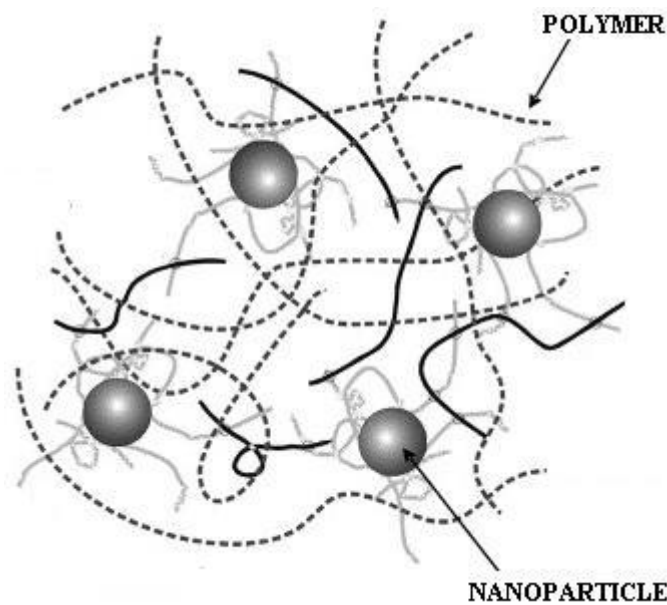


Figure 1.20: schematic drawing of the structure in nanoparticles filled polymer composites

By combining metallic nanomaterials and 1D conductive polymers, new properties can be developed thanks to the transfer of electrons and charges between the two components, besides the anisotropic electrical properties of the 1D conductive polymers and the optical ones of the metallic nanoparticles. One of the main properties of conductive polymers is their reversibility in the redox chemistry. This feature is suitable for the manufacture of 1D conductive polymeric nanocomposites at the presence of a metallic component.

PANI/Ag nanofiber composites can be obtained through the redox process between polyaniline nanofibers and a precursor like silver nitrate [117]. As for Ag, also Au, Cu and Pd nanoparticles are easily produced inside or on the surface of polyaniline nanofibers through redox reaction in situ [118]. Other kinds of polymeric structures revealed to be good matrices to load metallic nanoparticles to form 1D metallic nanocomposites. These have been used as loading matrices for Au nanoparticles to form 1D PpY-Au. By this method, the sizes of the synthesized nanoparticles result to be not uniform, although the addition of surfactant molecules into the reaction system produces a monodispersed population and constant sizes of Au nanoparticles. It is possible to produce nanoparticles of alloys mixing various precursors of different metals. The ease in controlling the CPC metallic composition makes them very interesting for potential applications for sensors and nanoelectronic devices. Metallic conductive polymers have been made from template techniques. In these structures, polyaniline could even protect nanotubes and metallic nanoparticles from oxidation and corrosion, which is an important property in the field of electronic devices. Au/PTH nanofibers composites may also be produced by electrochemistry. TEM imaging has shown the correlations between the synthesis methods and the structuration.

PANI nanocomposites and Au nanoparticles may be obtained by redox reaction between chlorauric acid and aniline at the presence of camphorsulfonic acid. [119]. Camphorsulfonic acid acts both as a doping and a surfactant.

The production of 1D conducting polymeric nanocomposites with metal oxides has become a fascinating feature thanks to the potentiality in the applications for sensors and energy devices. The self-assembly method, also called “template-free” method, is the easiest way to produce 1D conducting polymers and their nanocomposites with metallic oxides. 1D polyaniline-titanium dioxide nanocomposites can easily be produced through processes described above. In this synthesis, for example, surfactant micelle contain titanium dioxide, that can form nanotubes by using ultrasounds. In order to improve the workability, the mechanics and the chemical and thermal stability, the conductive polymers are often combined with other non-conductive polymers. For example, electrospinning is a technique where the use of insulating polymers is basic to form the necessary sub-micrometric fibers.

Among the first systems studied, electrospinning has been the first one leading to the production of PANI/PEO fiber composites, by the use of camphorsulfonic acid [120] as doping agent. The composition of PANI and PEO can be controlled by the ratio PANI/PEO. Also poly-3-alkylthiophenes have been combined with PEO to form composite fibers by electrospinning [121]. Besides, PEO can be removed by treating the composite with acetonitrile fibers, obtaining as a

consequence the formation of long fibers of the only conductive polymer. Conductive polymers and biodegradable and biocompatible polymers arose interest for their potential application in medical tissue engineering. An example is the electrospinning of PANI / PLA [122] based systems. The composite nanofibers can be obtained starting from monomers of conductive polymers polymerized in situ in an insulator and then applied to the electrospinning. PpY / PEO composite nanofibers have been produced in this way [123]. Nylon-6/PANI fiber composites have been synthesized by the chemical polymerization using electrospun nylon-6 fibres as templates [124].

One of the most important characteristics of conductive polymers is the reversibility of their process. For example, inorganic acids, organic acids and even polymeric acids are common doping for PANI. Therefore, insulated polymers with an acid group can easily be combined with conductive polymers by the doping process.

It is also possible to include chromophores in the conductive polymers, but when including substances like porphyrins the conduction of polymeric matrices will reduce the conduction of the conductive polymers [125]. Porphyrins tend to aggregate in J-aggregates, structures which can be used as templates in the polymerization to form conductive polymeric nanocomposites/porphyrins [126]. Polyaniline are among the mostly used conductive polymers to obtain these kinds of structures. The results of the 1D conductive polymers/porphyrins composites are important for many reasons: the aggregates can easily work as templates and besides the production of multifunctional materials can be obtained due to the photoluminescence and electrocatalysis of the system.

In order to obtain multifunctional materials, sometimes two or more nanocomponents are combined with conductive polymers to form nanocomposites. For example, incorporating nanoparticles of noble metals and magnetic nanoparticles into a conductive polymer we can obtain a conductive and magnetic nanocomposite with catalytic properties. Another example is the use of nanoparticles of metallic oxides and CNT in conductive polymers. For this type of material it has been possible to produce CNT/PANI/Fe₃O₄ composite, where the Fe₃O₄ nanoparticles had been previously stuck to the surface of the CNT. 1D CNT/PANI/ Fe₃O₄ nanocomposites can be used as electrochemical sensors [127].

Even by dissolving by electrospinning one or more components in the solution, it is possible to produce a system for multicomponent 1D nanocomposite conductive polymers. For example the PANI / PEO / MWCNTs nanofiber composites have been obtained by electrospinning [128]. TEM images have shown that MWCNTs with a diameter less than 20 nm can be dispersed in PANI/PEO fibers without the formation of aggregates. The good dispersion of multiwalled carbon nanotubes in

the conductive polymeric matrix is obtained through the direct interactions between the MWCNTs and the conductive polymers. Following a similar procedure also nanoparticles of different nature can be incorporated in PANI/PEO nanofibers [129]. The electrospinning process is widely followed to produce oxide nanocomposites or mixed oxides, where the same polymer can be eliminated through calcination.

Including nanomaterials into the conductive polymers it is possible to improve their properties and even to create new ones, among which magnetic, optical properties, wettability and, most of all, the electrically conductive properties. After doping, the electrical conductivity of conductive polymers may arrive up to 100 S/cm. The electrical conductivity of a single CPC nanofiber is one or two orders of magnitude bigger than that of the bulk materials. Besides, the conductivity of 1D PANI nanostructure increases with the decrease of the fiber dimensions. The combination of another component with the conductive polymers will increase or decrease their electrical conductivity. Generally, the electrical conductivity decreases when incorporating an insulating component in the polymeric nanomaterial due to the partial block in the conductive track induced by the insulating component. The typical example is represented by 1D nanofiber composite using metallic oxides [130]. When loading ever higher quantities of Fe_3O_4 the conductivity decreases. This conductivity decrease is due to the higher charge dispersion carrier between PANI and Fe_3O_4 nanoparticles. The interactions between Fe_3O_4 and PANI improve the detection of the charge carriers and therefore increase the resistance of the sample. On the other hand the incorporation of another nanocomponent with high electrical conductivity in conductive polymers improves the conductivity of nanocomponents. Generally CNT bear a higher electrical conductivity than the same conductive polymers without CNT. CNT may work as a “conductive bridge” between the conducting domains of ICP [131]. It is interesting to underline that the electrical conductivity depends on the temperature and it becomes weaker on increasing the load of CNT. The strong interactions between CNT and the PANI chains represent an important function in the improvement of the electronic properties in PANI because they increase the delocalizing length of the polymeric chains. In addition to CNTs, the incorporation of metallic nanoparticles in conductive polymers may improve the electrical conductivity. Same as for CNTs, metallic nanoparticles may act as conducting domains.

The applications for composite conductive polymers are many and range from the fields of sensors, catalysis, microwave absorption and electromagnetic frequency interference (EMI) shielding, drug delivery, tissue engineering, thus the most interesting ones are in nanoelectronics and energy applications.

The main part of conductive polymers are suitable for the production of electronic devices thanks to their high electrical conductivity, mechanical flexibility and cheapness. 1D CPC are good candidates to be basic blocks for electronic nanodevices. The introduction of nanomaterials of various kinds and different functionalization may influence the conductivity of conductive polymers but also make them useful for light-emitting diodes, transistors, memory and photovoltaic devices [132]. Schottky diode may be manufactured from electrospun fibers of on n-doped silicon substrate [133]. Field effect transistor (FET) can also be constructed using electrospun PANI/PEO composite nanofibers [134]. The parameters of the device have been improved in this system, progressively decreasing the PEO content. The development of new technologies in the information elaboration has made the study of non volatile memory devices ever more interesting. It is possible to produce bistable memory device using PANI/Au composite nanofibers [135]. The memory device made of PANI/Au composites exhibit high and stable performances so to make it a promising feature in the development of future technologies in the information field.

Cost reduction and efficiency increase of the energetic conversion in solar cells have become the center of the efforts of researchers. The high conductivity and the miniaturization of the CPC electrospun fibers make these materials very exciting for the solar cell field. Hybrid organic/inorganic cells with incorporated metallic oxides functionalized with photo-sensible compounds are very promising in this technological field. These kinds of devices are cheap and bear very important chemical, physical and mechanical properties. Photovoltaic devices fabricated with vertically aligned ZnO nanofibers/P3HT composites have promising technical characteristics [136]. CNT / PEDOT-PSS nanotubes composites have been used to produce DSSC. TiO₂ nanotube arrays may be used as a base to be filled with P3HT to form new solar cells [137].

CPCs nanofibers have been applied successfully to improve the technical characteristics in fuel cells, supercapacitors and lithium ion batteries.

References

- [107] Timp G., *Nanotechnology*, New York: Springer-Verlag, 1999.
- [108] Schenning A, Meijer EW., *Chem. Commun.*, 2005, 3245–58.
- [109] J.F. Feller, P. Chauvelon, I. Linossier, P. Glouannec, *Polymer Testing*, 22, 2003, 831-837.
- [110] Zhang X, Zhang J, Wang R, Zhu T, Liu Z., *ChemPhysChem.*, 5, 2004, 998–1002.
- [111] Kumar SA, Chen SM., *Sensors*, 8, 2008, 739–66.
- [112] Gao M, Huang S, Dai L, Wallace G, Gao R, Wang Z., *Angew.*, 39, 2000, 3664–7.

- [113] Xiaofeng Lu, Wanjin Zhang, Ce Wang, Ten-Chin Wen, Yen Wei, *Progress in Polymer Science*, 36, 2011, 671-712
- [114] Park JE, Saikawa M, Atobe M, Fuchigami T., *Chem. Commun.*, 2006, 2708–10.
- [115] Yu Y, Ouyang C, Gao Y, Si Z, Chen W, Wang Z, Xue G., *J. Polym. Sci. Part. A Polym. Chem.*, 43, 2005, 6105–15.
- [116] Xia Y, Xiong Y, Lim B, Skrabalak SE., *Angew. Chem.*, 48, 2008, 60–103.
- [117] Zhe-Fei Li, Frank D. Blum, Massimo F. Bertino, Chang-Soo Kim, *Sensors and Actuators B: Chemical*, 161, 2012, 390-395.
- [118] A. Drelinkiewicz, M. Hasik, M. Kloc, *Synthetic Metals*, 102, 1999, 1307-1308.
- [119] Huang K, Zhang Y, Long Y, Yuan J, Han D, Wang Z, Niu L, Chen Z., *Chem. Eur.J.*, 12, 2006, 5314–9.
- [120] Norris ID, Shaker MM, Ko FK, MacDiarmid AG., *Synth. Met.*, 114, 2000, 109–14.
- [121] Alexis Laforgue, Lucie Robitaille, *Synthetic Metals*, 158, 2008, 577-584
- [122] Picciani PHS, Medeiros ES, Pan Z, Orts WJ, Mattoso LHC, Soares BG., *J. Appl. Polym. Sci.*, 112, 2009, 744–53.
- [123] Nair S, Natarajan S, Kim SH., *Macromol Rapid. Commun.*, 26, 2005, 1599–603.
- [124] Habib Bagheri, Ali Aghakhan, *Analytica Chimica Acta*, 713, 2012, 63-69.
- [125] Saravanan S, Anantharaman MR, Venkatachalam S, *Mater. Sci. Eng. B*, 135, 2006, 113.
- [126] Koti ASR, Taneja J, Periasamy N., *Chem. Phys. Lett.*, 375, 2003, 171.
- [127] Liu Z, Wang J, Xie D, Chen G., *Small*, 4, 2008, 462.
- [128] Shin MK, Kim YJ, Kim SI, Kim SK, Lee H, Spinks GM, Kim SJ., *Sens Actuators B*, 134, 2008, 122.
- [129] Yu G, Li X, Cai X, Cui W, Zhou S, Weng, J., *Acta Mater.*, 56, 2008, 5775.
- [130] Yunze Long, Zhaojia Chen, Jean Luc Duvail, Zhiming Zhang, Meixiang Wan *Physica B:Condensed Matter*, 370, 2005, 121-130.
- [131] Su C, Wang G, Huang F., *J. Appl. Polym. Sci.*, 106, 2007, 4241.
- [132] Pérez R, Pinto NJ, Johnson Jr AT., *Synth. Met.*, 157,2007, 231.
- [133] Rivera R, Pinto NJ., *Physica. E.*, 41, 2009, 423.
- [134] Pinto NJ, Johnson Jr AT, MacDiarmid AG, Mueller CH, Theofylaktos N, Robinson DC, Miranda FA, *Appl. Phys. Lett.*, 83, 2003, 4244.
- [135] Tseng RJ, Baker CO, Shedd B, Huang J, Kaner RB, Ouyang J, Yang Y., *Appl. Phys. Lett.*90, 2007, 1.
- [136] Narayan Ch. Das, Paul E. Soko, *Renewable Energy*, 35, 2010, 2683-2688.
- [137] Jiwon Lee, Jae Young Jho, *Solar Energy Materials and Solar.*, 95, 2011, 3152-3156.

1.7 Electrospinning technique

In the last years the production of new artificial and synthetic materials has favored the development of processes to transform these polymeric masses into fibers. Great efforts have been made in the field of traditional fiber production with the extrusion of a polymer either fused or in a solution.

The conventional processes utilize mechanical forces to obtain the yarn extruding the fused polymers that are afterwards extended to assign these the needed mechanical and chemical-physical properties. Fibers with diameters of some tens of micrometers can be obtained through these techniques.

The technological evolution allowed to produce ever more miniaturized materials performing advanced characteristics. In this field the task is to obtain a fiber diameter not obtainable through the traditional electrospinning methods. Today more than ever the challenge is turning to nanotechnology.

Electrospinning is an alternative technique to the traditional ones, performing high miniaturizing potentialities. The patent for electrostatic spinning, afterwards called electrospinning, date to the '30 [138]. During the first decades the technique for electrospinning did not lead to new important application.

The reason for this low development is the low output and the big diameters of the obtained fibers; these factors and the insufficient research which followed the discovery prevented the interesting development of electrospinning manufacture. In recent years the request for nanostructured materials in many fields stimulated new studies, allowing the re-start of researches for electrospinning.

At present this is the only process able to supply polymeric fibers with nanometric diameters.

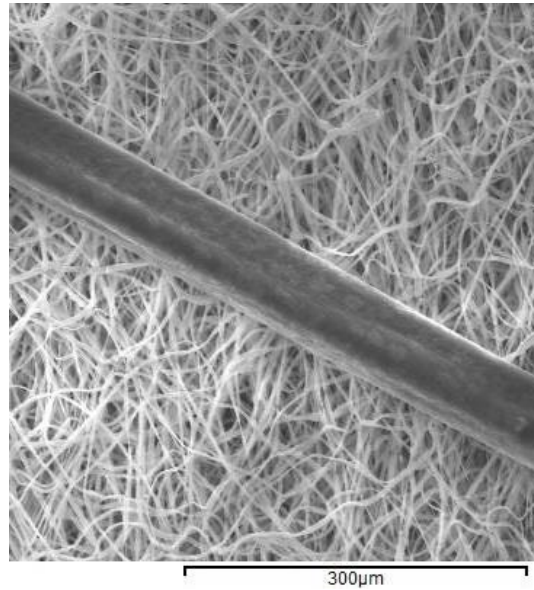


Figure 1.21: comparison between a hair and electrospun polymeric fibers

The great innovation coming from this technique relies in the replacement of mechanical force, to stretch the polymer, with the force exercised by the electric field between two electrodes.

Electrospinning is based on the use of a strong electric field in which the applied tension may vary from 5000 to 40000 Volts, producing an electrostatic force able to prevail on the surface tension of the polymer.

The result of this is the formation of a polymeric jet launching from an electrode to the other. The polymer ejects from the point of a syringe under regulated flow obtained by a volumetric pump; it is fluid and charged positively. The two electrodes are the points of the syringe and of a metallic collector where the electrospun fibers can be collected.

The jet flow, which is electrically charged and which comes from the base of the hole form a conic geometry (Taylor's cone), undergoes acceleration and slimming while crossing the electric field, forming a stretched fiber, also thanks to the evaporation of the solvent. Taylor's cone is generated close to the exit hole when the hydraulic transport induced to the fluid is overcome by the electrostatic one, due to the strong magnetic field existing between the electrodes (Fig. 1.22).

When using low weighted molecules, the jet fluid becomes instable, producing a spray made of tiny drops charged with static electricity (electrospraying). This process does not occur when using polymers whose viscoelastic forces stabilize the jet, forming charged fibers directing toward the electrode, where they collect forming a texture of very thin fibers.

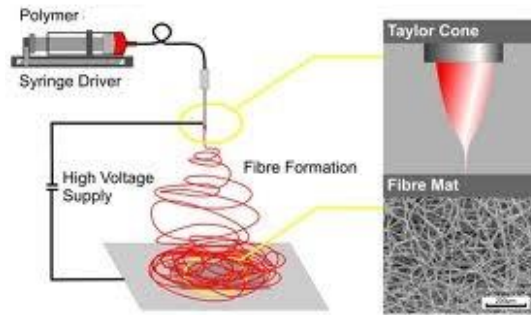


Figure 1.22: detailed scheme of Taylor's cone

The formation of nanometric fibers come through a phenomenon called splaying which breaks the main jet into many nanofibers and the following whipping motion [139, 140] (Fig. 1.23), which is not detectable at naked-eye, causes a quick spiral rotation of the jet flow.

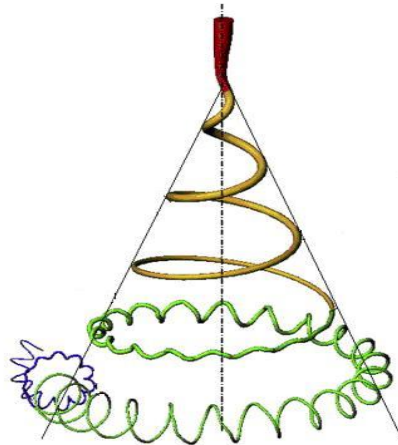


Figure 1.23: whipping movement of a polymeric fiber

So the obtained fibers gather on a screen made of metallic material electrically grounded.

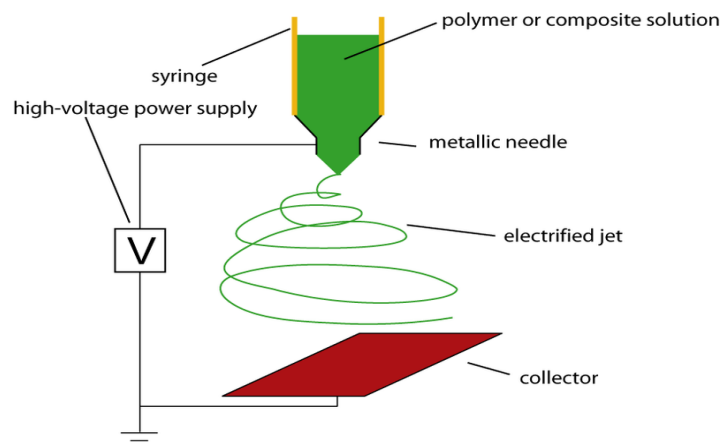


Figure 1.24: electrospinning process scheme

Electrospinning may be used for polyamides, polyfunctional polymers deriving from cellulose, conductive polymers, polymeric mixes and polymers containing solid nanostructures or small functional molecules.

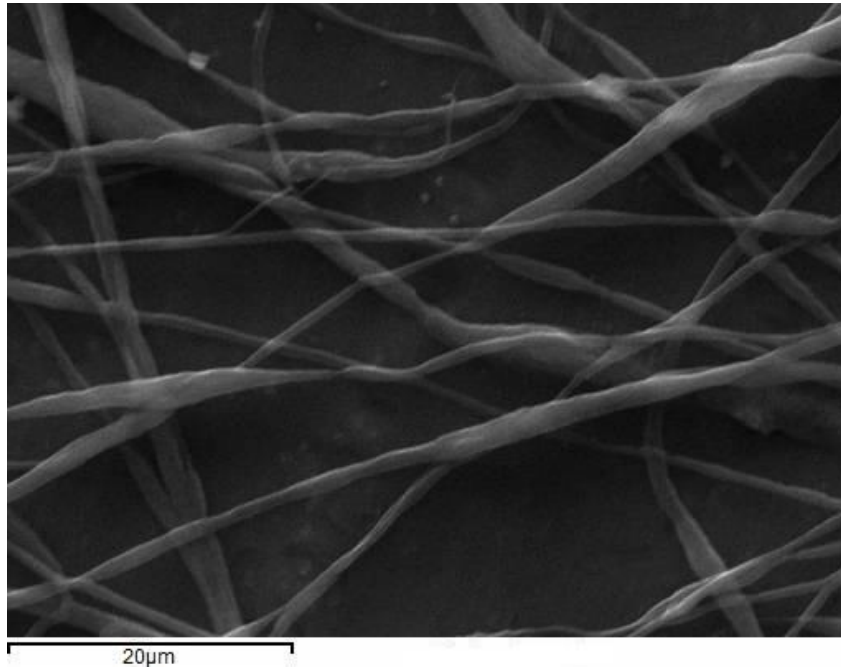


Figure 1.25: SEM image of a texture of polymeric fibers

To obtain an excellent electrospun material the experiment must control the polymeric properties, the process parameters and the environmental conditions.

Properties of the solution:

- medium molecular weight of the polymer
- polydispersity of the polymer
- viscosity of the solution
- concentration of the solution
- conductivity of the solution
- vapour pressure of the solvent
- dielectric constant of the solvent.

Instrumental parameters:

- electric potential
- speed flow of the solution
- distance needle-collector
- internal diameter of the needle.

Environmental conditions:

- temperature
- humidity.

The solution must pass a critical value of molecular weight, viscosity and concentration below which it is impossible to obtain fibers. Close to the critical concentration value some defects, beads [141] occur in the structure (Fig. 1.26).

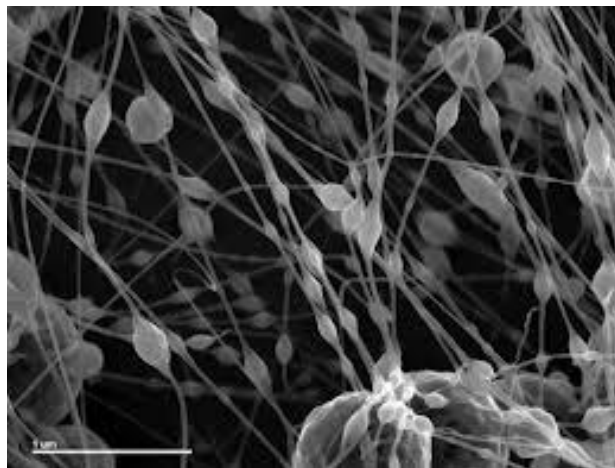


Figure 1.26: structural imperfections as beads in an electrospun polymer

Increasing the concentration of the polymer and keeping constant the other parameters, the diameter of the fibers increases.

The choice of the solvent is a very important item; this must interact with the polymer more than the polymeric chains interact together, in order to avoid the formation of yarns. The solvent must exhibit a high vapor tension to make the evaporation possible during the passage needle-collector.

Besides, the solvent must absolutely have a dielectric constant, in order to allow the solution a sufficient density charge to pass the surface tension, which is a basic feature to perform electrospinning.

As explained theoretically, the electrospinning process is possible only when a good exit speed of the polymer from the needle is followed by an electric field able to overcome the surface tension. The correct equilibrium between the instrumental parameters is essential to obtain the formation of Taylor's cone.

Usually, at equal potential applied, the flow increase increases the fiber diameter. As for the potential, consequences are different: increasing the value, the stretching force increases itself and therefore the fibers slim.

The distance from the needle and the collector is very important, since decreasing it the electrical field increases instead; therefore also the stretching force does and the time for which the fiber undergoes the field is lower, causing the consequent insufficient evaporation of the solvent of the fibers. The result is that when shortening the distance between the needle and the collector the fibers grow and may be subject to structural deformities like blobs (Fig. 1.27).

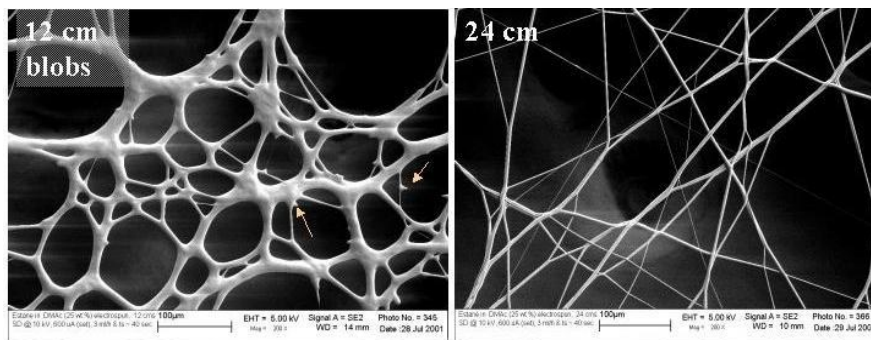


Figure 1.27: SEM images of an electrospun polymer with a distance needle-collector of 12 cm and of 24 cm, with consequent disappearing of the blobs

Usually the environmental parameters like temperature and air humidity are overlooked, even if these could influence the process. They should be considered better and kept constant in order to standardize the electrospinning.

Electrospinning is a very interesting technique since it performs potentialities and innovations and mostly it is the unique technique to obtain nanometric fibers. The exponential growth of the studies in this technique indicates the importance of this matter for the next years. Passing from micrometric to nanometric diameters, the polymeric fibers acquire new characteristics among which the high specific surface area (surface-volume ratio) and superior mechanical properties.

The nanometric diameter and the high specific surface area make these fibers suitable for those applications where the basic feature is the number of active sites per volume units, for example in the catalysts [142] or drug deliverers[143].

The main limit until some time ago was the impossibility to obtain an aligned system of the fibers and consequently to use them as single fibers, but some studies have solved this problem [144].

Commercial applications in industry of filters and membranes are currently being developed.

The polymeric fibers are used in the field of chemical engineering, thanks to the high adsorbing power and as a support for catalysts [142].

In biomedicine nanofibers find applications as tridimensional supports for the growth of biological tissues for transplants or reconstruction of organs and human body parts such as bone prostheses, skin, cartilage, nerves and veins [145].

Among the most interesting applications those foreseeing the use of fibers of conductive polymers in microelectronics and in designing solar cells [146, 147, 148] are to be underlined (Fig. 1.28).

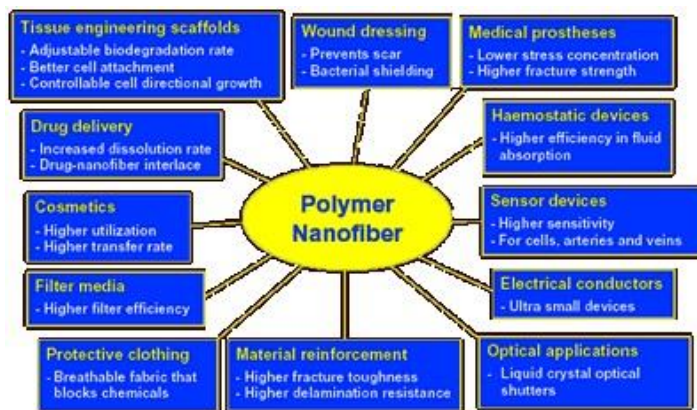


Figure 1.28: application of electrospun polymeric fibers

References

- [138] Formhals, *Us Patent*, 1934, 1-975-504.
- [139] Nandana Bhardwaj, Subhas C. Kundu, *Biotechnology Advances*, 28, 2010, 325-347.
- [140] Zheng-Ming Huang, Y.-Z. Zhang, M. Kotaki, S. Ramakrishna, *Composites Science and Technology*, 63, 2003, 2223-2253.
- [141] Pirjo Heikkilä, Ali Harlin, *European Polymer Journal*, 44, 2008, 3067-3079.
- [142] Shinji Sakai, Tetsu Yamaguchi, Rie Watanabe, Masaaki Kawabe, Koei Kawakami, *Catalysis Communications*, 11, 2010, 576-580.
- [143] El-Refaie Kenawy, Fouad I. Abdel-Hay, Mohamed H. El-Newehy, Gary E. Wnek, *Materials Chemistry and Physics*, 113, 2009, 296-302.
- [144] Dan Li, Yuliang Wang, and Younan Xia, *Nano Letters*, 3, 2003, 1167-1171.

- [145] Sangamesh G. Kumbar, Syam P. Nukavarapu, Roshan James, Lakshmi S. Nair, Cato T. Laurencin, *Biomaterials*, 29, 2008, 4100-4107.
- [146] Jing Zhang, Hongwei Han, Sujuan Wu, Sheng Xu, Ying Yang, Conghua Zhou, Xingzhong Zhao, *Solid State Ionics*, 178, 2007 1595-1601.
- [147] H. Liu, *Appl. Phys. Lett.*, 87, 2005, 253106.
- [148] D.R. Paul, L.M. Robeson, *Polymer*, 49, 2008, 3187-3204.

CHAPTER II: RESEARCH AIMS

The overall purpose of this research is to study the electrical, chemical, physical and thermal properties, as linked to their structure and morphology, of hybrid organic-inorganic materials for electrical devices. There were some intermediate objectives that we needed to meet in order to reach this goal.

The first part of our research consists of the synthesis and chemical, physical, thermal and morphological characterization of nanoparticles and nanotubes of different chemical composition, their structure and morphology to be utilized as filler for the production of conductive polymer composites (CPCs). A study of a number of different, and currently commercially available, one-dimensional (1D) nanostructured materials and two-dimensional (2D) nanostructured materials was also carried out in order to achieve our goals.

The purpose of the second part of this research is the production of two types of electrospun conductive polymers with good electrical properties. In particular, the production of materials of different chemical composition was identified as of the utmost importance. For this reason we used two different polymer blends but with similar electrical properties and conductivity mechanisms, two intrinsically conducting polymers (ICPs). This part of the research will focus on the optimization of instrumental and chemical parameters required in the electrospinning process used to produce morphologically uniform polymer fibers with no imperfections.

The purpose of the last part of this research is the production and study of electrospun conductive polymer composites (CPCs) using as filler the materials synthesized and analysed in the first part of this research within the electrospun polymer systems that were optimized during the second part of this research.

CHAPTER III: INSTRUMENTS AND CHEMICAL RAGENTS

3.1 Hydrothermal reactor

The reactor we used for the hydrothermal synthesis of stoichiometric chrysotile and anatase is a Parr model (Fig.2.1). The instrument has a reaction cell made of alloy steel which can withstand high pressures and high temperatures, with a capacity of 0.5 l. The reactor head locks into and hermetically seals the cell by teflon or graphite sealing gaskets and it also includes a pressure gauge, a thermocouple and a stirrer. These control instruments interface via a digital detector with an external heating mantle that can reach a temperature of 600°C.



Figure 3.1: Parr reactor

3.2 Electrospinning

The electrospinning system (Fig. 3.2) we used consists of a syringe connected to a steel needle with the inner diameter of 0.5 mm by means of a Teflon tube and placed inside a pump. We used a KD

Scientific 200-CE syringe pump which keeps a constant pressure on the polymer solution so that the liquid is extruded from the needle tip at a constant rate.

The needle is kept perpendicular to a metallic collector. The collector and the needle are connected to an electric field generator.

A Spellmann SL 150 high voltage generator with a maximum voltage output of 150 KV was used in this instance.

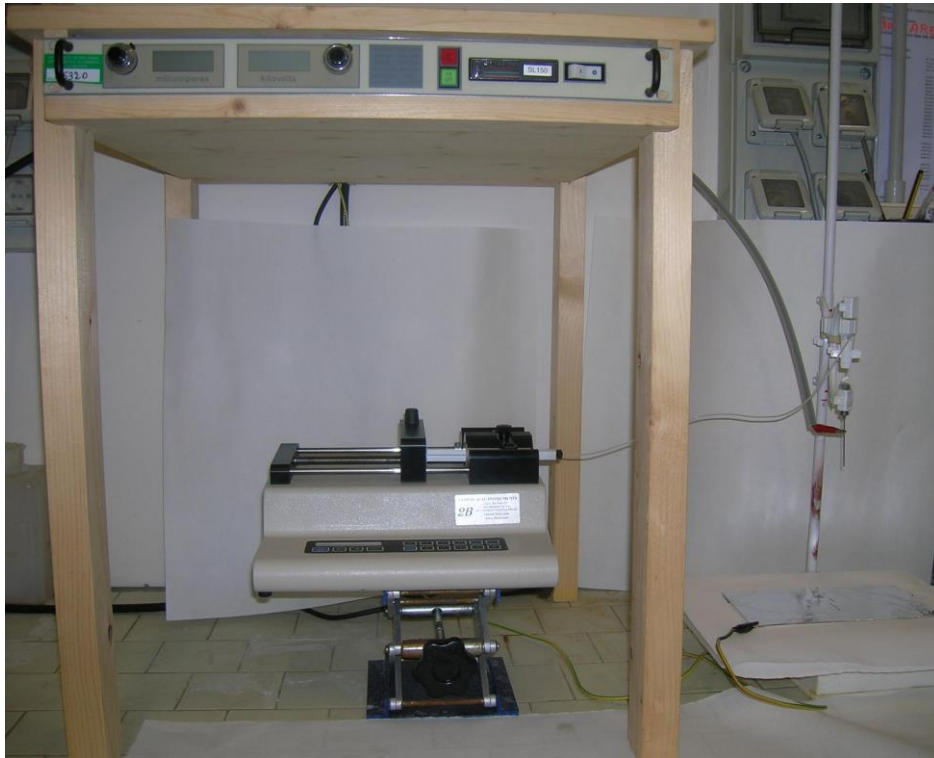


Figure 3.2: electrospinning apparatus

3.3 Scanning electron microscopy (SEM)

Scanning electron microscopy (Fig.3.3) provides morphological information on the surface of solids. This technique employs a beam of electrons, with energy between 1 and 50 KeV, highly focused and directed onto the sample. Typically the electron beam is emitted from a filament made of lanthanum hexaboride (LaB_6) and is composed of electrons called primary that will interact with the surface of the sample. Primary electrons give rise to two types of scattering:

- elastic scattering, where there is a variation of the propagation direction but with no noticeable energy variation. This is caused by an elastic collision with the nucleus of the atoms being bombarded;
- inelastic scattering, where there is an energy reduction without noticeable change in the propagation direction. This may be due to two distinct mechanisms: inelastic collision with the nucleus or inelastic collision against the electrons of the sample.

When inelastic collision occurs between primary electrons and the surface of the sample, secondary electrons are generated forming the image. Some backscattered electrons, which are those that penetrate below the surface of the sample, can produce more secondary electrons. The secondary electrons produced are transformed into an electrical signal, the intensity of which will depend on the sample's surface topography. By scanning a certain area of the sample with the primary electron beam, it is possible to form an image and enlarge it. The image is then displayed on a cathode ray tube. Resolution of the SEM depends on the size of the electron beam. Typically it will be approximately 5 nm.

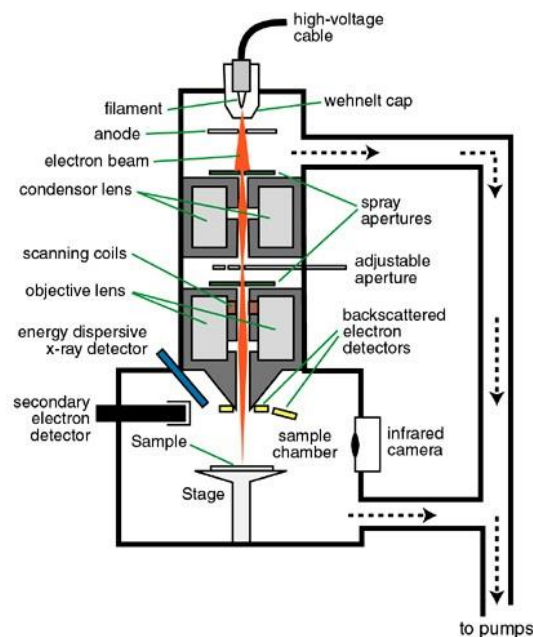


Figure 3.3: schematic model of a SEM

The SEM model we used is a Zeiss EVO MA 10 (Fig. 3.4).



Figure 3.4: SEM Zeiss EVO 10 MA

3.4 Energy dispersive X-ray spectroscopy (EDS)

Energy dispersive X-ray spectroscopy (EDS) is an analytical technique that provides qualitative and quantitative data derived from the interpretation of the X-ray spectrum emitted by a solid sample bombarded with a focused beam of electrons. Using this technique we can identify almost all of the chemical elements in the periodic table, those with an atomic number bigger than four. Qualitative data is obtained from the analysis of spectral lines; quantitative data is obtained from observation and analysis of spectral lines intensities. With EDS, a beam of X-rays or charged particles is focused in a punctiform manner into the sample being studied or into a portion of the sample. This technique is commonly used in association with scanning electron microscopy (SEM) and functions as its detector if applied in mapping mode.

EDS is based on the acceleration of a beam of electrons caused by an electric field. The beam strikes the sample and its interaction with this substance gives origin to signals (Fig. 3.5 – Fig. 3.6) that can be used to form EDS spectra.

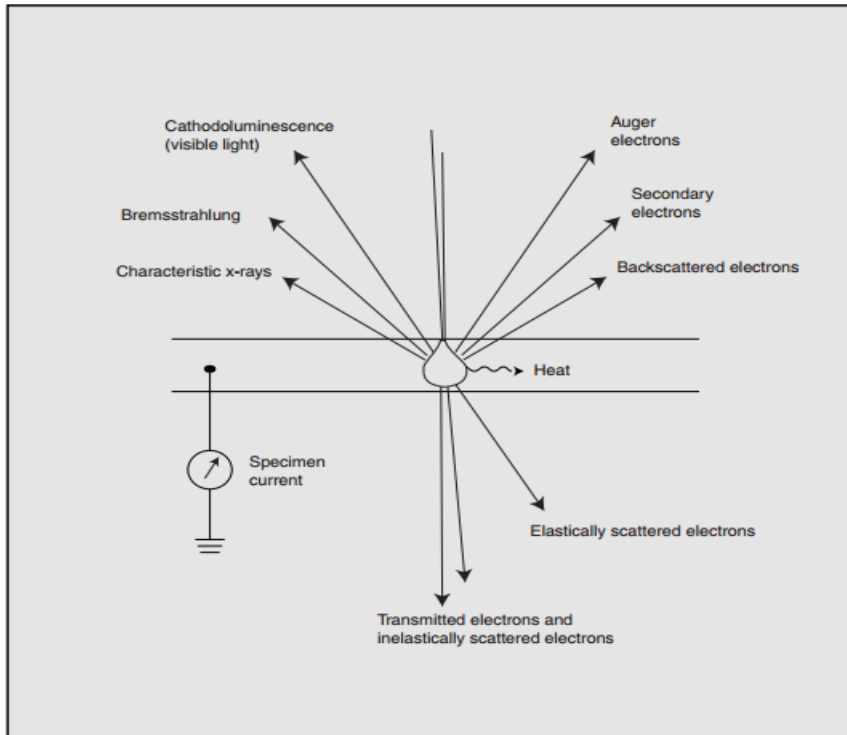


Figure 3.5: schematic model of the interaction between the electron beam and the sample

The volume of the part of the sample interacting with the beam is proportional to the energy of the incident beam. Every part of this area, depending on the depth from the surface, emits a different type of signal.

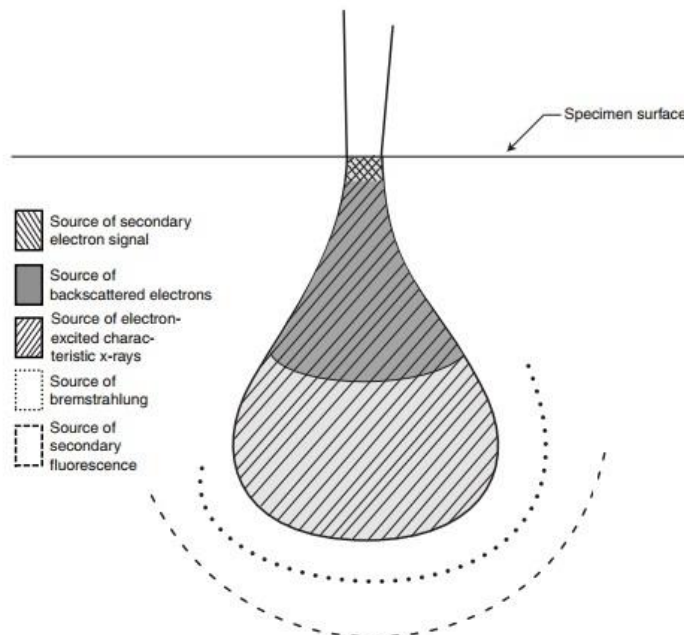


Figure 3.6: model of the different areas of electron-specimen interaction

EDS spectra are usually represented digitally as a graph with the x axis representing beams energy and the y axis expresses the counting ratio per channel (Fig. 3.7)

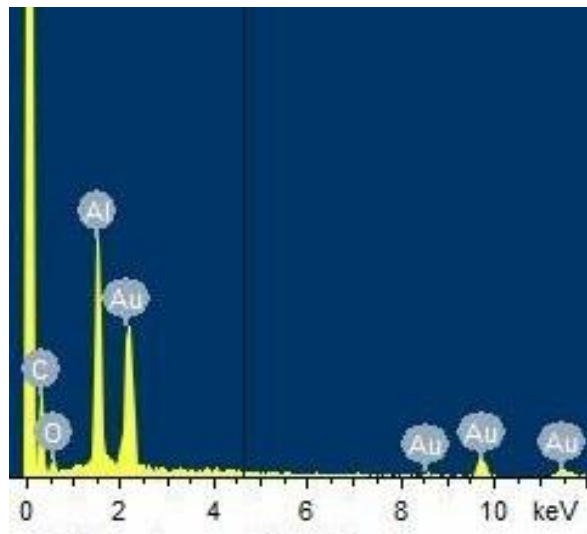


Figure 3.7: EDS spectrum

An EDS Oxford Inca x-act Energy 250 was used (Fig. 3.8).



Figure 3.8: EDS Oxford Inca x-act Energy 250

3.5 Transmission electron microscopy (TEM)

Transmission electron microscopy (TEM) is a microscopy technique that uses electromagnetic radiation emitted by electrons, as they have a small wavelength (smaller than that of photons). In transmission electron microscopy a beam of electrons is aimed at a sample using magnetic lenses. TEMs use high-energy electrons (200 KeV) which provide high-definition images ($< 10 \text{ \AA}$) focused onto a fluorescent screen or a layer of photographic film. In order to allow electrons to pass through, the specimen on the produced substance being analysed needs to be extremely thin, not thicker than 1 \mu m . TEMs allow the user to visualize the samples with a magnification up to 1,000,000 times and still produce high resolution images. This is 800 times bigger than the magnification allowed by the most powerful optical microscopes (1,200x). A carbon-coated copper mesh grid is used to hold the sample.

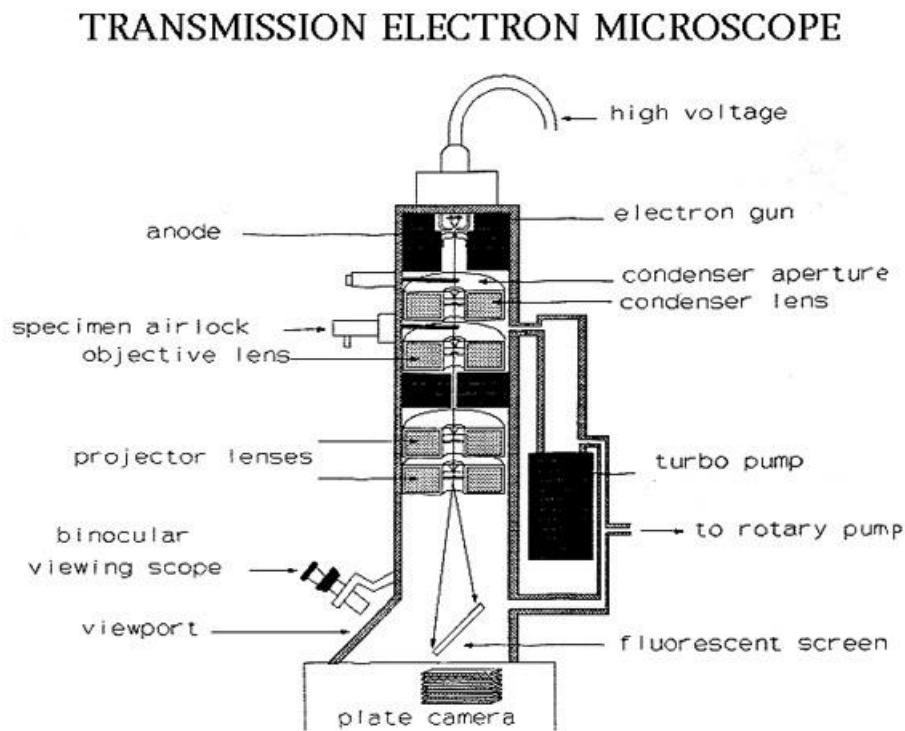


Figure 3.9: schematic model of a TEM

As per Fig. 3.9, TEMs include: high-voltage cable, electron gun, motors for centering the electron beam, condensers, sample holder, objective lens, projector lens, optical binoculars; fluorescent screen, vacuum pump leads, vacuum and magnification control. The intensity of the beam can be so high that samples being analysed can often be partially damaged.

TEMs are powerful instruments used to analyse the following characteristics:

- morphology: shape, size and position
- structure: the degree of atomic order and how atoms are arranged in the sample
- chemical composition: relationships between different compounds and elements

For all of the above, this technique is commonly used for the study of materials and their properties.

A Philips CM100 Transmission Electron Microscope operating at 100 KeV was used (Fig. 3.10).

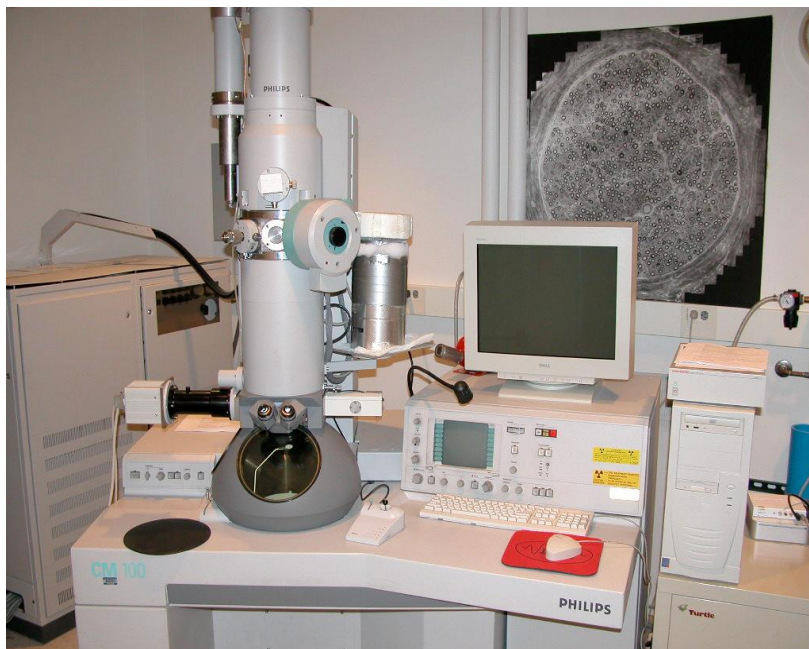


Figure 3.10: Philips CM100 Transmission Electron Microscope

3.6 Atomic force microscopy (AFM)

Atomic force microscopy is a high resolution imaging technique (on the order of fractions of a nanometer). It utilizes scanning probe technology and has 3D imaging capability.

An atomic force microscope (Fig. 3.11) consists of two parts: the first one controls the cantilever; the second one acquires morphological data and sends them to the computer for processing

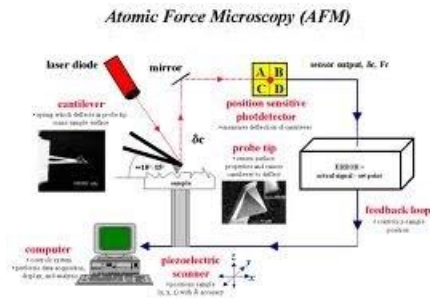


Figure 3.11: schematic model of an atomic force microscope's components

The mechanism that controls the cantilever is a piezoelectric tube scanner. It combines three independent piezoelectric electrodes for X, Y, and Z into a single tube. This tube forms the scanner, which can manipulate samples and probes with precision in three dimensions (Fig. 3.12). Movement range is a maximum of 150 μm in the x direction, 150 μm in the y directions and a few hundred micrometres in the z direction.

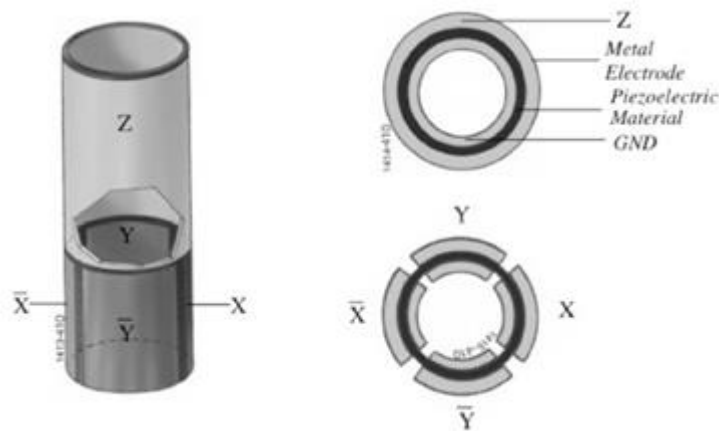


Figure 3.12: schematic model for piezoelectric electrodes for X, Y, and Z

The component tasked with acquiring morphological data uses a laser beam on the measurement probe scanning the sample surface (Fig. 3.13).

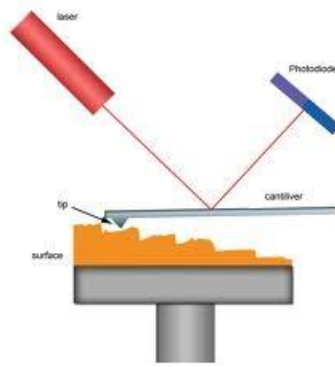


Figure 3.13: schematic model of data acquisition component:
laser, cantilever, photodiode and the sample located on the piezoelectric scanner

In analysing the 3D images obtained with this technology it is necessary to take into consideration the size of the cantilever tip (Fig. 3.14) as its degree of sensitivity will be inversely proportional to its radius of curvature.

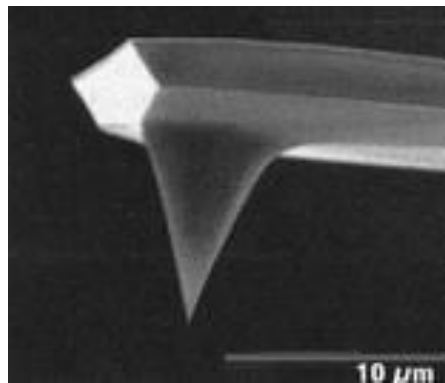


Figure 3.14: SEM image of AFM cantilever

The AFM used for this research was equipped with a silicon nitride cantilever, with a 10 nm curvature radius and a scanning range of 15 μm in the x direction and 15 μm in the y direction. The surface over which the sample is placed can be made of different materials. In this case a phyllosilicate mineral was used, mica.

The two primary modes of operation in AFM are contact mode and non-contact mode. Non-contact mode is where the tip of the cantilever does not contact the sample surface and instead oscillates at its resonant frequency. By measuring variations in resonance frequency of the cantilever a topographic image of the sample surface can be constructed.

With contact mode, morphological data are acquired by keeping the cantilever tip in contact with the sample. A third mode is intermittent contact or tapping mode where the cantilever is made to

oscillate up and down close to its resonance frequency. This technique allows us to detect the presence of materials with different composition in the sample surface as the cantilever tip interacts differently with different substances. Analysis of phase variations of the cantilever tip oscillating movement when it comes in contact with the sample will indicate if it possesses a higher or lower degree of affinity with the sample surface.

The AFM instrument used for this research work is a Nanoscope.

3.7 Fourier transform infrared spectroscopy (FT-IR)

Infrared spectroscopy is one of the most widely used spectroscopic techniques because it gives results quickly and the sample preparation is easy. This technique provides both quantitative and qualitative information about a given sample.

The infrared (IR) portion of the electromagnetic spectrum is where the radiation wavelength is between 700 nm and 1 mm. This kind of radiation carries energy quanta that can be absorbed and cause vibro-rotational transitions in the molecules. A molecule can absorb radiation when a transition takes place from a lower energy to a higher energy vibro-rotational state, that is when a variation of dipole moment between the two states occurs. The radiation wavelengths that a molecule can absorb depend on its atoms and the way they are bound together. The characteristic distribution of electromagnetic radiation absorbed by a particular molecule is a unique identifier.

For our IR analyses we used a Nicolet 380 FT-IR spectrometer (Fig. 3.15).



Figure 3.15: Nicolet 380 FT-IR spectrometer

Reflectance measurements can also be carried out by fitting a germanium attenuated total reflectance (ATR) head (Fig. 3.16).



Figure 3.16: Nicolet 380 ATR-FT-IR

3.8 X-ray diffraction (XRD)

X-rays are electromagnetic waves presenting wavelengths in the range of 0.01 to 10 nm. X-ray radiation is high energy and can be generated by decelerating charged particles (e.g. electrons). Diffraction occurs when a beam of X-rays hits a crystalline material and it diffracts into many specific directions. Diffraction is the result of the direction change of a wave whose wavelength is of the same order of magnitude as the diffracting object. This dimensional conformity between X-rays and the crystalline solid causes it to behave as diffraction grating.

Diffracted beams are affected by constructive or destructive interference. The interference is constructive when the wavelength of the incident wave (λ) and an angle (θ) between the incident ray and the crystal planes all conform to Bragg's Law:

$$n\lambda = 2d\sin\theta$$

where d is the spacing between adjacent crystal planes.

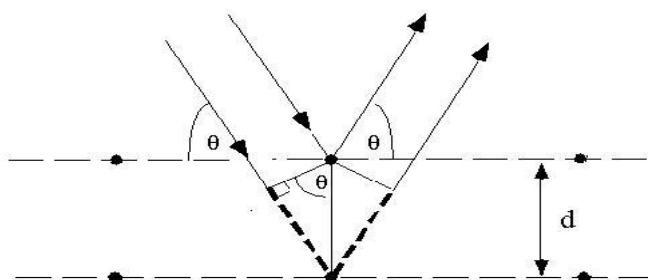


Figure 3.17: schematic diagram for X-ray diffraction between adjacent planes

X-ray diffraction is a technique used to carry out qualitative and quantitative analysis of crystals. Each crystal has a distinctive diffraction profile. These peaks can be found at an angle of 2θ and are distinctive for each compound.

A Philips 1050/81-PW1710 Powder Diffractometer (Fig. 3.18) was used. This instrument uses $\text{Cu K}\alpha$ radiation ($\lambda=1.5406 \text{ \AA}$), 40 kV working voltage and current equivalent to 40 mA. It has a graphite monochromator on which the diffracted beam is directed and a proportional counter. Scanning was carried out using a step angular value of 0.03° , 1 second per step.



Figure 3.18: Philips 1050/81-PW1710 Powder Diffractometer

3.9 Thermogravimetric analysis (TGA)

Thermal analysis studies the properties of materials (including physical properties and stability) as they change with temperature. Several methods are commonly used, amongst them thermogravimetric analysis (TGA), which determines selected characteristics of a material, by measuring mass change as a function of increasing temperature and in a specific atmosphere (Ar, N₂, O₂, air).

Mass loss or gain is the result of physical or chemical reactions that modify the nature of the compound, e.g. oxidation, reduction or the loss of volatiles present in the substance being analysed. This type of analysis provides useful information on the temperature range in which a certain material can be used and its possible degradation.

As a result of this analysis, a thermogram or thermal decomposition curve is obtained through which the weight percentage of each resulting mass change can be measured.

In this particular case we used the thermal analyser SDT Q600, which has a two arm balance: in one arm a 5-10 mg quantity of the sample is placed on an alumina plate. The second arm of the balance also has a plate but it remains empty and it functions as reference.

The microbalance component is located inside a furnace where both temperature and atmosphere can be controlled. The instrument is connected to a PC through which the scanning speed and temperature range are set.

In this particular case the parameters chosen are a constant heating rate of 10 °C/min and an inert gas atmosphere (N₂).



Figure 3.19: picture of a TA SDT Q600 instrument

3.10 Differential scanning calorimetry (DSC)

Differential scanning calorimetry (DSC) is a thermoanalytical technique which measures variations in heat capacity (C_p), which is the amount of energy a unit of matter of a given substance can hold, by changing its temperature. A sample is heated or cooled and changes in heat capacity are monitored as changes in the heat flow. This allows the detection of transitions like melts, glass transitions and phase changes. DSC is a thermal characterization used for a large number of materials but is used widely for examining polymeric materials. DSC is a technique that is both fast and easy to use.

DSC measures the amount of heat which is released or absorbed in greater or smaller measure by the sample on the basis of a temperature difference between the sample and the reference material. There are two different types of DSCs: heat-flux DSC and power-compensated DSC. In heat-flux DSC, the sample, located in an enclosed pan, is placed next to an empty reference pan on a thermoelectric disk inside a furnace (Fig. 3.20).

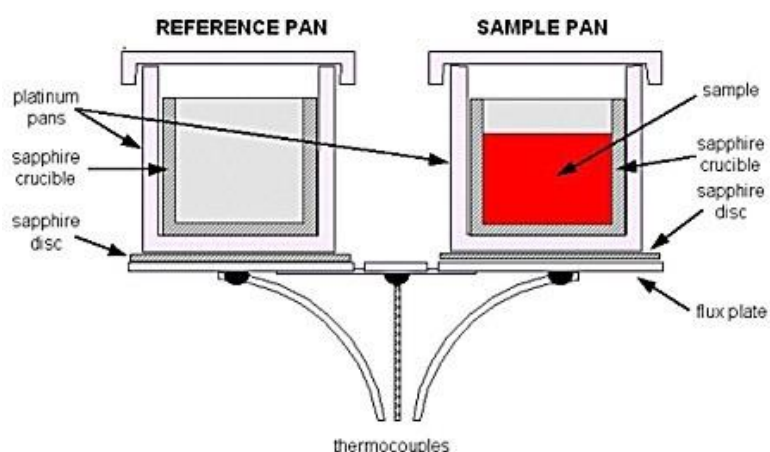


Figure 3.20: model for the thermocouples to be located inside the furnace of a heat-flux DSC

A controlled increase in temperature within the furnace is carried out. Heat flows from the thermoelectric disk to the sample and the reference. Both the sample and the reference are heated at a pre-determined speed. Due to the different C_p the sample and the reference will have a different temperature. The difference between the temperature of the sample and that of the reference is measured using thermocouples. Energy is introduced simultaneously in the sample holder and in the reference holder. Both their temperatures are monitored. The difference between the energy input required to ensure that the sample temperature and the reference temperature remain the same

is the amount of heat absorbed or released by molecules of the sample being analysed. The presence of the sample molecules will require more energy in order to bring the sample temperature to be the same as the reference temperature. Measuring this excess energy will provide information on C_p and other thermal characteristic of the sample.

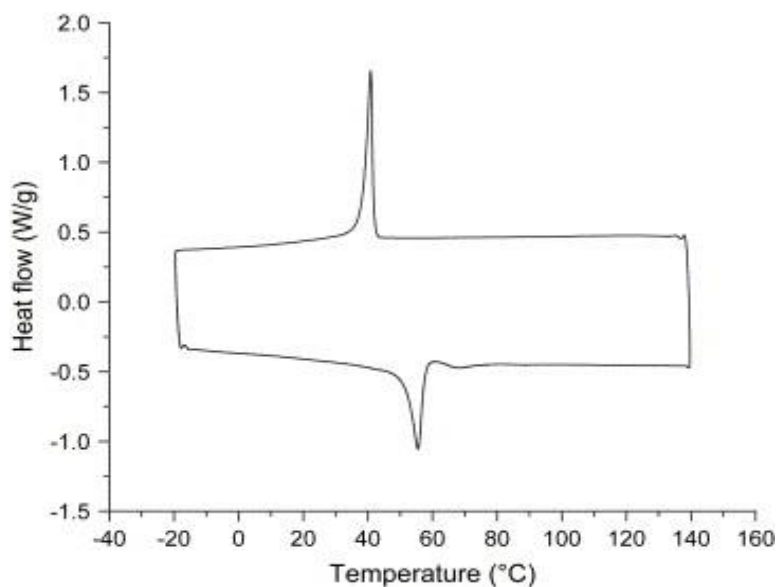


Figure 3.21: DSC curve for polymer

Melting points and glass transition temperatures are an example of the extremely useful information that can be obtained using DSC in polymer science.

The apparatus we used is a DSC TA Instruments 2920 (Fig. 3.22).



Figure 3.22: DSC TA Instruments 2920

3.11 Ultraviolet and visible spectroscopy (UV-Vis)

UV-Vis absorption spectroscopy is an electronic spectroscopy which utilizes electromagnetic waves between 100 nm and 750 nm in length.

A Varian Cary 300 Bio UV-Vis Bio Spectrophotometer was used (Fig. 3.23).



Figure 3.23: Varian Cary 300 Bio UV-Vis Bio Spectrophotometer

This is a double beam spectrophotometer, capable of wavelength calculation with a margin of error of $\pm 2\text{nm}$. The device comprises of: a light source (deuterium lamp for UV and incandescent lamp for Vis); monochromator; optical filter; chopper; sample; blank solution; calibration system; phototube; computer.

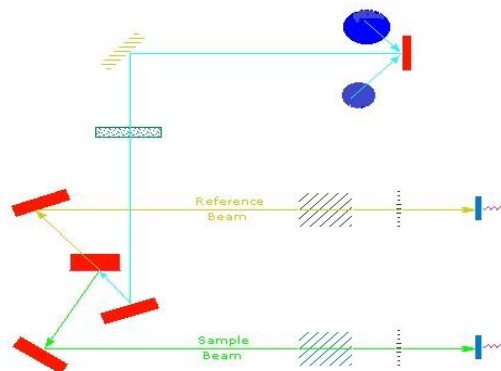


Figure 3.24: block diagram of a UV-Vis spectrophotometer

It uses quartz cuvettes which are 2 cm in length and have opaque sides to minimize scattering.

The spectrophotometer will produce spectra which are a graphic representation of the level of absorbance for the sample in question, as a function of the light source.

Lambert–Beer law $A = \epsilon c l$

Where ϵ represents molar absorptivity, l is the pathlength through the sample and c is the concentration of the substance being analysed.

3.12 Four-Point Probe method of conductivity measurement

Conductivity measurements of electrospun polymeric mats were obtained starting from the experimental values of electrical resistance of a given substance.

Resistance was measured using a digital teraohmmeter connected to 4 platinum filaments.

A teraohmmeter is an instrument that uses a four-point probe to scan the flow of electrical current between two given points on the surface of a material and measures the corresponding electrical potential within. The teraohmmeter measures the polymeric film resistance (R) using a I-V scan.

The probes in question are four platinum filaments, flattened and laid parallel to each other on a slide. They form a rectangle measuring 0.5 cm^2 in surface, with each platinum filament laid at 0.33 cm from the next. The instrument performs a I-V scan, forcing an electrical current between the 2 external probes and measuring the resulting electrical field that forms between the other 2 probes (Fig. 3.25).

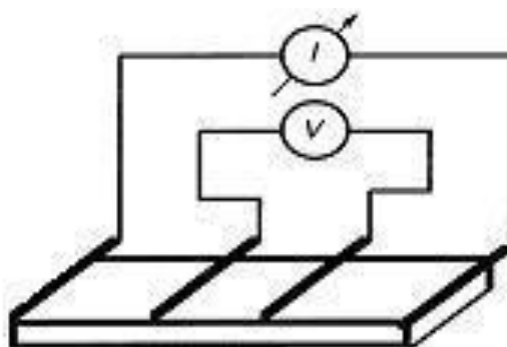


Figure 3.25: model for a four-point probe method of conductivity measurement

The teraohmmeter used is an AlphaLab 11300.

3.13 Chemical reagents and solvents

Analytical grade magnesium chloride hexahydrate ($\text{MgCl}_2 \cdot 6\text{H}_2\text{O}$ Riedel-de-Haen), sodium hydroxide (NaOH, Aldrich), poly(ethylene oxide) (PEO, average MW= 900000, Sigma-Aldrich), polyaniline emeraldine base (PANI, average MW= 65000, Sigma-Aldrich), (\pm)-10-camphorsulfonic acid (HCSA, Fluka), silicon dioxide (SiO_2 , Aerosil380 Degussa), copper(II) chloride dihydrate ($\text{CuCl}_2 \cdot 2\text{H}_2\text{O}$, Aldrich), silver nitrate (AgNO_3 Sigma-Aldrich), chloroauric acid (HAuCl_4 , Aldrich), 1-butanethiol (BuSH - $\text{C}_4\text{H}_{10}\text{S}$, Aldrich), titanium tetrachloride (TiCl_4 , Fluka), L-ascorbic acid ($\text{C}_6\text{H}_8\text{O}_6$, Sigma), lithium chloride (LiCl , Sigma-Aldrich), sodium bromide (NaBr, Sigma-Aldrich), potassium bromide (KBr, Aldrich), sodium chloride (NaCl, Sigma-Aldrich), tetraoctylammonium bromide TOABr ($\text{C}_{32}\text{H}_{68}\text{NBr}$, Sigma), 4-methylbenzenethiol (MTB - $\text{C}_7\text{H}_7\text{SH}$, Aldrich), sodium sulfate anhydrous (Na_2SO_4 , Sigma), sodium borohydride (NaBH_4 , Aldrich), graphene oxide (GO, Single Layered Graphene Oxide, Cheap Tubes Inc), multi-wall carbon nanotubes (MWCNT, Nanocyl 3100), chloroform (CHCl_3 , Sigma-Aldrich), toluene (C_7H_8 , Sigma-Aldrich), methanol (MeOH - CH_3OH , Sigma-Aldrich), ethanol (EtOH - $\text{C}_2\text{H}_5\text{OH}$, Sigma-Aldrich), dichloromethane (CH_2Cl_2 , Sigma-Aldrich), tetrahydrofuran ($\text{C}_4\text{H}_8\text{O}$, Sigma), diethylene glycol dimethyl ether (diglyme - $\text{C}_6\text{H}_{14}\text{O}_3$, Fluka) diethyl ether ($\text{C}_4\text{H}_{10}\text{O}$, Sigma-Aldrich) were used without further purification.

Regioregular poly(3-hexylthiophene) (P3HT) was synthesized by Prof.M.Lanzi.

Water was deionized using a Milli-Q Ultra-Pure-Water Purification 10 System (18.50 M Ω).
Acqua milliQ H₂O 18 M Ω .

CHAPTER IV: EXPERIMENTAL

4.1 Synthesis of chrysotile nanotubes

The procedure used for the synthesis of chrysotile is as follows: 21.75 g (0.107 moles) of magnesium chloride hexahydrate ($\text{MgCl}_2 \cdot 6\text{H}_2\text{O}$) were added to 4.40 g (0.073 moles) of amorphous silica (SiO_2). The two reactants were used in stoichiometric amounts, so that the ratio of silicon to magnesium is 2:3. In addition to the reactants, 240 ml of aqueous solution of sodium hydroxide (6.95 g of NaOH in 240 ml of water) were added to form a suspension whose pH is 10.40. We then added a solution of sodium hydroxide 5 M in water to bring the pH to 12.70. The sol was subjected to vigorous stirring for 1 hour. The suspension was placed in the hydrothermal reactor for hydrothermal synthesis (capacity of 0.5 l), it was brought to a temperature of 300 °C (the reactor equilibrium pressure is 82 bar) and it was left for 24 hours. The product obtained was filtered, washed with distilled water and freeze-dried.

4.2 Synthesis of nanoparticles

4.2.1 Synthesis of 1-butanethiol capped silver nanoparticles

Silver nanoparticles were synthesized in solution with a biphasic reaction, using a procedure developed in our laboratory. The entire reaction was done in an inert atmosphere under a stream of N_2 to prevent oxidation of the metal and at room temperature. 104 mg of silver nitrate (0.00612 moles) were dissolved in 10 ml of water in a reaction flask. We subsequently added 642 mg of tetraoctylammonium bromide (TOABr) in 20 ml of toluene, keeping the molar ratio of Ag to TOABr as 1:2 and left the reaction mixture to be vigorously stirred for 1 hour, after which 120 μl of 1-butanethiol (BuSH) were added to the flask content. The molar ratio of silver and 1-butanethiol was kept as 1:2. At this stage the colloidal suspension was a greenish-grey colour. After 20 minutes stirring, we started to drip a solution of 230 mg of sodium borohydride in 20 ml of water for approximately 10 seconds. During the adding process of the reducing solution the colour of the mixture slowly changed from yellow to brown and finally to black. The molar ratio of silver and sodium borohydride was kept as 1:10, in line with the existing literature. The reaction mixture was

then kept at room temperature and stirred vigorously for approximately 3 hours. Then the aqueous phase was removed using a separatory funnel and the toluene was removed under vacuum, thus obtaining a black solid substance which was subsequently taken up in cold methanol and repeatedly washed with the same solvent. Part of the silver nanoparticles were preserved in ethanol suspension at 5 °C, the remainder were lyophilized.

4.2.2 Synthesis of 4-methylbenzenethiol capped silver nanoparticles

The 4-methylbenzenethiol (MBT) capped silver nanoparticles were produced by chemical reduction of silver salt in biphasic reaction in an inert atmosphere (N₂) so as to avoid unwanted oxidation of the metal. 163 mg (1 mmol) of silver nitrate were dissolved in 25 mL of water in a 250 mL flask. Potassium bromide aqueous solution was then added (235 mg, 2 mmol in 10 mL of water) working under magnetic stirring. A solution of 1639 mg of tetraoctylammonium bromide (3.0 mmol) in 20mL of toluene was added after 10 minutes of stirring. [AgBr₂]⁻ [TOA]⁺, which was created by the biphasic reaction, tends to move into the organic phase. A solution of 4-methylbenzenethiol (150 mg - 1.2 mmol) in 30 mL of toluene is subsequently added and the mixture is stirred vigorously for 5 minutes. A solution of 379.9 mg of sodium borohydride (10mmol) is then slowly dripped in 15 mL of water. The reduction of the silver causes the suspension to change from transparent to yellow to brown to black.

The reduction reaction was shaken vigorously for about 2 hours. The shaking was then stopped and the aqueous phase was separated from the organic phase containing the capped nanoparticles. The organic phase was washed 3-4 times with plenty of water so as to eliminate impurities then dried with sodium sulfate anhydrous, filtered and taken to the rotary evaporator to remove the excess solvent. The product, dark oil, is dripped into 80 ml of methanol previously cooled. The suspension was washed 3 times with methanol by centrifugation at 6000 rpm. Part of the precipitate is then lyophilized and part is suspended in dichloromethane.

4.2.3 Synthesis of silver nanoparticles

Part of the capped silver nanoparticles were heat-treated in an inert atmosphere (N_2) reaching a temperature of 300 °C using a TGA instrument. Uncapped nanoparticles were kept in an inert atmosphere.

4.2.4 Synthesis of 1-butanethiol capped copper nanoparticles

The synthesis of 1-butanethiol capped copper nanoparticles was carried out in an inert atmosphere (N_2) with a monophasic reaction. A solution of 1-butanethiol (0.33 ml – 3.1 mmol) in 30 ml of tetrahydrofuran (THF) was placed in a flask. We then added a solution with 172 mg of copper(II) chloride dihydrate (1.0 mmol) in 10 ml di tetrahydrofuran. A suspension of lithium chloride (639 mg - 15 mmol) and sodium borohydride (371 mg - 10 mmol) in 15 ml of diethylene glycol dimethyl ether was subsequently dripped into the solution. The suspension, brown in colour, was stirred vigorously for 1 hour. Subsequently, the organic phase was extracted with 150 ml of diethyl ether and washed with a sodium chloride concentrated saline solution. The suspension was vacuum filtered and then the solvent was allowed to evaporate. The nanoparticles were kept in an ethanol suspension and part of them was lyophilised.

4.2.5 Synthesis of 4-methylbenzenethiol capped copper nanoparticles

4-methylbenzenethiol capped copper nanoparticles were obtained from a reduction of a copper sulphate in biphasic reaction in an inert atmosphere of N_2 .

169 mg (1.0 mmol) of copper(II) chloride dihydrate were dissolved in 20 mL of water placed in a 250 mL flask. We then added an aqueous solution of potassium bromide (240 mg, 2 mmol in 10 mL of water) working under magnetic stirring. After a few minutes stirring, we added a solution of 2200 mg of tetraoctylammonium bromide (4.0 mmol) in 20 mL of dichloromethane, followed by 154 mg of 4-methylbenzenethiol (approximately 1.2 mmol in 30 mL of dichloromethane). The mixture was stirred vigorously for 5 minutes. Subsequently, a solution of 382.7 mg of sodium borohydride (10 mmol) in 15 mL of water was dripped into the mixture. The organic phase became progressively darker, while in the aqueous phase it became transparent.

The suspension was stirred vigorously for 2 hours then the aqueous phase separated from the organic phase which containing the capped nanoparticles. The organic phase was washed 2-3 times with plenty of water to eliminate impurities then dried with sodium sulfate anhydrous, filtered and taken to the rotary evaporator to remove the excess solvent.

The product looked like a dark oil and was dripped into 80 ml of methanol previously cooled. The suspension was washed 5 times with methanol by centrifugation at 6000 rpm. Part of the precipitate was then lyophilized and part of it suspended in dichloromethane.

4.2.6 Synthesis of copper nanoparticles

Part of the capped copper nanoparticles were heat-treated in an inert atmosphere (N_2) reaching a temperature of 300 °C using a TGA instrument. Uncapped nanoparticles were kept in an inert atmosphere.

4.2.7 Synthesis of 4-methylbenzenethiol capped gold nanoparticles

4-methylbenzenethiol capped gold nanoparticles were obtained from a reduction of chloroauric acid reaction. 342 μ L (0.5 mmol) of chloroauric acid ($HAuCl_4$) were dissolved in 20 mL of water in a 250 mL flask. We added an aqueous solution with potassium bromide (120 mg, 1 mmol in 10 mL of water) under magnetic stirring. In this instance the solution is added to keep conditions constant and not to simplify the reduction of the metal.

The mixture was stirred vigorously for a few minutes, then a solution of 548 mg tetraoctylammonium bromide (1.0 mmol) in 20 mL of toluene was added. $[AuBr_4]^- [TOA]^+$ resulting from this reaction moved into the organic phase, where a reduction occurred at a later stage. The biphasic suspension at this stage appeared reddish in colour. A capping agent was subsequently added in the form of 76.6 mg of 4-methylbenzenethiol, approximately 1.2 mmol, in 30 mL of toluene, the mixture was stirred vigorously for 5 minutes. The suspension colour turned orange. A solution of 192 mg of sodium borohydride (approximately 5 mmol) in 15 mL of water was dripped into the mixture. The suspension colour turned from orange to brown to black.

The suspension was stirred vigorously for 2 hours. The aqueous phase was separated from the organic phase which contained the capped nanoparticles. The organic phase was washed 3-4 times

with plenty of water to eliminate impurities then dried with sodium sulfate anhydrous, filtered and dried further using a rotary evaporator.

The product, dark oil, was dripped into 80 ml of methanol previously cooled. The suspension was washed 3 times with methanol by centrifugation at 6000 rpm. Part of the precipitate was then lyophilized and part was suspended in dichloromethane.

4.2.8 Synthesis of 4-methylbenzenethiol capped gold-silver 1:4 nanoparticles

4-methylbenzenethiol capped gold-silver 1:4 nanoparticles were obtained from a reduction of chloroauric acid reaction with silver nitrate with a 1:4 molar ratio in a biphasic reaction.

67.5 mg (0.4 mmol) of silver nitrate (AgNO_3) and 69.1 μL (0.1 mmol) of chloroauric acid (HAuCl_4) were dissolved in 20 mL of water in a 250 mL flask. We added a solution of potassium bromide (119 mg, 1 mmol) in 10 mL of water under magnetic stirring. The suspension colour appeared to be yellowish at this stage.

After 5 minutes stirring, a solution of 547 mg of tetraoctylammonium bromide (1.0 mmol) in 20 mL of toluene was added. The suspension at this stage was biphasic and the colour turned a lighter shade of yellow. A capping solution was subsequently added (76.5 mg of 4-methylbenzenethiol, approximately 1.2 mmol, in 30 mL of toluene). The solution was stirred vigorously for 5 minutes and the suspension became transparent. Then the suspension was dripped into a solution of 192.0 mg of sodium borohydride (5 mmol) in 15 mL of water to eliminate impurities. At this stage the suspension colour turned from transparent to brown to black.

The reduction reaction was stirred vigorously for 2 hours. The aqueous phase was then separated from the organic phase which contained the capped nanoparticles. The organic phase was washed 2-3 times with plenty of water to eliminate impurities then dried with anhydrous sodium sulfate anhydrous, filtered and taken to the rotary evaporator to remove the excessive solvent.

The product (dark oil) was dripped into 80 ml of methanol previously cooled. The suspension was washed 3 times with methanol by centrifugation at 6000 rpm. Part of the precipitate was then lyophilized and part was suspended in dichloromethane.

4.2.9 Synthesis of 4-methylbenzenethiol capped gold-silver 4:1 nanoparticles

4-methylbenzenethiol (MBT) capped gold-silver 4:1 nanoparticles were obtained from a reduction of chloroauric acid reaction with silver nitrate with a 1:4 molar ratio in a biphasic reaction in an inert atmosphere (N_2).

16.9 mg (0.1 mmol) of silver nitrate ($AgNO_3$) and 276 μL (0.4 mmol) of chloroauric acid ($HAuCl_4$) were dissolved in 20 mL of water in a 250 mL flask. We added an aqueous solution of potassium bromide (119 mg, 1 mmol) in 10 mL of water and left it under magnetic stirring for approximately 5 minutes. At this stage the suspension was yellowish in colour. A solution of 551 mg of tetraoctylammonium bromide (1.0 mmol) in 20 mL of toluene was added. The biphasic suspension turned dark red. Then a solution of capping agent (76.5 mg – 1.2 mmol of 4-methylbenzenethiol, in 30 mL of toluene) was added and stirred vigorously for 5 minutes. The suspension became transparent. Subsequently it was slowly dripped into a solution of 191.8 mg of sodium borohydride (5 mmol) in 15 mL of water. The suspension colour turned from transparent to brown to black.

The suspension was stirred vigorously for approximately 2 hours. The aqueous phase was then separated from the organic one which contained the capped nanoparticles. The organic phase was washed 2-3 times with plenty of water to eliminate impurities then dried with sodium sulfate anhydrous, filtered and taken to the rotary evaporator to remove the excessive solvent.

The product (dark oil) was dripped into 80 mL of methanol previously cooled. The suspension was washed 4 times with methanol by centrifugation at 6000 rpm. Part of the precipitate was then lyophilized and part was suspended in dichloromethane.

4.2.10 Synthesis of 1-butanethiol capped silver-copper 1:1 nanoparticles

The synthesis of 1-butanethiol capped silver-copper 1:1 nanoparticles was carried out with a biphasic reaction in an inert atmosphere (N_2).

A solution of 250.3 mg (2.4 mmol) of sodium bromide in 30 mL of water was placed in a flask. We added an equimolar amount of silver nitrate ($AgNO_3$) (85.3 mg – 0.50 mmol) and copper(II) chloride dihydrate ($CuCl_2 \cdot 2H_2O$) (85.4 mg 0.50 mmol). We then added a solution with 995 mg (1.85 mmol) of tetraoctylammonium bromide (TOABr) in 20 mL of toluene. The mixture was stirred for 30 minutes, after which a solution of 0.33 mL (3.1 mmol) of 1-butanethiol (BuSH) in 30 mL of

toluene. The organic phase was separated from the aqueous phase using a separatory funnel and in an N₂ atmosphere a solution of 380.8mg (10 mmol) of sodium borohydride in 15 ml of H₂O was added. The suspension was stirred for 3 hours. Subsequently the organic phase was separated from the aqueous phase and the excessive solvent was allowed to evaporate using a rotary evaporator. The resulting nanoparticles were rinsed abundantly with methanol and kept in a methanol suspension. Part of them was lyophilised and kept in an inert atmosphere.

4.2.11 Synthesis of silver-copper 1:1 nanoparticles

Part of the capped silver-copper 1:1 nanoparticles were heat-treated in an inert atmosphere (N₂) reaching a temperature of 300 °C using a TGA instrument. Heat treatment, carried out in an inert atmosphere so as to prevent oxidation, helps eliminate the capping protective layer that covers the metal core. The nanoparticles were kept in an inert atmosphere.

4.2.12 Synthesis of anatase nanoparticles

The synthesis of anatase (TiO₂) nanoparticles was achieved through a hydrothermal reaction. A aqueous solution of sodium hydroxide (NaOH 3.54 g - 0.089 mol in 100ml) was placed in a three neck reaction flask and under an inert N₂ atmosphere. 2.5 ml (0.023 mol) of titanium tetrachloride was added slowly using an addition funnel. The resulting sol was stirred for 30 minutes. The suspension was placed in the hydrothermal reactor reactor and heated to a temperature of 230 °C (pressure inside the reactor is 23 bar) under constant stirring for 2 hours. The solid obtained was washed with bidistilled water and lyophilized to dryness.

4.2.13 Synthesis of copper (I) chloride nanoparticles

A solution of L-ascorbic acid (8.8106 g; 0.05 moles) in 70 ml of water was dripped into a flask containing a solution of copper (II) chloride dihydrate (CuCl₂*2H₂O) (17.057 g; 0.10 moles) in 50 ml water. The colloidal precipitate, white in colour, was stirred for half an hour. It was subsequently

centrifuged and washed with water, methanol and diethyl ether. The solid obtained was lyophilized to dryness.

4.3 Preparation of inorganic nanostructured composites

A suspension was prepared with 50 mg of chrysotile nanotubes previously synthesized and ground in an agate mortar with 10ml of dichloromethane. The suspension was sonicated twice for one second in order to separate the aggregates without damaging the inorganic nanotubes. The suspension is stirred for 24 hours. The excessive solvent was then eliminated leaving a small amount of liquid above the solid phase.

Then a suspension was prepared with 10 mg of metal nanoparticles previously synthesized in dichloromethane. The suspension was sonicated for 5 minutes to separate the aggregates and it was centrifuged at 10,000 rpm for 15 minutes. 7 mg of the metal nanoparticle suspension were added to the nanotubes, taking care to gather the material from the upper layers containing only nanoparticles of smaller size as it is necessary that the nanoparticles have a diameter smaller than 7 nm. The mixture was sonicated for 2-3 seconds and then kept at 5 °C for a week.

With this procedure we prepared the following types of materials:

- chrysotile nanotubes and 1-butanethiol capped copper nanoparticles system
- chrysotile nanotubes and 4-methylbenzenethiol capped copper nanoparticles system
- chrysotile nanotubes and 4-methylbenzenethiol capped gold nanoparticle system
- chrysotile nanotubes and 4-methylbenzenethiol capped gold-silver 1:4 nanoparticles system
- chrysotile nanotubes and 4-methylbenzenethiol capped gold-silver 4:1 nanoparticles system
- chrysotile nanotubes and 1-butanethiol capped silver nanoparticles system
- chrysotile nanotubes and 4-methylbenzenethiol capped silver nanoparticles system

4.4 Electrospun conductive polymer fibers

4.4.1 Electrospun polyaniline (PANI) fibers

We prepared a solution of polyaniline emeraldine base (500 mg) and of (\pm)-(10)-camphorsulfonic acid (645 mg) in 50 ml of chloroform. The solution was centrifuged at 500 rpm for 5 minutes. 500mg of poly(ethylene oxide) (PEO) were then added to the supernatant liquid. The solution was stirred for 24 hours then centrifuged at 500 rpm for 5 minutes. The supernatant liquid was kept at +5 °C.

This solution is used to obtain PANI mats and yarns and as basic solution for certain types of nanocomposites.

4.4.1.1 Electrospun polyaniline (PANI) mat

We filled a glass syringe with 2 ml of the above polymer solution. The syringe was placed in the electrospinning apparatus pump. The collector and the needle were connected to the electric field generator. When the electric field was applied, the pump was activated to start the electrospinning process. The mat of nonwoven fabric was placed on the glass slide located at the centre of the grounded collector.

The following instrumental parameters were used:

- Electrical potential difference: 8 KV
- Distance collector-needle: 15 cm
- Rate: 1.0 ml/h

4.4.1.2 Electrospun polyaniline (PANI) yarn

We filled a glass syringe with 2 ml of the above polymer solution. The syringe was placed in the electrospinning apparatus pump. The collector and the needle were connected to the electric field generator. When the electric field was applied, the pump was activated to start the electrospinning process. The polymeric yarn was placed between the two ends of a rotating grounded collector.

The following instrumental parameters were used:

- Electrical potential difference: 8 KV
- Distance collector-needle: 15 cm
- Rate: 1.0 ml/h
- Rotation speed of collector: 200 rpm

4.4.2 Electrospun poly(3-hexylthiophene) (P3HT) fibers

First we prepared a solution of poly(3-hexylthiophene) (200 mg) in 10 ml of chloroform. The solution was stirred for 24 h at 50 °C. It was then centrifuged at 500 rpm for 5 minutes. Then 200mg of poly(ethylene oxide) were added to the supernatant liquid. The solution was stirred again for 24 h at 50 °C, and then centrifuged at 500 rpm for 5 minutes.

We filled a glass syringe with 2ml of the above polymer solution. The syringe was placed in the electrospinning apparatus pump. The collector and the needle were connected to the electric field generator. When the electric field was applied, the pump was activated to start the electrospinning process. The mat of nonwoven fabric was placed on the glass slide located at the centre of the grounded collector.

The following instrumental parameters were used:

- Electrical potential difference: 19.5 KV
- Distance collector-needle: 18 cm
- Rate: 0.5 ml/h

4.5 Electrospun conductive polymer composite fibers

Polyaniline (PANI) composites were prepared by the following method:

5.0mg of nanostructured material were added to 2 ml of the PANI solution in chloroform previously prepared in order to obtain a composite with an amount of filler equivalent to 7.06% of the total hybrid system mass.

This suspension was sonicated for 1 minute (5 seconds in chrysotile system) and stirred for 30 minutes.

4.5.1 Electrospun polyaniline (PANI) and 4-methylbenzenethiol capped silver nanoparticles fibers

Electrospinning of this suspension was carried out using the following instrumental parameters:

- Electrical potential difference: 8.0 KV
- Distance collector-needle: 7.0 cm
- Rate: 1.0 ml/h

4.5.2 Electrospun polyaniline (PANI) and 1-butanethiol capped copper nanoparticles fibers

Electrospinning of this suspension was carried out using the following instrumental parameters:

- Electrical potential difference: 8.0 KV
- Distance collector-needle: 5.0 cm
- Rate: 1.0 ml/h

4.5.3 Electrospun polyaniline (PANI) and copper nanoparticles fibers

Electrospinning of this suspension was carried out using the following instrumental parameters:

- Electrical potential difference: 8 KV
- Distance collector-needle: 15 cm
- Rate: 1.0 ml/h

4.5.4 Electrospun polyaniline (PANI) and 4-methylbenzenethiol capped gold nanoparticles fibers

Electrospinning of this suspension was carried out using the following instrumental parameters:

- Electrical potential difference: 8 KV

- Distance collector-needle: 15 cm
- Rate: 0.5 ml/h

4.5.5 Electrospun polyaniline (PANI) and 4-methylbenzenethiol capped gold-silver 1:4 nanoparticles fibers

Electrospinning of this suspension was carried out using the following instrumental parameters:

- Electrical potential difference: 7.0 KV
- Distance collector-needle: 10.0 cm
- Rate: 1.0 ml/h

4.5.6 Electrospun polyaniline (PANI) and 4-methylbenzenethiol capped gold-silver 4:1 nanoparticles fibers

Electrospinning of this suspension was carried out using the following instrumental parameters:

- Electrical potential difference: 7.0 KV
- Distance collector-needle: 10.0 cm
- Rate: 1.0 ml/h

4.5.7 Electrospun polyaniline (PANI) and 1-butanethiol capped silver-copper 1:1 nanoparticles fibers

Electrospinning of this suspension was carried out using the following instrumental parameters:

- Electrical potential difference: 8.0 KV
- Distance collector-needle: 7.0 cm
- Rate: 1.0 ml/h

4.5.8 Electrospun polyaniline (PANI) and silver-copper 1:1 nanoparticles fibers

Electrospinning of this suspension was carried out using the following instrumental parameters:

- Electrical potential difference: 7.5 KV
- Distance collector-needle: 10.0 cm
- Rate: 1.0 ml/h

4.5.9 Electrospun polyaniline (PANI) and anatase nanoparticles fibers

Electrospinning of this suspension was carried out using the following instrumental parameters:

- Electrical potential difference: 8,0 KV
- Distance collector-needle: 10,0 cm
- Rate: 1,0 ml/h

4.5.10 Electrospun polyaniline (PANI) and copper (I) chloride nanoparticles fibers

Electrospinning of this suspension was carried out using the following instrumental parameters:

- Electrical potential difference: 8.0 KV
- Distance collector-needle: 9.0 cm
- Rate: 1.0 ml/h

4.5.11 Electrospun polyaniline (PANI) and chrysotile nanotubes 1-butanthiol capped copper nanoparticles system fibers

This suspension was sonicated for 1 minute and stirred for 30 minutes.

Electrospinning of this suspension was carried out using the following instrumental parameters:

- Electrical potential difference: 8.5 KV
- Distance collector-needle: 10.0 cm
- Rate: 1.0 ml/h

4.5.12 Electrospun polyaniline (PANI) and chrysotile nanotubes 4-methylbenzenethiol capped copper nanoparticles system fibers

Electrospinning of this suspension was carried out using the following instrumental parameters:

- Electrical potential difference: 8.0 KV
- Distance collector-needle: 9.0 cm
- Rate: 0.5 ml/h

4.5.13 Electrospun polyaniline (PANI) and chrysotile nanotubes 4-methylbenzenethiol capped gold nanoparticles system fibers

Electrospinning of this suspension was carried out using the following instrumental parameters:

- Electrical potential difference: 8.0 KV
- Distance collector-needle: 10.0 cm
- Rate: 1.0 ml/h

4.5.14 Electrospun polyaniline (PANI) and chrysotile nanotubes 4-methylbenzenethiol capped gold-silver 1:4 nanoparticles system fibers

Electrospinning of this suspension was carried out using the following instrumental parameters:

- Electrical potential difference: 7.5 KV
- Distance collector-needle: 10.0 cm
- Rate: 1.0 ml/h

4.5.15 Electrospun polyaniline (PANI) and chrysotile nanotubes 4-methylbenzenethiol capped gold-silver 4:1 nanoparticles system fibers

Electrospinning of this suspension was carried out using the following instrumental parameters:

- Electrical potential difference: 8.0 KV
- Distance collector-needle: 10.5 cm
- Rate: 1.0 ml/h

4.5.16 Electrospun polyaniline (PANI) and chrysotile nanotubes 1-butanethiol capped silver nanoparticles system fibers

Electrospinning of this suspension was carried out using the following instrumental parameters:

- Electrical potential difference: 8.0 KV
- Distance collector-needle: 9.0 cm
- Rate: 1.0 ml/h

4.5.17 Electrospun polyaniline (PANI) and chrysotile nanotubes 4-methylbenzenethiol capped silver nanoparticles system fiber

Electrospinning of this suspension was carried out using the following instrumental parameters:

- Electrical potential difference: 7.0 KV
- Distance collector-needle: 9.0 cm
- Rate: 1.0 ml/h

4.5.18 Electrospun polyaniline (PANI) and multiwalled carbon nanotubes fibers

We prepared a suspension with 5.0 mg of multi-walled carbon nanotubes (MWCNT) in 2 ml of chloroform. The solution was sonicated for 10 minutes using an ultrasound probe. We then added polyaniline emeraldine base (20 mg) and (\pm)-(10)-camphorsulfonic acid (25.8 mg). The solution was stirred for 24 h. Subsequently 20 mg of poly(ethylene oxide) were added. The solution was then stirred again for 24 h to obtain a composite with an amount of filler equivalent to 7.0 % of the total hybrid system mass. This suspension was sonicated for 1 minute and stirred for 30 minutes.

Electrospinning of this suspension was carried out using the following instrumental parameters:

- Electrical potential difference: 10.0 KV
- Distance collector-needle: 8.0 cm
- Rate: 1.0 ml/h

4.5.19 Electrospun polyaniline (PANI) and chrysotile nanotubes fibers

5.0 mg of chrysotile nanotubes were added to 2 ml of the PANI solution in chloroform previously prepared to obtain a composite with an amount of filler equivalent to 7.0 % of the total hybrid system mass.

This suspension was sonicated for 5 seconds and stirred for 30 minutes.

Electrospinning of this suspension was carried out using the following instrumental parameters:

- Electrical potential difference: 8.0 KV
- Distance collector-needle: 15.0 cm
- Rate: 1.0 ml/h

4.5.20 Electrospun of poly(3-hexylthiophene) (P3HT) and graphene oxide fibers

We prepared a suspension with 3.0 mg of graphene oxide in 2 ml of chloroform. The suspension was sonicated for 10 minutes using an ultrasound probe. We then added poly(3-hexylthiophene) (P3HT)

(20 mg). The suspension was stirred for 24 h at 50 °C. Subsequently 20 mg of poly(ethylene oxide) were added. The suspension was stirred again for 24 h at 50 °C to obtain a composite with an amount of filler equivalent to 7.0 % of the total hybrid system mass. This suspension was sonicated for 1 minute and stirred for 30 minutes.

Electrospinning of this suspension was carried out using the following instrumental parameters:

- Electrical potential difference: 17.0 KV
- Distance collector-needle: 18.0 cm
- Rate: 0.5 ml/h

4.5.21 Electrospun of poly(3-hexylthiophene) (P3HT) and multiwalled carbon nanotubes fibers

We prepared a suspension with 3.0 mg of multi-walled carbon nanotubes (MWCNT) in 2 ml di chloroform. The suspension was sonicated for 10` using an ultrasound probe. We then added poly(3-hexylthiophene) (P3HT) (20 mg).The suspension was stirred for 24 h at 50 °C. Subsequently 20 mg of poly(ethylene oxide) were added. The suspension was stirred again for 24 h at 50 °C to obtain a composite with an amount of filler equivalent to 7.0 % of the total hybrid system mass. This suspension was sonicated for 1 minute and stirred for 30 minutes.

Electrospinning of this suspension was carried out using the following instrumental parameters:

- Electrical potential difference: 21.0 KV
- Distance collector-needle: 18.0 cm
- Rate: 0.5 ml/h

4.5.22 Electrospun of poly(3-hexylthiophene) (P3HT) and chrysotile nanotubes fibers

5.0 mg of chrysotile nanotubes were added to 2 ml of the P3HT solution in chloroform previously prepared to obtain a composite with an amount of filler equivalent to 7.0 % of the total hybrid system mass.

This suspension was sonicated for 5 seconds and stirred for 30 minutes.

Electrospinning of this suspension was carried out using the following instrumental parameters:

- Electrical potential difference: 16.5 KV
- Distance collector-needle: 18.0 cm
- Rate: 0.5 ml/h

CHAPTER V: RESULTS AND DISCUSSION

5.1 Characterization of chrysotile nanotubes

The geomimetic chrysotile ($\text{Mg}_3\text{Si}_2\text{O}_5(\text{OH})_4$) obtained by the hydrothermal synthesis previously described has been characterized through several different technical methods, in order to define its purity, crystallinity and structure. The diffraction pattern (XRPD) of the synthetic product (Fig. 5.1) displays the characteristic reflections of high crystalline chrysotile, with brucite ($\text{Mg}(\text{OH})_2$) impurities in small amounts.

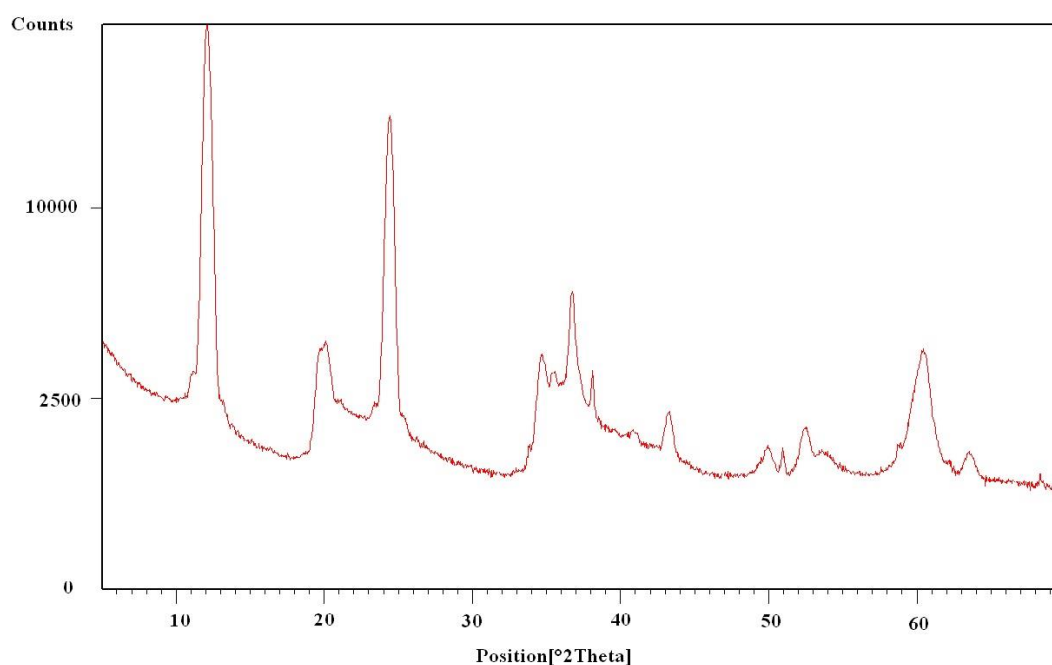


Figure 5.1: diffraction pattern of a synthetic chrysotile sample

The spectroscopic analysis through ATR-FT-IR confirms the data obtained with the previous analysis, generating a –ATR-FT-IR spectrum typical for chrysotile (Fig 5.2).

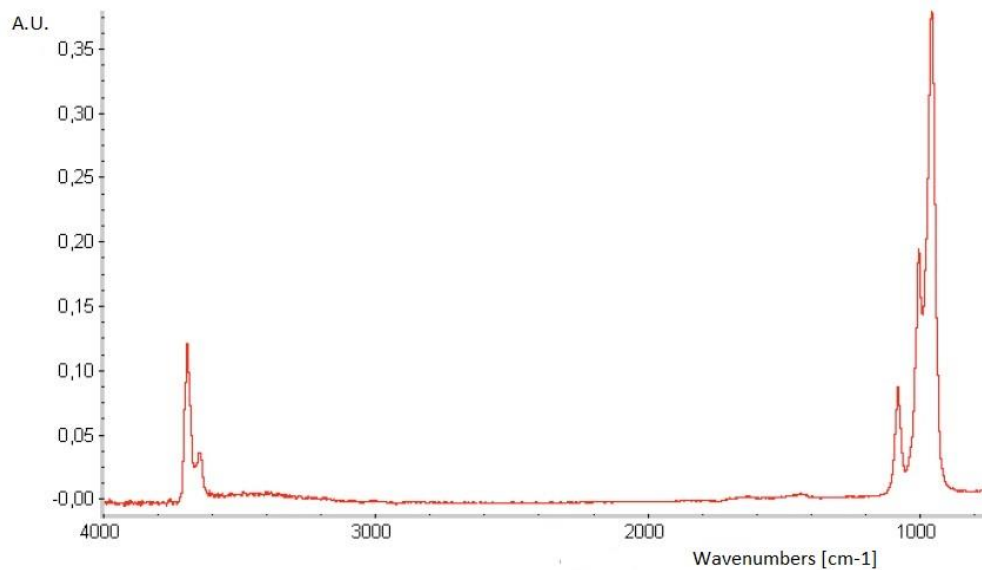


Figure 5.2: ATR-FT-IR spectrum of a synthetic chrysotile sample

The characteristic bands of chrysotile are 3692.2 cm^{-1} (stretching of Mg-(OH) present on the outer surface of the nanotubes), 3646.4 cm^{-1} (stretching of Mg-(OH) present on the inner surface of the nanotubes), 1081.8 cm^{-1} (out-of-plane symmetric stretching Si-O); 1005.2 cm^{-1} (in plane parallel to the b axis stretching Si-O); 958.1 cm^{-1} (in plane parallel to the a axis stretching Si-O).

Different microscopic analyses have been carried out to deepen the morphologic and structural understanding. TEM microscopy showed the nanotubular morphology of the synthetic chrysotile (Fig. 5.3).

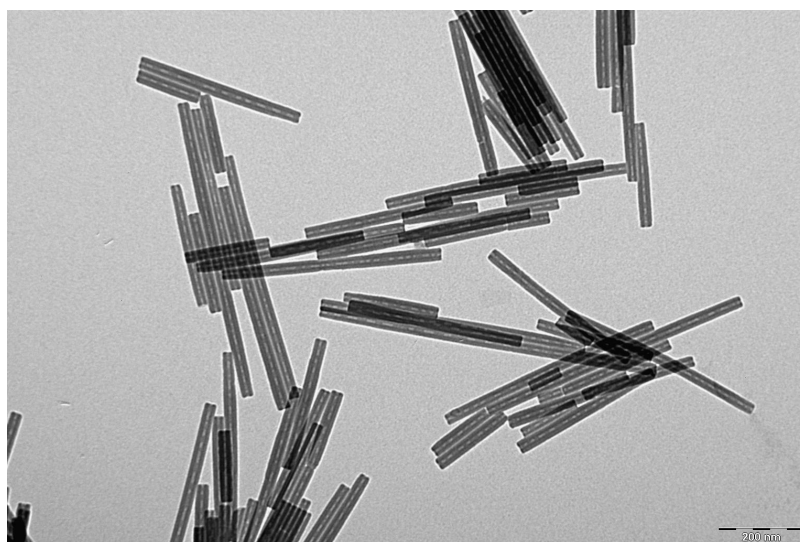


Figure 5.3: TEM image of synthetic chrysotile nanotubes

The images show the high uniformity of these single walled nanotubes, with an outside diameter of 21 nm and a hollow diameter of 7 nm. An image magnification (Fig. 5.4) shows that the edges of the tube are open and that a wall is made of 10 O-T layers, each of them 0.73 nm thick.

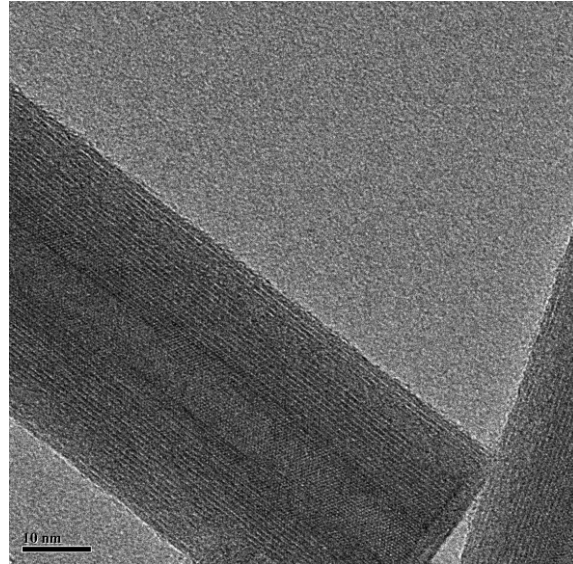
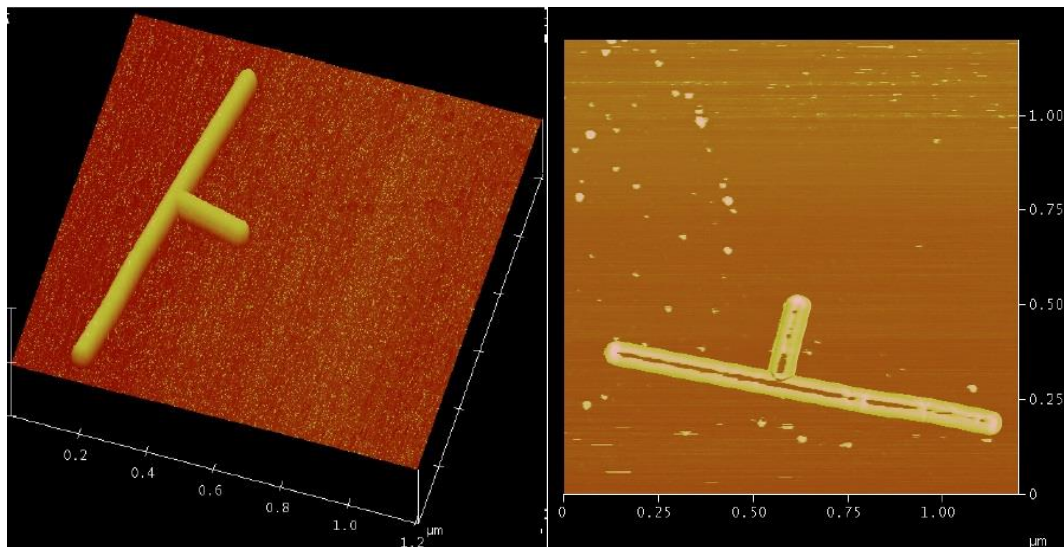


Figure 5.4: TEM image of a chrysotile nanotube

Also atomic force microscopy (AFM) analyses show the structural homogeneity of the nanotubes obtained (Fig. 5.5 A) and the presence of the central tube evidenced with the analysis of the phase.



A

B

Figure 5.5: (A) AFM image of two synthetic chrysotile nanotubes
(B) phase variation in two synthetic chrysotile nanotubes obtained by AFM

Thermal gravimetric analyses TGA (Fig. 5.6) on the sample clearly show the peak corresponding to the main endothermic reaction of de-hydrossilation of the chrysotile at 620 °C. Even the previous peak at 525 °C may be due to the de-hydrossilation of the sample. The sample crystallizes again into forsterite (Mg_2SiO_4) at about 810 °C, close to the narrow exothermic peak. The small endothermic transition at 350 °C is due to the dehydration of brucite, which is present in the sample as impurity.

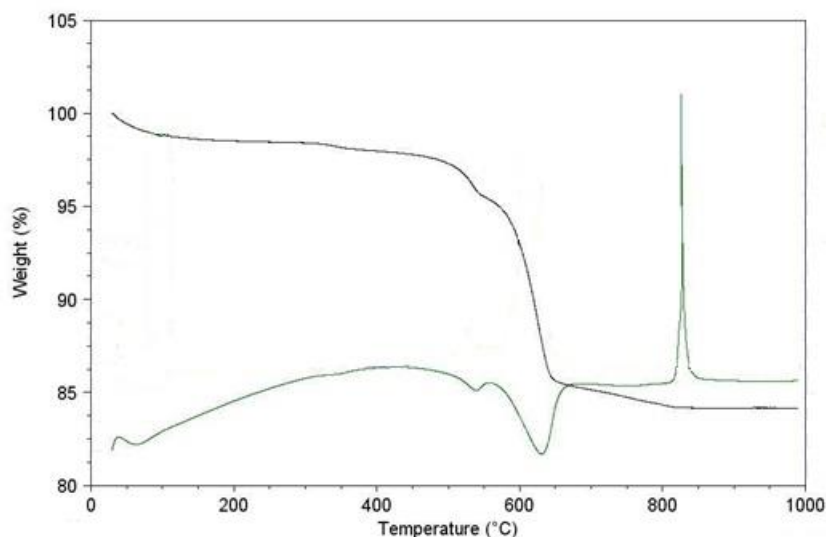


Figure 5.6: TGA (blue line) and DTA (green line) curves of a sample of synthetic chrysotile nanotubes

The product obtained is a homogeneous composite which makes this hydrothermal synthesis a reliable and reproducible mean for the synthesis of geomimetic stoichiometric chrysotile.

5.2 Characterization of nanoparticles

5.2.1 Characterization of 1-butanethiol capped silver nanoparticles

The first investigation carried out on the sample of nanoparticles has been an ATR-FT-IR spectroscopy of a part from the freeze-dried material. The spectroscopy has been used to analyze the composition and morphology of the organic shell protecting the silver particles (Fig. 5.7).

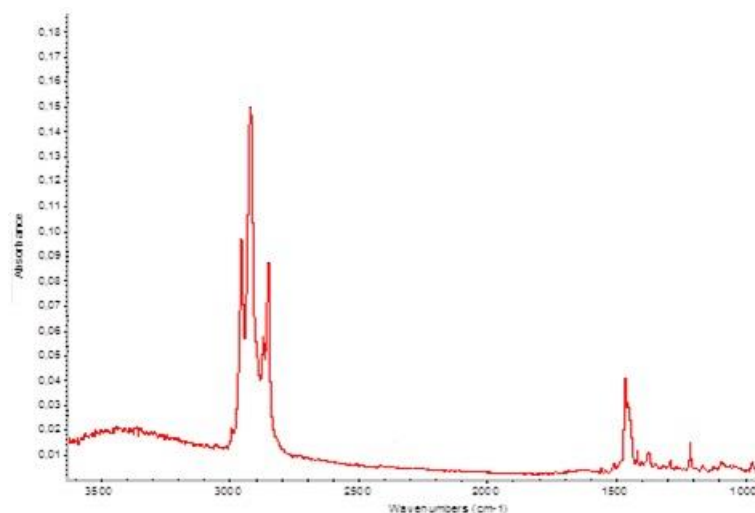


Figure 5.7: ATR-FT-IR spectrum of a sample of 1-butanethiol capped silver nanoparticles

The most important item evidenced in this spectrum is the absence of the stretching signal at about 2600 cm^{-1} of the S-H group. This information confirms that there are no free titles and that all the thiol molecules are bond to the metallic core.

The FT-IR spectrum also shows peaks corresponding to about 2870 cm^{-1} and 2926 cm^{-1} due to the symmetric and asymmetric stretching respectively of the CH_2 units present in the thiol chains. At about 2957 cm^{-1} the signal corresponding to the C-H terminal bond is present. Also the signal at about 1500 cm^{-1} is ascribable to the alkyl chain of the capping agent, especially the bending.

A UV-Vis spectroscopic analysis has been made on the part of samples preserved in dichloromethane (Fig. 5.8).

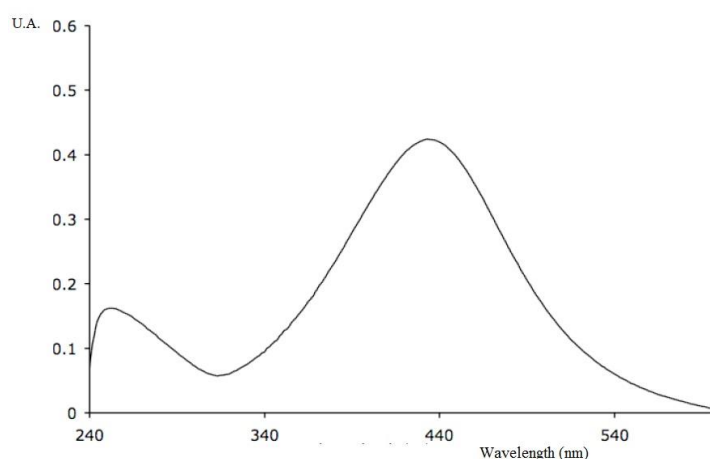


Figure 5.8: UV-Vis spectrum of a 1-butanethiol capped silver nanoparticles

Some capped metallic nanoparticles show a surface plasmon resonance band (SPR) evidenced in the UV-Vis spectrum. In this case a characteristic SPR band at 440 nm can be noted. The position of SPR band is influenced by many factors among which the dimension, morphology, nature of the capping agent.

The TEM analysis allowed to characterize the morphology and sizes of the mentioned nanoparticles (Fig 5.9).

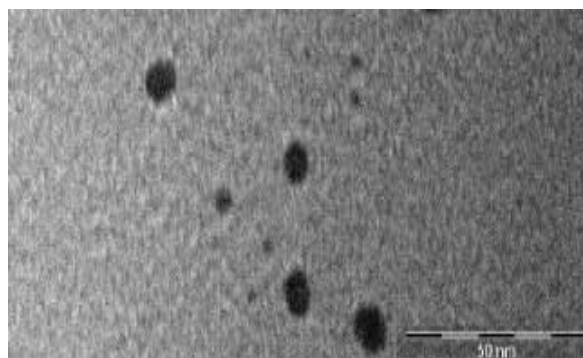


Figure 5.9: TEM image of 1-butanethiol capped silver nanoparticles

The nanoparticles have a medium diameter of 7 nm and a good homogeneity, they are stable and do not tend to aggregation in time.

5.2.2 Characterization of 4-methylbenzenethiol capped silver nanoparticles

FT-IR spectroscopy has been utilized to analyze the composition and morphology of the organic shell protecting the silver nanoparticles (Fig. 5.10).

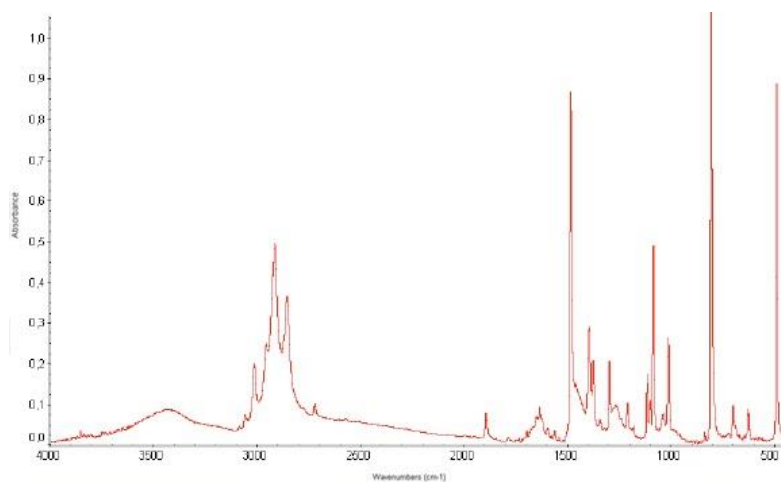


Figure 5.10: FT-IR spectrum of 4-methylbenzenethiol capped silver nanoparticles

The most important item evidenced in this spectrum is the absence of the stretching signal at about 2600 cm^{-1} of the S-H group. This information confirms that there are no free titles and that all the thiol molecules are bond to the metallic core.

In the FT-IR spectrum it is possible to note also the typical peaks of the aromatic rings present in the capping molecule: at about 3015 cm^{-1} and at 800 cm^{-1} there are signal due to the stretching and bending of the C-H groups; besides, at about 1500 cm^{-1} a strong signal due to the stretching of the C=C bonds is present. Signals corresponding to 2865 cm^{-1} and 2920 cm^{-1} due to CH_3 groups are also present. A UV-Vis spectroscopic analysis has been carried out on the part of sample dispersed in dichloromethane (Fig.5.11).

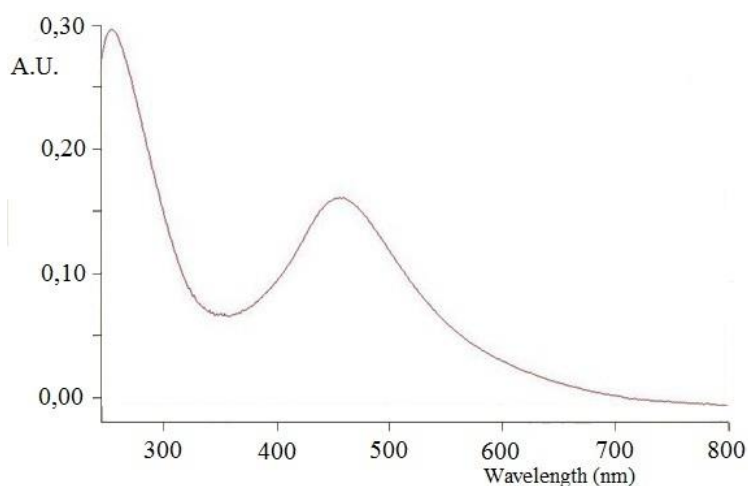


Figure 5.11: UV-Vis spectrum of 4-methylbenzenethiol capped silver nanoparticles

Also in this case it is possible to note a surface plasmon resonance characteristic band at 455 nm in the UV-Vis signal.

TEM analysis allowed to characterize the morphology and size of the mentioned nanoparticles (Fig 5.12).

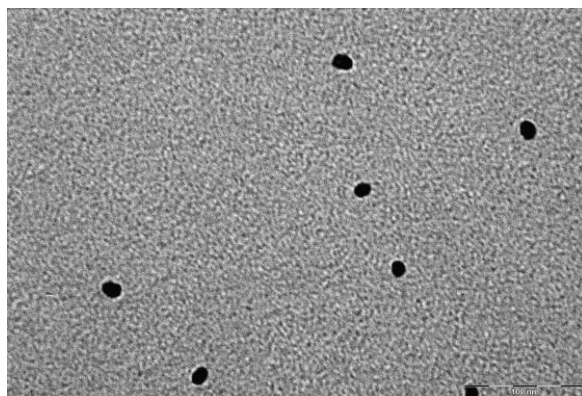


Figure 5.12: TEM image of 4-methylbenzenethiol capped silver nanoparticles

The nanoparticles are spherical and have a medium diameter of about 6 nm, they are stable and do not tend aggregation in time.

5.2.3 Characterization of silver nanoparticles

Ag nanoparticles were obtained by thermal treatment of thiol capped silver nanoparticles. As shown in the thermograph (Fig. 5.12), starting from 4-methylbenzenethiol capped silver nanoparticles the release of the capping agent occurs because of the heating in inert atmosphere, causing a loss of about 20% of the initial bulk.

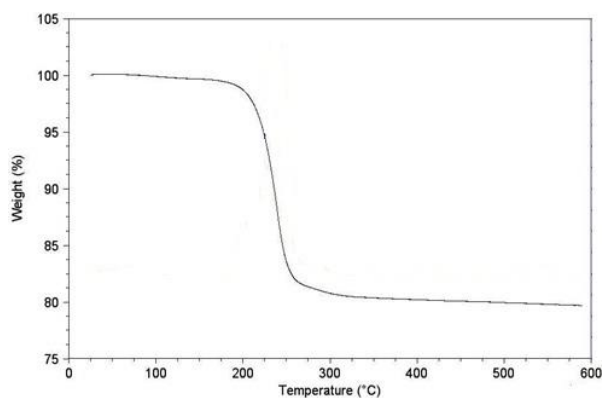


Figure 5.13: TGA curve of 4-methylbenzenethiol capped silver nanoparticles

5.2.4 Characterization of 1-butanethiol capped copper nanoparticles

The first analysis on nanoparticles has been an ATR-FT-IR spectroscopy of a freeze-dried sample. Using this technique we were able to analyze the composition and morphology of the organic shell protecting copper particles (Fig. 5.14).

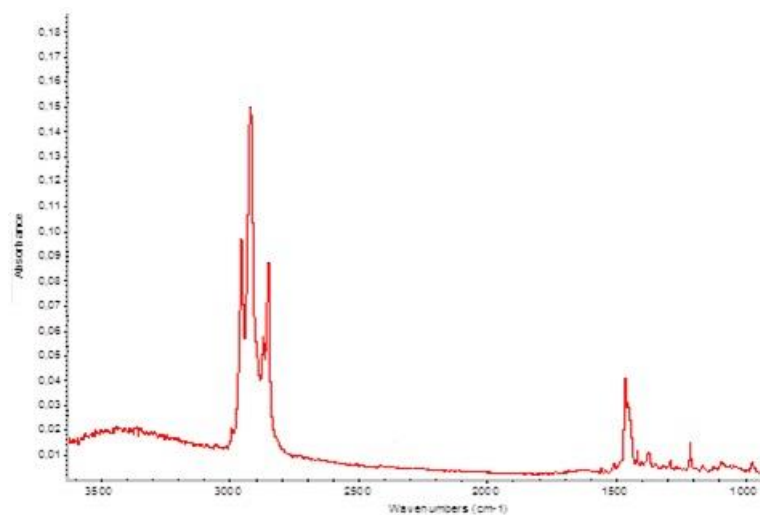


Figure 5.14: ATR-FT-IR spectrum of 1-butanethiol capped copper nanoparticles

The main data outlined by this spectrum is the absence of a stretching signal at 2600 cm^{-1} of the S-H group. This confirms that there are no free thiols and that all the thiol molecules are bonded to the metallic core. The spectrum also shows peaks at 2870 cm^{-1} and at 2926 cm^{-1} caused by the symmetric and antisymmetric stretching respectively of the CH_2 units present in the thiol chains. The signal caused by the stretching of the final C-H bond can be found at about 2957 cm^{-1} . The signal at about 1500 cm^{-1} is ascribable to the alkyl chain of the capping agent, in particular to the bending.

A UV-Vis spectroscopy was carried out on the part of samples preserved in dichloromethane (Fig. 5.15).

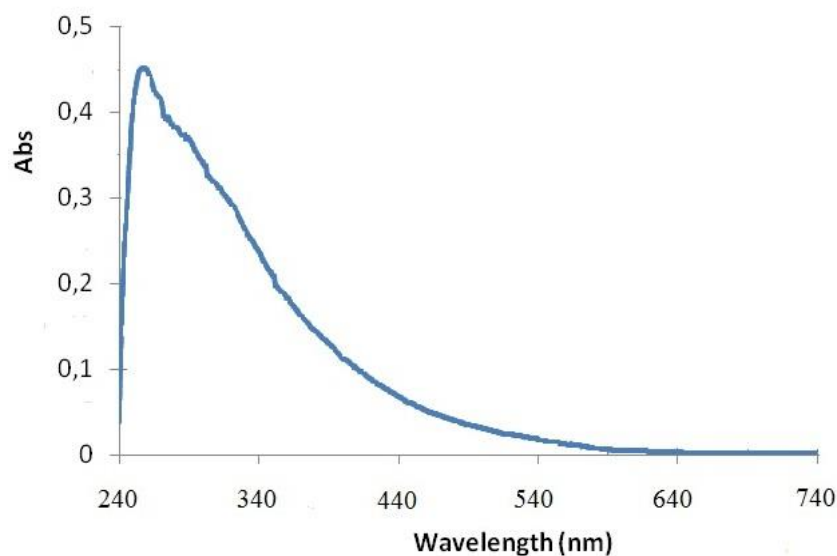


Figure 5.15: UV-Vis spectrum of 1-butanethiol capped copper nanoparticles

Consistent available research evidence the copper nanoparticles capped with thiol do not present a surface plasmon resonance, typical of other capped metallic nanoparticles, ranging from 400 nm and 600 nm.

Using TEM analysis we were able to characterized the morphology and size of these nanoparticles (Fig 5.16).

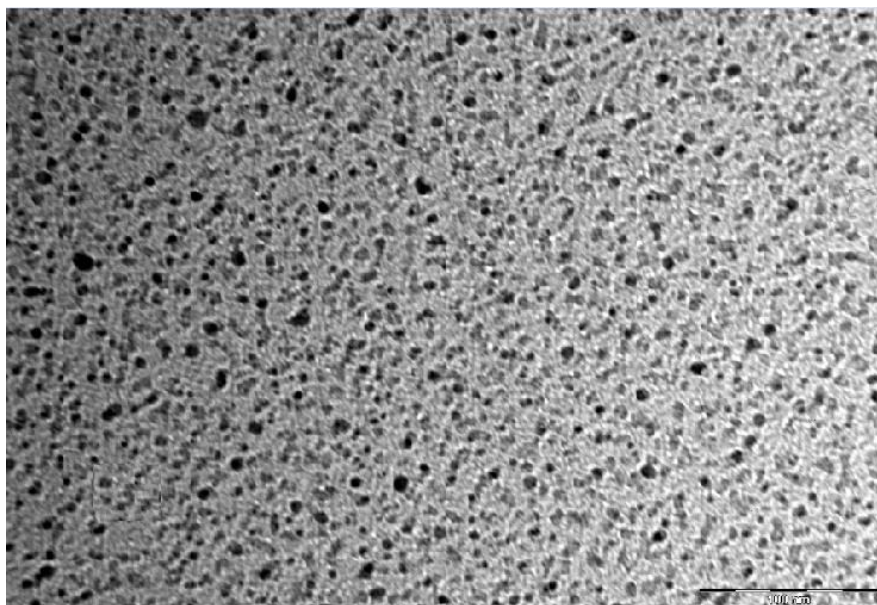


Figure 5.16: TEM image of 1-butanethiol capped copper nanoparticles

The nanoparticles have an average diameter of about 5 nm and good homogeneity, they are stable and do not tend to aggregate.

5.2.5 Characterization of 4-methylbenzenethiol capped copper nanoparticles

FT-IR spectroscopy of a part of freeze-dried sample was used to analyze the composition and morphology of the organic shell protecting the nanoparticles (Fig 5.17).

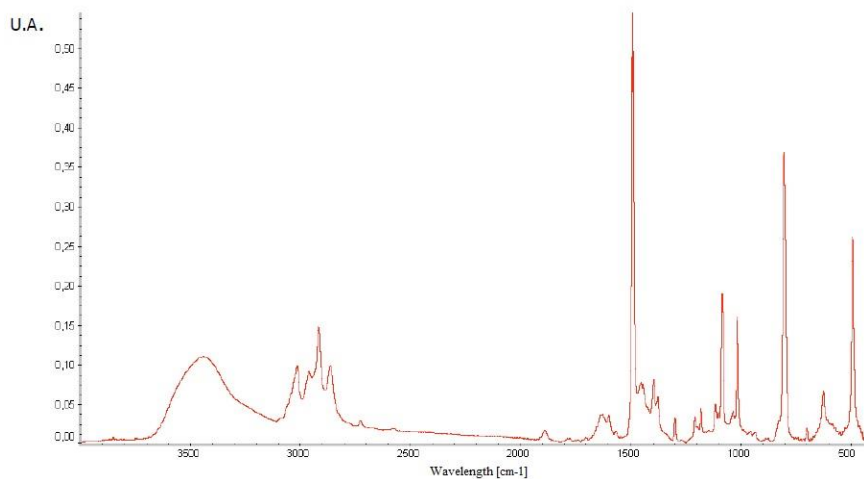


Figure 5.17: FT-IR spectrum of a sample of 4-methylbenzenethiol capped copper nanoparticles

The main data outlined by this spectrum is the absence of a stretching signal at 2600 cm^{-1} of the S-H group. This confirms that there are no free thiols and that all thiol molecules are bonded to the metallic core. The FT-IR spectrum also shows the typical peaks of aromatic rings present in the capping molecule: at about 3014 cm^{-1} and 800 cm^{-1} signals are present caused by the stretching and bending of the C-H groups; additionally at about 1500 cm^{-1} the strong signal caused by the stretching of the C=C bond is present. There are also signals at 2864 cm^{-1} and at 2921 cm^{-1} caused by the CH_3 group.

UV-Vis spectroscopy was used on the part of sample preserved in dichloromethane (Fig. 5.18).

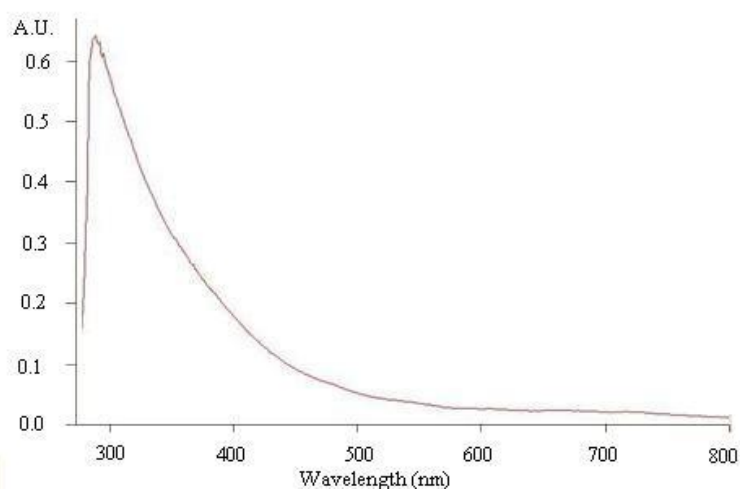


Figure 5.18: UV-Vis spectrum of a sample of 4-methylbenzenethiol capped copper nanoparticles

Consistent with available research evidence, these copper nanoparticles capped with thiol do not display any surface plasmon resonance.

TEM analysis was used to obtain the characterization and size of these nanoparticles (Fig. 5.19).

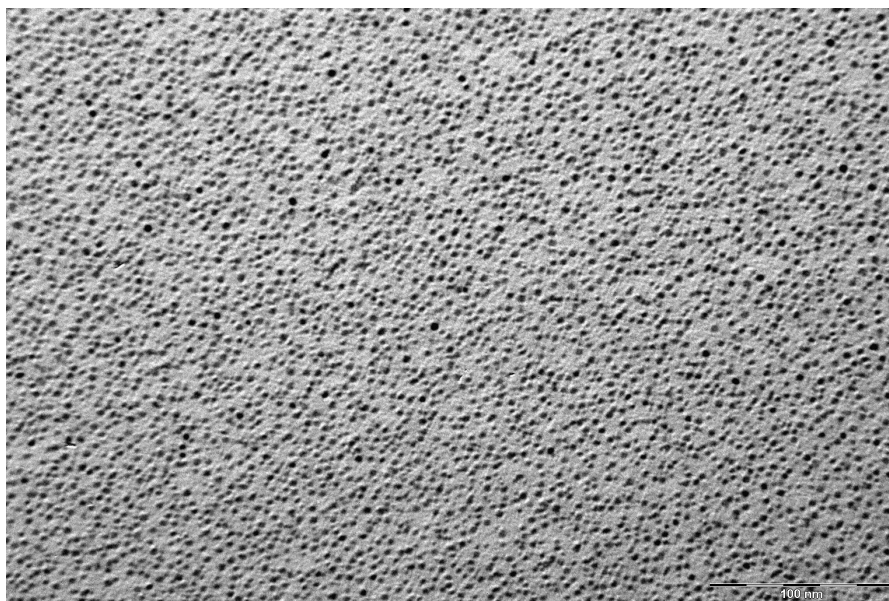


Figure 5.19: TEM image of 4-methylbenzenethiol capped copper nanoparticles

The nanoparticles are spherical and have an average diameter of about 5nm, with good homogeneity, they are stable and do not tend to aggregate over time.

5.2.6 Characterization of copper nanoparticles

Cu nanoparticles were produced by thermal treatment of thiol capped copper nanoparticles. Due to their tendency to aggregate and oxidize, they have been immediately used for the production of CPC.

As shown in the thermograph (Fig. 5.20), starting from 4-methylbenzenethiol capped copper nanoparticles by heating in inert atmosphere the capping agent is released causing a 45% loss of the initial bulk.

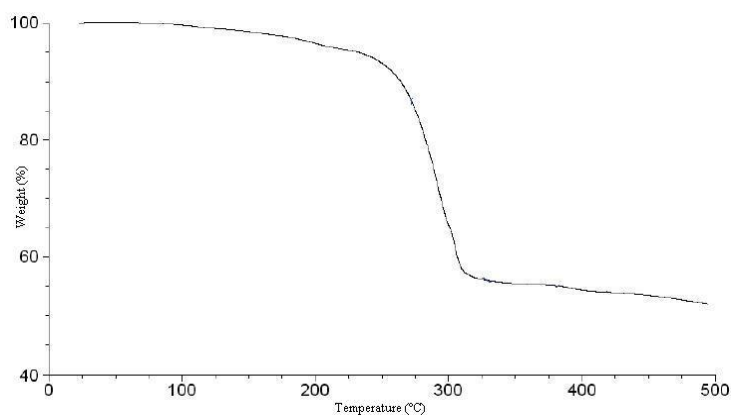


Figure 5.20: TGA of 4-methylbenzenethiol capped copper nanoparticles

5.2.7 Characterization of 4-methylbenzenethiol capped gold nanoparticles

ATR-FT-IR spectroscopy of a part of freeze-dried sample was used to analyze the composition and morphology of the organic shell protecting the nanoparticles (Fig 5.21).

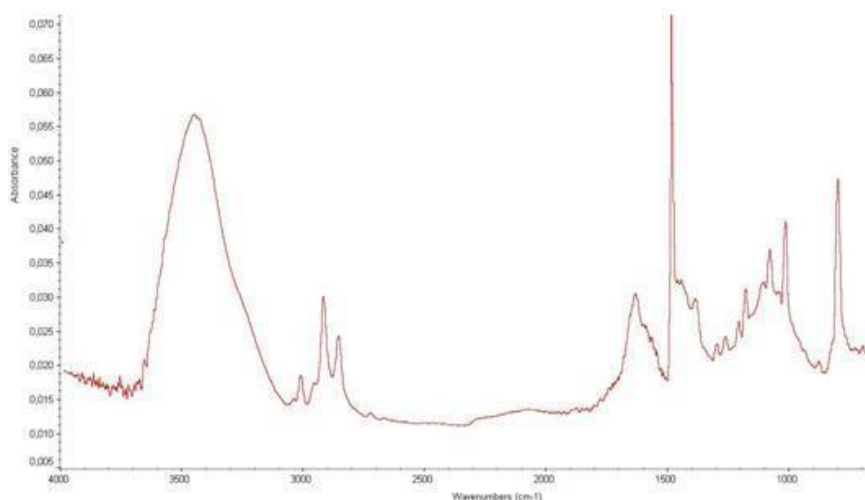


Figure 5.21: ATR-FT-IR spectrum of 4-methylbenzenethiol capped gold nanoparticles

It is clear to see from this spectrum that a stretching signal at 2600 cm^{-1} of the S-H group is absent. This feature confirms that there are no free thiols and that all thiol molecules are bonded to the metallic core. The FT-IR spectrum also shows the typical peaks of aromatic rings present in the capping molecule: at about 3015 cm^{-1} and 800 cm^{-1} signals are present as a result of the stretching and bending of the C-H groups; additionally at about 1500 cm^{-1} the strong signal caused by

stretching of the C=C bond can be found. There are also signals at 2866 cm^{-1} and at 2920 cm^{-1} caused by CH_3 group.

UV-Vis spectroscopy was used on the part of sample preserved in dichloromethane (Fig. 5.22).

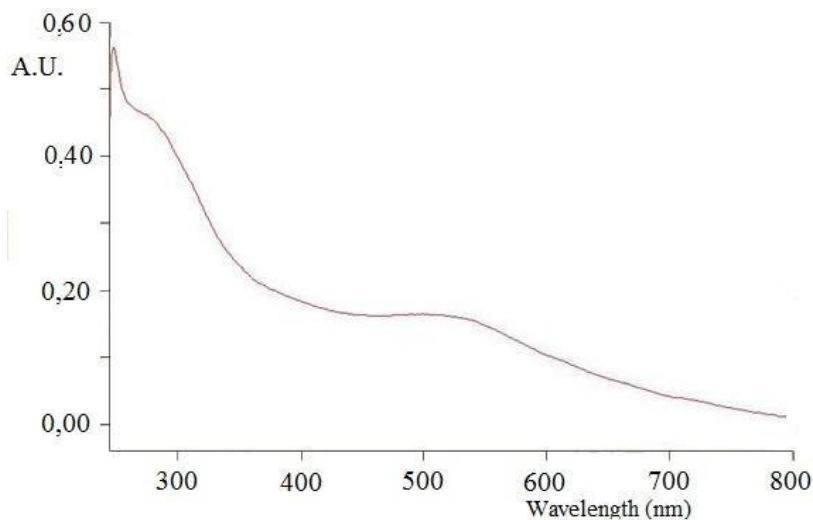


Figure 5.22: UV-Vis spectrum of 4-methylbenzenethiol capped gold nanoparticles

Some metallic nanoparticles show a surface plasmon resonance (SPR) evidenced by the UV-Vis spectrum. In this case a characteristic SPR band can be seen at about 530 nm.

Using TEM analysis we were able to characterize the morphology and size of the above nanoparticles (Fig. 5.23).

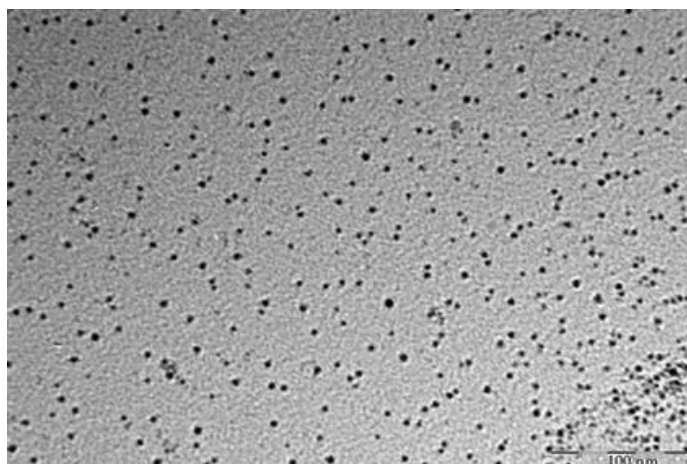


Figure 5.23: TEM image of 4-methylbenzenethiol capped gold nanoparticles

The nanoparticles are spherical and have an average diameter of about 6nm, with good homogeneity.

5.2.8 Characterization of 4-methylbenzenethiol capped gold-silver 1:4 nanoparticles

FT-IR spectroscopy of a part of freeze-dried sample was used to analyze the composition and morphology of the organic shell protecting the gold-silver 1:4 nanoparticles (Fig. 5.24).

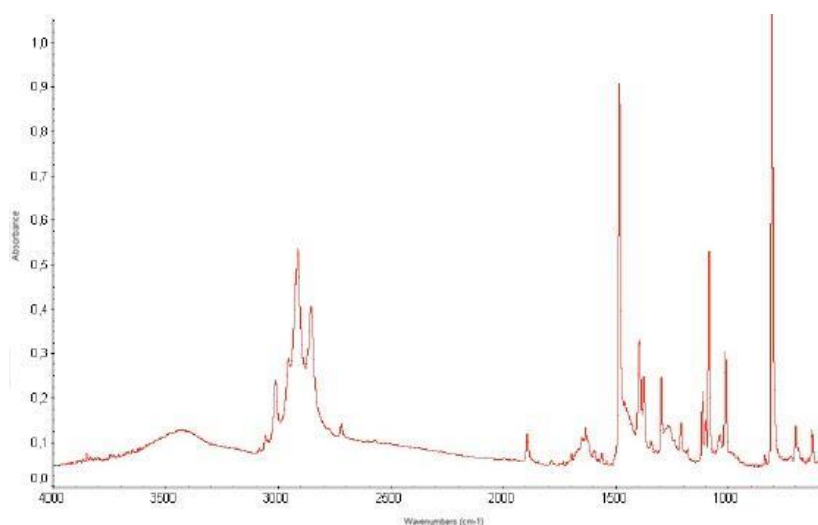


Figure 5.24: FT-IR spectrum of 4-methylbenzenethiol capped gold-silver 1:4 nanoparticles

The main data outlined by this spectrum is the absence of a stretching signal at 2600 cm^{-1} of the S-H group. The FT-IR spectrum also shows the typical peaks of aromatic rings present in the capping molecule: at about 3015 cm^{-1} and 800 cm^{-1} signals caused by the stretching and bending of the C-H groups can also be found. At about 1500 cm^{-1} the strong signal caused by the stretching of the C=C bond is present. There are also signals at about 2868 cm^{-1} and at 2920 cm^{-1} caused by the CH_3 group.

UV-Vis spectroscopy was used on the part of sample preserved in dichloromethane (Fig. 5.25).

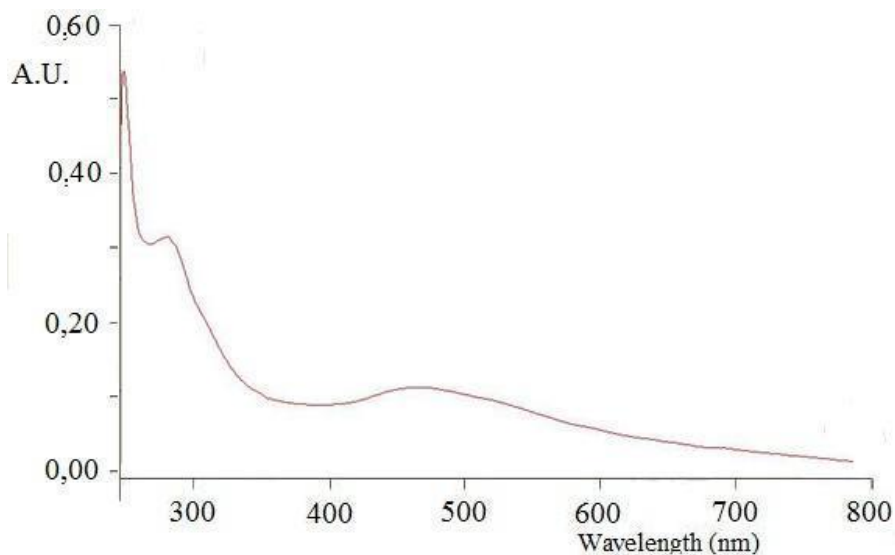


Figure 5.25: UV-Vis spectrum of 4-methylbenzenethiol capped gold-silver 1:4 nanoparticles

Some metallic nanoparticles show a surface plasmon resonance (SPR) evidenced by the UV-Vis spectrum. In this case a characteristic SPR band can be seen at about 470 nm.

Using TEM analysis we were able to characterize the morphology and size of the above nanoparticles (Fig. 5.26).

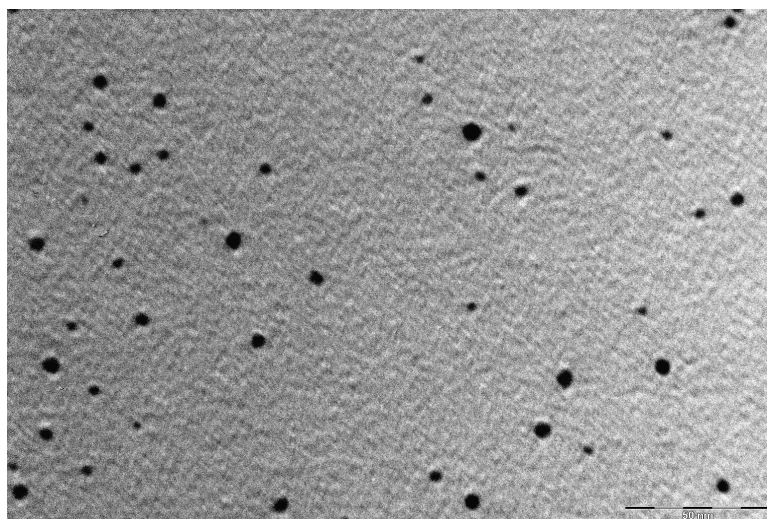


Figure 5.26: TEM image of 4-methylbenzenethiol capped gold-silver 1:4 nanoparticles

The nanoparticles are spherical and all show a diameter smaller than 7 nm.

TGA analyses (Fig. 5.27) show that the nanoparticles are stable up to 200 °C and that afterwards the separation of the organic shell of the capping agent causes a loss of about 33% in the total bulk of the nanoparticles capped with 4-methylbenzenethiol.

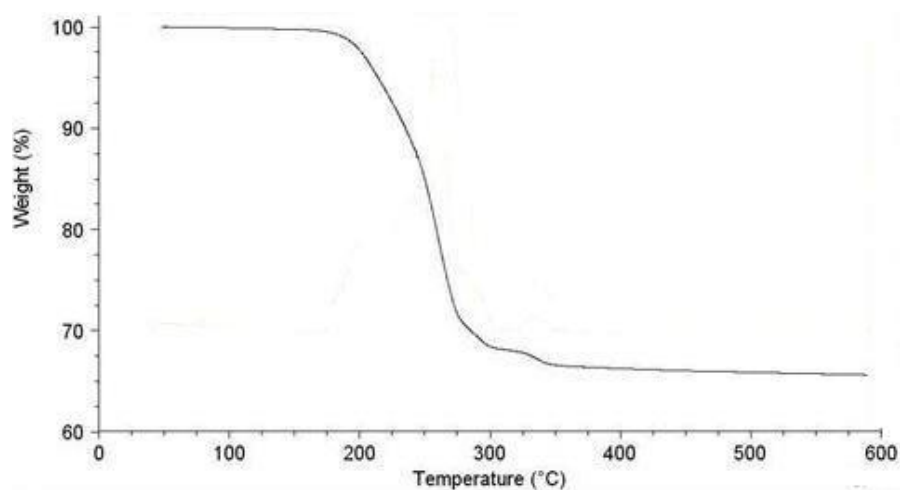


Figure 5.27: TGA curve of 4-methylbenzenethiol capped gold-silver 1:4 nanoparticles

5.2.9 Characterization of 4-methylbenzenethiol capped gold-silver 4:1 nanoparticles

ATR-FT-IR spectroscopy of a part of freeze-dried sample was used to analyze the composition and morphology of the organic shell protecting the gold-silver 4:1 nanoparticles (Fig. 5.28).

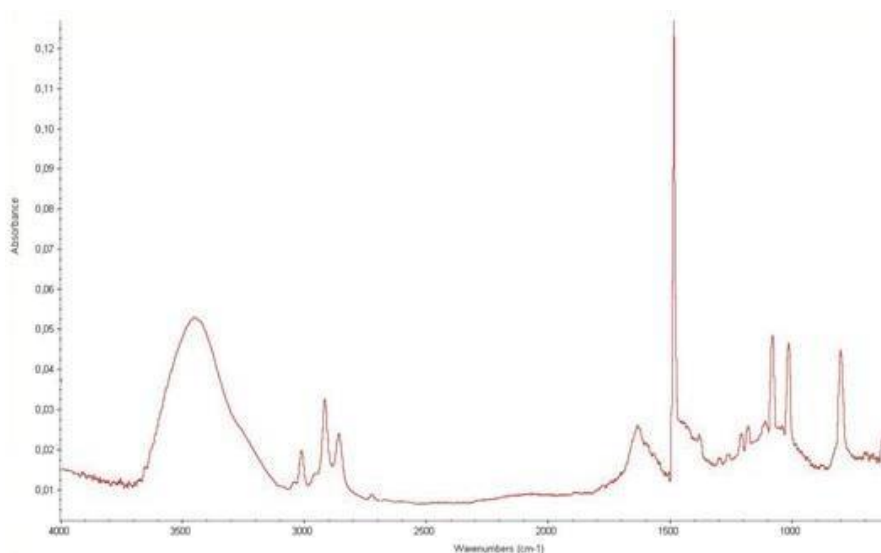


Figure 5.28: ATR-FT-IR spectrum of 4-methylbenzenethiol capped gold-silver 4:1 nanoparticles

The main data outlined by this spectrum is the absence of a stretching signal at 2600 cm^{-1} of the S-H group. The FT-IR spectrum also shows the typical peaks of aromatic rings present in the capping molecule: at about 3018 cm^{-1} and 800 cm^{-1} signals caused by the stretching and bending of the C-H groups can also be found. At about 1500 cm^{-1} the strong signal caused by the stretching of the C=C bond is present. There are also signals at about 2870 cm^{-1} and at 2922 cm^{-1} caused by the CH_3 group.

UV-Vis spectroscopy was used on the part of sample preserved in dichloromethane (Fig. 5.29).

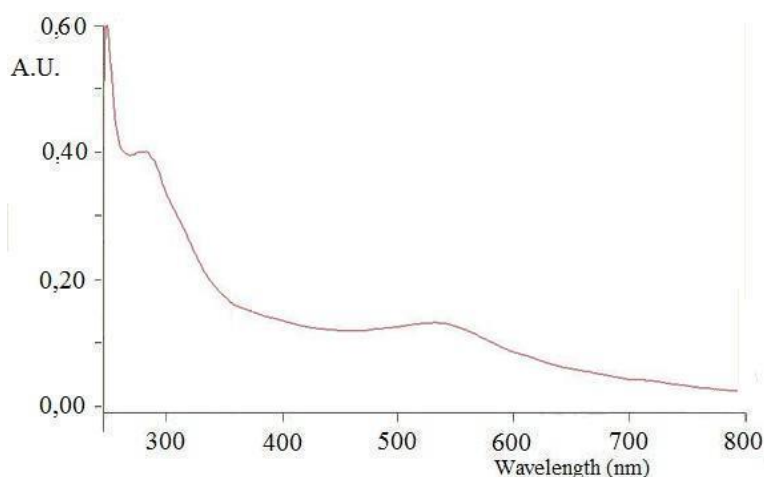


Figure 5.29: UV-Vis spectrum of 4-methylbenzenethiol capped gold-silver 4:1 nanoparticles

The UV-Vis spectrum for 4-methylbenzenethiol capped gold-silver 4:1 nanoparticles shows a characteristic surface plasmon resonance band at about 525 nm.

Using TEM analysis we were able to characterize the morphology and size of the above nanoparticles (Fig 5.30).

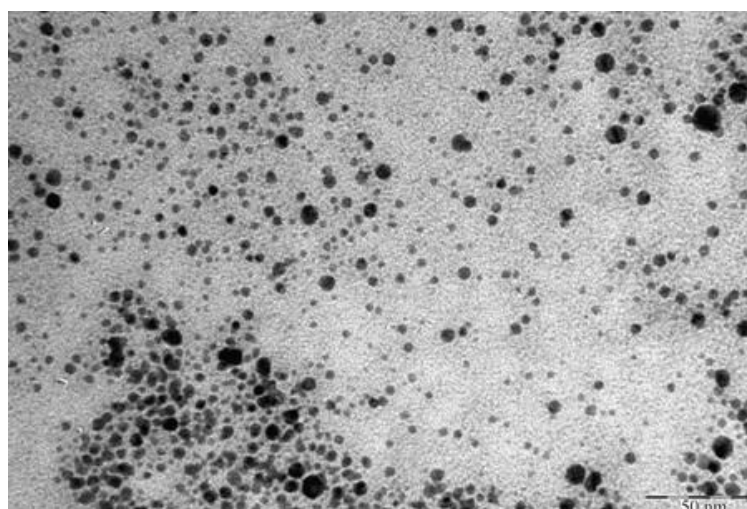


Figure 5.30: TEM image of 4-methylbenzenethiol capped gold-silver 4:1 nanoparticles

The nanoparticles are spherical and do not exhibit homogeneous sizes.

TGA analyses (Fig. 5.31) show that the nanoparticles are stable up to 200 °C and that afterwards the separation of the organic shell of the capping agent causes a loss of about 16% in the total bulk of the nanoparticles capped with 4-methylbenzenethiol.

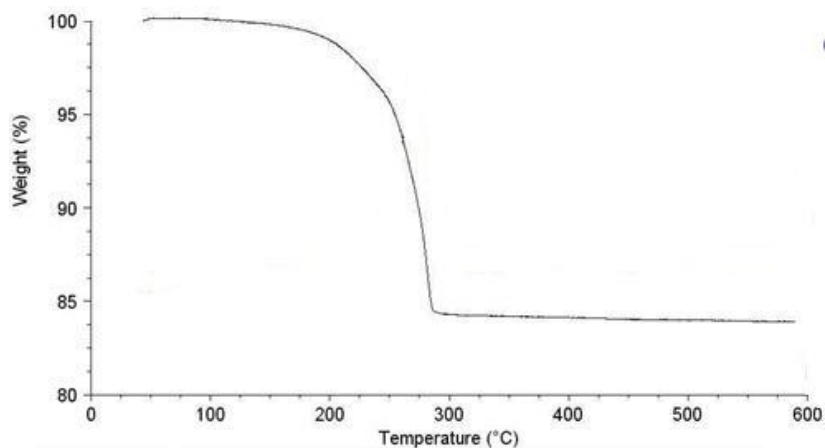


Figure 5.31: TGA curve of 4-methylbenzenethiol capped gold-silver 4:1 nanoparticles

5.2.10 Characterization of 1-butanethiol capped silver-copper 1:1 nanoparticles

We first analysed a freeze-dried sample of nanoparticles using ATR-FT-IR spectroscopy. Using this technique we were able to analyze the composition and morphology of the organic shell protecting the silver-copper 1:1 nanoparticles (Fig. 5.32).

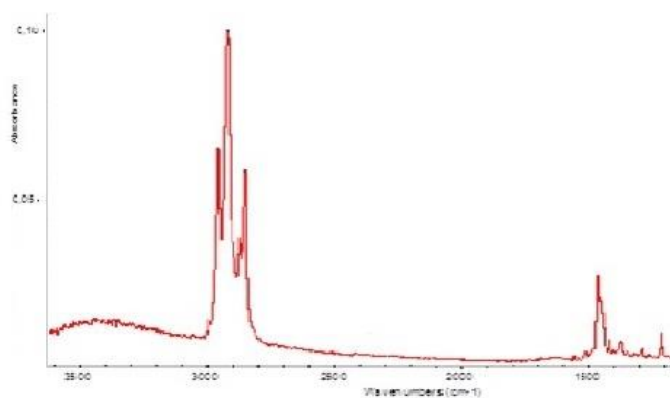


Figure 5.32: ATR-FT-IR spectrum of 1-butanethiol capped silver-copper 1:1 nanoparticles

What is most significant in this spectrum is the absence of a stretching signal at 2600 cm^{-1} of the S-H group. This confirms that there are no free thiols and that all the thiol molecules are bonded to the metallic core. The ATR-FT-IR spectrum also shows peaks at about 2869 cm^{-1} and 2924 cm^{-1} signals caused by the symmetric and antisymmetric stretching respectively of the CH_2 units present in the thiol chains. The signal caused by the stretching of the final C-H bond can be found at about 2957 cm^{-1} . Also the signal at about 1500 cm^{-1} is ascribable to the alkyl chain of the capping agent, in particular to the bending.

UV-Vis spectroscopy was used on the part of the sample preserved in dichloromethane (Fig. 5.33).

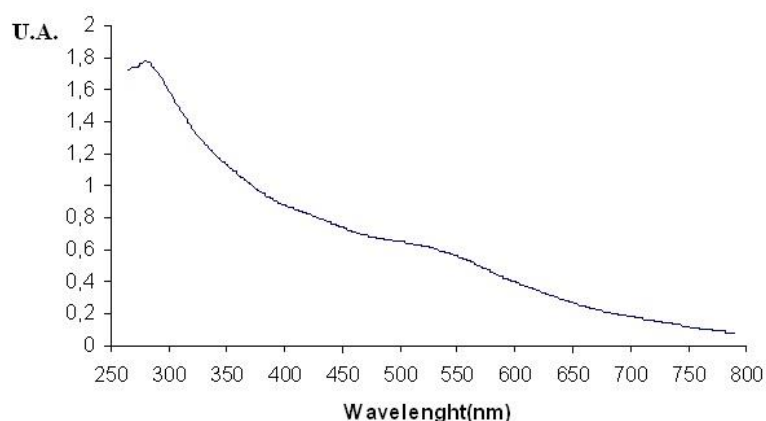


Figure 5.33: UV-Vis spectrum of 1-butanethiol capped silver-copper 1:1 nanoparticles

The UV-Vis spectrum for 1-butanethiol capped silver-copper 1:1 nanoparticles shows a characteristic surface plasmon resonance (SPR) band at about 525 nm. The position of the SPR band is influenced by many factors among which the size and morphology of the nanoparticles and the kind of capping agent used.

Using TEM analysis we were able to characterize the morphology and size of the above nanoparticles (Fig. 5.34).

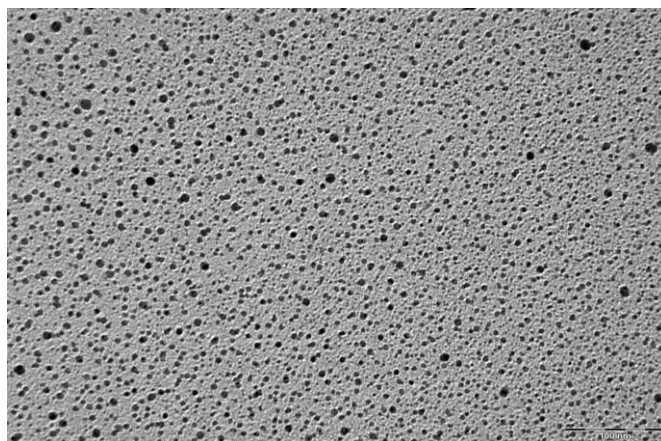


Figure 5.34: TEM micrograph of 1-butanethiol capped silver-copper 1:1 nanoparticles

The nanoparticles have an average diameter of 5 nm, they present a good homogeneity, they are stable and do not tend to aggregation over time.

5.2.11 Characterization of silver-copper 1:1 nanoparticles

Silver-copper 1:1 nanoparticles were produced by thermal treatment of the thiol capped silver-copper 1:1 nanoparticles. Due to their tendency to aggregate and oxidize, they have been immediately used for the production of CPC. As shown in the thermogram (Fig. 5.35), starting from 1-butanethiol capped silver-copper 1:1 nanoparticles by heating in inert atmosphere the capping agent is released causing about 16 % loss of the initial bulk.

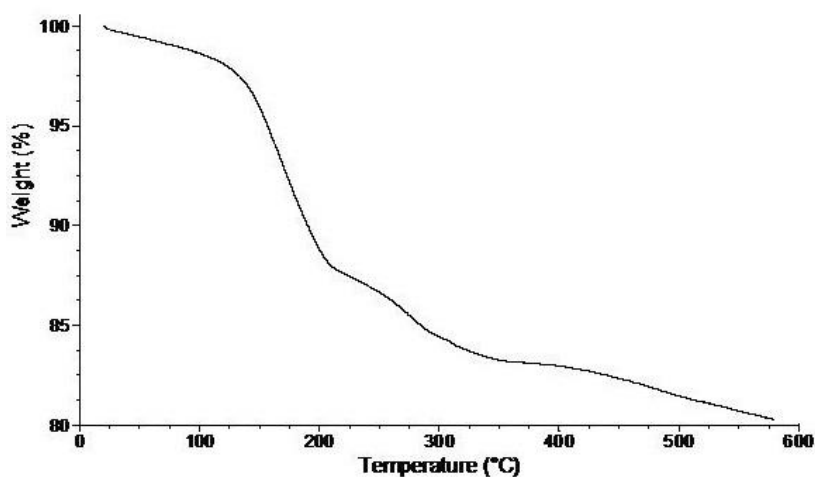


Figure 5.35: TGA thermogram of 1-butanethiol capped silver-copper 1:1 nanoparticles

5.2.12 Characterization of anatase nanoparticles

The sample was analysed using a XRD diffractometer.

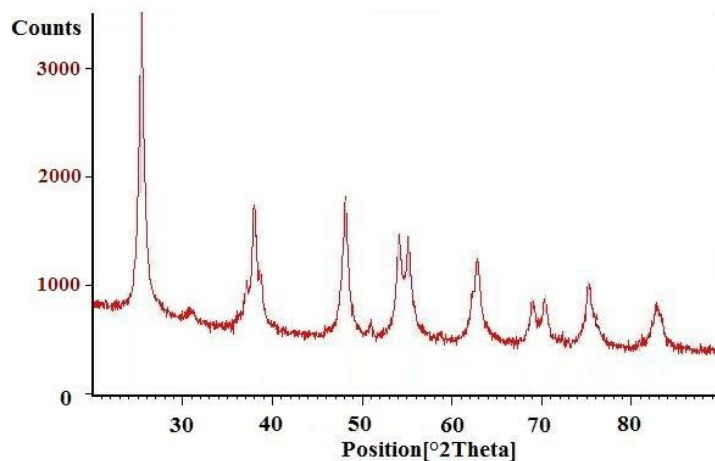


Figure 5.36: XRPD diffractogram of anatase nanoparticles

The diffractogram obtained (Fig. 5.36) shows the high crystallinity of the product; furthermore, only the TiO_2 characteristic peaks are present.

Crystalline anatase nanoparticles were obtained. There are no traces of amorphous titanium dioxide or of other polymorphic forms of crystalline titanium dioxide (rutile and brookite). The product obtained is therefore made of pure anatase (TiO_2).

TEM analysis was used to determine the morphology and size of these nanoparticles. TEM images show anatase particles with nanometric dimensions (Fig. 5.37). Particles do not have a spherical shape, but a cylindrical one and aggregation tendency is low.

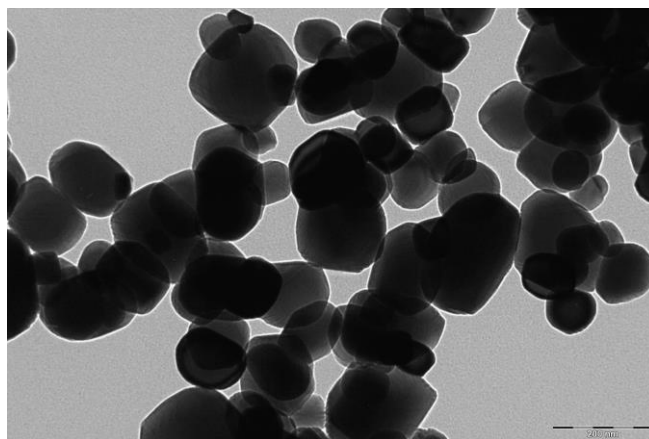


Figure 5.37: TEM image of anatase nanoparticles

5.2.13 Characterization of copper (I) chloride nanoparticles

XPRD analysis was used on the freeze-dried sample of nanoparticles. The diffractogram (Fig. 5.38) shows that the sample is made of one crystalline phase; in fact, only the diffraction typical peaks for copper (I) chloride are present. The sample shows very good purity and crystallinity.

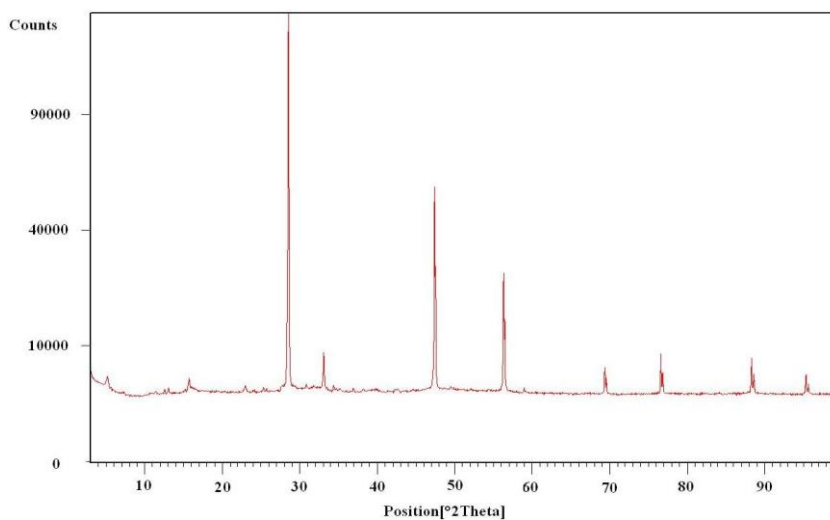


Figure 5.38: XRPD diffractogram of a copper (I) chloride sample

Finally, the sample morphology and dimensions were characterized using transmission electron microscopy. The nanoparticles have an average diameter of 5 nm, they present a good homogeneity, they are stable and do not tend to aggregation in time (Fig 5.39).

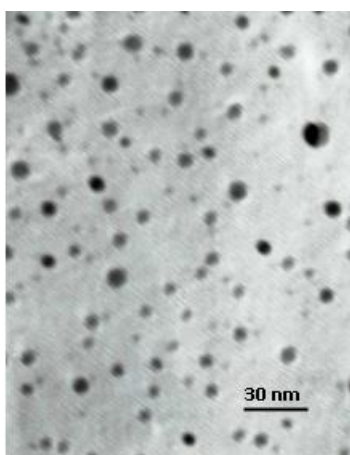


Figure 5.39: TEM image of copper (I) chloride nanoparticles

5.2.14 Characterization of multiwalled carbon nanotubes

A number of characterization techniques were employed on a sample of multiwalled carbon nanotubes. First, we used ATR-FT-IR spectroscopy in order to detect the presence of impurities.

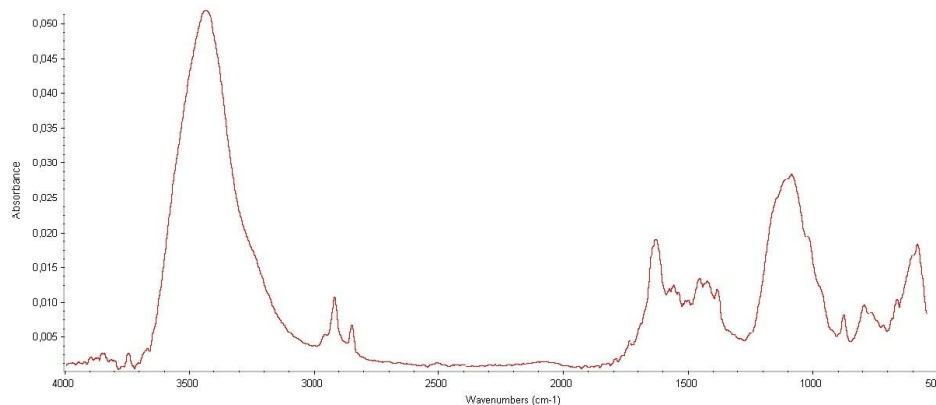


Figure 5.40: ATR-FT-IR spectrum of multiwalled carbon nanotubes

The ATR-FT-IR spectrum (Fig. 5.40) shows the presence of a triplet at about 2900 cm^{-1} characteristic of the $-\text{CH}_n-$ asymmetric and symmetric stretching vibrations. A few other signals are also observed which are caused by the presence of foreign groups, among them the most evident is the intense one at 3435 cm^{-1} caused by O-H stretching vibrations, and also the presence of a band at about 1700 cm^{-1} due to the presence of C=O groups.

XRPD analyses confirm that the material is not very pure.

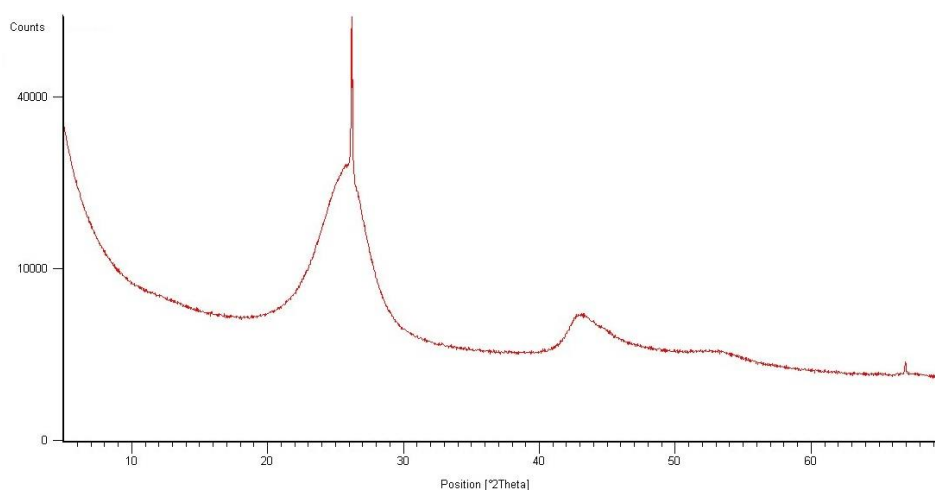


Figure 5.41: XRPD diffractogram of multiwalled carbon nanotubes

The diffractogram (Fig. 5.41) shows the typical patterns of multiwalled carbon nanotubes at $2\theta = 25.9^\circ$, $2\theta = 43^\circ$ e $2\theta = 53.6^\circ$, and also a strong effect at a $2\theta = 26.3^\circ$ caused by the presence of graphite. The strong slope of the baseline at $2\theta \leq 10^\circ$ is due to the presence of aggregates.

TEM microscopy (Fig. 5.42) shows that multiwalled carbon nanotubes are uniform from a morphological point of view, with a constant diameter. These nanotubes show a tendency to aggregate even after ultrasonic treatment.

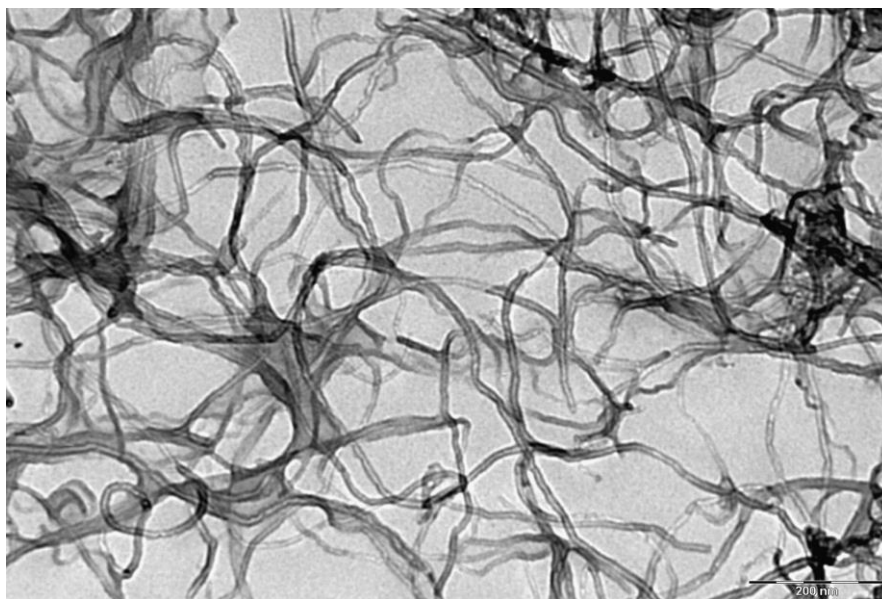


Figure 5.42: TEM micrograph of multiwalled carbon nanotubes

Thermogravimetric analysis (Fig. 5.43) of this sample shows thermal stability up to approximately 850°C , but some weight loss occurs, for example at 550°C , possibly due to the impurities present in the material.

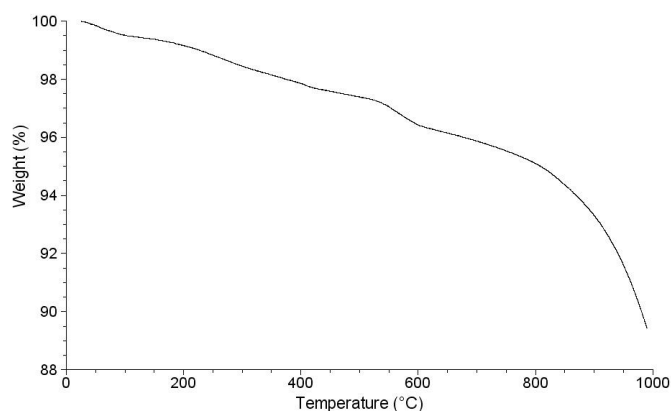


Figure 5.43: TGA thermogram of multiwalled carbon nanotubes

5.2.15 Characterization of graphene oxide

We began our analysis of graphene oxide by using ATR-FT-IR spectroscopy. This characterization technique helped identify the functional groups present in this substance.

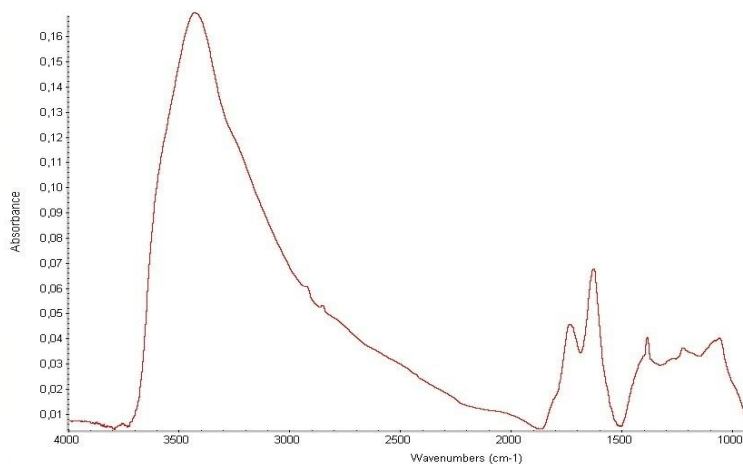


Figure 5.44: ATR-FT-IR spectrum of graphene oxide

The IR spectrum (Fig. 5.44) shows two signals at about 2900 cm^{-1} , which are characteristic of the $\text{—CH}_n\text{—}$ stretching vibrations. Additionally, a few other signals are visible which are caused by to the presence of functional groups, among them the most evident is the intense signal at 3430 cm^{-1} caused by O-H stretching vibrations. Furthermore a strong band at about 1700 cm^{-1} can also be observed, which is caused by the presence of C=O groups. The following adsorption bands are also present: 1590 cm^{-1} (skeletal vibrations from unoxidized graphitic domains), 1210 cm^{-1} (C-OH stretching vibrations) and 1060 cm^{-1} (C-O stretching vibrations).

XRPD analysis was used to study the structure and purity of the material.

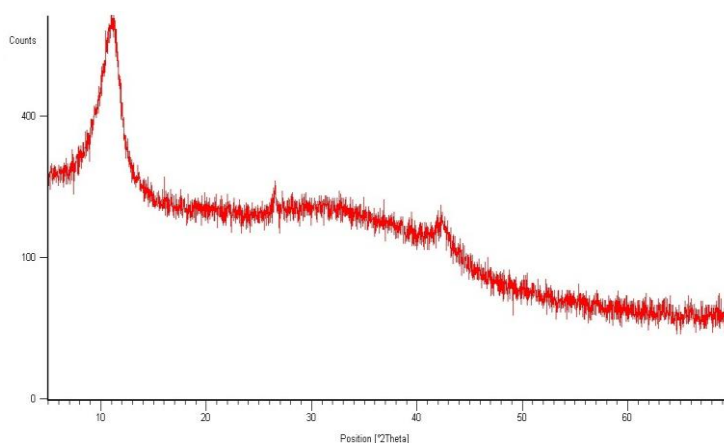


Figure 5.45: XRPD diffractogram pattern of graphene oxide

The diffractogram (Fig. 5.45) shows the typical pattern of graphene oxide like the one at about $2\theta = 11^\circ$.

This signal is slightly shifted towards 2θ values lower than those reported in available research literature; this phenomenon is due to the greater distance between the layers of graphene oxide. The greater distance between the layers may be due to the presence of graphite impurities which can be detected by the presence of a characteristic small signal at $2\theta = 26^\circ$.

The UV-Vis spectrum of graphene oxide (Fig. 5.46), after it underwent ultrasonic treatment and was dispersed in water, exhibits two characteristic features that can be used as a means of identification: 230 nm, corresponding to $\pi \rightarrow \pi^*$ transition of aromatic C-C bonds and at 300 nm which can be attributed to $n \rightarrow \pi^*$ transition of C=O bonds.

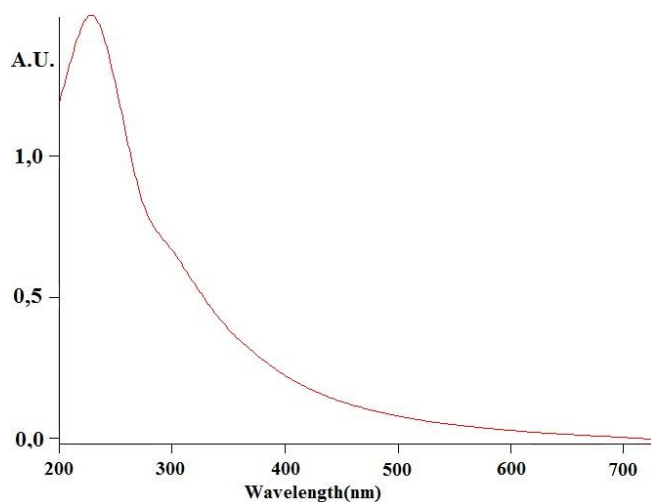


Figure 5.46: UV-Vis spectra of graphene oxide

TEM microscopy (Fig. 5.47) shows that morphologically graphene oxides are arranged as rectangular sheets with sides smaller than $1 \mu\text{m}$. Grapheme oxides appear well exfoliated after ultrasonic treatment and do not display a significant tendency to re-stratify or aggregate.

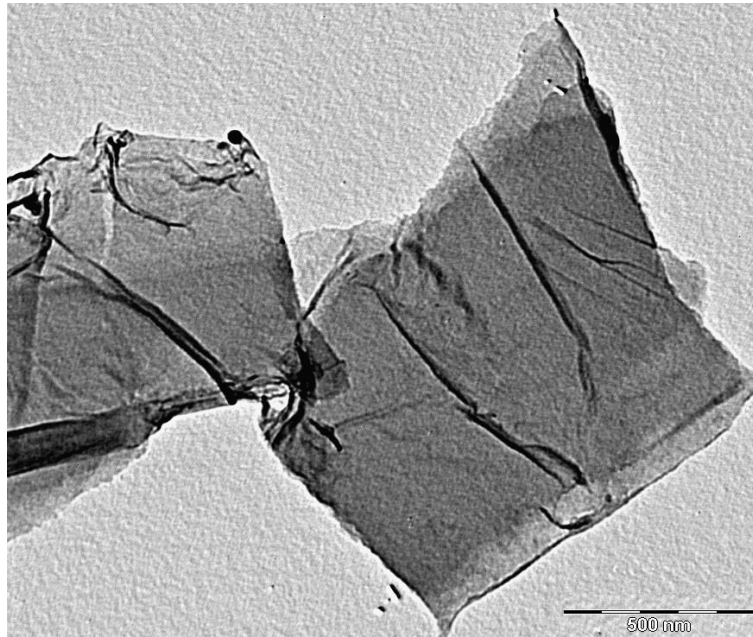


Figure 5.47: TEM micrograph of graphene oxide

Thermogravimetric analysis (Fig. 5.48) shows a loss of weight at 100 °C due to the loss of water adsorbed by the material; another considerable loss of weight occurs at 200 °C and this is due to the decomposition of labile oxygen functional groups present in the material. The intensity of this loss is directly proportional to the functionalization degree of the material.

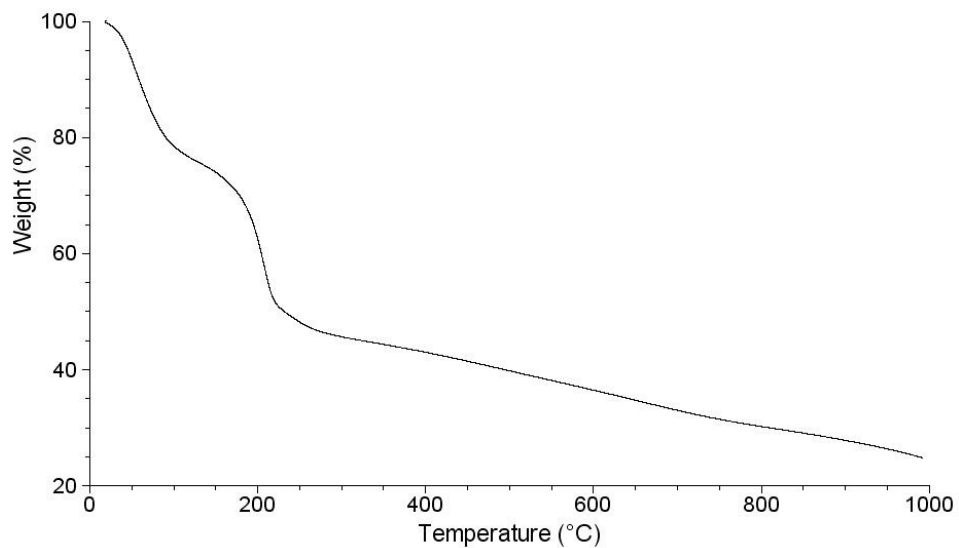


Figure 5.48: TGA curve of graphene oxide

5.2.16 Conclusion

Various inorganic nanomaterials were synthesized and characterized both with 0D and 1D structures. Chrysotile nanotubes were obtained by hydrothermal synthesis. Using this technique we were able to control the morphology, structure and composition of the material, so as to produce a nanomaterial homogeneous, pure and with high crystallinity.

Thiol capped metal nanoparticles were obtained using a modified version of the Brust method. Characterization of these materials was carried out using a wide range of techniques. The result of these analyses confirmed our expectations; nanoparticles have dimensions smaller than 7 nm, totally capped, without impurities and stable over time. It is interesting to note that synthesis conditions may modify the size and composition of the particles and the core/shell ratio; moreover, by modifying the kind of metal or alloy we used, some of the characteristics of the metal may also change, demonstrated by a shifting of the surface plasmon resonance (SPR).

Pure and crystalline uncapped inorganic particles with nanometric sizes were been synthesized and characterized, like those of anatase (TiO₂) and copper (I) chloride.

Finally, two commercial materials with different structures were characterized, one is a 1D nanoamaterial (multiwalled carbon nanotubes) and the other is a 2D nanomaterial (graphene oxide). Both materials display morphological and structural characteristics suitable for them to be used in this study, but they contain some impurities due to the synthesis processes and this makes them qualitatively less attractive compared to those we synthesized.

5.3 Characterization of inorganic nanostructured composites

5.3.1 Characterization of chrysotile nanotubes and 1-butanethiol capped copper nanoparticles system

Dimensional and morphological characterization of the above particles was carried out using TEM analysis. TEM micrographs show (Fig.5.49) that 1-butanethiol capped copper nanoparticles, even though they are smaller than 7 nm, are not to be found inside chrysotile nanotubes. For this reason no further characterizations were carried out.

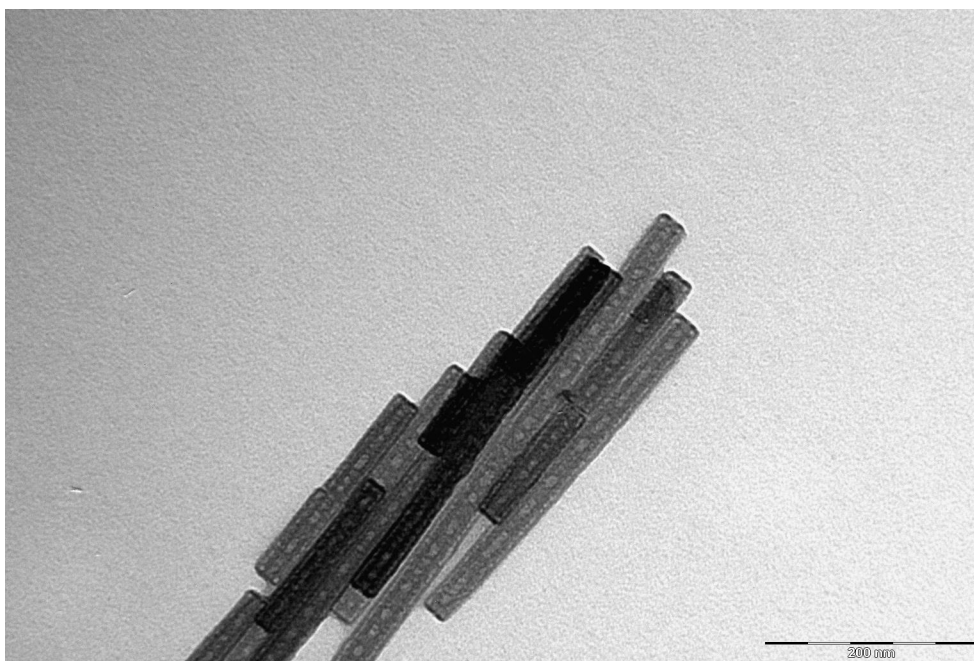


Figure 5.49: TEM image of chrysotile nanotubes and 1-butanethiol capped copper nanoparticles system

5.3.2 Characterization of chrysotile nanotubes and 4-methylbenzenethiol capped copper nanoparticles system

Dimensional and morphological characterization of the above particles was carried out using TEM analysis. TEM micrographs show (Fig. 5.50) that 4-methylbenzenethiol capped copper nanoparticles, even though they are smaller than 7 nm, do not penetrate inside the chrysotile nanotubes. For this reason no further characterizations were carried out.

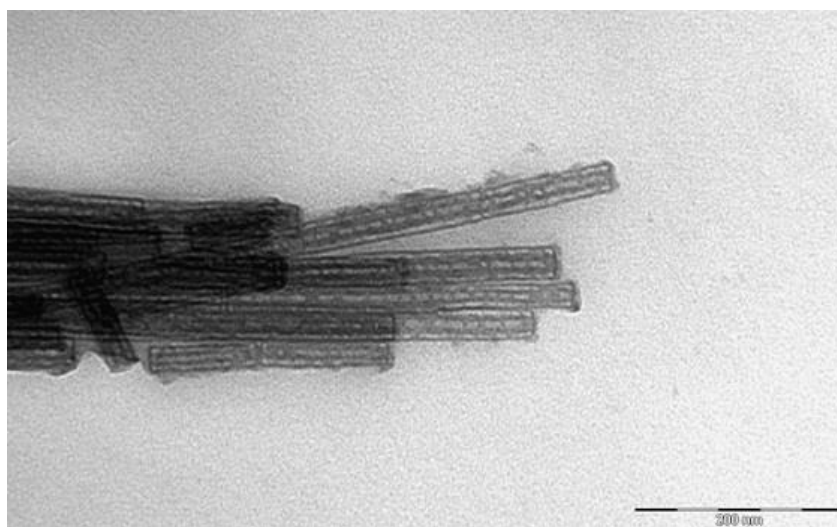


Figure 5.50: TEM image of chrysotile nanotubes and 4-methylbenzenethiol capped copper nanoparticles system

5.3.3 Characterization of chrysotile nanotubes and 4-methylbenzenethiol capped gold nanoparticles system

We first analysed the sample of nanoparticles using FT-IR spectroscopy.

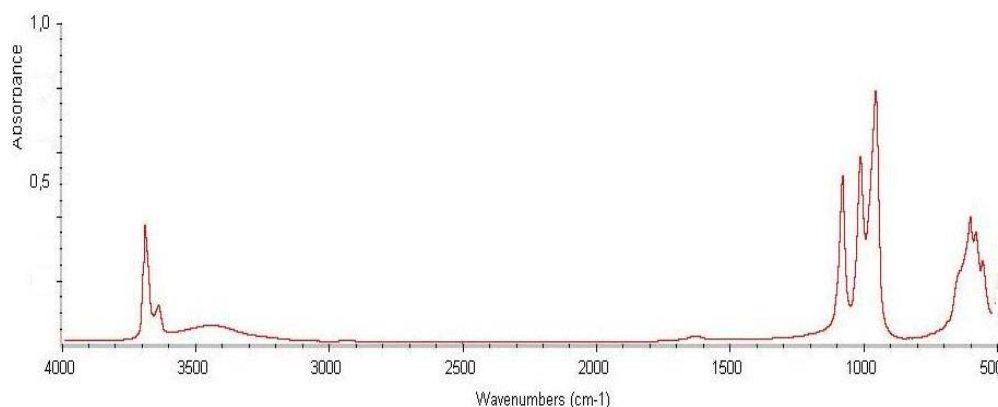


Figure 5.51: FT-IR spectrum of chrysotile nanotubes and 4-methylbenzenethiol capped gold nanoparticles system

The spectrum (Fig. 5.51) clearly shows 2 signals around the 3600-3700 cm^{-1} mark and 3 signals at approximately 900-1100 cm^{-1} of the chrysotile nanotubes. Signals from the capping agent, particularly signal with bandwidth of 2900 cm^{-1} from the methyl group, demonstrate the presence of nanoparticles. Typical absorption levels from 4-methylbenzenethiol capped gold nanoparticles are very low due to the low relative amount of capping agent analysed.

Part of the sample was analysed using UV-Vis spectroscopy (Fig. 5.52).

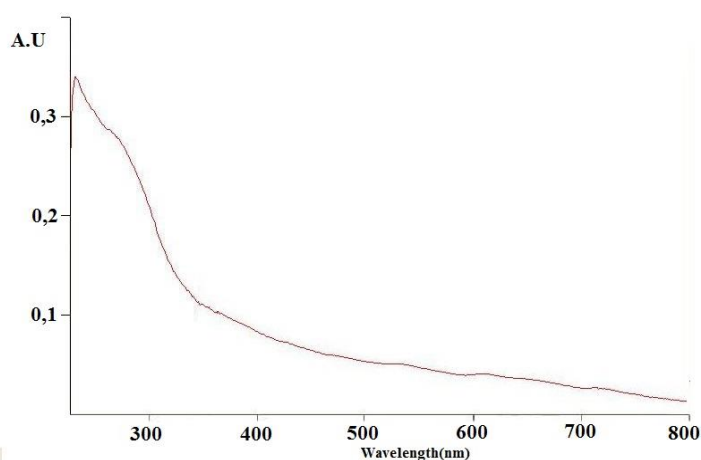


Figure 5.52: UV-Vis spectrum of a sample of chrysotile nanotubes and 4-methylbenzenethiol capped gold nanoparticles system

UV-Vis spectroscopy of chrysotile nanotubes and 4-methylbenzenethiol capped gold nanoparticles system shows characteristic surface plasmon resonance band of approximately 530 nm, typical of capped gold nanoparticles, that proves they are present.

TEM analysis was used for the dimensional and morphological characterisation of this system.

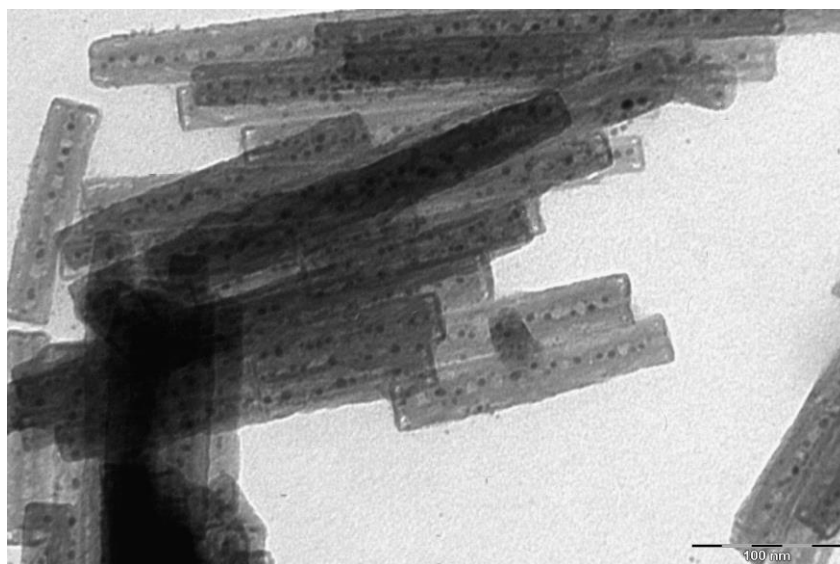


Figure 5.53: TEM image of chrysotile nanotubes and 4-methylbenzenethiol capped gold nanoparticles system

TEM micrographs (Fig. 5.53) show that nanoparticles can be found within the central cavity of the nanotubes. These inorganic structures are homogeneous and stable.

5.3.4 Characterization of chrysotile nanotubes and 4-methylbenzenethiol capped gold-silver 1:4 nanoparticles system

We first analysed the sample of nanoparticles using FT-IR spectroscopy.

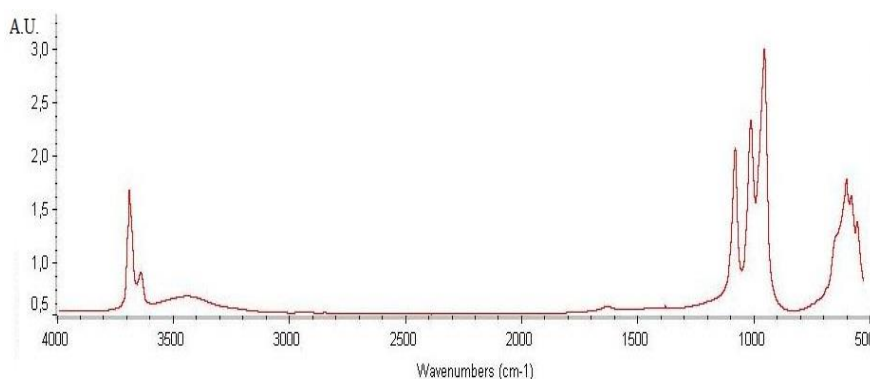


Figure 5.54: FT-IR spectrum of chrysotile nanotubes and 4-methylbenzenethiol capped gold-silver 1:4 nanoparticles system

The spectrum (Fig. 5.54) clearly shows 2 signals around the 3600-3700 cm⁻¹ mark and 3 signals at approximately 900-1100 cm⁻¹ of the chrysotile nanotubes. Signals from the capping agent, particularly signal with bandwidth of 2900 cm⁻¹ from the methyl group, demonstrate the presence of nanoparticles. Typical absorption levels from 4-methylbenzenethiol capped gold-silver 1:4 nanoparticles are very low due to the low relative amount of capping agent analysed.

Part of the sample was analysed using UV-Vis spectroscopy.

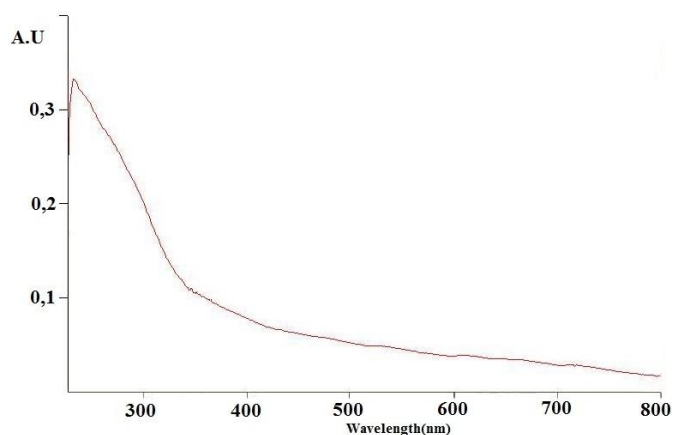


Figure 5.55: UV-Vis spectrum of a sample of chrysotile nanotubes and 4-methylbenzenethiol capped gold-silver 1:4 nanoparticles system

UV-Vis spectroscopy of chrysotile nanotubes and 4-methylbenzenethiol capped gold-silver nanoparticles system (Fig. 5.55) shows a faint characteristic SPR band of approximately 470 nm, typical of capped gold-silver 1:4 nanoparticles, that proves they are present. Also in this case, the small amount of material arouses a lower intensity signal from surface plasmon resonance detected using this type of analysis.

TEM analysis was used for the dimensional and morphological characterisation of this system.

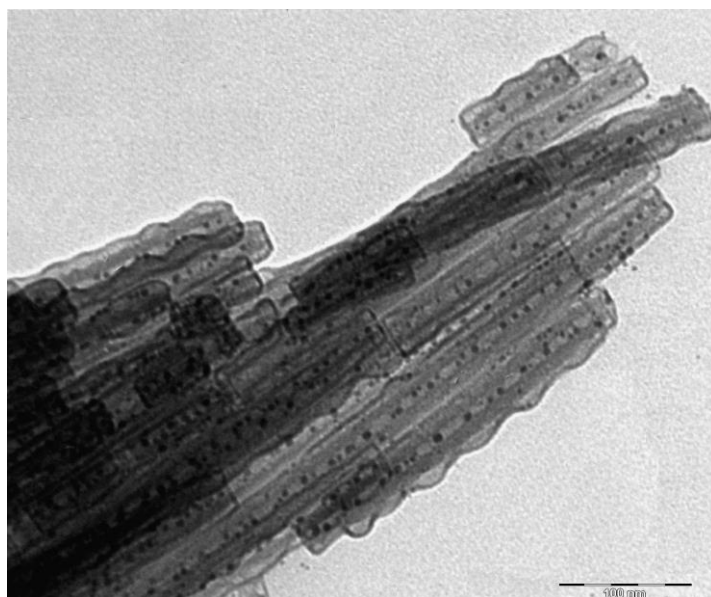


Figure 5.56: TEM image of chrysotile nanotubes and 4-methylbenzenethiol capped gold-silver 1:4 nanoparticles system

TEM micrographs (Fig. 5.56) show that nanoparticles can be found within the central cavity of the nanotubes. These inorganic nanostructures are homogeneous and stable.

5.3.5 Characterization of chrysotile nanotubes and 4-methylbenzenethiol capped gold-silver 4:1 nanoparticles system

We first analyzed the sample of nanoparticles using FT-IR spectroscopy.

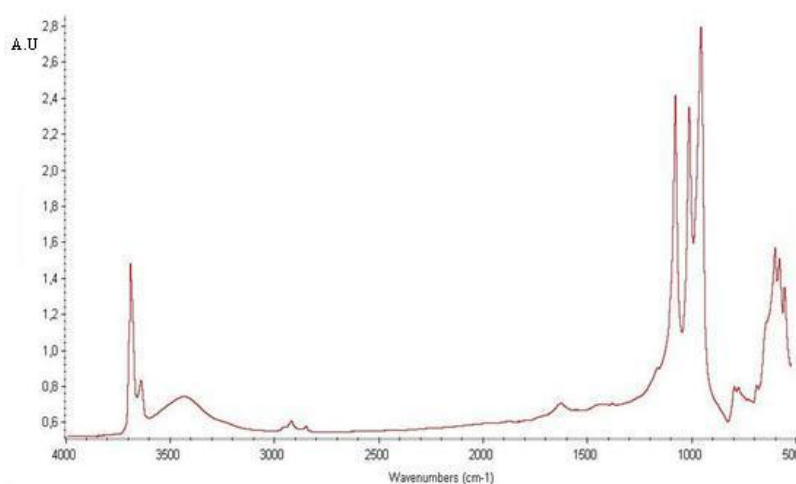


Figure 5.57: FT-IR spectrum of chrysotile nanotubes and 4-methylbenzenethiol capped gold-silver 4:1 nanoparticles system

The spectrum (Fig. 5.57) clearly shows two signals around the $3600\text{-}3700\text{ cm}^{-1}$ mark and three signals at approximately $900\text{-}1100\text{ cm}^{-1}$ of the chrysotile nanotubes. Signals from the capping agent, particularly signal with bandwidth of 2900 cm^{-1} from the methyl group, demonstrate the presence of nanoparticles. Typical absorption levels from 4-methylbenzenethiol capped gold-silver 4:1 nanoparticles are very low due to the low relative amount of capping agent analysed. Part of the sample was analysed using UV-Vis spectroscopy (Fig. 5.58).

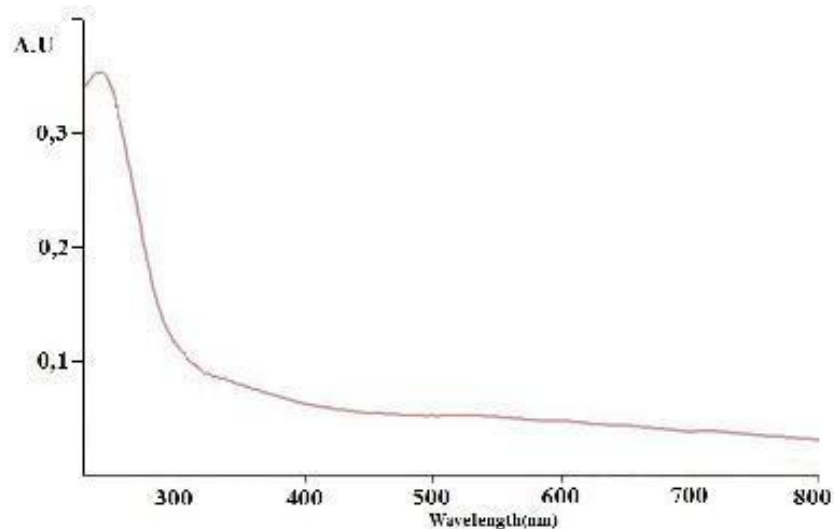


Figure 5.58: UV-Vis spectrum of a sample of chrysotile nanotubes and 4-methylbenzenethiol capped gold-silver 4:1 nanoparticles system

UV-Vis spectroscopy of chrysotile nanotubes and 4-methylbenzenethiol capped gold-silver 4:1 nanoparticles system shows a faint characteristic surface plasmon resonance band of approximately 525nm, typical of capped gold-silver 4:1 nanoparticles, that proves they are present. Also in this case the small amount of material analysed results in a lower intensity signal from SPR detected using this type of analysis.

TEM analysis was used for the dimensional and morphological characterisation of this system.

5.3.6 Characterization of chrysotile nanotubes and 1-butanethiol capped silver nanoparticles system

TEM analysis was used for the dimensional and morphological characterisation of this system.

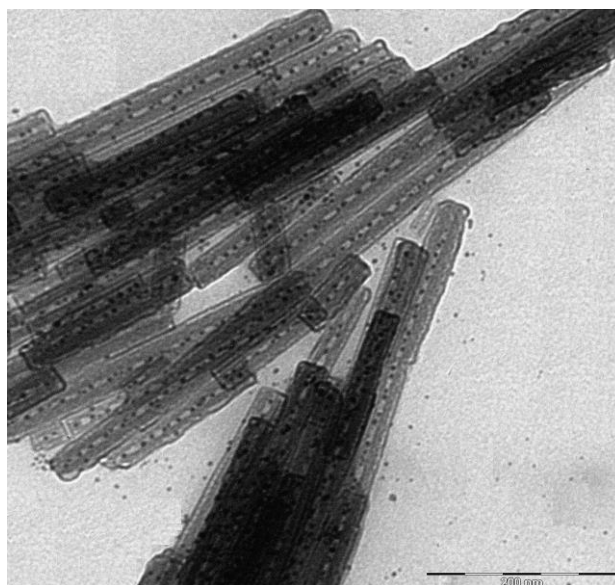


Figure 5.59: TEM image of chrysotile nanotubes and 1-butanethiol capped silver nanoparticles system

TEM micrographs (Fig.5.59) show that nanoparticles can be found within the central cavity of the nanotubes. These inorganic nanostructures are homogeneous and stable.

5.3.7 Characterization of chrysotile nanotubes and 4-methylbenzenethiol capped silver nanoparticles system

We first analysed the sample using FT-IR spectroscopy.

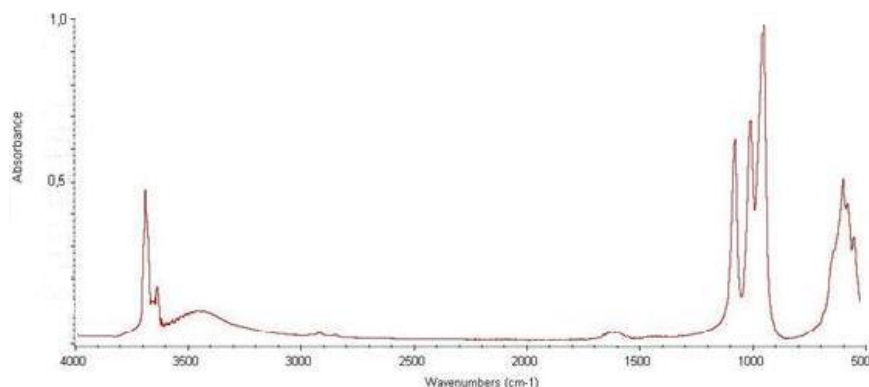


Figure 5.60: FT-IR spectrum of chrysotile nanotubes and 4-methylbenzenethiol capped silver nanoparticles system

The spectrum (Fig. 5.60) clearly shows two signals around the 3600-3700 cm^{-1} mark and 3 signals at approximately 900-1100 cm^{-1} of the chrysotile nanotubes. Signals from the capping agent, particularly unresolved signals with bandwidth of 2900 cm^{-1} from the methylene group, demonstrate the presence of nanoparticles. Typical absorption levels from 4-methylbenzenethiol capped silver nanoparticles are very low due to the low relative amount of capping agent analysed. TEM analysis was used for the dimensional and morphological characterization of this system.

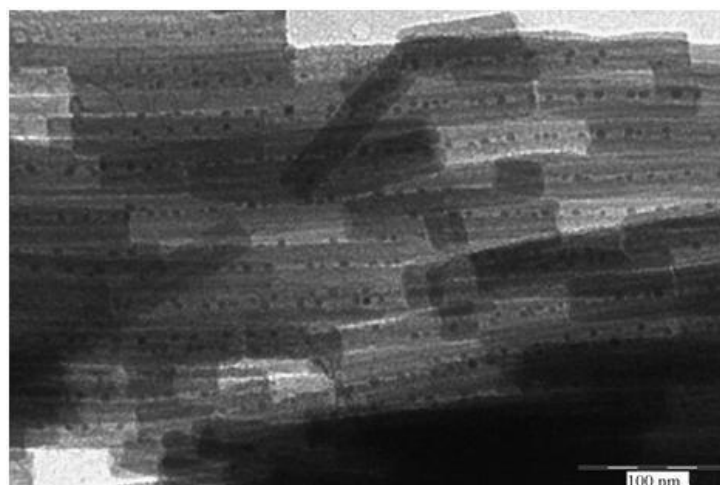


Figure 5.61: TEM image of chrysotile nanotubes and 4-methylbenzenethiol capped silver nanoparticles system

TEM micrographs (Fig. 5.61) show that nanoparticles can be found within the central cavity of the nanotubes. These inorganic nanostructures are homogeneous and stable.

5.3.8 Conclusion

A number of different 1D inorganic nanostructured composites were synthesized and characterized during this phase.

Within synthetic chrysotile nanocrystals different types of thiol capped metal nanoparticles can be found, ensuring that these structures remain stable over time.

TEM micrographs show that the way these structures are formed results in the nanotubes being filled in a constant and homogenous way.

The nature of the capping agent does not have a particular influence over the formation process of these structures: nanoparticles with the same metallic core and different organic shell display the same behavior.

The type of metal that makes up the nanoparticles cores instead plays a fundamental role: copper particles, with both capping agents, do not enter the nanotubes structures, leaving the central core completely empty. Surface plasmon resonance (SPR) absence has shown variations of some of the chemical and physical properties of copper particles. These nanoparticles are the only thiol capped metal nanoparticles analysed that do not display this type of absorption. All other metal nanoparticles fill the central cores of chrysotile nanotubes.

The high ratio of synthetic chrysotile nanotubes mass to the thiol capped metal nanoparticles mass in these systems makes it difficult to detect signals which are typical of nanoparticles using FT-IR spectroscopy and UV-Vis spectroscopy.

5.4 Characterization of electrospun conductive polymer fibers

5.4.1 Characterization of electrospun polyaniline (PANI) fibers

5.4.1.1 Characterization of electrospun polyaniline (PANI) mat

A portion of the conductive polymeric mixed solution has been dried on a slide and then submitted to XRD diffraction pattern and conductivity measurements. XRD diffraction pattern has been carried out also to investigate the basic components of the polymeric blend. The analyses will work as comparison tests respect to the electrospun samples, both for single polymer and the nanocomposite. Below the diffraction patterns concerning polyaniline (Fig. 5.62), poly(ethylene oxide) (Fig. 5.63), camphorsulfonic acid (Fig. 5.64) and not electrospun polymeric blend (Fig. 5.65) are reported.

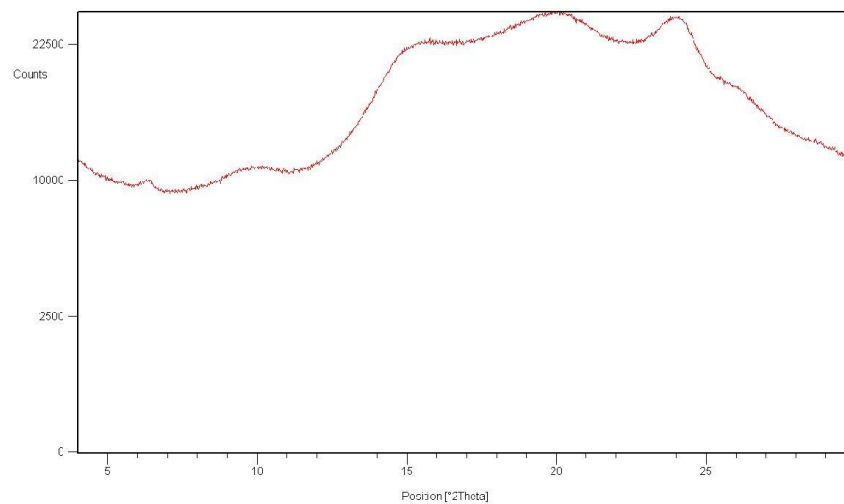


Figure 5.62: XRD diffractogram of polyaniline (PANI)

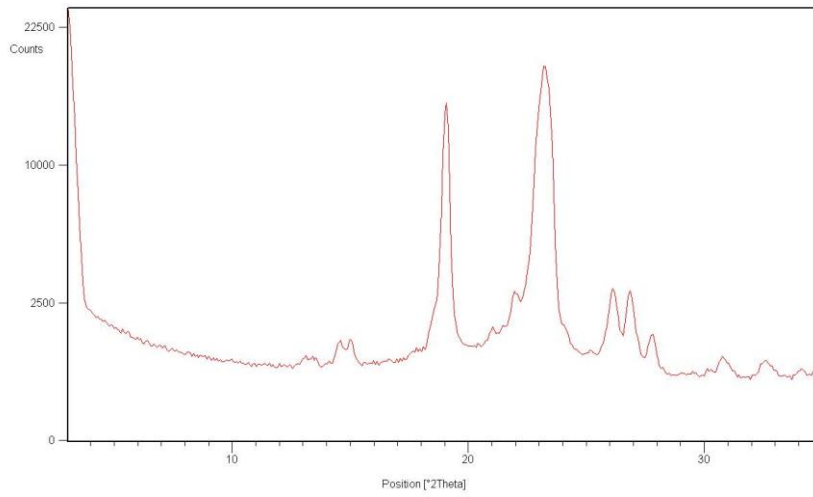


Figure 5.63: XRD diffractogram of poly(ethylene oxide) (PEO)

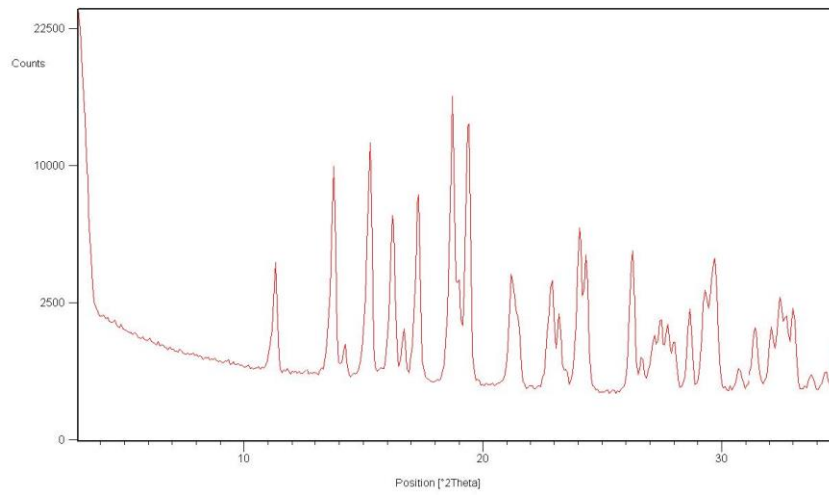


Figure 5.64: XRD diffractogram of camphorsulfonic acid (HCSA)

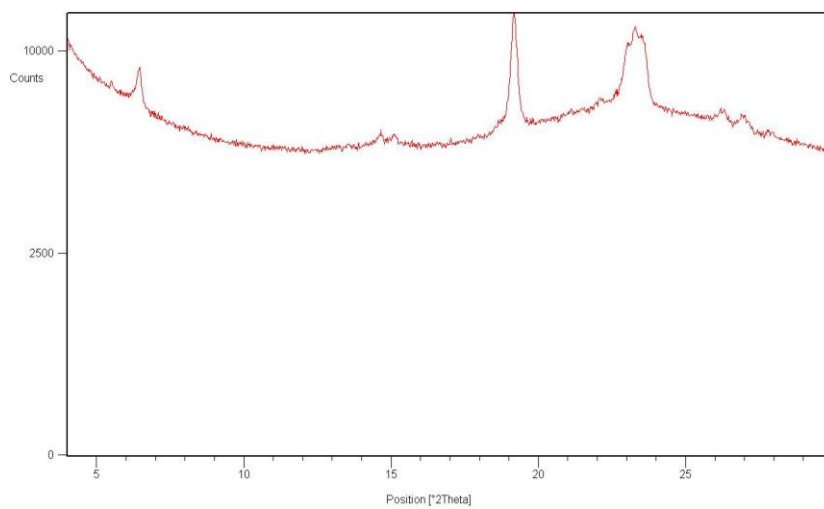


Figure 5.65: XRD diffractogram of not electrospun polymeric blend

Observing the diffraction patterns of the not electrospun polymeric blend it is possible to note the reflections at $2\theta = 19^\circ$ e $2\theta = 24^\circ$ which may be referred to one of the constituents, poly(ethylene oxide) and also the raising of the basic line confirms the presence of polyaniline. The peak at low angle, which is a new feature, is probably due to the rearrangement of the polymeric blend during the re-crystallizing occurred during the evaporation of the solvent.

Morphological, structural, thermal and electrical characterizations have been carried out on the electrospun polymer.

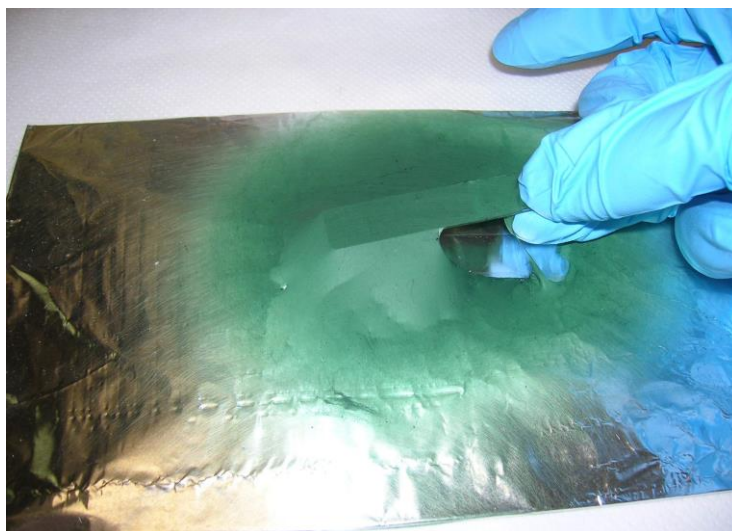


Figure 5.66: image of electrospun (PANI-HCSA-PEO) mat

SEM micrograph (Fig. 5.67) shows a not oriented network of the polymeric fibers stable over time, which have a good dimensional homogeneity and a medium diameter smaller than $1 \mu\text{m}$. The fibers obtained do not show any breakages or structural imperfections like beads and blobs.

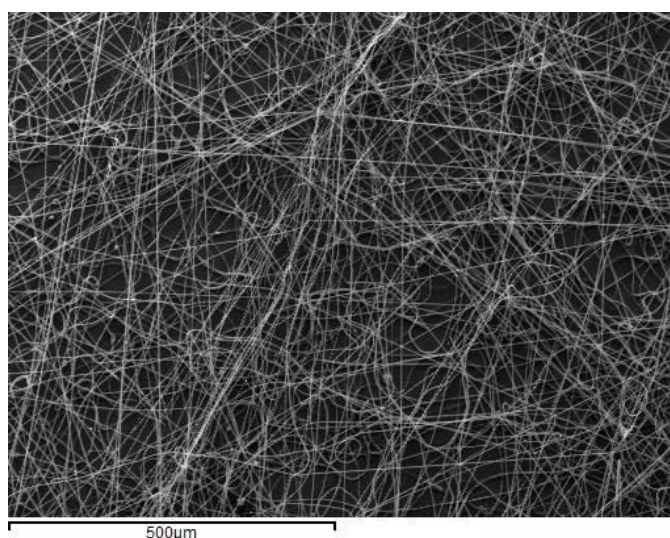


Figure 5.67: SEM image of electrospun (PANI-HCSA-PEO) fibers

XRD diffraction patterns of an electrospun polymeric mat (Fig. 568) have been carried out.

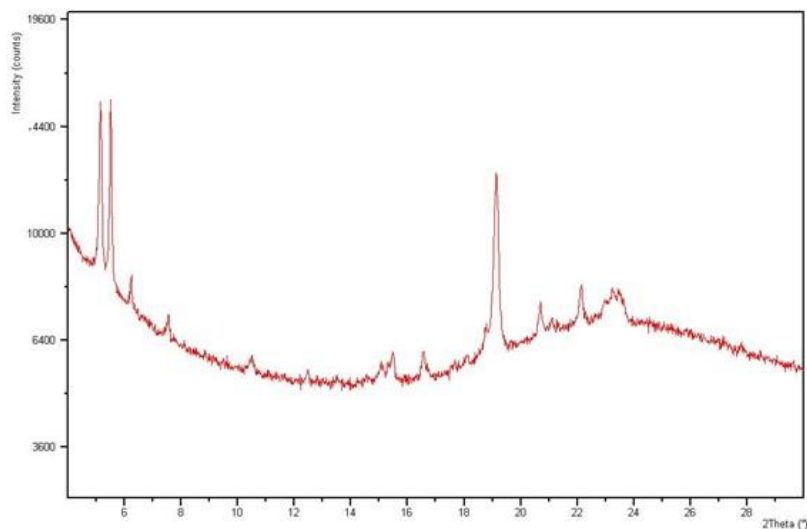


Figure 5.68: XRD diffractogram of electrospun (PANI-HCSA-PEO) fibers

The XRD diffractogram of electrospun (PANI-HCSA-PEO) fibers shows the typical reflections of the components in the polymeric blend. Besides, many other signals are visible which are probably due to a new structural arrangement induced by the preferential orientation caused by the electrospinning. The two most intense reflections, at about $2\theta = 5^\circ$, are a consequence of the arrangement of the polymeric chains, which dispose according to two preferential distances.

The less intense reflections, at $2\theta = 6^\circ$, $2\theta = 7.5^\circ$, $2\theta = 10.2^\circ$, $2\theta = 12.3^\circ$, are due to higher spacing of the bigger orders among the polymeric chains. The intense signal at about $2\theta = 19^\circ$ refers to the distance between the side-chains: in our case, referring to polyaniline it represents the length of the hydrogen bonds placing themselves between the side-chains. The widest peak at about $2\theta = 23^\circ$ is due the interplanar distance between the aromatic units which appear to interact by π - π stacking.

DSC thermal analyses (Fig. 5.69) have been made for these samples. DSC analyses show two endothermic peaks, the first one around 50°C ($\Delta H = +14\text{ J/g}$) and ascribable to the melting of poly(ethylene oxide) domains and the second one, around 96°C ($\Delta H = +151\text{ J/g}$), ascribable to the melting of polyaniline crystalline domains.

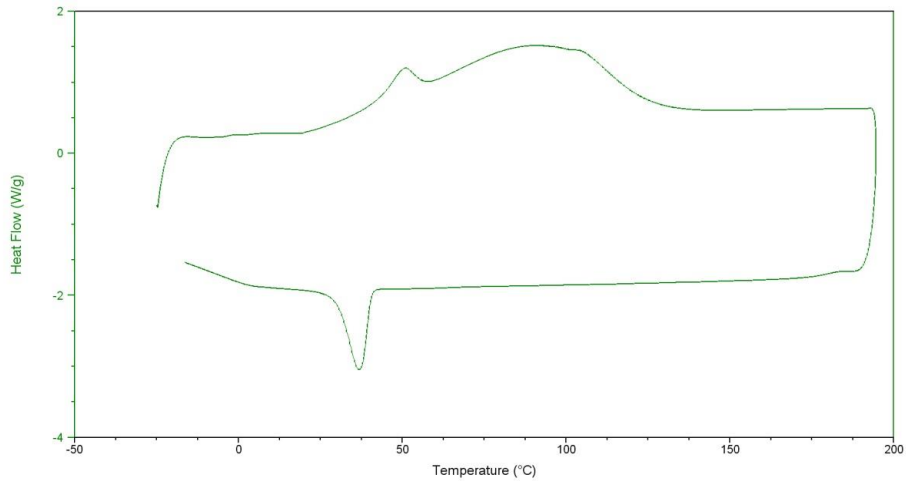


Figure 5.69: DSC curve of electrospun (PANI-HCSA-PEO) fibers

The analysis for the electrical conductivity with a teraohmter allowed to calculate the conductivity of the electrospun polymer.

$$\sigma = 1.26 * 10^{-7} \text{ S}\square$$

5.4.1.2 Characterization of electrospun polyaniline (PANI) yarn

SEM characterization (Fig. 5.70 - Fig. 5.71) show the formation of polymeric yarns made of single fibers rolled up around the same axis. The yarns are homogeneous, without any imperfections and with a regular diameter. In these systems the fibers still remain without imperfections and they dispose parallel orientated to each other (Fig. 5.72).

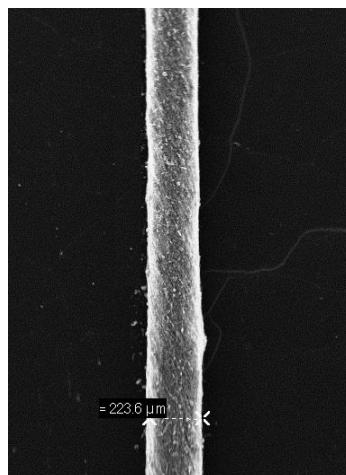


Figure 5.70: SEM micrograph of electrospun polyaniline (PANI) yarn

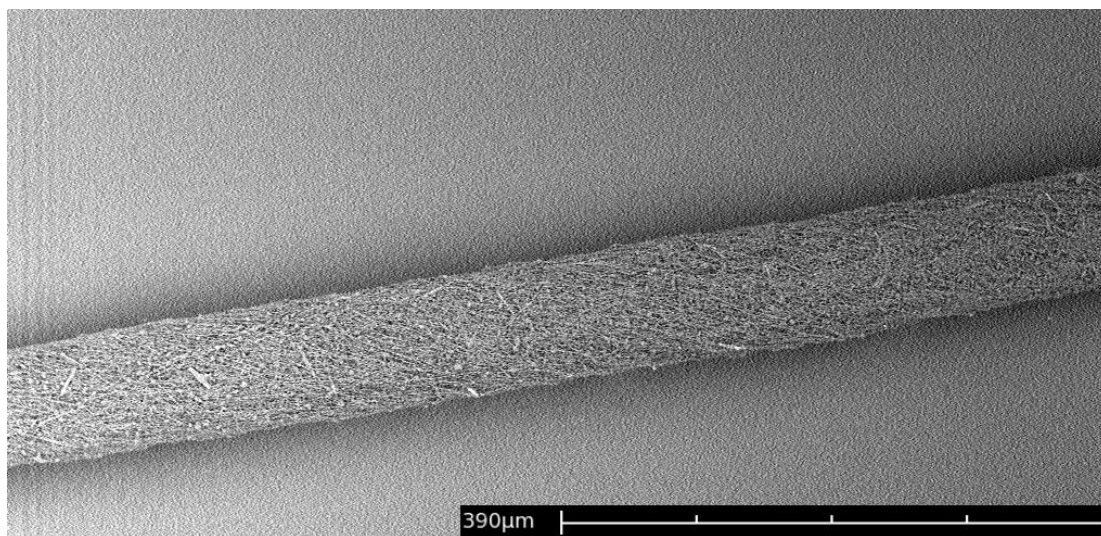


Figure 5.71: SEM micrograph of electrospun polyaniline (PANI) yarn

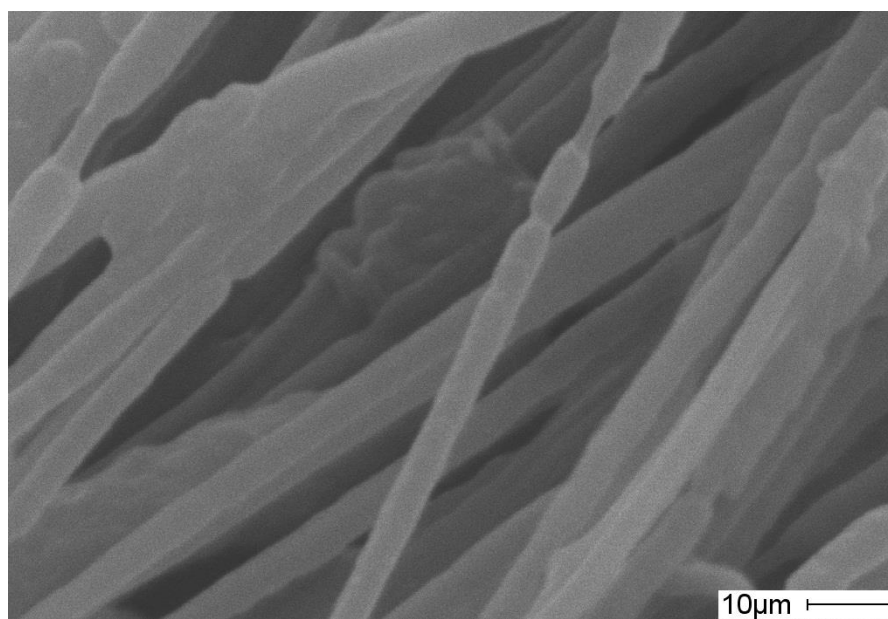


Figure 5.72: SEM micrograph of electrospun polyaniline (PANI) yarn

5.4.2 Characterization of electrospun poly(3-hexylthiophene) (P3HT) fibers

At first XRD diffraction patterns of the basic components of the polymeric blend have been carried out. The analyses will be a comparison feature for electrospun samples, made of a single polymer or a nanocomposite. Below the diffraction patterns of poly(3-hexylthiophene) (Fig. 5.73) and poly(ethylene oxide) (Fig. 5.74) are reported.

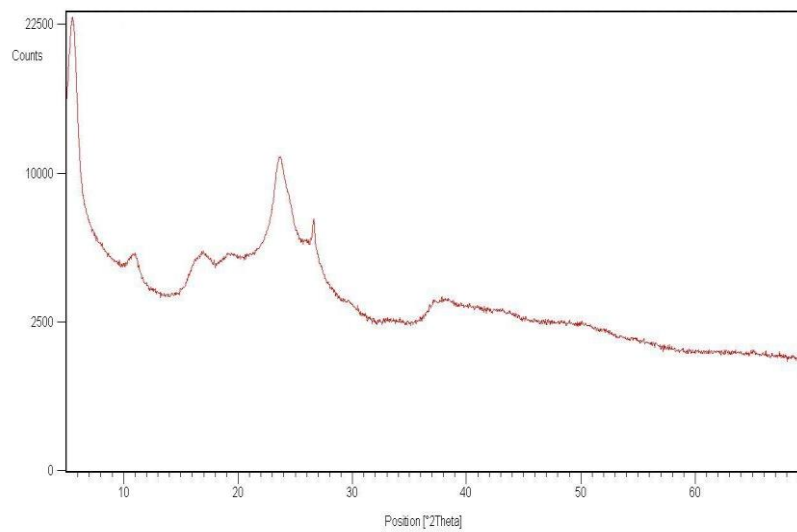


Figure 5.73: XRD diffractogram of poly(3-hexylthiophene) (P3HT)

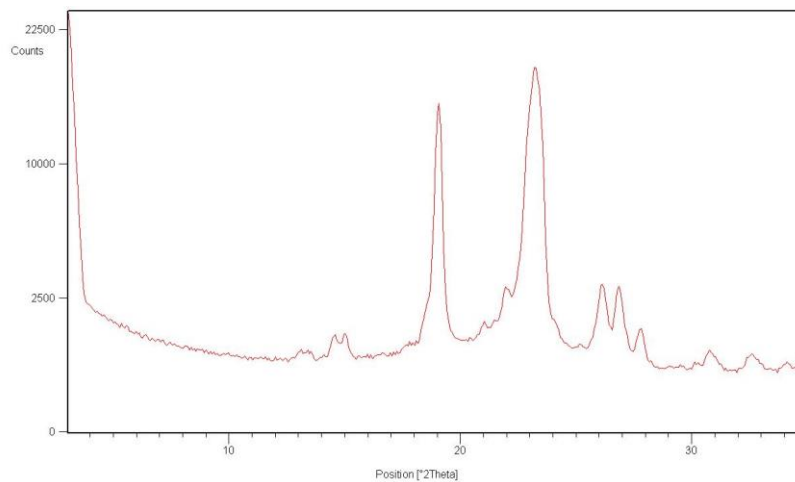


Figure 5.74: XRD diffractogram of poly(ethylene oxide) PEO

Morphological, structural, thermal and electrical characterizations have been made on the electrospun polymer.



Figure 5.75: image of electrospun (P3HT-PEO) mat

SEM micrographs (Fig. 5.76 – Fig. 5.77) show a not oriented network of polymeric fibers stable in time, with a good dimensional homogeneity and a medium diameter smaller than 1 μm . The observed fibers do not show any breakage or structural imperfections like beads and blobs.

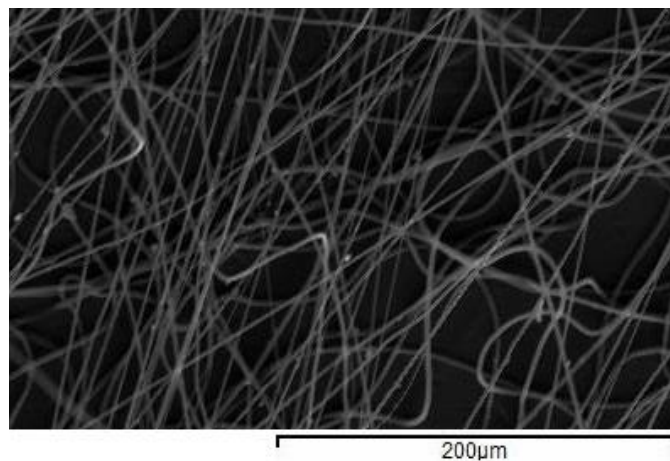


Figura 5.76: SEM immagine of electrospun (P3HT-PEO) fibers

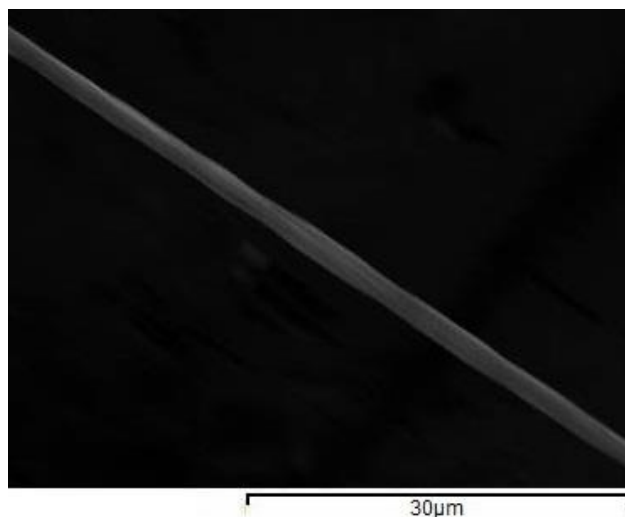


Figura 5.77: SEM image of electrospun (P3HT -PEO) fiber

XRD analyses of the electrospun (Fig. 5.78) polymeric mat have been made.

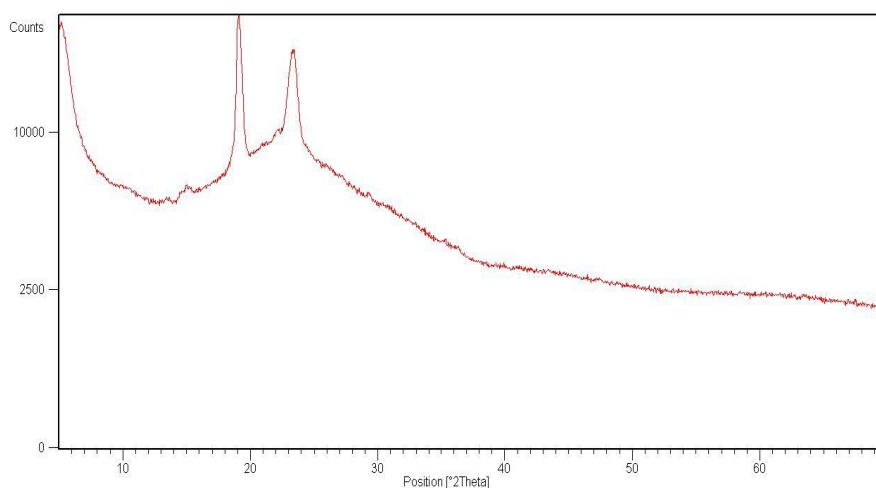


Figure 5.78: XRD diffractogram of electrospun (P3HT-PEO) fibers

In the XRD diffraction patterns of the electrospun (P3HT-PEO) fibers it is possible to note the typical signals referred to the components of the polymeric blend. Besides it is possible to see many other reflections due to the new structural arrangement induced by the preferential orientation caused by the electrospinning

The most intense reflection, at about $2\theta = 5^\circ$, is the consequence of the arrangement of the polymeric chains in the same plane. The peak at about $2\theta = 11^\circ$ is due the distance between the hexyl chains of poly(3-hexylthiophene). The peak at about $2\theta = 26^\circ$ is due the interplanar distance between the aromatic units which appear to interact by π - π stacking.

Thermal analysis of the samples using DSC (Fig. 5.79) reveals the presence of two endothermic peaks, the first around 64.05 °C ($\Delta H = +61.27$ J/g) ascribable to the melting of poly(ethylene oxide) domains and the second, around 234.73 °C ($\Delta H = +5.18$ J/g) to the melting of poly(3-hexylthiophene) crystalline domains.

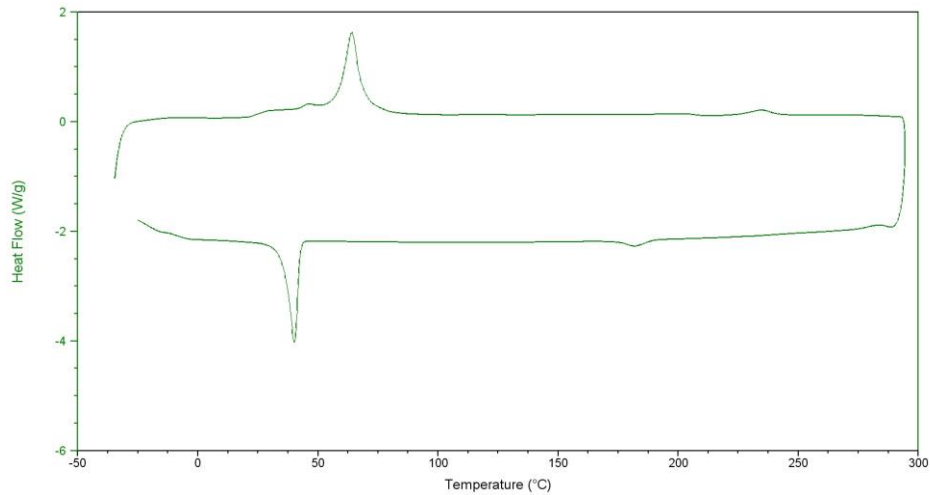


Figure 5.79: DSC curve of electrospun (P3HT-PEO) fibers

The analysis for the electrical conductivity with a teraohmometer allowed to calculate the conductivity of the electrospun polymer.

$$\sigma_{\text{UNDOPEd}} = 6.94 * 10^{-9} \text{ S}\square$$

$$\sigma_{\text{DOPEd}} = 1.04 * 10^{-3} \text{ S}\square$$

5.4.3 Conclusion

Both conductive polymers used can be electrospun by adding poly(ethylene oxide) (PEO), which however limits the electrical properties since this is an insulating material. The polymeric fibers are stable in time, they do not tend to deteriorate and do not present imperfections either when producing mats or yarns. The use of double rotating collectors allows of the production of electrospun fibers with morphology and orientation which are different respect to the mat produced using planar collectors. As already explained the conductivity in both materials is not very high

because of the presence of poly(ethylene oxide); besides, the measured conductivity does not concern one fiber but the whole material.

Both DSC thermal analyses and XRD structural analyses confirm the presence of the basic components of the polymeric blend used; besides the latter analyses put in evidence that the electrospinning technique is able to produce structures with different characteristics respect to the material in film. Applying a strong magnetic field extend the polymeric chains along the axis of the fibers producing structures with a considerably high surface/mass ratio. The conductivity of the poly(3-hexylthiophene) - poly(ethylene oxide) fibers increases significantly with the doping.

5.5 Characterization of electrospun conductive polymer fibers

5.5.1 Characterization of electrospun polyaniline (PANI) and 4-methylbenzenethiol capped silver nanoparticles fibers

TEM micrographs of electrospun polyaniline (PANI) and 4-methylbenzenethiol capped silver nanoparticles fibers (Fig.5.80) show the presence of the filler within the fiber.

Fibers have a submicron diameter and are filled evenly and without aggregates of nanoparticles.

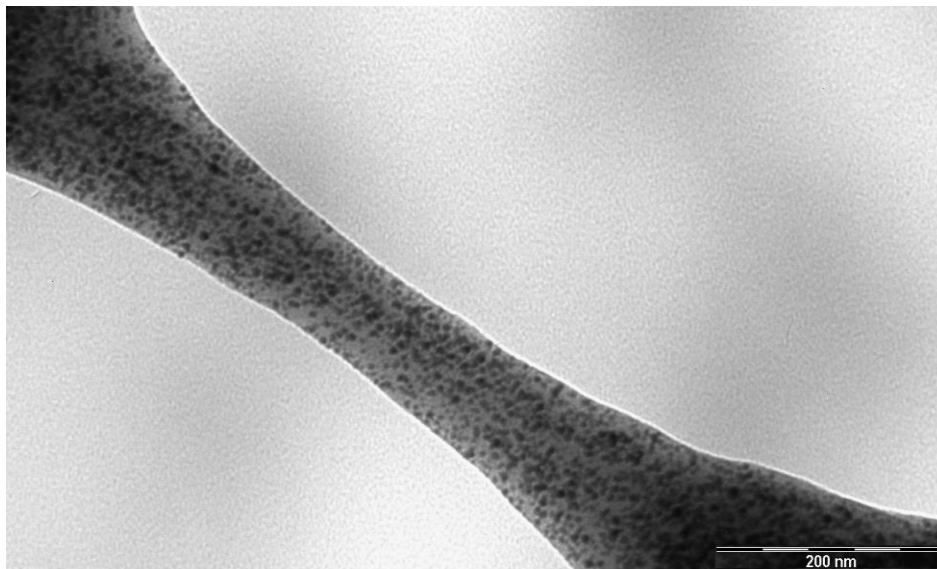


Figure 5.80: TEM micrograph electrospun polyaniline (PANI) and 4-methylbenzenethiol capped silver nanoparticles fibers

SEM analysis of electrospun polyaniline (PANI) and 4-methylbenzenethiol capped Ag nanoparticles fibers (Fig.5.81) show the presence of fibers with a submicron diameter which display didn't display any imperfection.

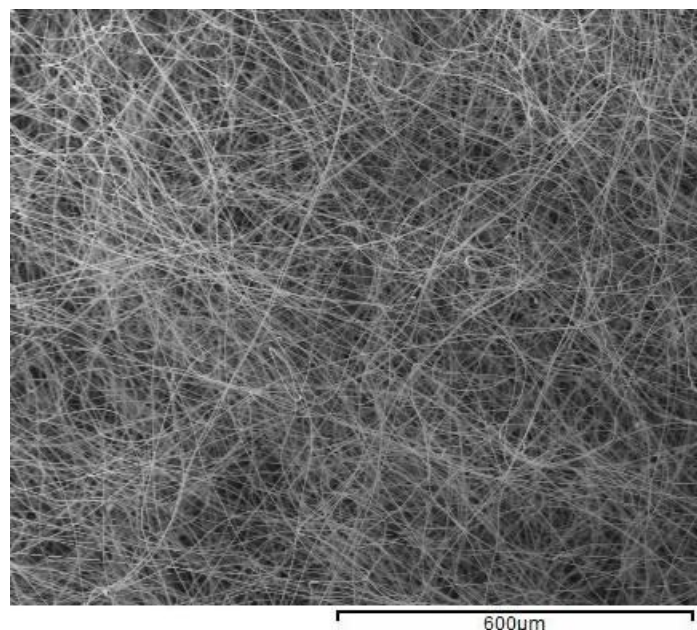


Figure 5.81: SEM micrograph of electrospun polyaniline (PANI) and 4-methylbenzenethiol capped silver nanoparticles fibers

Reflections highlighted by XRD analysis (Fig. 5.82) are characteristic of the basic components of the polymeric blend we used. Moreover, reflections at low angle (caused by the structural order of the material) display a change in intensity. This confirms the changes in the organization of the polymer chains within the fibers due to the insertion of the filler.

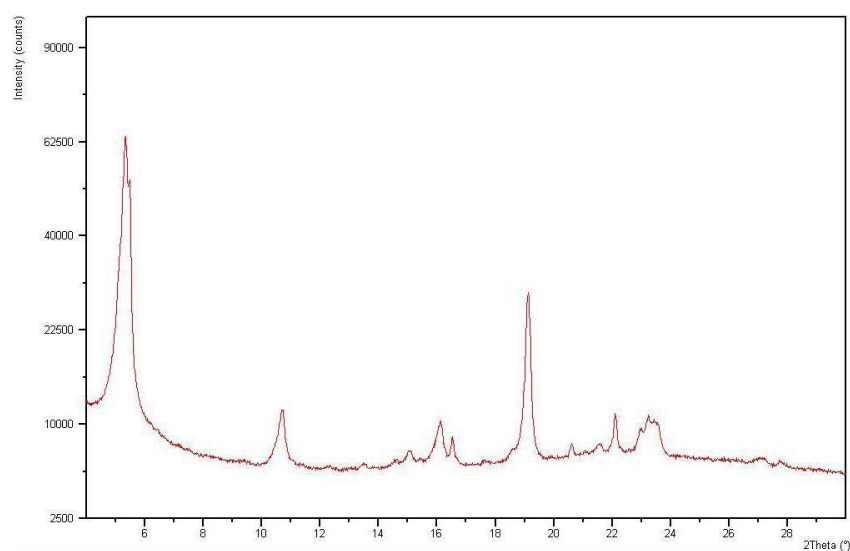


Figure 5.82 XRD diffractogram of electrospun polyaniline (PANI) and 4-methylbenzenethiol capped silver nanoparticles fibers

An analysis of electrical properties of electrospun polyaniline (PANI) and 4-methylbenzenethiol capped silver nanoparticles fibers was used to measure its electrical conductivity:

$$\sigma = 5.68 * 10^{-7} \text{ S}\square$$

5.5.2 Characterization of electrospun polyaniline (PANI) and 1-butanethiol capped copper nanoparticles fibers

TEM micrographs of electrospun polyaniline (PANI) and 1-butanethiol capped copper nanoparticles fibers (Fig. 5.83) show the presence of the filler within the fiber.

Fibers have a submicron diameter and are filled evenly and without aggregates of nanoparticles.

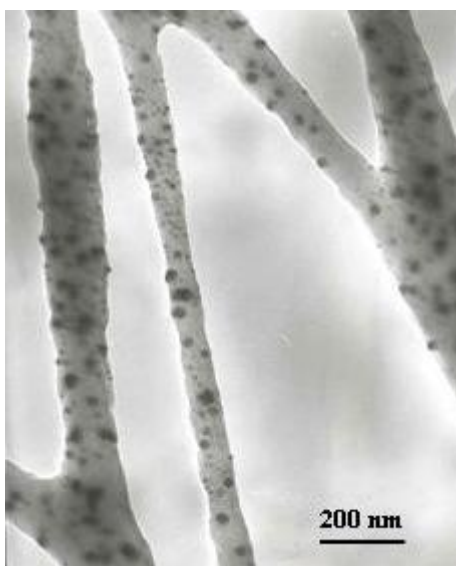


Figure 5.83: TEM micrograph electrospun polyaniline (PANI) and 1-butanethiol capped copper nanoparticles fibers

SEM analysis of electrospun polyaniline (PANI) and 1-butanethiol capped copper nanoparticles fibers (Fig. 5.84) show the presence of fibers with a submicron diameter which don't display any imperfection.

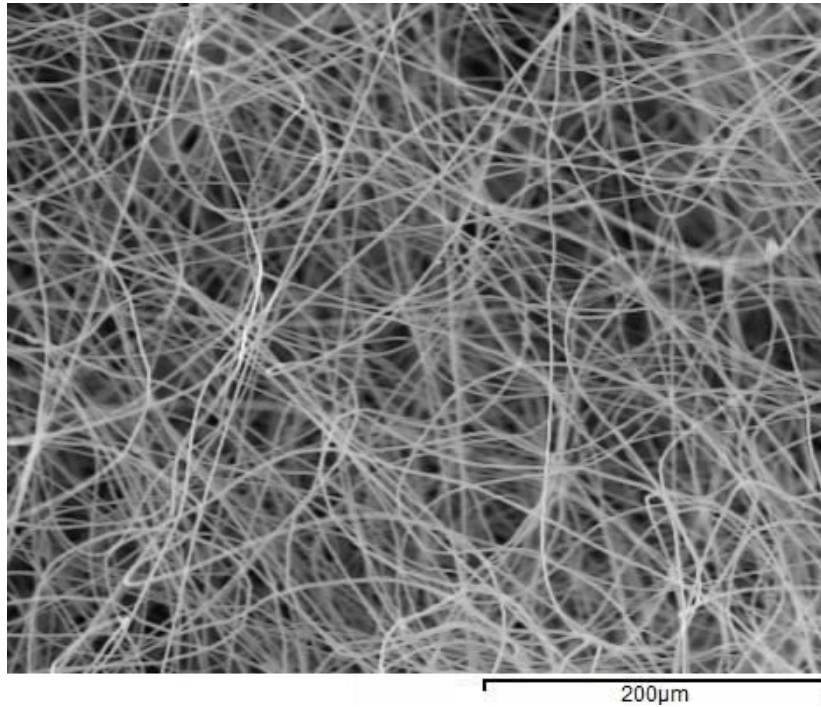


Figure 5.84: SEM micrograph of electrospun polyaniline (PANI) and 1-butanethiol capped copper nanoparticles fibers

An analysis of electrical properties of electrospun polyaniline (PANI) and 1-butanethiol capped copper nanoparticles fibers was used to measure its electrical conductivity:

$$\sigma = 4.00 * 10^{-11} \text{ S}\square$$

5.5.3 Characterization of electrospun polyaniline (PANI) and copper nanoparticles fibers

TEM micrographs of electrospun polyaniline (PANI) and copper nanoparticles fibers (Fig. 5.85) show the presence of filler within the fibers. Fibers have a non-constant diameter greater than a micrometer and are filled with aggregates of nanoparticles in a rather inhomogeneous manner.

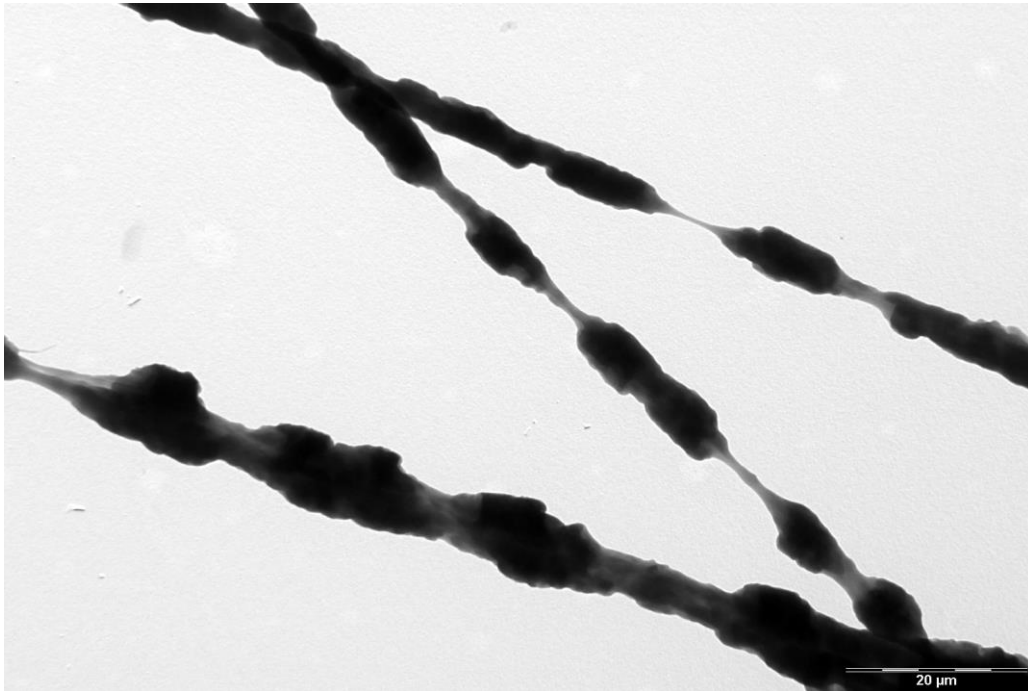


Figure 5.85: TEM micrograph of electrospun polyaniline (PANI) and copper nanoparticles fibers

An analysis of electrical properties of electrospun polyaniline (PANI) and copper nanoparticles fibers was used to measure their electrical conductivity:

$$\sigma = 1.40 * 10^{-7} \text{ S}\square$$

5.5.4 Characterization of electrospun polyaniline (PANI) and 4-methylbenzenethiol capped gold nanoparticles fibers

TEM micrographs of electrospun polyaniline (PANI) and 4-methylbenzenethiol capped gold nanoparticles fibers (Fig. 5.86) show the presence of filler within the fibers. Fibers have a submicron diameter and are filled evenly and without aggregates of nanoparticles.

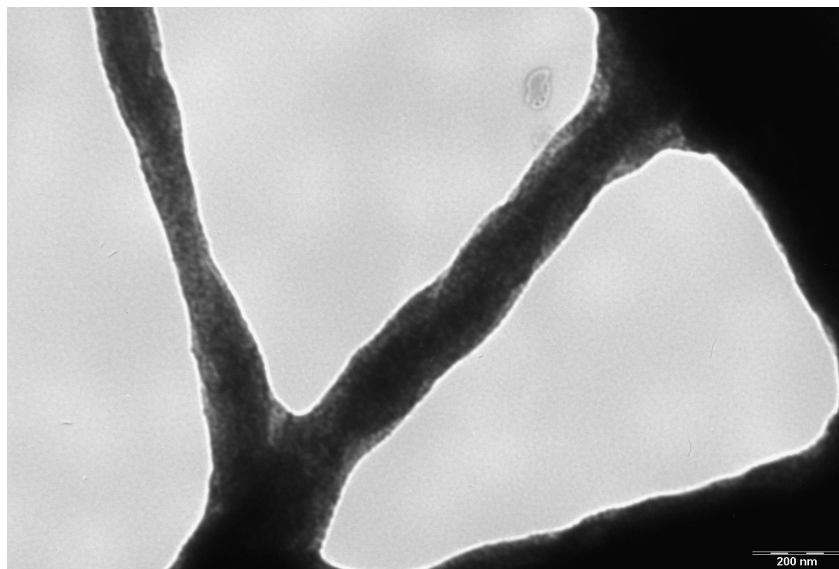


Figure 5.86: TEM micrograph of electrospun polyaniline (PANI) and 4-methylbenzenethiol capped gold nanoparticles fibers

SEM analysis of electrospun polyaniline (PANI) and 4-methylbenzenethiol capped gold nanoparticles fibers (Fig. 5.87) show the presence of fibers with a submicron diameter which don't display any imperfection.

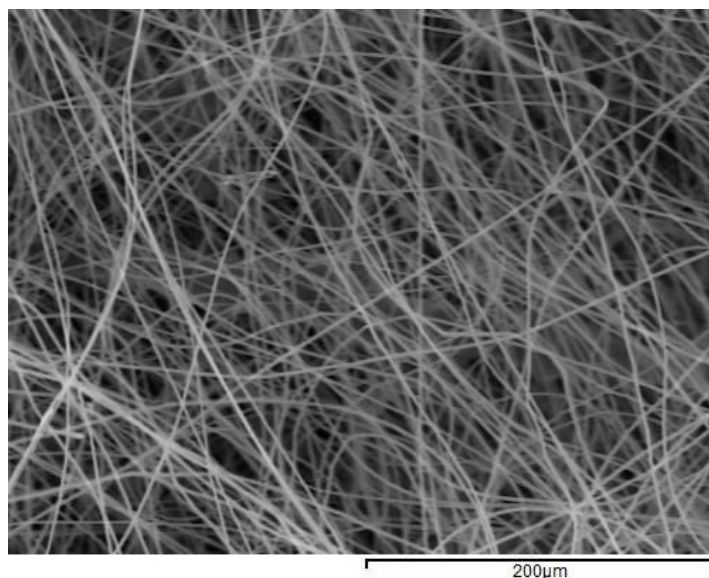


Figure 5.87: SEM micrograph of electrospun polyaniline (PANI) and 4-methylbenzenethiol capped gold nanoparticles fibers

Reflections highlighted by XRD analysis (Fig. 5.88) are characteristic of the basic components of the polymeric blend we used. Three signals around the $2\theta = 5^\circ$ mark are clearly noticeable which show that three interchain distances occur preferentially. Moreover, the intensity of a reflection with an angle of $2\theta = 19^\circ$ is significantly lower.

We can postulate that the differences we observed between these samples and the samples previously analysed are due to changes to the structural order caused by the presence of a second phase formed by nanometric particles.

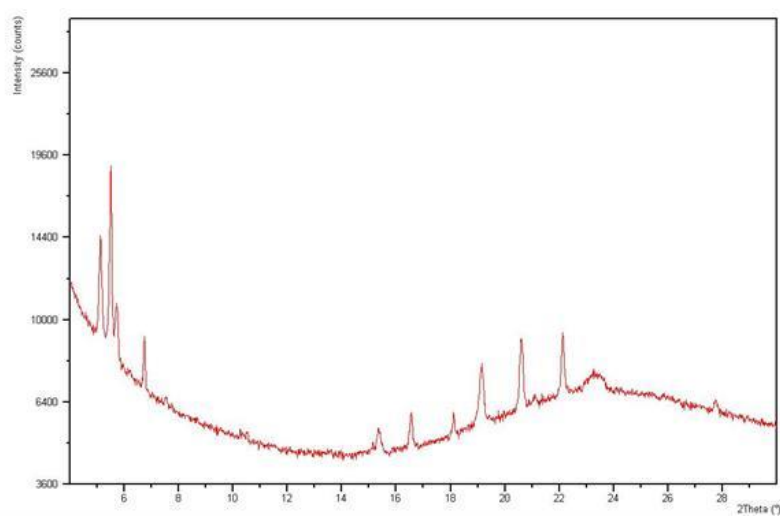


Figure 5.88: XRD diffractogram of electrospun polyaniline (PANI) and 4-methylbenzenethiol capped gold nanoparticles fibers

An analysis of electrical properties of electrospun polyaniline (PANI) and 4-methylbenzenethiol capped gold nanoparticles fibers was used to measure their electrical conductivity:

$$\sigma = 3.33 * 10^{-7} \text{ S}\square$$

5.5.5 Characterization of electrospun polyaniline (PANI) and 4-methylbenzenethiol capped gold-silver 1:4 nanoparticles fibers

TEM micrographs of electrospun polyaniline (PANI) and 4-methylbenzenethiol capped gold-silver 1:4 nanoparticles fibers (Fig. 5.89) show the presence of filler within the fibers. Fibers have a submicron diameter and are filled evenly and without aggregates of nanoparticles.



Figure 5.89: TEM micrograph of electrospun polyaniline (PANI) and 4-methylbenzenethiol capped gold-silver 1:4 nanoparticles fibers

SEM analysis of electrospun polyaniline (PANI) and 4-methylbenzenethiol capped gold-silver 1:4 nanoparticles fibers (Fig. 5.90) show the presence of fibers with a submicron diameter which don't display any imperfection.

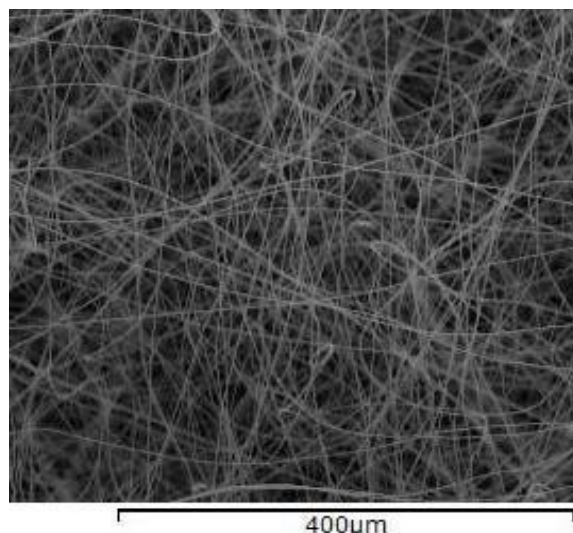


Figure 5.90: SEM micrograph of electrospun polyaniline (PANI) and 4-methylbenzenethiol capped gold-silver 1:4 nanoparticles fibers

Reflections highlighted by XRD analysis (Fig. 5.91) are characteristic of the basic components of the employed polymeric blend. Also, the ratio of peak intensities related to all the signals remains practically unchanged. Again, three signals around the $2\theta = 5^\circ$ mark are clearly noticeable which show that three interchain distances occur preferentially.

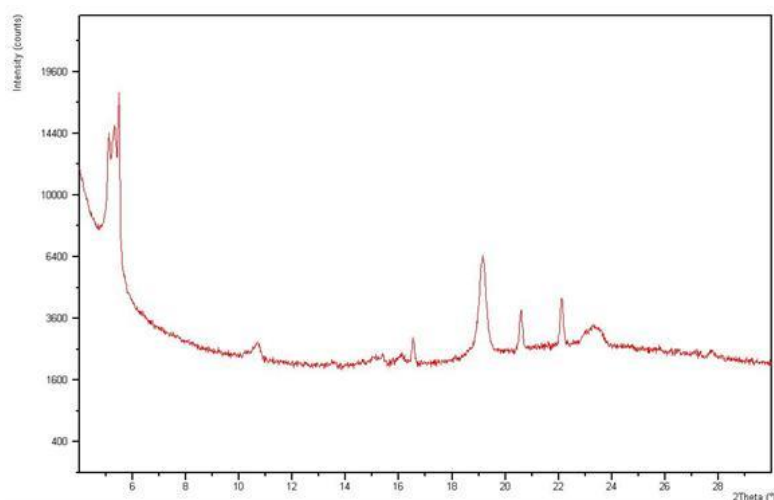


Figure 5.91: XRD diffractogram of electrospun polyaniline (PANI) and 4-methylbenzenethiol capped gold-silver 1:4 nanoparticles fibers

An analysis of electrical properties of electrospun polyaniline (PANI) and 4-methylbenzenethiol capped gold-silver 1:4 nanoparticles fibers was used to measure their electrical conductivity:

$$\sigma = 1.63 * 10^{-7} \text{ S}\square$$

5.5.6 Characterization of electrospun polyaniline (PANI) and 4-methylbenzenethiol capped gold-silver 4:1 nanoparticles fibers

TEM micrographs of electrospun polyaniline (PANI) and 4-methylbenzenethiol capped gold-silver 1:4 nanoparticles fibers (Fig. 5.92) show the presence of filler within the fibers. Fibers have a submicron diameter and are filled evenly and without aggregates of nanoparticles.



Figure 5.92: TEM micrograph of electrospun polyaniline (PANI) and 4-methylbenzenethiol capped gold-silver 4:1 nanoparticles fibers

SEM analysis of electrospun polyaniline (PANI) and 4-methylbenzenethiol capped gold-silver 4:1 nanoparticles fibers (Fig. 5.93) show the presence of fibers with a submicron diameter which don't display any imperfection.

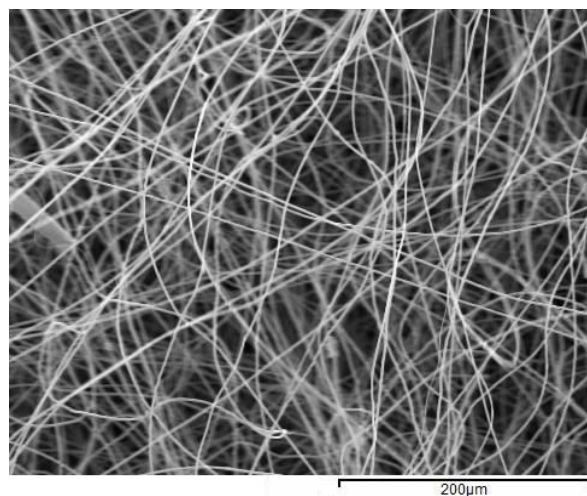


Figure 5.93: SEM micrograph of electrospun polyaniline (PANI) and 4-methylbenzenethiol capped gold-silver 4:1 nanoparticles fibers

Reflections highlighted by XRD analysis (Fig. 5.94) are characteristic of the basic components of the used polymeric blend. Also, the ratio of peak intensities related to all the signals remains practically unchanged. Again, three signals around the $2\theta = 5^\circ$ mark are clearly noticeable which show that two interchain distances preferentially occur within the fibers.

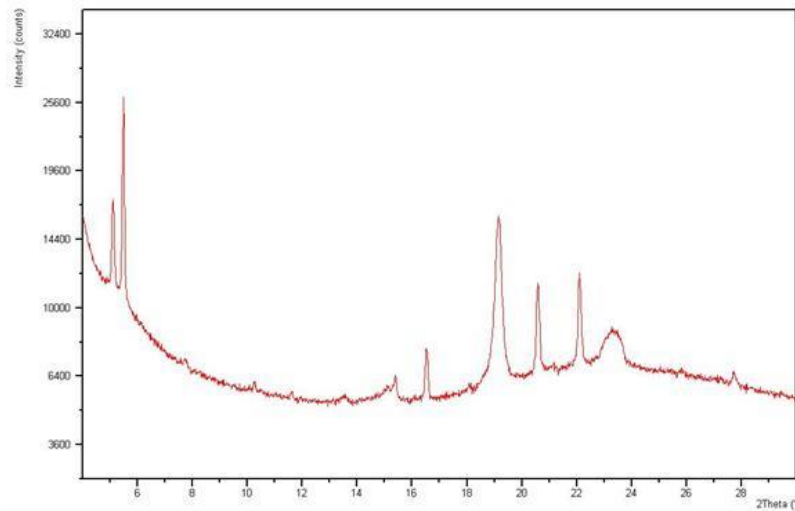


Figure 5.94: XRD diffractogram of electrospun polyaniline (PANI) and 4-methylbenzenethiol capped gold-silver 4:1 nanoparticles fibers

An analysis of electrical properties of electrospun polyaniline (PANI) and 4-methylbenzenethiol capped gold-silver 4:1 nanoparticles fibers was used to measure their electrical conductivity:

$$\sigma = 1.81 * 10^{-7} \text{ S}\square$$

5.5.7 Characterization of electrospun polyaniline (PANI) and 1-butanethiol capped silver-copper 1:1 nanoparticles fibers

TEM micrographs of electrospun polyaniline (PANI) and 1-butanethiol capped silver-copper 1:1 nanoparticles fibers (Fig.5.95) show the presence of filler within the fibers. Fibers have a submicron diameter and are filled evenly and without aggregates of nanoparticles.

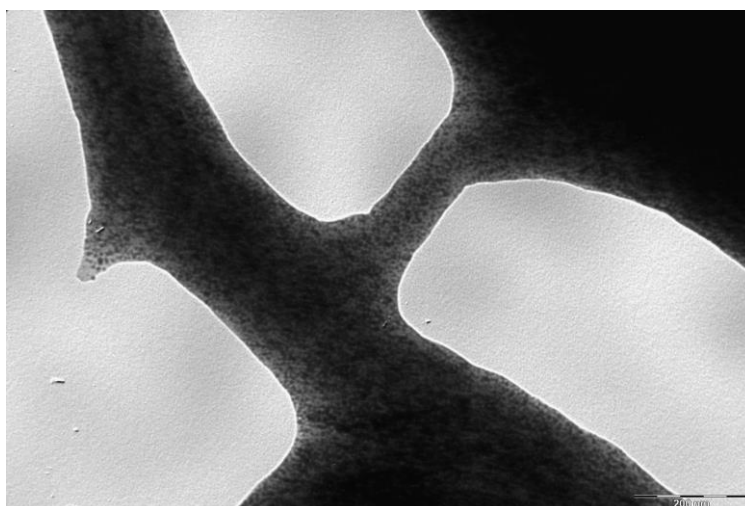


Figure 5.95: TEM micrograph electrospun polyaniline (PANI) and 1-butanethiol capped silver-copper 1:1 nanoparticles fibers

SEM analysis of electrospun polyaniline (PANI) and 1-butanethiol capped silver-copper 1:1 nanoparticles fibers (Fig. 5.96) show the presence of fibers with a submicron diameter which don't show any imperfection

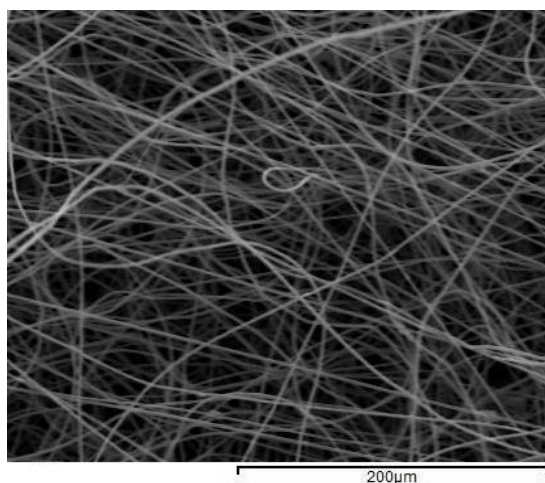


Figure 5.96: SEM micrograph of electrospun polyaniline (PANI) and 1-butanethiol capped silver-copper 1:1 nanoparticles fibers

An analysis of electrical properties of electrospun polyaniline (PANI) and 1-butanethiol capped silver-copper 1:1 nanoparticles fibers was used to measure their electrical conductivity:

$$\sigma = 1.94 * 10^{-7} \text{ S}\square$$

5.5.8 Characterization of electrospun polyaniline (PANI) and silver-copper 1:1 nanoparticles fibers

TEM micrographs of electrospun polyaniline (PANI) and silver-copper 1:1 nanoparticles fibers (Fig. 5.97) show the presence of filler within the fibers. Fibers have a non-constant diameter and are filled with aggregates of nanoparticles in a rather inhomogeneous manner.

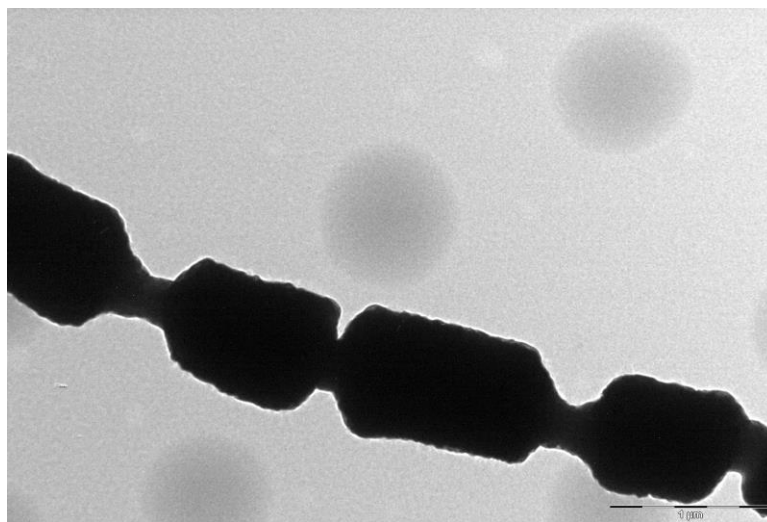


Figure 5.97: TEM micrograph of electrospun polyaniline (PANI) silver-copper 1:1 nanoparticles fibers

An analysis of electrical properties of electrospun polyaniline (PANI) and silver-copper 1:1 nanoparticles fibers was used to measure their electrical conductivity:

$$\sigma = 4.40 * 10^{-7} \text{ S}\square$$

5.5.9 Characterization of electrospun polyaniline (PANI) and anatase nanoparticles fibers

TEM micrographs of electrospun polyaniline (PANI) and anatase (TiO₂) nanoparticles fibers (Fig. 5.98) show the presence of filler within the fibers. Fibers have a non-constant diameter and are filled with aggregates of nanoparticles in a rather inhomogeneous manner.

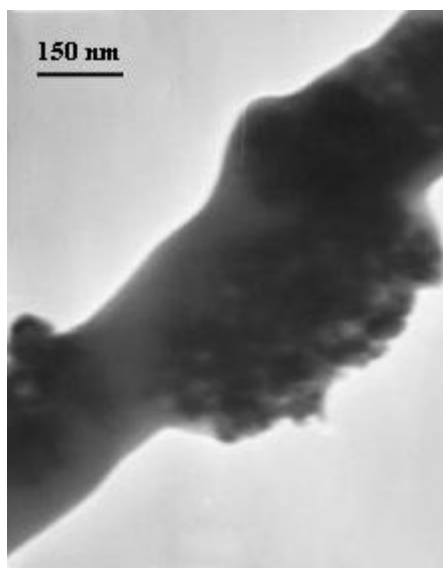


Figure 5.98: TEM micrograph of electrospun polyaniline (PANI) anatase nanoparticles fibers

An analysis of electrical properties of electrospun polyaniline (PANI) and anatase nanoparticles fibers was used to measure their electrical conductivity:

$$\sigma = 1.25 * 10^{-7} \text{ S}\square$$

5.5.10 Characterization of electrospun polyaniline (PANI) and copper (I) chloride nanoparticles fibers

TEM micrographs of electrospun polyaniline (PANI) and copper (I) chloride nanoparticles fibers (Fig. 5.99) show the presence of filler within the fibers. Fibers have a submicron, constant diameter. Fibers are filled evenly and homogeneously, without aggregates of nanoparticles.

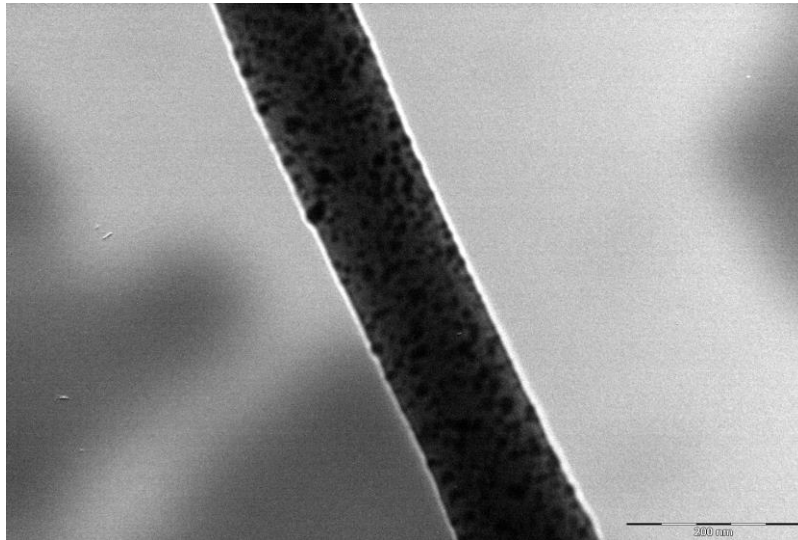


Figure 5.99: TEM micrograph of electrospun polyaniline (PANI) copper (I) chloride nanoparticles fibers

An analysis of electrical properties of electrospun polyaniline (PANI) and copper (I) chloride nanoparticles fibers was used to measure their electrical conductivity:

$$\sigma = 1.06 * 10^{-8} \text{ S}\square$$

5.5.11 Characterization of electrospun polyaniline (PANI) and chrysotile nanotubes 1-butanethiol capped copper nanoparticles system fibers

SEM analysis of electrospun polyaniline (PANI) and chrysotile nanotubes 1-butanethiol capped copper nanoparticles system fibers (Fig. 5.100) show the presence of fibers with a submicron diameter which don't display any imperfection.

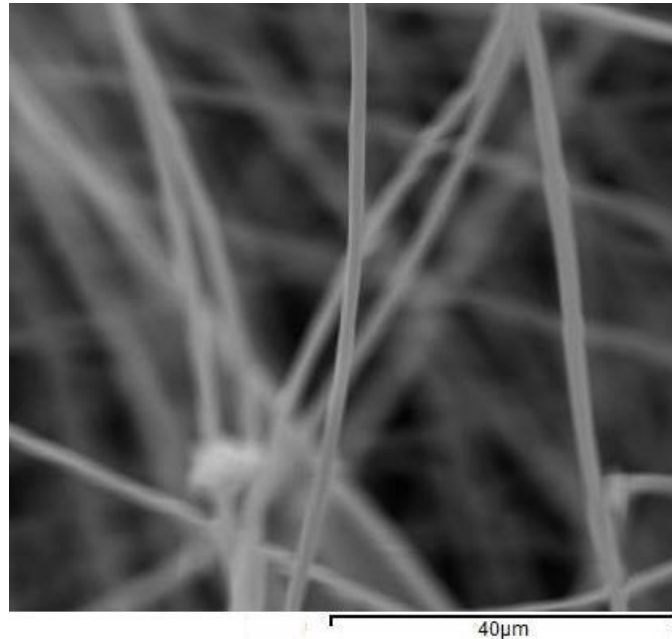


Figure 5.100: SEM micrograph of electrospun polyaniline (PANI) and chrysotile nanotubes 1-butanethiol capped copper nanoparticles system fibers

An analysis of electrical properties of electrospun polyaniline (PANI) and chrysotile nanotubes 1-butanethiol capped copper nanoparticles system fibers was used to measure their electrical conductivity:

$$\sigma = 1.15 * 10^{-7} \text{ S}\square$$

5.5.12 Characterization of electrospun polyaniline (PANI) and chrysotile nanotubes 4-methylbenzenethiol capped copper nanoparticles system fibers

SEM analysis of electrospun polyaniline (PANI) and chrysotile nanotubes 4-methylbenzenethiol capped copper nanoparticles system fibers (Fig. 5.101) show the presence of fibers with a submicron diameter which don't display any imperfection.

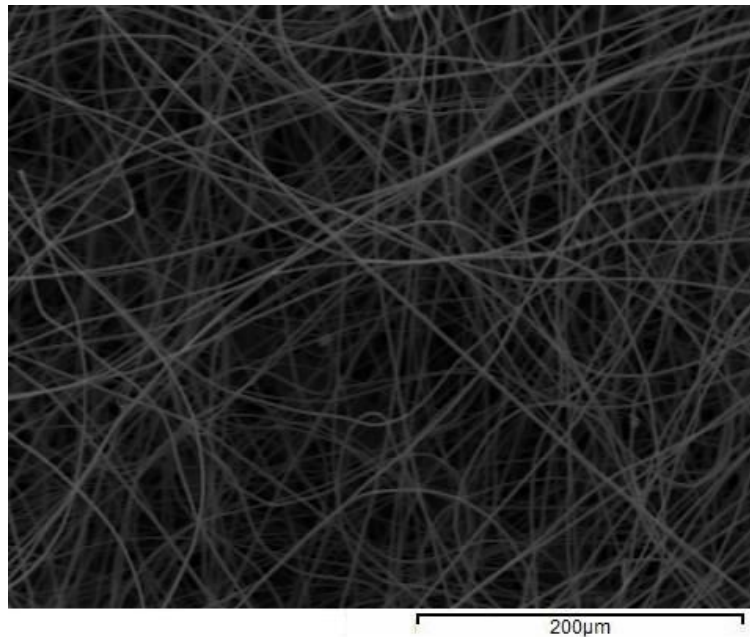


Figure 5.101: SEM micrograph of electrospun polyaniline (PANI) and chrysotile nanotubes 4-methylbenzenethiol capped copper nanoparticles system fibers

An analysis of electrical properties of electrospun polyaniline (PANI) and chrysotile nanotubes 4-methylbenzenethiol capped copper nanoparticles system fibers was used to measure their electrical conductivity:

$$\sigma = 1.15 * 10^{-7} \text{ S}\square$$

5.5.13 Characterization of electrospun polyaniline (PANI) and chrysotile nanotubes 4-methylbenzenethiol capped gold nanoparticles system fibers

SEM analysis of electrospun polyaniline (PANI) and chrysotile nanotubes 4-methylbenzenethiol capped Au nanoparticles system fibers (Fig. 5.102) show the presence of fibers with a submicron diameter which don't display any imperfection.

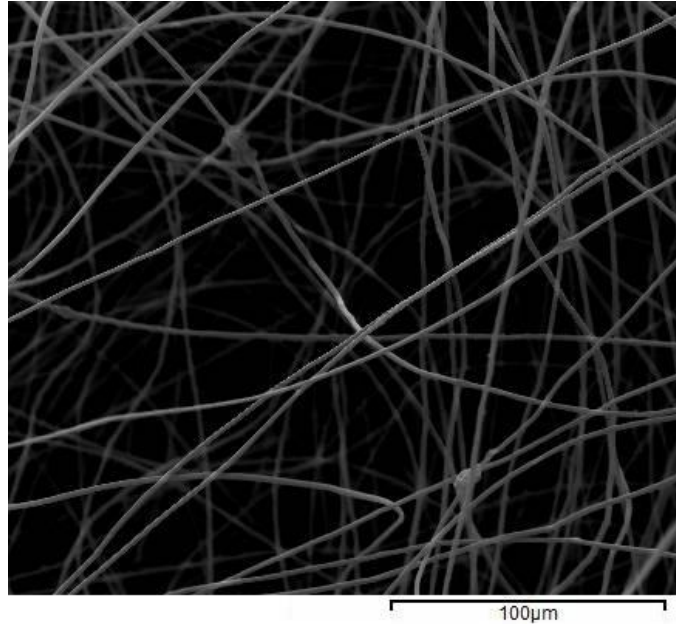


Figure 5.102: SEM micrograph of electrospun polyaniline (PANI) and chrysotile nanotubes 4-methylbenzenethiol capped gold nanoparticles system fibers

Reflections highlighted by XRD analysis (Fig. 5.103) are characteristic of the basic components of the polymeric blend we used. The $2\theta = 12^\circ$ signal typical of chrysotile was also highlighted. Two signals around the $2\theta = 5^\circ$ mark are clearly noticeable which show that two interchain distances preferentially occur.

Changes in the relative intensity of reflections typical of this polymer blend, particularly the reflection with an angle of $2\theta = 19^\circ$, are due to changes to the structural order caused by the presence of inorganic phase. This is not the case when the polymer has no filler.

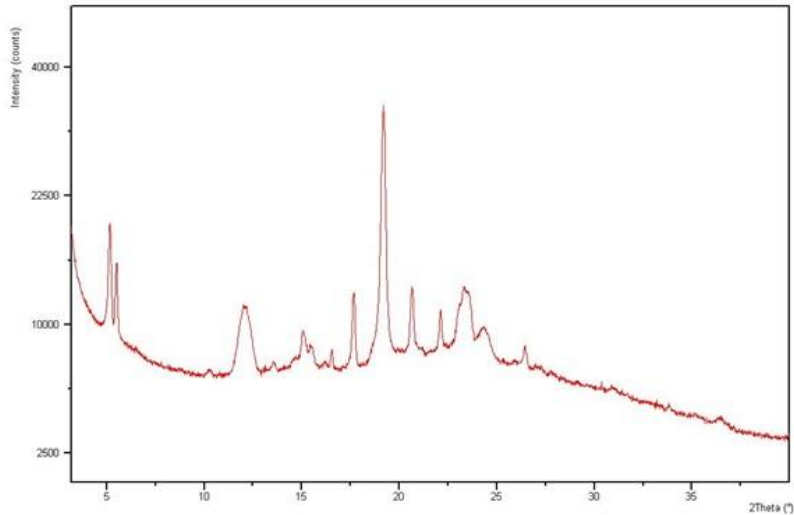


Figure 5.103: XRD diffractogram of electrospun polyaniline (PANI) and chrysotile nanotubes 4-methylbenzenethiol capped gold nanoparticles system fibers

An analysis of electrical properties of electrospun polyaniline (PANI) and chrysotile nanotubes 4-methylbenzenethiol capped gold nanoparticles system fibers was used to measure their electrical conductivity:

$$\sigma = 2.50 * 10^{-7} \text{ S}\square$$

5.5.14 Characterization of electrospun polyaniline (PANI) and chrysotile nanotubes 4-methylbenzenethiol capped gold-silver 1:4 nanoparticles system fibers

SEM analysis of electrospun polyaniline (PANI) and chrysotile nanotubes 4-methylbenzenethiol capped gold-silver 1:4 nanoparticles system fibers (Fig. 5.104) show the presence of fibers with a submicron diameter which don't display any imperfection.

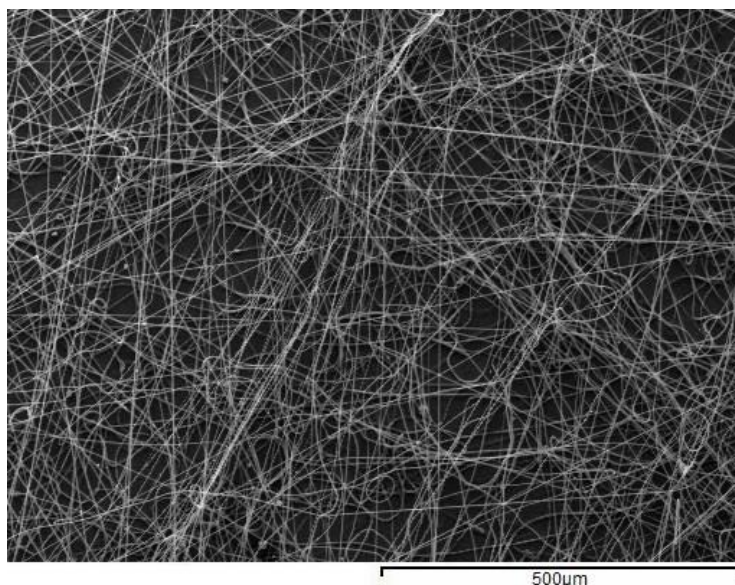


Figure 5.104: SEM micrograph of electrospun polyaniline (PANI) and chrysotile nanotubes 4-methylbenzenethiol capped gold-silver 1:4 nanoparticles system fibers

Reflections highlighted by XRD analysis (Fig. 5.105) are characteristic of the basic components of the polymeric blend we used, including the $2\theta = 12^\circ$ signal typical of chrysotile. Two signals around the $2\theta = 5^\circ$ mark are clearly noticeable which show that two interchain distances preferentially occur.

Changes in the relative intensity of reflections typical of this polymer blend, particularly the reflection with an angle of $2\theta = 19^\circ$, are due to changes to the structural order caused by the presence of inorganic phase. This is not the case when the polymer has no filler.

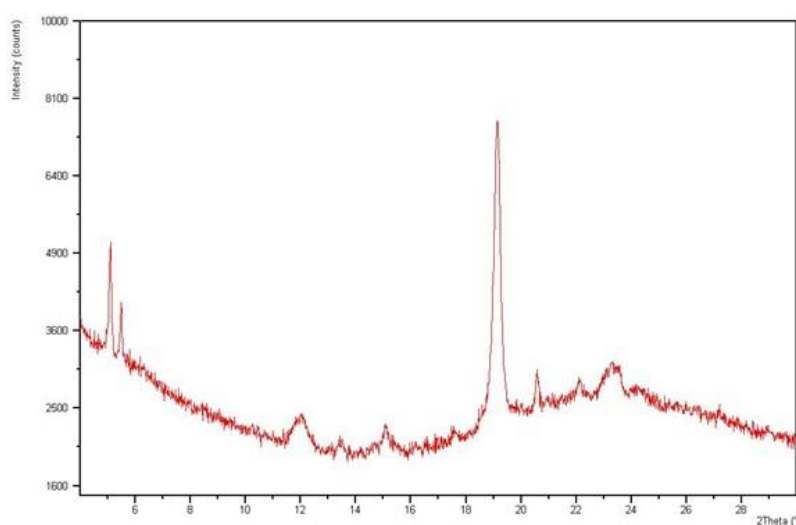


Figure 5.105: XRD diffractogram of electrospun polyaniline (PANI) and chrysotile nanotubes 4-methylbenzenethiol capped gold-silver 1:4 nanoparticles system fibers

An analysis of electrical properties of electrospun polyaniline (PANI) and chrysotile nanotubes 4-methylbenzenethiol capped gold-silver 1:4 nanoparticles system fibers was used to measure their electrical conductivity:

$$\sigma = 2.07 * 10^{-7} \text{ S}\square$$

5.5.15 Characterization of electrospun polyaniline (PANI) and chrysotile nanotubes 4-methylbenzenethiol capped gold-silver 4:1 nanoparticles system fibers

SEM analysis of electrospun polyaniline (PANI) and chrysotile nanotubes 4-methylbenzenethiol capped gold-silver 4:1 nanoparticles system fibers (Fig. 5.106) show the presence of fibers with a submicron diameter which don't display any imperfection.

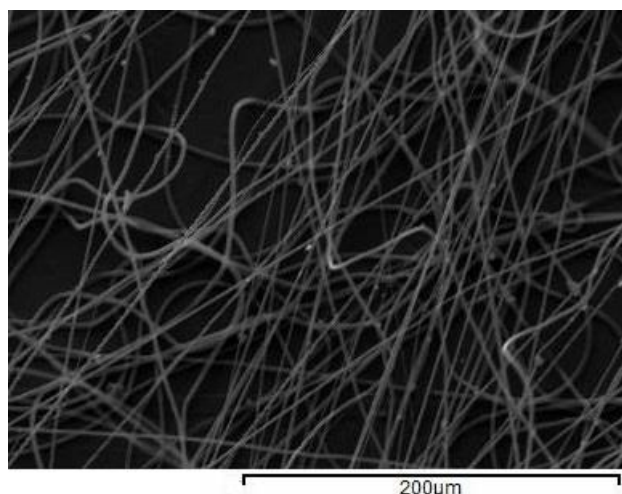


Figure 5.106: SEM micrograph of electrospun polyaniline (PANI) and chrysotile nanotubes 4-methylbenzenethiol capped gold-silver 4:1 nanoparticles system fibers

XRD analysis (Fig. 5.107) highlights the $2\theta = 12^\circ$ chrysotile signal. XRD analysis also reveals a remarkable difference in the reflections caused by the way in which polymer chains are organized: only one reflection at $2\theta = 5^\circ$ appears, due to a single interchain distance occurring preferentially. The a $2\theta = 19^\circ$ reflection, from the length of the hydrogen bonds, gains in intensity as a result of a less pronounced stacking of aromatic rings.

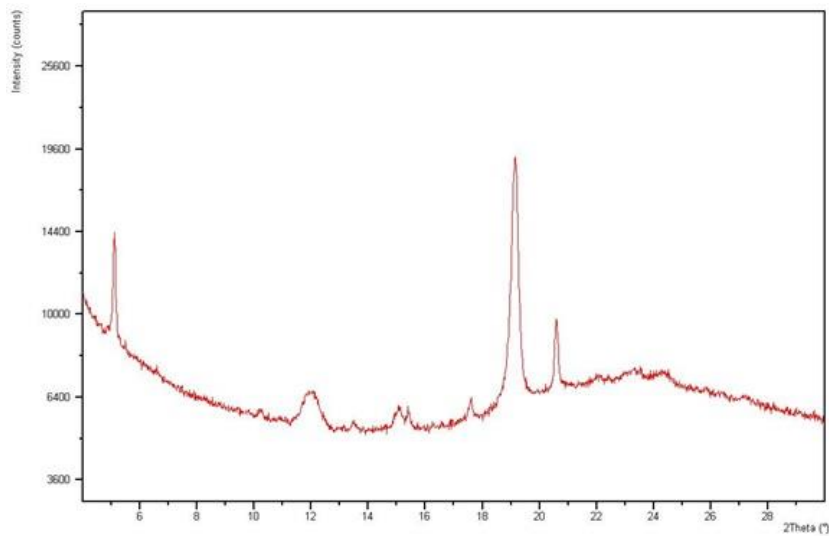


Figure 5.107: XRD diffractogram of electrospun polyaniline (PANI) and chrysotile nanotubes 4-methylbenzenethiol capped gold-silver 4:1 nanoparticles system fibers

An analysis of electrical properties of electrospun polyaniline (PANI) and chrysotile nanotubes 4-methylbenzenethiol capped gold-silver 4:1 nanoparticles system fibers was used to measure their electrical conductivity:

$$\sigma = 2.50 * 10^{-7} \text{ S}\square$$

5.5.16 Characterization of electrospun polyaniline (PANI) and of chrysotile nanotubes and 1-butanethiol capped silver nanoparticles system fibers

SEM analysis of electrospun polyaniline (PANI) and chrysotile nanotubes 1-butanethiol capped silver nanoparticles system fibers (Fig. 5.108) show the presence of fibers with a submicron diameter which don't display any imperfection.

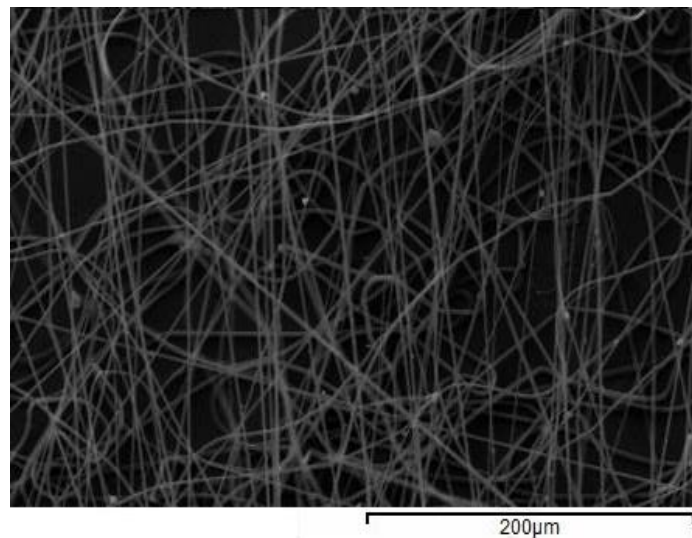


Figure 5.108: SEM micrograph of electrospun polyaniline (PANI) and chrysotile nanotubes 1-butanethiol capped silver nanoparticles system fibers

An analysis of electrical properties of electrospun polyaniline (PANI) and and chrysotile nanotubes 1-butanethiol capped silver nanoparticles system fibers was used to measure their electrical conductivity:

$$\sigma = 1.48 * 10^{-7} \text{ S}\square$$

5.5.17 Characterization of electrospun polyaniline (PANI) and of chrysotile nanotubes and 4-methylbenzenethiol capped silver nanoparticles system fibers

SEM analysis of electrospun polyaniline (PANI) and chrysotile nanotubes 4-methylbenzenethiol capped silver nanoparticles system fibers (Fig. 5.109) show the presence of fibers with a submicron diameter which don't display any imperfection.

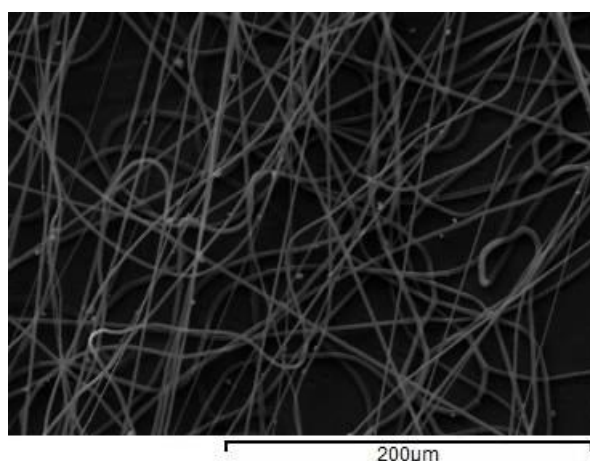


Figure 5.109: SEM micrograph of electrospun polyaniline (PANI) and chrysotile nanotubes 4-methylbenzenethiol capped silver nanoparticles system fibers

XRD analysis (Fig. 5.110) highlights the $2\theta = 12^\circ$ chrysotile signal. XRD analysis also reveals three lower angle peaks (around the 5° mark) related to the interchain distance and the other reflections caused by greater distances. The $2\theta = 19^\circ$ peak shows a lower intensity due to the smaller hydrogen bond between the lateral chains. This is also the case with the large $2\theta = 23^\circ$ stacking reflection.

We can postulate that the presence of this type of filler causes a chain structure that discourages this kind of interaction.

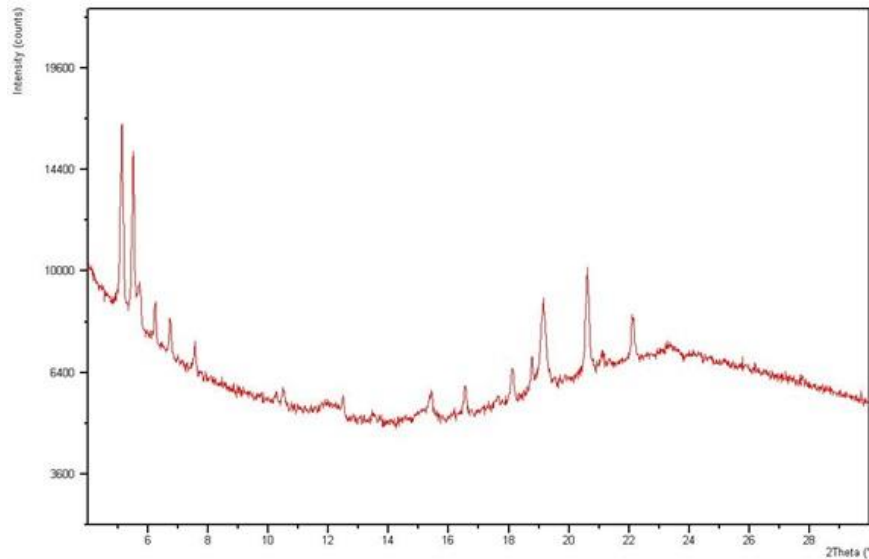


Figure 5.110: XRD diffractogram of electrospun polyaniline (PANI) and chrysotile nanotubes 4-methylbenzenethiol capped silver nanoparticles system fibers

An analysis of electrical properties of electrospun polyaniline (PANI) and and chrysotile nanotubes 4-methylbenzenethiol capped silver nanoparticles system fibers was used to measure their electrical conductivity:

$$\sigma = 1.48 * 10^{-7} \text{ S}\square$$

5.5.18 Characterization of electrospun polyaniline (PANI) and multiwalled carbon nanotubes fibers

Analyses of the sample of electrospun polyaniline (PANI) and multiwalled carbon nanotubes (MWCNT) fibers were carried out in order to obtain morphological, structural, thermal and electrical characterizations.

TEM micrographs (Fig. 5.111) show the presence of multiwalled carbon nanotubes which are evenly distributed within the fibers, but also the presence of some impurity agglomeration.

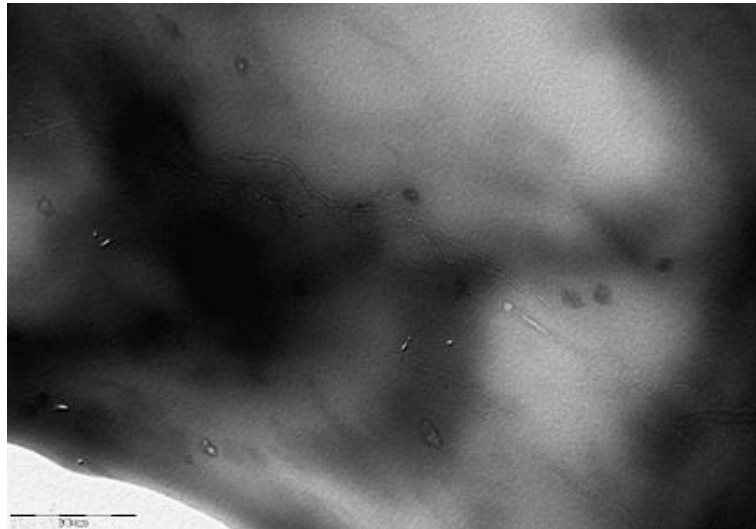


Figure 5.111: TEM image of electrospun polyaniline (PANI) and multiwalled carbon nanotubes fibers

SEM micrographs (Fig. 5.112) show a network of non-oriented polymer fibers. Adding multiwalled carbon nanotubes to the polymeric blend produced fibers that display morphological imperfections in the form of agglomerations. The diameter of these fibers is comparable with the diameter of fibers without filler.

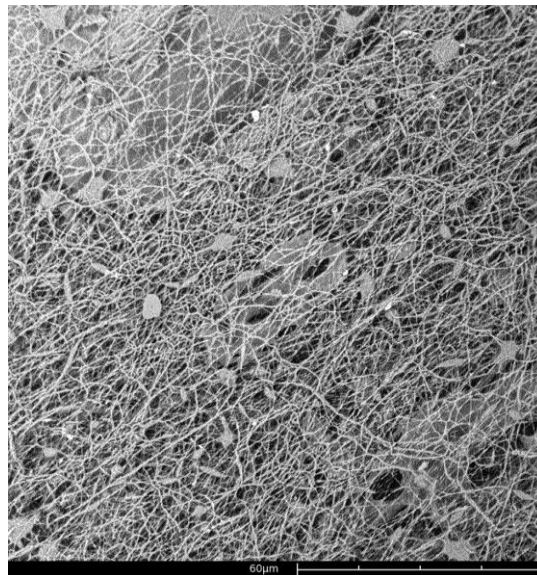


Figure 5.112: SEM image of electrospun polyaniline (PANI) and multiwalled carbon nanotubes fibers

XRD analysis of electrospun polymer mat (Fig 5.113) did not detect any measurable multiwalled carbon nanotubes due to the low concentration of these fibers within the polymer and their low degree of crystallinity. As a result, the XRD diffractogram of this sample is very similar to that of the same polymer but without filler.

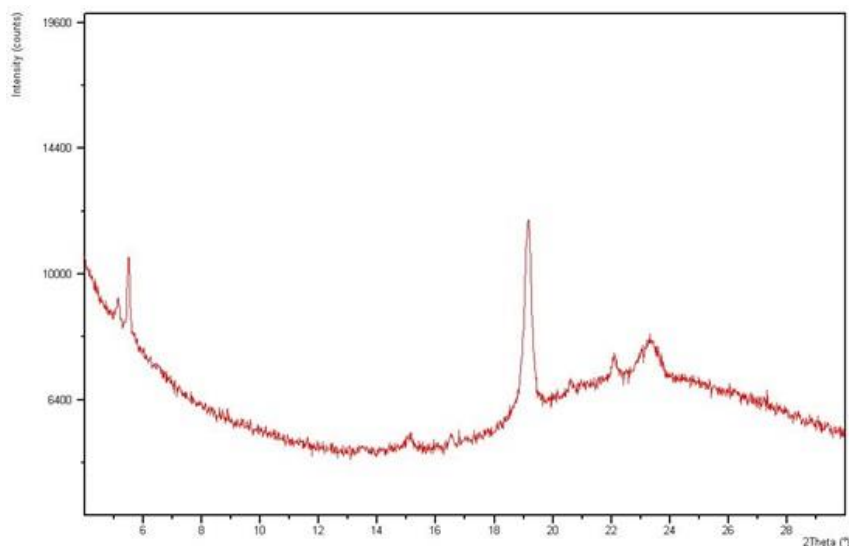


Figure 5.113: XRD diffractogram of electrospun polyaniline (PANI) and multiwalled carbon nanotubes fibers

Thermal analysis of the samples using DSC (Fig. 5.114) reveals the presence of two endothermic peaks, the first around 53°C ($\Delta H = +34$ J/g) and ascribable to the melting of poly(ethylene oxide) domains and the second, around 112°C ($\Delta H = +235$ J/g), to the melting of polyaniline crystalline domains. These results, particularly the temperature value and enthalpy change of the second signal, demonstrate how the sample thermal properties and degree of crystallinity are significantly influenced by the presence of multiwalled carbon nanotubes.

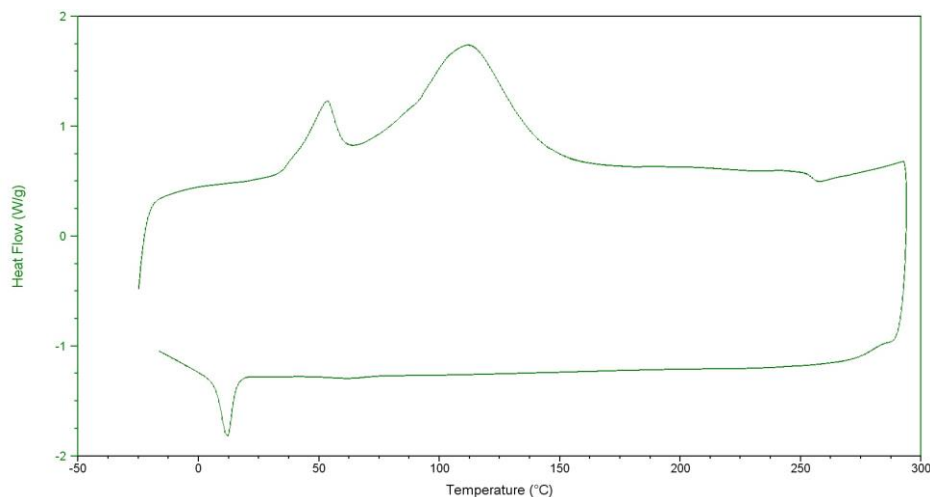


Figure 5.114: DSC curve of electrospun polyaniline (PANI) and multiwalled carbon nanotubes fibers

A teraohmmeter was used to measure the electrospun polymer electrical conductivity:

$$\sigma = 5.21 * 10^{-6} \text{ S}\square$$

5.5.19 Characterization of electrospun polyaniline (PANI) and chrysotile nanotubes fibers

Analyses of the sample of electrospun polyaniline (PANI) and chrysotile nanotubes fibers were carried out in order to obtain morphological, structural, thermal and electrical characterizations.

TEM micrographs (Fig. 5.115 – Fig. 5.116) show the presence of chrysotile nanotubes evenly distributed within the fibers and without aggregates. Nanotubes are perfectly oriented along the polymeric fiber axis.

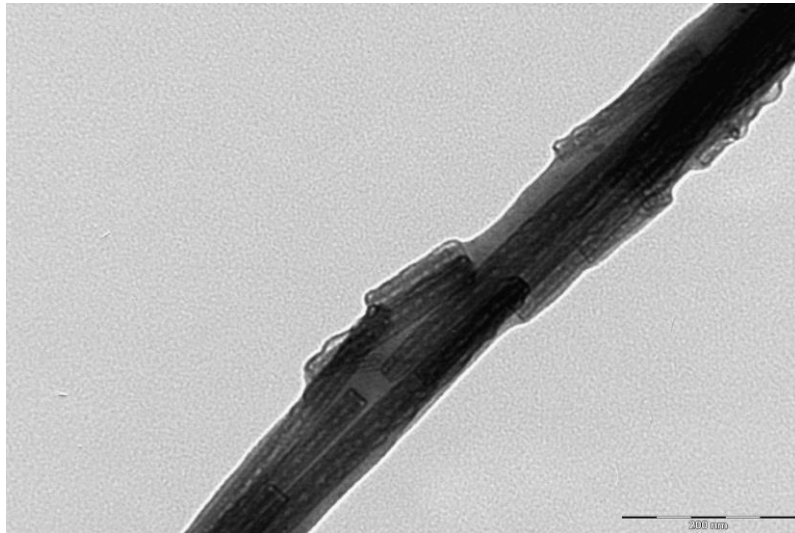


Figure 5.115: TEM image of electrospun polyaniline (PANI) and chrysotile nanotubes fibers

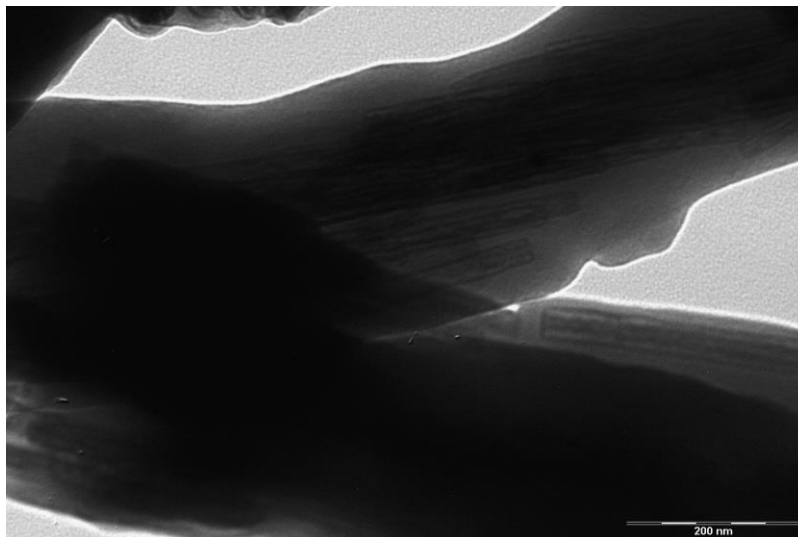


Figure 5.116: TEM image of electrospun polyaniline (PANI) and chrysotile nanotubes fibers

SEM micrographs (Fig. 5.117) show a network of non-oriented polymer fibers. By adding chrysotile nanotubes fibers to the polymeric blend we produced fibers that are more straight and with a more rigid appearance than those without filler. These fibers do not display structural imperfections and their diameter is comparable with the diameter of the unfilled ones.

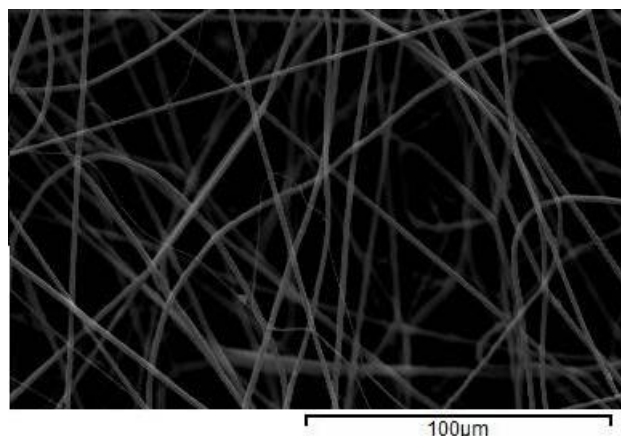


Figure 5.117: SEM image of electrospun polyaniline (PANI) and chrysotile nanotubes fibers

XRD analysis of electrospun polymer mat (Fig.5.118) highlighted the $2\theta = 12^\circ$ signal typical of chrysotile. This demonstrates the presence of inorganic nanotubes in the sample.

Changes in the relative intensity of reflections are due to the structural order of the electrospun polymer. This shows that the presence of chrysotile nanotubes causes the alignment of the polymer chains according to certain patterns and not others.

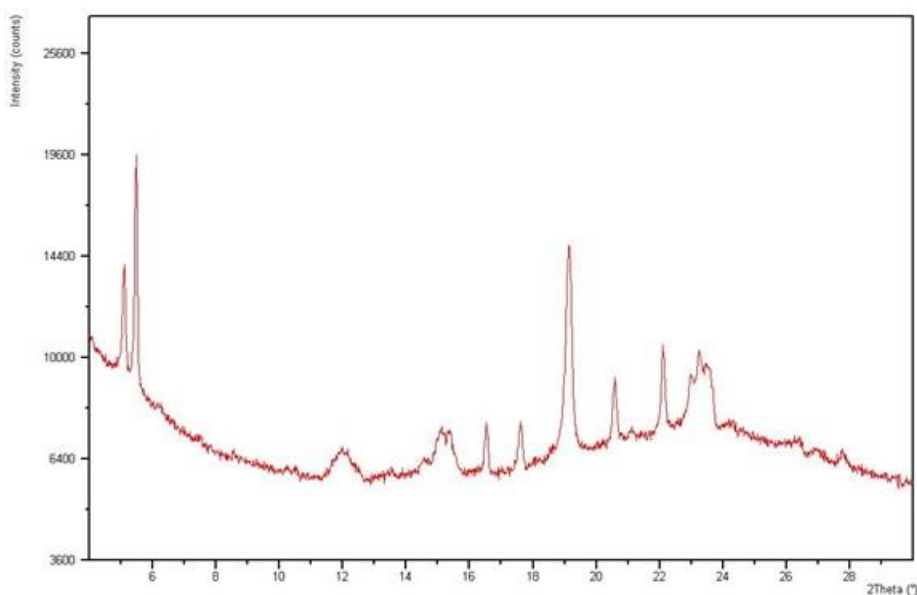


Figure 5.118: XRD diffractogram of electrospun polyaniline (PANI) and chrysotile nanotubes fibers

Thermal analysis of the samples using DSC (Fig. 5.119) reveals the presence of two endothermic peaks, the first around 64°C ($\Delta H = +57 \text{ J/g}$) and ascribable to the melting of poly(ethylene oxide) domains and the second, around 98°C ($\Delta H = +28 \text{ J/g}$), to the melting of polyaniline crystalline domains. These results, particularly the temperature value and enthalpy change of the second signal,

demonstrate how the sample thermal properties and degree of crystallinity are significantly influenced by the presence of chrysotile nanotubes.

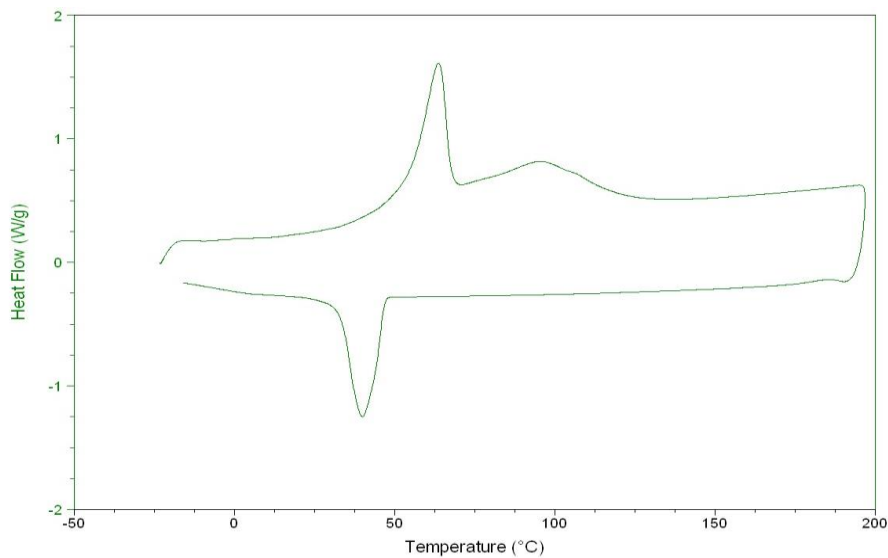


Figure 5.119: DSC curve of electrospun polyaniline (PANI) and chrysotile nanotubes fibers

A teraohmmeter was used to measure the electrospun polymer electrical conductivity:

$$\sigma = 5.68 * 10^{-7} \text{ S}\square$$

5.5.20 Characterization of electrospun of poly(3-hexylthiophene) (P3HT) and graphene oxide

Analyses of the sample of electrospun of poly(3-hexylthiophene) (P3HT) and graphene oxide fibers were carried out in order to obtain morphological, structural, thermal and electrical characterizations.

TEM micrographs (Fig. 5.120 – Fig. 5.121) show the presence of graphene oxide evenly distributed within the fibers. Sheets do not tend to aggregate or fold on themselves and the presence of filler does not cause any imperfection.

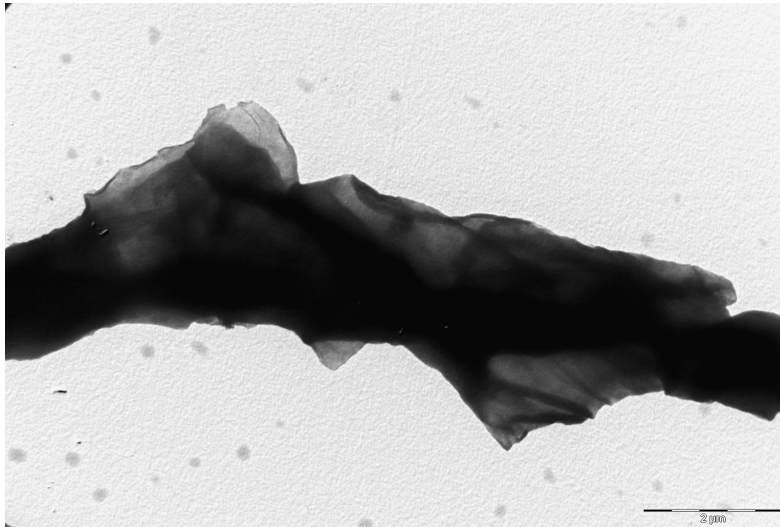


Figure 5.120: TEM image of electrospun poly(3-hexylthiophene) and graphene oxide fibers

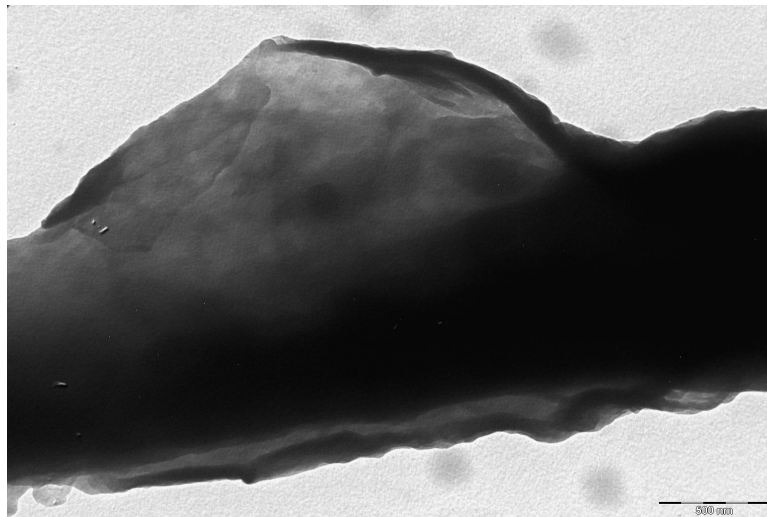


Figure 5.121: TEM image of electrospun poly(3-hexylthiophene) and graphene oxide fibers

SEM micrographs (Fig. 5.122 – Fig. 5.123) show a network of non-oriented polymer fibers. By adding graphene oxide to the polymeric blend we produced fibers that do not display imperfections like beads and pearls. They do display, however, a wrinkled topography and a more uneven spatial distribution when compared to the other samples produced with all tested polymeric blends and have an average diameter slightly greater than a micrometer.

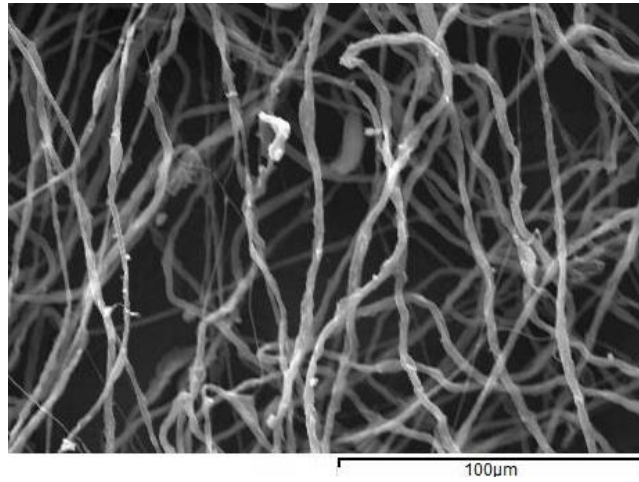


Figure 5.122: SEM image of electrospun poly(3-hexylthiophene) and graphene oxide fibers

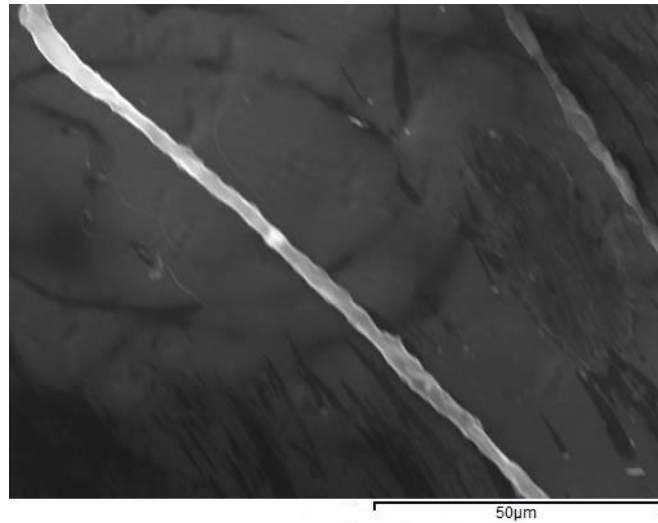


Figure 5.123: SEM image of electrospun poly(3-hexylthiophene) and graphene oxide fibers

EDS analysis of the sample in mapping mode show how both sulfur (Fig. 5.124), which is only present in poly(3-hexylthiophene) and not in the filler, and carbon (Fig. 5.125), the basic element in graphene oxide, are evenly distributed within the fibers. This confirms that fibers are filled in a homogenous way and without aggregates.

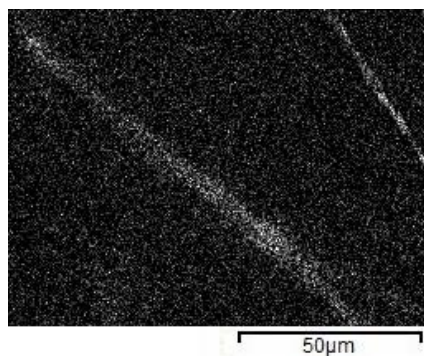


Figure 5.124: reconstruction of the presence of sulfur using mapping mode EDS analysis of electrospun of poly(3-hexylthiophene) and graphene oxide fibers

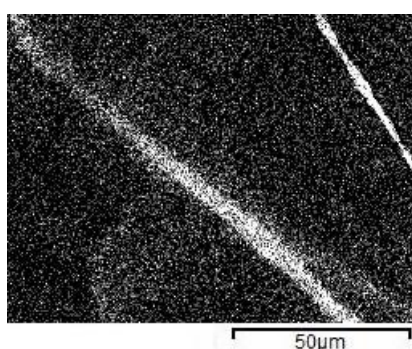


Figure 5.125: reconstruction of the presence of carbon using mapping mode EDS analysis of electrospun of poly(3-hexylthiophene) and graphene oxide fibers

XRD analysis of electrospun polymer mat (Fig.5.126) did not detect any measurable graphene oxide due to the low degree of crystallinity of the filler. As a result, the XRD diffractogram of this sample is very similar to that of the same electrospun polymer blend but without filler. Reflections characteristic of planar interchain distances and those of interplanar distance between aromatic units are found at angles lower than those for electrospun polymer without filler. This is caused by the greater space between polymeric chains.

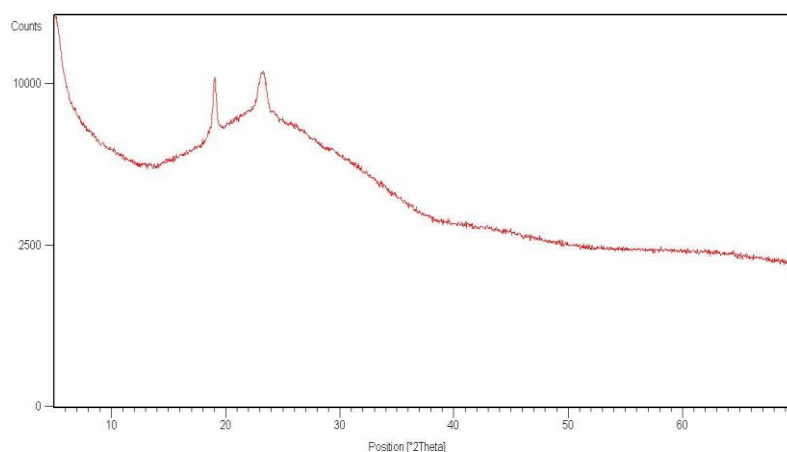


Figure 5.126: XRD diffractogram of electrospun of poly(3-hexylthiophene) and graphene oxide fibers

Thermal analysis of the samples using DSC (Fig. 5.127) reveals the presence of two endothermic peaks, the first around 63.96°C ($\Delta H = +60.94$ J/g) and ascribable to the melting of poly(ethylene oxide) domains and the second, around 231.46°C ($\Delta H = +4.67$ J/g), to the melting of poly(3-hexylthiophene) crystalline domains. The second transition occurs at a temperature considerably higher and this is due to the interaction of graphene oxide with poly(3-hexylthiophene).

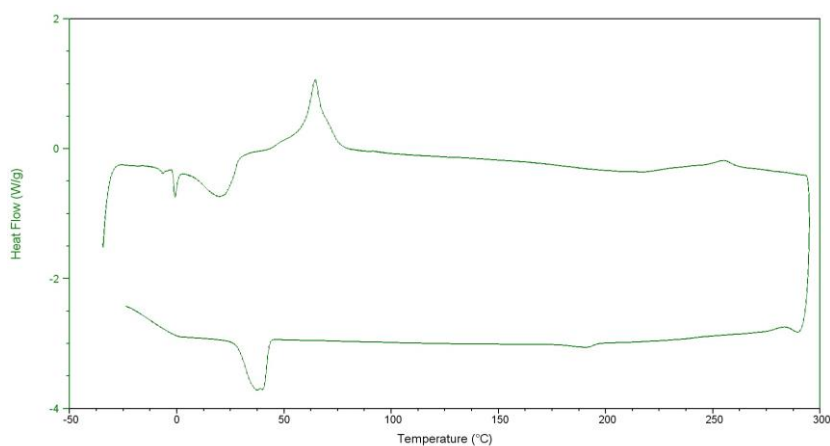


Figure 5.127: DSC curve of electrospun of poly(3-hexylthiophene) and graphene oxide fibers

A teraohmmeter was used to measure the electrospun polymer electrical conductivity:

$$\sigma_{\text{UNDOPED}} = 1.30 * 10^{-9} \text{ S}\square$$

$$\sigma_{\text{DOPED}} = 2.19 * 10^{-4} \text{ S}\square$$

5.5.21 Characterization of electrospun of poly(3-hexylthiophene) (P3HT) and multiwalled carbon nanotubes fibers

Analyses of the sample of electrospun of poly(3-hexylthiophene) (P3HT) and multiwalled carbon nanotubes (MWCNT) fibers were carried out in order to obtain morphological, structural, thermal and electrical characterizations.

TEM micrographs (Fig.5.128 – Fig.5.129) show the presence of multiwalled carbon nanotubes within the fibers. Carbon nanotubes tend to aggregate creating areas rich in MWCNT next to others that are devoid of filler.

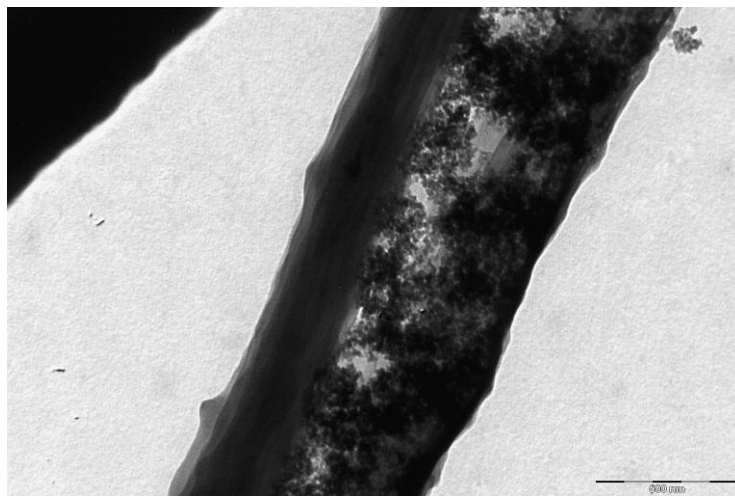


Figure 5.128: TEM image of electrospun poly(3-hexylthiophene) and multiwalled carbon nanotubes fibers

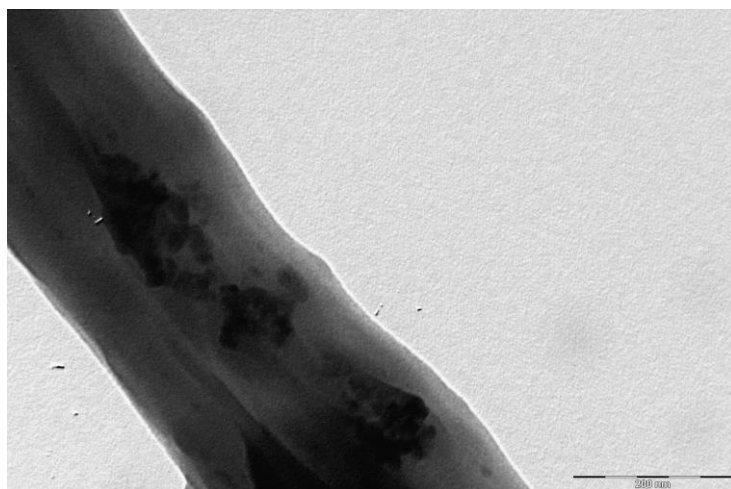


Figure 5.129: TEM image of electrospun poly(3-hexylthiophene) and multiwalled carbon nanotubes fibers

SEM micrographs (Fig. 5.130 - Fig.5.131) show a network of non-oriented polymer fibers. Adding multiwalled carbon nanotubes to the polymeric blend produced fibers that display morphological imperfections in the form of polymeric piles. Also this time these fibers have an average diameter slightly greater than a micrometer.

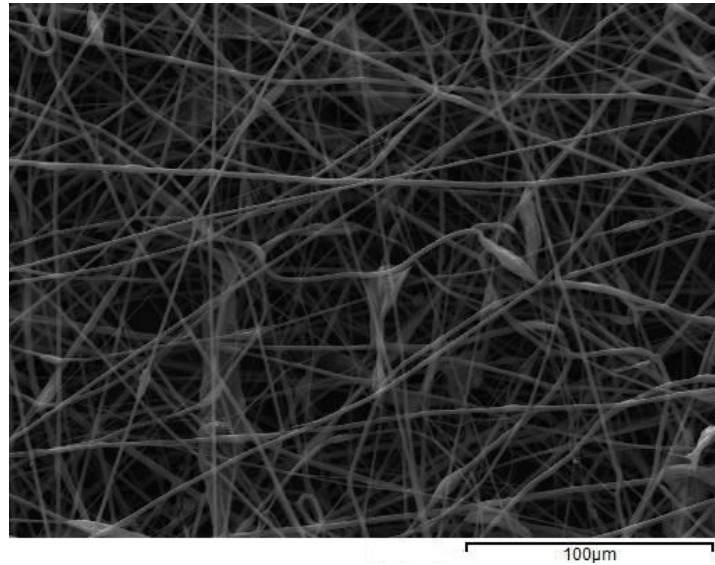


Figure 5.130: SEM image of electrospun poly(3-hexylthiophene) and multiwalled carbon nanotubes fibers

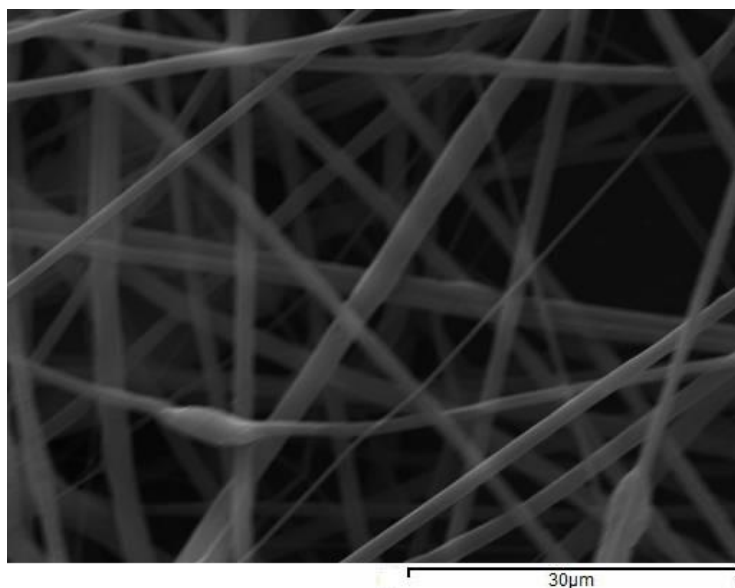


Figure 5.131: SEM image of electrospun poly(3-hexylthiophene) and multiwalled carbon nanotubes fibers

EDS analysis of the sample in mapping mode show how both sulfur (Fig. 5.132), which is only present in poly(3-hexylthiophene) and not in the filler, and carbon (Fig. 5.133), the basic element in multiwalled carbon nanotubes, are not evenly distributed in the mat. This confirms that fibers are filled in inhomogeneous way and that aggregates are present.

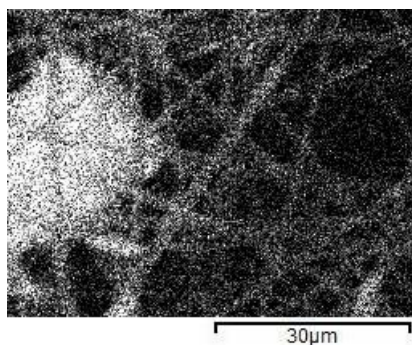


Figure 5.132: reconstruction of the presence of sulfur using mapping mode EDS analysis of electrospun of poly(3-hexylthiophene) and multiwalled carbon nanotubes fibers

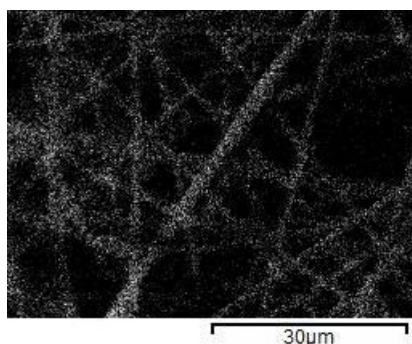


Figure 5.133: reconstruction of the presence of carbon using mapping mode EDS analysis of electrospun of poly(3-hexylthiophene) and multiwalled carbon nanotubes fibers

XRD analysis of electrospun polymer mats (Fig. 5.134) did not detect any measurable multiwalled carbon nanotubes due to the low degree of crystallinity of the filler. As a result, the XRD diffractogram of this sample is very similar to that of the same electrospun polymer blend but without filler. Characteristic reflections of planar interchain distances and those ascribable to the interplanar distance between aromatic units are 2θ higher than those for electrospun polymer without filler. This is caused by greater space between polymeric chains. The signals display a lower intensity and wider peaks denote low repeatability of crystalline domains. This is because the

presence of filler discourages the homogeneous distribution of polymeric chains in electrospun fibers.

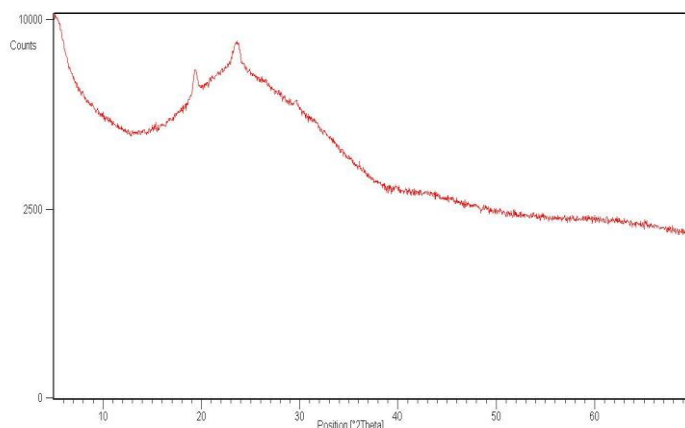


Figure 5.134: XRD diffractogram of electrospun of poly(3-hexylthiophene) and multiwalled carbon nanotubes fibers

Thermal analysis of the samples using DSC (Fig. 5.135) reveals the presence of two endothermic peaks, the first around 66.11 °C ($\Delta H = +55.56$ J/g) and ascribable to the melting of poly(ethylene oxide) domains and the second, around 253.07 °C ($\Delta H = +2.41$ J/g), to the melting of poly(3-hexylthiophene) crystalline domains. These results, particularly the temperature value and enthalpy change of the second signal, demonstrate how the sample thermal properties and degree of crystallinity are significantly influenced by the presence of chrysotile nanotubes.

The fact that the transition occurs at a temperature higher than 250°C indicates that multiwalled carbon nanotubes is interacting with poly(3-hexylthiophene).

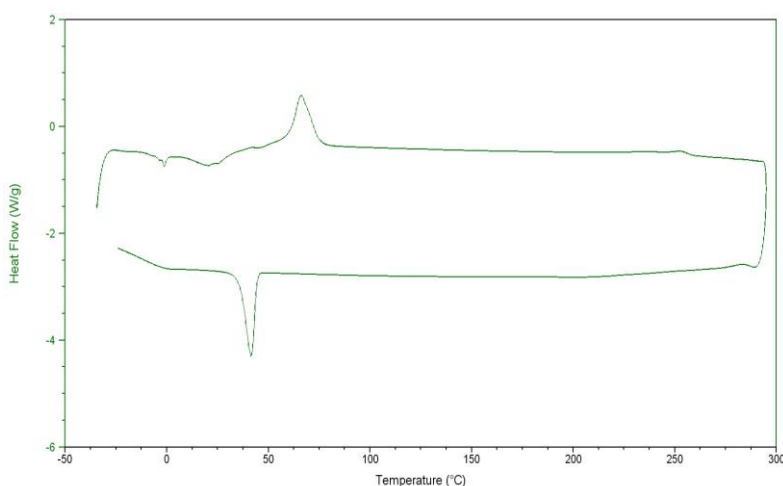


Figure 5.135: DSC curve of electrospun of poly(3-hexylthiophene) and multiwalled carbon nanotubes fibers

A teraohmmeter was used to measure the electrospun polymer electrical conductivity:

$$\sigma_{\text{UNDOPE}} = 2.03 * 10^{-9} \text{ S}\square$$

$$\sigma_{\text{DOPE}} = 9.47 * 10^{-5} \text{ S}\square$$

5.5.22 Characterization of electrospun of poly(3-hexylthiophene) (P3HT) and chrysotile nanotubes fibers

Analyses of the sample of electrospun of poly(3-hexylthiophene) and chrysotile nanotubes fibers were carried out in order to obtain morphological, structural, thermal and electrical characterizations.

TEM micrographs (Fig. 5.136 – Fig. 5.137) show the presence of chrysotile nanotubes within the fibers. Nanotubes do not tend to aggregate and are distributed along the fibers but not aligned with their axis, mostly in an unsystematic and uneven way.

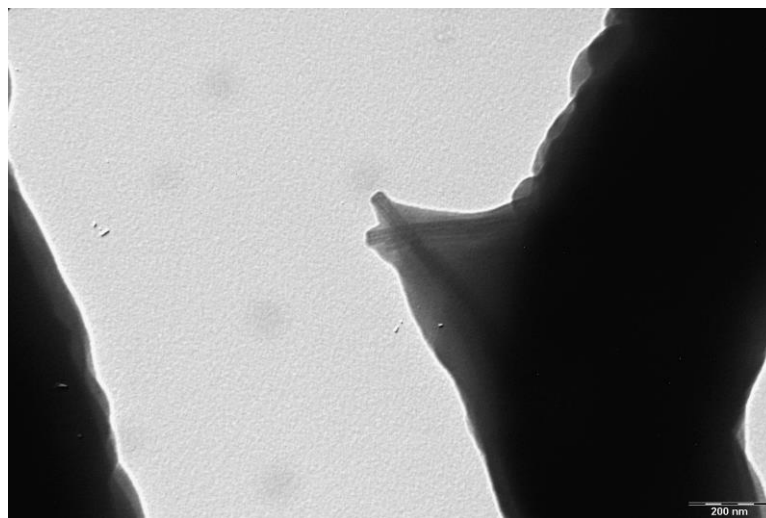


Figure 5.136: TEM image of electrospun poly(3-hexylthiophene) and chrysotile nanotubes fibers

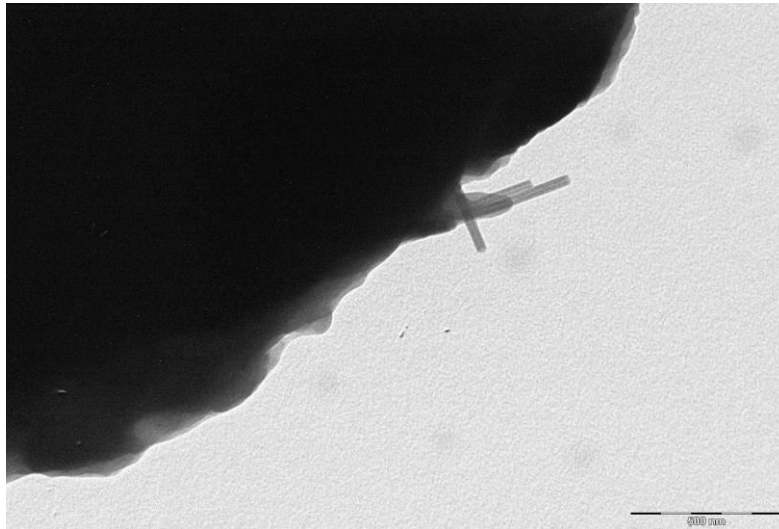


Figure 5.137: TEM image of electrospun poly(3-hexylthiophene) and chrysotile nanotubes fibers

SEM micrographs (Fig. 5.138 - Fig. 5.139) show a network of non-oriented polymer fibers. By adding chrysotile nanotubes fibers to the polymeric blend we produced fibers that do not display morphological imperfections.

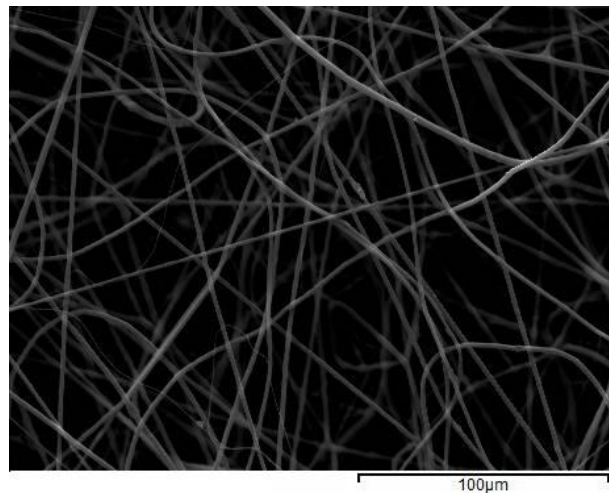


Figure 5.138: SEM image of electrospun poly(3-hexylthiophene) and chrysotile nanotubes fibers

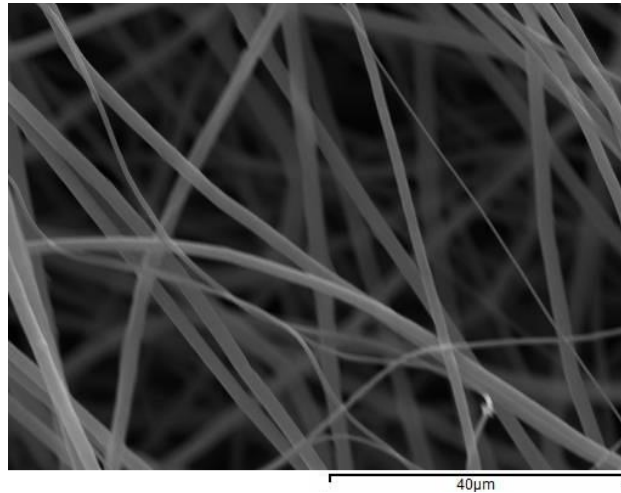


Figure 5.139: SEM image of electrospun of poly(3-hexylthiophene) and chrysotile nanotubes fibers

EDS analysis of the sample in mapping mode show how both carbon (Fig. 5.140), which is only present in the polymeric part of the fibers (poly(3-hexylthiophene) and poly(ethylene oxide)) and not in the filler, and silicon (Fig.5.141), the main element of chrysotile, are evenly distributed in the system. This confirms that fibers are filled in a homogeneous way.

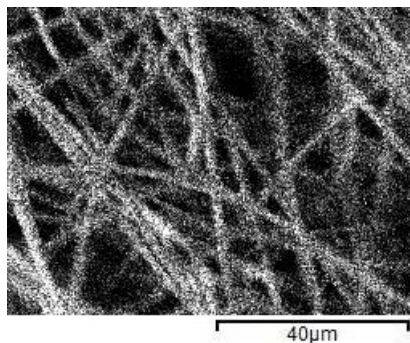


Figure 5.140: reconstruction of the presence of carbon using mapping mode EDS analysis of electrospun of poly(3-hexylthiophene) and chrysotile nanotubes fibers

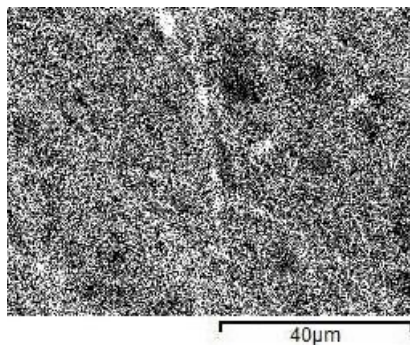


Figure 5.141: reconstruction of the presence of silicon using mapping mode EDS analysis of electrospun of poly(3-hexylthiophene) and chrysotile nanotubes fibers

XRD analysis of electrospun polymer mats (Fig. 5.142) highlighted the $2\theta = 12^\circ$ signal typical of chrysotile and the presence of the other components of the polymeric blend we used. Reflections characteristic of planar interchain distances and those of interplanar distance between aromatic units are 2θ higher than those for electrospun polymer without filler. This is caused by diminishing space between polymeric chains.

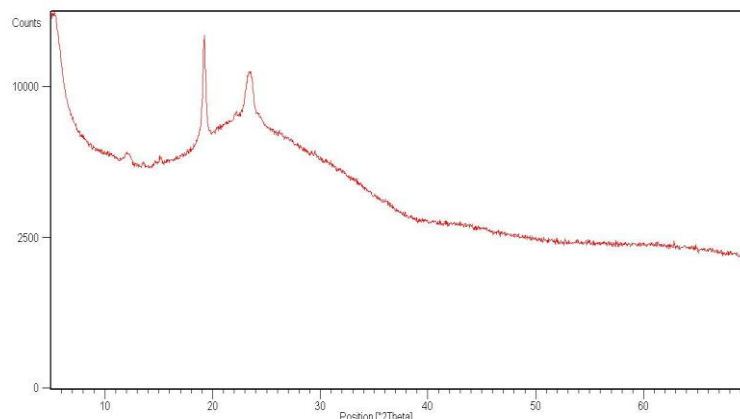


Figure 5.142: XRD diffractogram of electrospun of poly(3-hexylthiophene) and chrysotile nanotubes fibers

Thermal analysis of the samples using DSC (Fig. 5.143) reveals the presence of two endothermic peaks, the first around 63.96°C ($\Delta H = +60.94\text{ J/g}$) and ascribable to the melting of poly(ethylene oxide) domains and the second, around 231.46°C ($\Delta H = +4.67\text{ J/g}$), to the melting of poly(3-hexylthiophene) crystalline domains. These results show that there are no significant changes in comparison to the thermal analysis of the same polymer without inorganic filler.

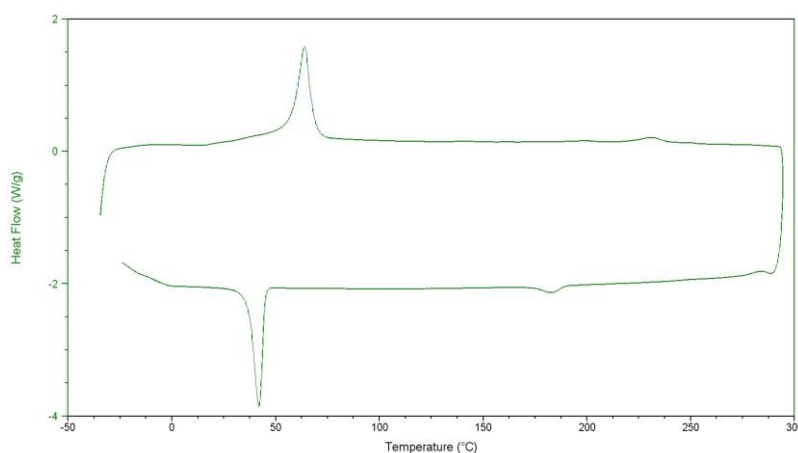


Figure 5.143: DSC curve of electrospun of poly(3-hexylthiophene) and chrysotile nanotubes fibers

A teraohmmeter was used to measure the electrospun polymer electrical conductivity:

$$\sigma_{\text{UNDOPE}} = 3.47 * 10^{-9} \text{ S}\square$$

$$\sigma_{\text{DOPE}} = 1.26 * 10^{-4} \text{ S}\square$$

5.5.23 Conclusion

This phase of the project was dedicated to analysing morphological and structural changes and changes in thermal and electrical properties brought about by adding different types of fillers to two types of electrospun polymer blend: polyaniline (PANI) and poly(3-hexylthiophene) (P3HT).

A number of very different fillers were used. In terms of morphology, we used zero-dimensional (0D) nanostructured materials, one-dimensional (1D) nanostructured materials and two-dimensional (2D) nanostructured materials. We used metals, metal oxides, silicates, carbon-based materials and nanostructured materials made of different inorganic phases.

In order to fully understand how structural variations impact upon the electrical conductivity of different polymers it was necessary to study how electrical impulses travel within the fiber. We used blends of intrinsically conductive polymers (ICPs). In these materials electrical conductivity is the result of the movement of charge carriers between localized states, such as polaronic and bipolaronic states. The hopping motion of charge carriers can occur between two points in the same chain or between different polymer chains. Our studies also show that when a polymer is subjected to the force of an electric field, molecular chains within the polymer stretch out and align themselves parallel to each other to form a fiber. It is possible to create a discontinuity in the charge carriers hopping motion by adding foreign insert in polymeric fibers. As a result, electrical conductivity greatly differs according to the ability of the filler to allow or not the passage of electrical charges towards polaronic and bipolaronic localized states within the chains. Alternatively, the presence of a second phase with a certain geometry and spatial disposition can create preferential paths within the structure of a fiber (this is directly caused by the introduction of a second phase).

The morphology of both systems, polyaniline and poly(3-hexylthiophene), was analysed through SEM and TEM microscopy. This, together with XRD and EDS analysis, provided data on the structure of the materials. DSC analysis provided important data on thermal properties and on the interaction between different phases. Electrical conductivity of the individual conductive polymer composite (CPC) was measured and the results compared to its reference sample, the same electrospun polymer blend but without the filler.

The presence of nanoparticles, which can be classified as zero-dimensional (0D) nanostructured material, causes variations in the electrical conductivity of polyaniline polymer mats (Fig. 5.144).

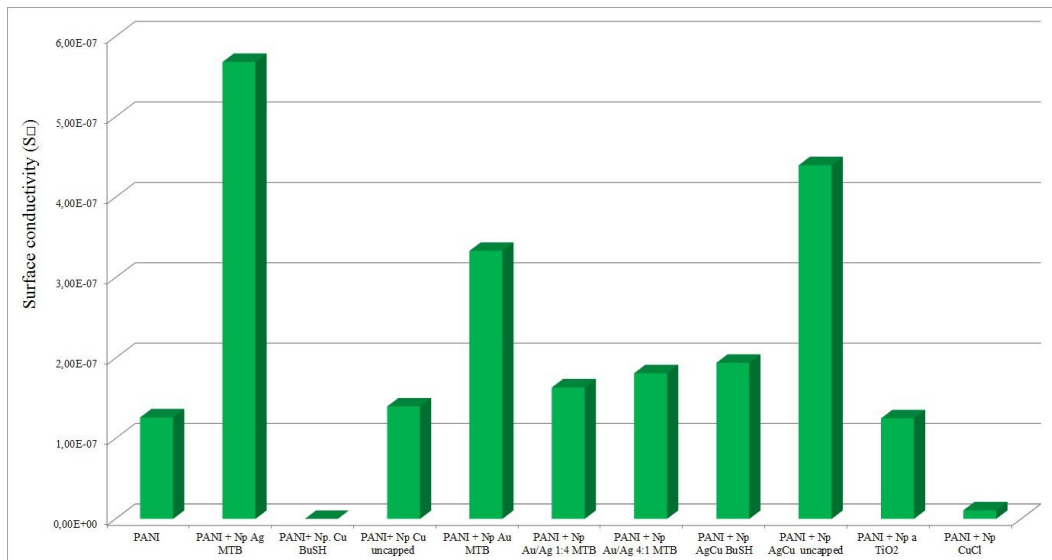


Figure 5.144: chart of surface conductivity values for electrospun polyaniline CPCs and zero-dimensional (0D) nanostructured materials

Every time capped metal nanoparticles were used, TEM and SEM micrographs showed that the filler was evenly distributed within the fibers. No aggregates were formed and fibers displayed no imperfections. The presence of a second phase which is aligned in an unsystematic and uneven way does not allow high repeatability crystalline domains to be formed in the fibers. This is confirmed by the presence of various signals approximately at the $2\theta = 5^\circ$, clearly evident in XRD diffractograms for these samples. Areas in the diffractogram such as this, denoted by low 2θ values, is where we can find signals indicating the distance on the same plane between polymer chains. The presence of more than one signal indicates the presence of domains with different interchain distances. The presence of inorganic material between polymer chains causes a discontinuity in the physiological hopping motion of the electrical charge carrier within ICP. The greater is the isolating effect of the discontinuity, the lower will be the value of electrical conductivity. All the metal particles we used were covered by a shell made of dielectric material and for this reason electrical conductivity did not greatly increased when they were utilized. Electrical conductivity is greater when silver nanoparticles are used. Uncapped metal nanoparticles CPCs show a remarkably improved conductivity despite being a inhomogeneous system characterized by the presence of metal aggregates, as shown by TEM micrographs.

Based on these finding, it is not surprising that the use of metal oxides like anatase does not improve the electrical properties of polymer mats and that the presence of copper (I) chloride nanoparticles has a significant adverse effect on the electrical conductivity of electrospun material.

The presence of nanotubes, which can be classified as one-dimensional (1D) nanostructured material, causes variations in the electrical conductivity of polyaniline polymer mats (Fig. 5.145).

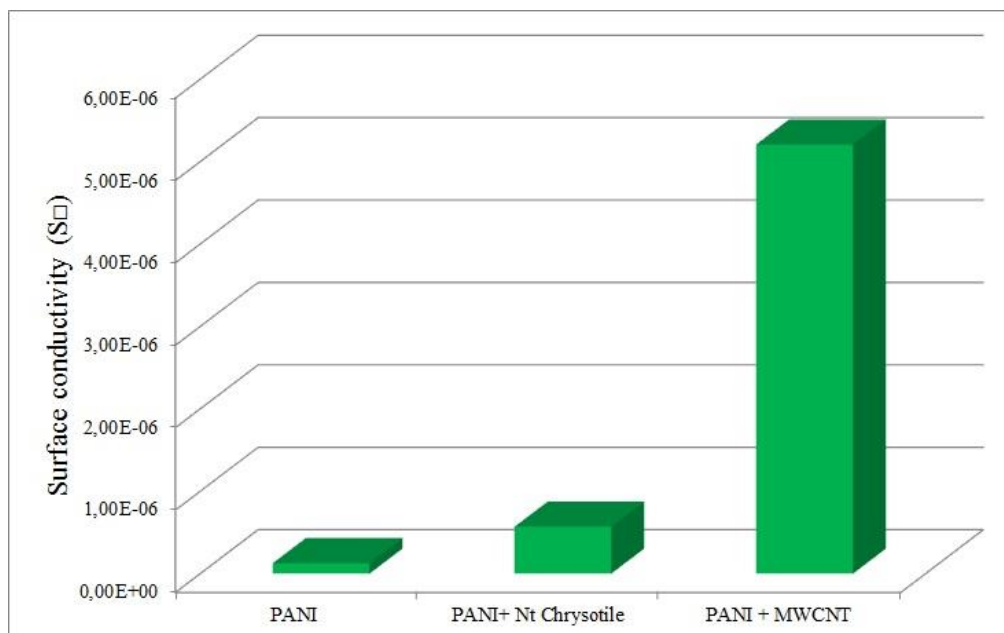


Figure 5.145: chart with values for surface conductivity of electrospun polyaniline CPCs and one-dimensional (1D) nanostructured materials

Looking at the chart with values for surface conductivity of electrospun polyaniline CPCs (Fig. 5.145), we can see that it shows in both cases an improvement of electrical properties. These two cases demonstrate that both the type of filler and control of the structure of the CPC produced are fundamental in order to obtain a superior type of material.

TEM micrographs show that multiwalled carbon nanotubes are evenly distributed within the polymer fiber, with a π - π stacking interaction among the aromatic rings with polyaniline, as shown by DSC analysis revealing a significant increase in temperature in the second transition. SEM micrographs show that a large quantity of multiwalled carbon nanotubes leads to morphological imperfections in the fibers. Despite of this, electrical conductivity improves due to the intrinsic properties of multiwalled carbon nanotubes. As for the composite obtained by adding chrysotile nanotubes, an improvement in electrical conductivity can also be observed but in this case it is not due to the use of a conducting material (chrysotile is an excellent insulator) but because of the increased regularity of the fiber's structure.

TEM micrographs show that chrysotile nanotubes are aligned parallel to each other and to the main axis of the polymer fiber. This makes the fiber straight and rigid. The new structure helps forming long, highly regular polymer chains that are conducive to charge carriers interchain hops.

Even though the presence of insulating nanotubes between different chains hinders hopping motion between the chains, the optimization of interchain hopping is fundamental in electrospun systems and this leads to greater electrical conductivity. This confirms that using materials with a certain set of macroscopic properties can lead to unexpected properties by controlling the hierarchical structure of materials, from the nanoscale to the macroscale through the microscale.

Using chrysotile nanotubes thiol capped metal nanoparticles system in the polyaniline blend (Fig. 5.146) leads to improved conductivity when compared to electrospun material without filler, but this is not true when compared to polyaniline and chrysotile CPC. This is probably because of their uneven distribution within the chrysotile nanotubes and the sporadic presence of particles outside the nanotubes post electrospinning. This could be hindering the charge carriers hopping motion in the preferential paths created by the inorganic phase.

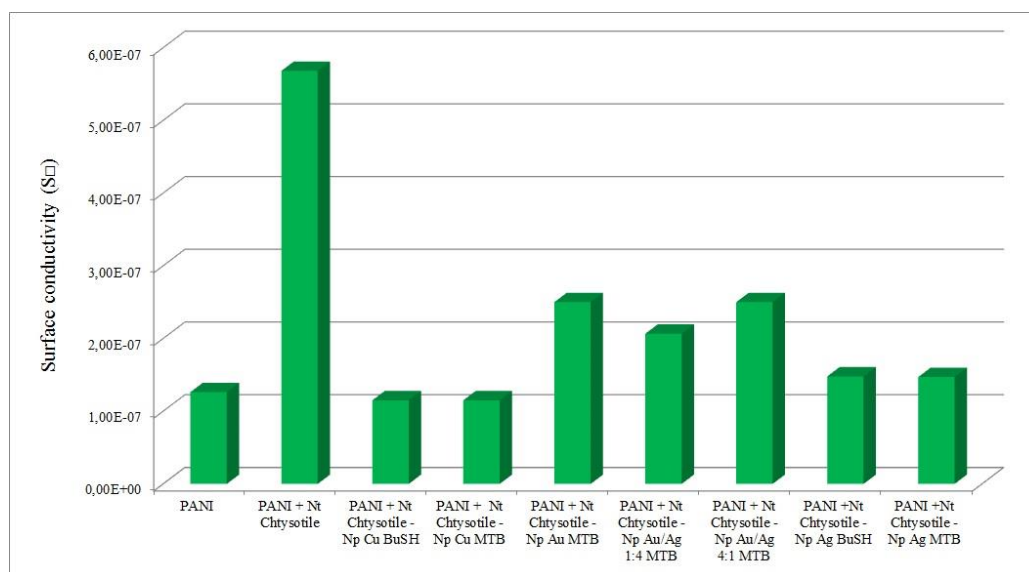


Figure 5.146: chart with values for surface conductivity of electrospun polyaniline and chrysotile nanotubes thiol capped metal nanoparticles system mats

The second phase of this project was dedicated to studying poly(3-hexylthiophene). As we can see from surface conductivity charts below (Fig. 5.147 – Fig. 5.148), this system has much greater electrical conductivity than the polyaniline system and proves that control over structure impacts conductivity.

By using chrysotile as filler, with the same concentration of polyaniline electrospun system, the resulting material does not have an improved electrical conductivity, but quite the opposite. TEM micrographs show that this is due to an uneven distribution of the nanotubes that do not align themselves parallel to the fiber. The absence of hierarchical structures enhances the insulating properties of this material. In this case the filler does not show any particular affinity with polymer chains, as can be observed through DSC analysis which shows that there are no significant variations for the transition characteristic of poly(ethylene oxide) and that of poly(3-hexylthiophene). Both transitions are not influenced by the inorganic phase.

When adding multiwalled carbon nanotubes to the poly(3-hexylthiophene) polymer blend we also encounter a lower electrical conductivity, the opposite of what happens when using a polyaniline polymer blend chains. Also in this case a π - π stacking interaction occurs among the aromatic rings of the polymer. DSC analysis highlights this by showing that thermal transition caused by poly(3-hexylthiophene) occurs at temperatures greater than 250°C. In this CPC, however, multiwalled carbon nanotubes are not distributed evenly and create a discontinuity that adversely impacts the fibers electrical conductivity. In this case we have a situation where, despite using a conductive material, we do not see any beneficial effect on electrical conductivity due to the formation of an inhomogeneous system.

Using a material like graphene oxide does not significantly improve electrical properties, but an analysis of variations in the oxidation state and of additional functionalization may be the object of future studies.

Graphene oxide is evenly distributed within the fiber and sheets do not aggregate or fold on themselves. Within the fiber it interacts with poly(3-hexylthiophene) as shown both by the increase in transition temperatures caused by poly(3-hexylthiophene), and by the decrease in the value of 2θ angles displayed in XRD diffractogram, particularly in the reflection due to π - π stacking and ascribable to the distance between polymer chains in different planes.

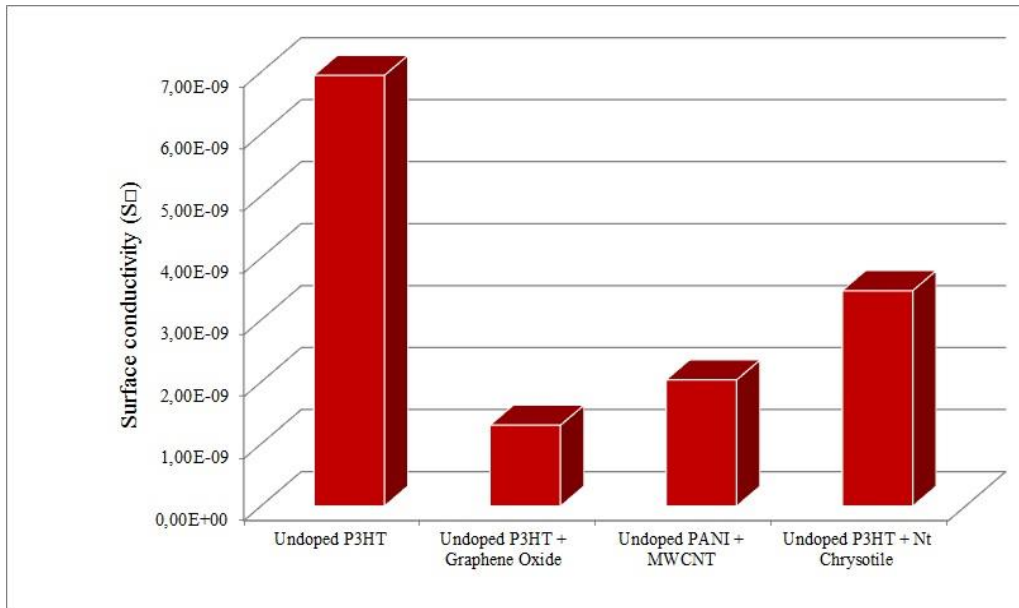


Figure 5.147: chart with values for surface conductivity of electrospun mats based on undoped poly(3-hexylthiophene)

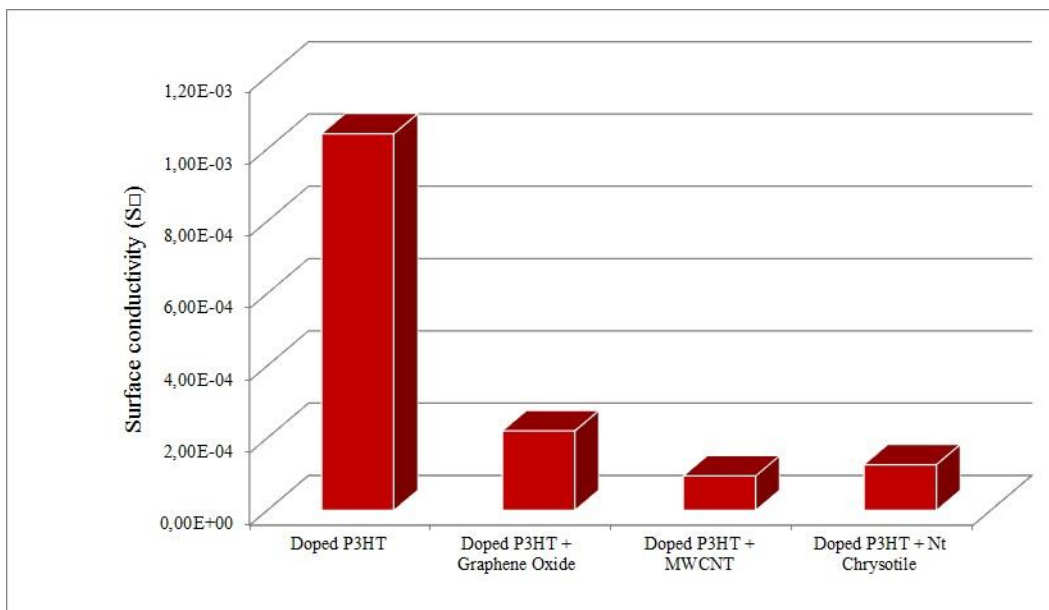


Figure 5.148: chart with values for surface conductivity of electrospun mats based on doped poly(3-hexylthiophene)

Finally, it is interesting to note that doping obtained by exposure to iodine vapors for 10 minutes greatly enhances the electrical properties of mats when a second phase was not added and not in composite materials. This is due to the interaction between the filler and iodine vapors. It can be observed that when adding chrysotile to CPC, especially when carbon nanotubes are also present,

these materials prevent the interaction between the doping agent and ICP. When multiwalled carbon nanotubes is used, iodine vapors even function as doping agent for carbon nanotubes, being easily absorbed by them in a process that occurs in competition with poly(3-hexylthiophene) doping.

CHAPTER VI: COMPREHENSIVE CONCLUSION AND FUTURE PROSPECTS

Over the last few decades science has focused on the possibilities offered by nanotechnologies, particularly to alter a material's properties by manipulation or arrangement of nanoscale components.

The main purpose of this research work was accomplished, namely to establish a correlation between the electrical properties of electrospun conductive polymer composites to their regular, hierarchical structure. In particular, the structural and spatial disposition of the building blocks of these materials was shown to be just as important, if not more important, than the nature of these materials and their intrinsic properties. The possibility to create preferential paths with no obstacles to adversely affect electron mobility is of fundamental importance to system optimization.

In the first part of our research we used bottom-up methodologies to successfully synthesize geomimetic stoichiometric chrysotile nanotubes and a number of different types of zero-dimensional (0D) nanostructured materials, including thiol capped metal nanoparticles and metal oxide nanoparticles. The chemical, physical, structural and morphological characterization of nanoparticles and nanotubes indicated that it is possible to synthesize materials that can be reproduced and are homogeneous and stable. The synthesized metal nanoparticles display different properties according to the type of metal used and also to the lack or presence of a capping agent.

Nanosized anatase particles and copper(I) chloride particles were obtained. These particles display a low ability to form aggregates, are stable, crystalline and remarkably pure.

The production of nanostructured composite materials made of synthetic chrysotile nanotubes and thiol capped metal nanoparticles was developed throughout our research work to the point of being able to obtain systems with highly filled nanotubes. Among the main themes for future studies will be the isolation similar systems without nanoparticles distributed in the area outside the central core, and the identification of a methodology to firmly anchor nanoparticles within nanotubes, together with the external functionalization of nanotubes with antenna molecules that can interact with light.

In the first part of this research we also studied commercially available materials like multiwalled carbon nanotubes and graphene oxide. Their characterizations confirmed their structure and functionalization but revealed a low degree of purity. The analysis of these materials proved

fundamental to the final study of the properties of CPCs products. Currently, a lot of attention is being paid to these materials because of their properties. It is envisaged that a future development of the study we carried out will be to keep working towards a higher degree of purification. The next stage of this research will be the reduction and functionalization of graphene oxide. This is in order to create systems from the interaction of this material with synthesized nanoparticles and nanotubes that will lead to the production of CPCs with superior electrical, mechanical and thermal properties. During the second part of this research we successfully produced mats with interesting electrical characteristic from two different polymer blends. The first system we produced was polyaniline based, the second was a system of poly(3-hexylthiophene) (P3HT). In both cases it was decided to use these systems with poly(ethylene oxide) (PEO). Adding poly(ethylene oxide), an insulating material, adversely impacted their electrical conductivity but led to the production of fibers with no imperfection and morphologically constant, which is fundamental to the study of structure-properties correlations.

The next step of this study will be to try and lower the PEO:ICP ration and the average diameter of the fibers in order to maximize the mat electrical conductivity and conduct further analysis of fiber orientation and study the possibility of using new conducting polymers. Despite sharing the same conductivity mechanism, the two electrospun polymer blends we produced displayed very different levels of superficial electrical conductivity and a very different way of interacting with inorganic materials.

In the last part of this research a large quantity of conductive polymer composites was produced starting from two different polyaniline and poly(3-hexylthiophene) polymer blends. Their electrical, thermal and structural characterization was also completed. The large quantity of these materials, which had been synthesized during the first part of the research, and their different structures were instrumental to achieving the goal of this study which was to establish a correlation between structure and CPCs properties, but also to produce materials that would be of interest and could be used in various fields.

We envisage that the materials we produced can greatly enhance a vast range of devices, such as diodes, transistors, sensors, printed circuits, microchips, solar cells, fuel cells, supercapacitors and lithium ion batteries.